UiT
THE ARCTIC
UNIVERSITY
OF NORWAY

Faculty of Science and Technology
Department of Physics and Technology

Analysis of Oil Spill and Sea Ice Measurements Using Full-Polarimetric and Hybrid-Polarity Synthetic Aperture Radar data

—

Martine M. Espeseth
A dissertation of the degree of Philosophiae Doctor – September 2019

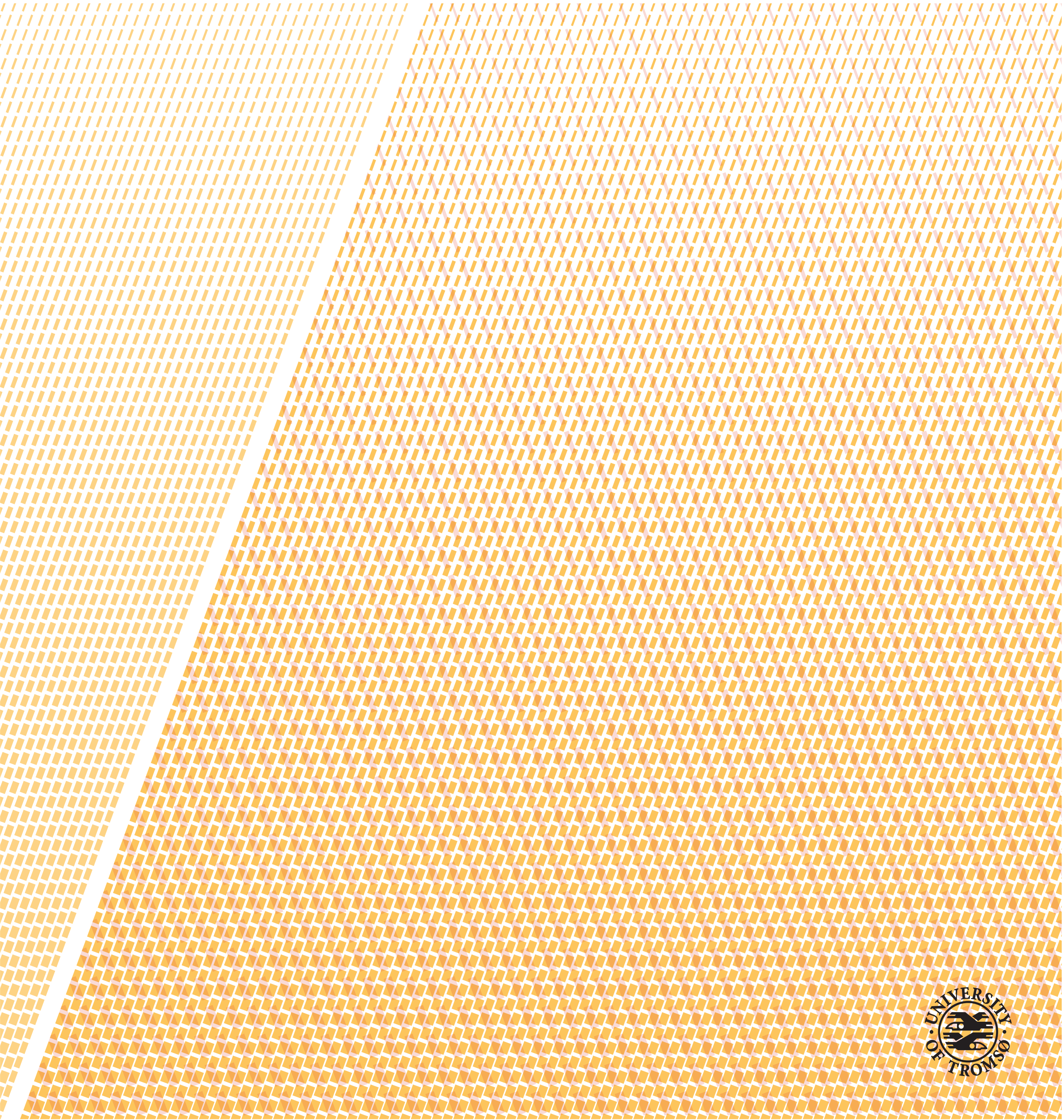

This thesis document was typeset using the *UiT Thesis LaTeX Template*.

“Physics isn’t the most important thing. Love is.” — Richard P. Feynman

Abstract

Synthetic Aperture Radar (SAR) data has been used for decades to detect oil slicks and monitoring sea ice. With increased oil and gas exploration in the Arctic follows higher risk for oil spills. Knowledge of the sea ice and oil spills is important for making clever and efficient decisions in a hectic and also non-hectic operational situation, e.g., oil recovery operations or during nautical navigation procedures. The first aim of this thesis is to understand the potential and limitations of multipolarization SAR data for detecting and characterizing marine oil spills. The second aim of this thesis involves investigating the use of real and simulated hybrid-polarity (HP) SAR data for separating different types of sea ice. The analyses are performed on unique data sets acquired during oil spill exercises in the North Sea and on sea ice in-situ data collected in Fram Strait. The potential and limitations of HP mode for oil spill and sea ice applications are evaluated, and results show that the HP mode is almost as good as the full-polarimetric (FP) SAR mode. This thesis also recommends FP and HP features suitable for oil slick detection. These are identified to have a strong connection to oil damping of the small-scale ocean surface roughness in two-scale Bragg models. Separability of various Arctic sea ice is evaluated, and results based on both real- and simulated HP data are compared. Overall, the results indicate a similar separability performance using real- and simulated HP data. The backscattered signal from oil slicks might be contaminated by various system noise sources, especially for spaceborne instruments. This will limit the ability to use the data for any scattering analysis or information extraction of physical oil properties. A set of well known polarimetric features are shown to be highly influenced by system noise, both additive and multiplicative. It is demonstrated that including several multiplicative system noise factors reduces the signal-to-noise ratio. The reasons for what has often been assumed a different scattering mechanism within oil slicks, frequently termed non-Bragg in the literature, is concluded to mainly be result of system noise. This thesis also explores methods that provide complementary information products that could be valuable in the oil spill recovery process. The methodologies are aimed at creating maps that combine several SAR images to make products that quantify and visually depict the temporal evolution of the slick in an easily understandable representation. The work presented in this thesis adds to the on-going discussion on the use of multipolarization and HP data for oil spill detection/characterization and sea ice monitoring, including the effect of varying sensor parameters, with a special focus on additive and multiplicative system noise sources.

Acknowledgements

Few PhD students are blessed with a team of supervisors so dedicated and brilliant as mine. First, I would like to express my sincere gratitude to my main supervisor and *partner in crime* Camilla Brekke. Thanks for the valuable contributions, discussions, support, and for sending me to exotic locations all around the world. I am looking forward to our continued collaboration. Thanks to my co-supervisor Stine Skrunes, your feedback and our discussions have been extremely valuable throughout this work. Your open door policy has been truly appreciated and it has been great fun learning from you. A huge thank you to my co-supervisor Cathleen E. Jones for your continuous support and contributions throughout my project. It has been a true pleasure to work with you. Special thanks are in order for inviting me to JPL and for your last visit to Norway during my final phase of submission. To my mentor Benjamin Holt, thanks for your support, and for hosting and taking care of me in the USA. Our meandering discussions ranging from sea ice in the north to oil spills in the south have been both inspiring and fun. Thanks for telling me about *Quinuitiuq*, it has come in handy on multiple occasions. Thanks to my co-supervisor Arnt-Børre Salberg for proof reading my work, and for your great advice and discussions.

Thanks to JPL for hosting and welcoming me two times during my project. My exchanges to JPL have been truly great experiences. I would like to thank the JPL/UAVSAR-team for the collection and help with UAVSAR data, and NOFO for letting us participate in the oil-on-water exercises and for generously sharing the data with us. I would also like to extend my gratitude to the Norwegian Polar Institute for collecting sea ice measurements in the Fram Strait, and MET Norway for the great collaborations and discussions. I am looking forward to further collaborating with all of you.

Thanks to A. Malin Johansson for your help throughout this project, and for being my traveling companion to conferences during my time at CIRFA. I have really benefited from our discussions and collaboration. I want to express my gratitude to Thomas Kræmer for helping me with programming, *googling*, and for always asking the difficult questions. A huge thanks to Johannes Lohse, Anthony Doulgeris, Jakob Grahn, and Vebjørn Karisari for all your help related to programming, our valuable discussions and making every day at CIRFA fun.

I would like to acknowledge CIRFA and center leader Torbjørn Eltoft, who founded this project, and thus gave me the great opportunity to research these interesting topics.

Thanks to UiT for all the administrative help and for the exchange scholarship to the USA. Also a warm thanks to my colleagues at CIRFA; the only thing more fun than discussing science with a researcher is having lunch with one. Thanks to KSAT, and a special thanks to Hugo Isaksen. I so enjoyed our collaboration together with Line Steinbakk. It has been a great experience to get a different perspective on my research. I'm looking forward to our continued collaboration.

I want to express my sincere gratitude to my family and friends for supporting me through these years. Finally, to my husband and best friend, Jan-Ove Karlberg. Thanks for your love, support, proof reading my work several times, and for advising me to sometimes take a break.

Contents

List of Figures

List of Tables

List of Abbreviations

BAQ Block Adaptive Quantization

CIRFA Centre for Integrated Remote Sensing and Forecasting for Arctic Operations

CP Compact-Polarimetry

DCP Dual-Circular Polarization

DLR German Aerospace Center

DP Dual-polarimetric

ESA European Space Agency

EM Electromagnetic

FP Full-Polarimetric

HP Hybrid-Polarity

IR Infrared

ISLR Integrated Sidelobe Ratio

JM Jeffries-Matusita

JPL Jet Propulsion Laboratory

KS Kolmogorov–Smirnov

KSAT Kongsberg Satellite Services

MNR Multiplicative-Noise-Ratio

NASA National Aeronautics and Space Administration

NESZ Noise-Equivalent-Sigma-Zero

NOFO Norwegian Clean Seas Association for Operating Companies

PRF Pulse Repetition Frequency

PSLR Peak-to-Sidelobe Ratio

QP Quad-Polarimetric

RAR Real Aperture Radar

RCM Radarsat Constellation Mission

RCS Radar Cross-Section

SAR Synthetic Aperture Radar

SFI Centre for Research-based Innovation

SLAR Side-Looking Airborne Radar

SNR Signal-to-Noise Ratio

SP Single-Polarimetric

SPM Small Perturbation Model

UAVSAR Uninhabited Aerial Vehicle Synthetic Aperture Radar

WMS Web Map Service

Nomenclature

B_r	Bandwidth of transmitted pulse
$\boldsymbol{C}$	Covariance matrix
c	Speed of light
D_A	Antenna length
D_R	Antenna width
DR	Damping ratio
DoP	Degree of Polarization
d	Bhattacharyya distance
d_R	Difference between ranked pairs
E^{sc}	Scattered electric field vector
E^{tr}	Transmitted electric field vector
$F_X(x)$	Cumulative distribution function
f	Frequency
$f(x)$	Probability density function
H	Horizontal polarization
h	Height between sensor and surface
k	Wavenumber
$\boldsymbol{k}_{HP}$	Target vector for a hybrid-polarity system
$\boldsymbol{k}_{GH,GV}$	Target vector for general transmit and linear receive
k_s	Calibration and processing scaling factor
L	Synthetic aperture length
$\boldsymbol{M}$	Measured Sinclair matrix
$\boldsymbol{m}$	Mean of a class
$\boldsymbol{N}$	Complex additive noise matrix
n_{pq}	Complex additive noise coefficient at p and q polarizations
$\boldsymbol{q}$	Stokes vector
R_{pq}	Bragg scattering coefficients at p and q polarizations
$\boldsymbol{R}_s$	Cross-talk and channel imbalance in the receiving system
$\boldsymbol{S}$	Sinclair matrix
s_h	Standard deviation of the surface height
$\boldsymbol{s}_L$	Target vector in lexicographic basis
$\boldsymbol{s}_P$	Target vector in Pauli basis
$\boldsymbol{T}$	Coherency matrix
$\boldsymbol{T}_s$	Cross-talk and channel imbalance in the transmitting system

V	Vertical polarization
W	Wave number spectral density of the surface roughness
χ	Ellipticity angle
δ_A	Azimuth resolution
δ_{CI}	Channel imbalance
δ_p	Penetration depth
δ_{R_g}	Ground range resolution
δ_1/δ_2	Cross-talk values
ϵ_r	Relative dielectric constant
λ	Wavelength
λ_B	Wavelength of Bragg waves
ψ_{ti}	Tilt angle: angle between the normal to the surface and the normal of a facet in the plane of incidence
ψ	Orientation angle
ϕ	Rotation angle of tilted facet
ρ_S	Spearman's correlation coefficient
Σ	Covariance of two classes
σ_{pq}^n	Additive noise power at p and q polarizations
σ_{pq}^0	Radar backscatter coefficient at p and q polarizations
θ	Incidence angle
θ_i	Local incidence angle
ζ_{ti}	Tilt angle: angle between the normal to the surface and the normal of a facet in the plane perpendicular to the plane of incidence

1

Introduction

This thesis explores the potential of using Synthetic Aperture Radar (SAR) polarimetry for observing oil spills and sea ice. The upcoming sections outline the objectives and motivation of the studies presented in the thesis.

1.1 Motivation

The work presented in this thesis is funded by a Centre for Research-based Innovation (SFI), the Centre for Integrated Remote Sensing and Forecasting for Arctic Operations (CIRFA). The focus of CIRFA is integrating remote sensing and forecasting, understood as the process of combining remote sensing data from various sensors, in-situ information and numerical models, for predictions of oceans and sea ice. Since the Arctic is remote, often cloud-covered, and dark for several months of the year, remote sensing instruments are key tools for extracting information from these areas. There are currently several satellites that can be used, and the large amount of available data has created a need for new and efficient methods capable of extracting useful information. CIRFA focuses on the remote sensing of sea ice, oil spills, and the ocean itself. Due to commercial interests, both shipping vessels and petroleum rigs have an increasing presence in the Arctic, and remote sensing instruments are a valuable resource capable of improving operations and monitoring for potential environmental damage. For example, oil spills at sea have been a serious problem for a long time and can cause great harm to the environment. Both active and passive remote sensing systems have proven useful for detecting and also characterizing oil spills. It is well known that SAR can detect oil spills, but recent studies have investigated the possibility of characterizing the oil in terms of its composition (oil type), thickness, and/or the oil fraction in the oil/water mixture. In-situ measurements are necessary to understand and develop algorithms from remote sensing data. Therefore, participation in various field campaigns and experiments in collaboration with other institutes like the Norwegian Polar Institute, Norwegian Clean Seas Association for Operating Companies (NOFO), Jet Propulsion Laboratory (JPL), and German Aerospace Center (DLR) has been a priority. The work presented in this thesis focuses on remote sensing using SAR.

Operational sea ice and oil spill services use SAR as their main source when producing sea ice maps, oil spill detection reports, and other products. Operationally, the single-polarimetric (SP) and the conventional dual-polarimetric (DP) modes are used due to their large spatial coverage. The conventional DP mode is referred to as having one co- and one cross-polarization channel. However, these conventional polarization modes do not offer the high polarimetric information of a quad-polarimetric (QP) (also known as the full-polarimetric (FP)) system. In the last decade researchers have demonstrated that QP modes can yield better separation of different sea ice types compared to the conventional SP and DP modes. The potential of QP modes for distinguishing various types of oils has also been studied, but this must yet be proven for various oil types under different environmental conditions. Low backscattering targets, such as oil slicks and some sea ice types, can be dominated by system noise in remote sensing data. Much research has ignored the large impact of system noise on the measured signal from these low backscattering areas. Ignoring system noise can lead to misinterpretation and miscalculation of scattering properties and information extracted from these targets. More research on separating system noise from the backscattered signal could therefore be beneficial.

Large spatial coverage, fine resolution, high polarimetric information, and minimal radar noise are "dream" properties of an imaging mode. Unfortunately, there will always be a trade-off between these properties. The hybrid-polarity (HP) SAR mode was introduced to improve this trade-off, and has the following advantages: (1) the doubling of the swath width compared to the QP SAR mode; (2) higher polarimetric information than the conventional DP SAR mode; (3) two polarization channels with better signal-to-noise ratios than cross-polarization channels for ocean applications [Raney, 2007]. The HP SAR transmits a circular polarized wave and receives in linear horizontal and vertical polarization channels. The HP mode lies within the group of compact-polarimetry [Souyris et al., 2005]. Currently, the Radarsat Constellation Mission (RCM) (launched June 12, 2019) and ALOS-2 (launched 2014) carries the HP SAR mode. RISAT-1 also offered the HP SAR mode, but this instrument is no longer active. Several research communities have investigated the potential of the HP mode within the fields of sea ice, oil spill detection and classification, crop monitoring, etc., and the majority have concluded that the HP mode is almost "as good" as QP SAR [Atteia and Collins, 2013, Souyris et al., 2005, Li and Perrie, 2016, Collins et al., 2013, Espeseth et al., 2017, Panigraphi and Mishra, 2012]. Most of the published research around the HP mode do not have real HP SAR data available, and thus have to simulate the HP from FP SAR data. It still remains to be tested whether real HP data is as "good" as the FP data.

Several core topics are explored in this thesis. Figure 1.1 shows which topics are covered by each paper (Papers I-IV). The four papers are:

> **Paper I:** M. M. Espeseth, S. Skrunes, C. E. Jones, C. Brekke, B. Holt, and A. P. Doulgeris. "**Analysis of Evolving Oil Spills in Full-Polarimetric and Hybrid-Polarity SAR**", IEEE Transactions on Geoscience and Remote Sensing, vol. 55, no. 7, pp. 4190-4210, July 2017.
>
> **Paper II:** M. M. Espeseth, C. Brekke, C. E. Jones, B. Holt, and A. Freeman "**Interpreting backscattering from oil spills in view of system noise in polarimetric SAR imagery**", IEEE Transactions on Geoscience and Remote Sensing, 2019, in review.
>
> **Paper III:** M. M. Espeseth, C. E. Jones, B. Holt, C. Brekke, and S. Skrunes "**Oil Spill Response-Oriented Information Products Derived from a Rapid Repeat Time-Series of SAR Images**", IEEE Journal of Selected Topics in Applied Earth Observations and Remote Sensing, 2019, submitted.
>
> **Paper IV:** M. M. Espeseth, C. Brekke, and M. Johansson, "**Assessment of RISAT-1 and Radarsat-2 for Sea Ice Observations from a Hybrid-Polarity Perspective**", Remote Sensing. vol. 9, no. 11, September 2017.

Other published papers (as first author or co-author) that are left out of this thesis, but listed in Section 6.2, are indicated in Figure 1.1 by relevance to the core topics. These four papers compose the research contributions of the thesis and the main objectives are:

- To compare the usefulness of various multipolarization SAR features from a FP and HP perspective in relation to oil spill detection, and identify the most important SAR features (FP and HP) when detecting oil spills in high wind conditions (Paper I).

- To evaluate the impact of system noise on polarimetric SAR measurements for oil spill observations, including both additive and multiplicative noise (Paper II).

- To propose algorithms that produce oil spill response-oriented information products derived from time series of SAR images from an operational perspective (Paper III).

- To identify the potential of HP for separating various types of Arctic sea ice and to demonstrate a technique for comparing simulated and real HP SAR data (Paper IV).

1.2 Thesis Outline

This thesis is structured as follows. Chapter 2 covers the basic theory of SAR and polarimetry. Chapter 3 provides an introduction to SAR remote sensing of oil spills, and Chapter 4 discusses SAR remote sensing of sea ice mostly from a HP perspective. Chapter 5 describes the SAR data gathered from the different exercises and campaigns. The paper summaries and other work are presented in Chapter 6. Papers I-IV are presented in Chapters 7-10. An innovation project embedded the PhD project, which is a collaborative effort between CIRFA and Kongsberg Satellite Services (KSAT), is presented in Chapter 11. Finally, Chapter 12 concludes this thesis and presents a future outlook.

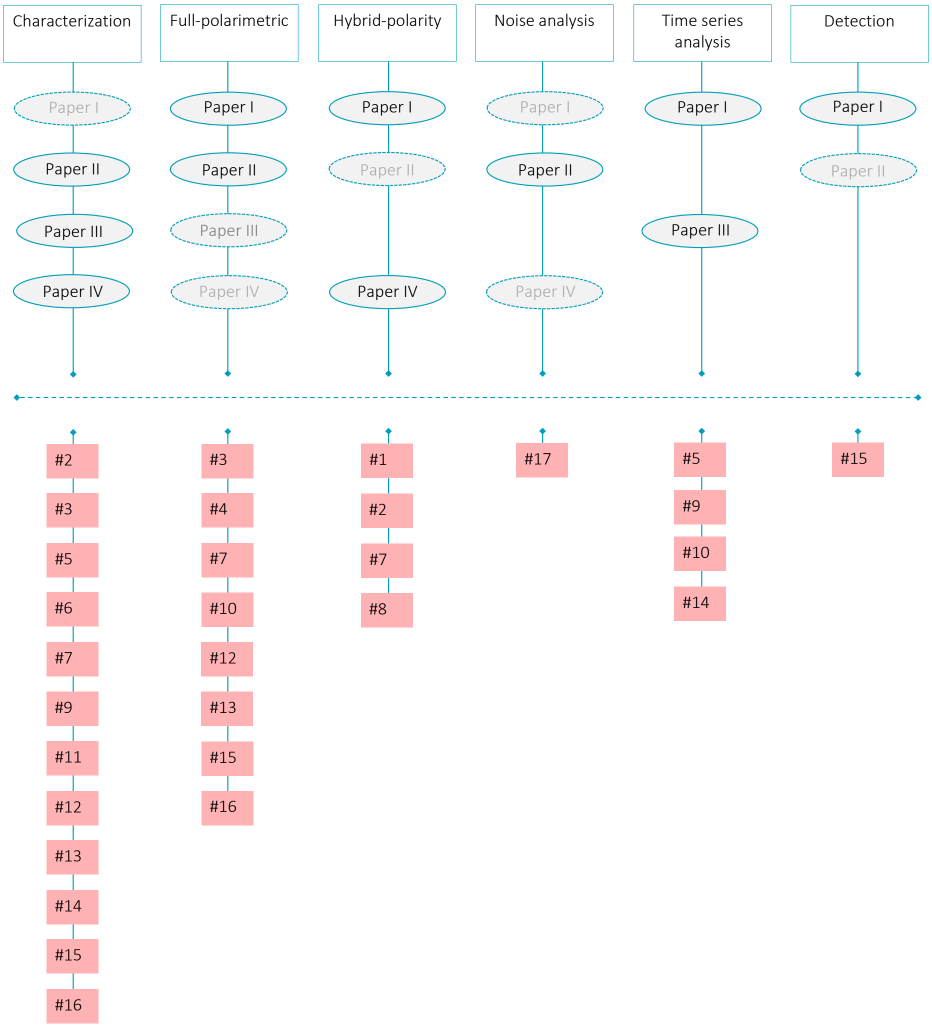

Figure 1.1: Overview of the four papers presented in this thesis (ellipses), in addition to other publications (squares) listed in Section 6.2. Each paper is connected to relevant key-words. The transparent ellipses indicate a weak connection to the key-word.

2

Remote Sensing by SAR

The groundwork and development of radar instruments started during World War II [Jensen, 2000]. Real Aperture Radar (RAR) and SAR instruments were developed from the 1950s, and the first public domain orbital SAR was provided in late 1970s by National Aeronautics and Space Administration (NASA). Since then, multiple satellites with SAR capabilities have been launched, for example SEASAT (1978), Radarsat-1 (1995) [Jensen, 2000], Radarsat-2 (2007) [Canadian Space Agency, nd], and TerraSAR-X (2007) [Fritz and Eineder, 2010]. During the last decades, the introduction of polarimetry and different imaging modes in spaceborne SAR has improved monitoring and forecasting capabilities that can be of aid in environmental crises, and also benefit industrial operators and governments. Science communities have explored SAR polarimetry and its wide potential in many different applications using methods spanning the field of machine learning to physical modelling.

SAR systems are *active*; the radars provide their own signal to measure the surface backscatter, which enables monitoring both day and night. SAR systems transmit pulses in the microwave region, which is beneficial since these wavelengths penetrate most cloud and weather conditions. This is especially suitable in the Arctic, which is covered in darkness several months of the year and also known for heavy cloud cover.

The upcoming sections describe the SAR geometry, spatial and temporal resolution, and frequency. Additionally, speckle and noise artifacts, surface characteristics, and scattering mechanisms relevant for SAR remote sensing are also discussed as these topics are necessary background for all the papers.

2.1 SAR Geometry

Figure 2.1 shows the geometry of a side-looking radar, such as RAR or SAR. The SAR system is mounted on a platform (aircraft or satellite) and records the backscattered signal, both in *range* and *azimuth* direction (see Figure 2.1), resulting in a two-dimensional image [van Zyl and Kim, 2010]. The two-dimensional image is represented as a matrix where each pixel, i.e., resolution cell, contains unique information about the reflectivity of the scatterers. The reflectivity, also known as the backscatter coefficient, and the radar cross-section (RCS) σ^0, possess unique signatures about the physical composition of the scatterers. The measured RCS is also impacted by the sensor properties, such as the frequency, incidence angle, bandwidth, polarization, and system noise.

The sensor travels along the azimuth direction and the side-looking antenna is pointed in the slant range direction while transmitting electromagnetic (EM) pules towards the ground [Curlander and McDonough, 1991]. The coverage of a scene in ground range direction is equal to the swath width. The physical size of the antenna ($D_R \times D_A$) impacts the resolution on the ground.

The principal difference between SAR and RAR is the azimuth compression applied to the recorded backscattered signal in SAR [Curlander and McDonough, 1991]. With this technique in place, one can achieve extremely fine resolution in the azimuth direction compared to RAR systems.

2.2 Spatial Resolution

Spatial resolution is "the minimum distance between two points on the surface that can still be separable" [Elachi and van Zyl, 2006]. The resulting two-dimensional SAR image has one resolution in range direction (ground and slant range resolution) and one in azimuth direction (azimuth resolution). The ground range resolution (δR_g) is expressed as [Curlander and McDonough, 1991]

$$\delta R_g = \frac{c}{2B_r \sin(\theta)}, \tag{2.1}$$

where c is the speed of light, B_r is the bandwidth of the transmitted pulse, and θ is the incidence angle. Both RAR and SAR use frequency modulated chirp pulses with a large B_r to achieve a fine range resolution [Elachi and van Zyl, 2006]. Further, a matched filter is applied on the recorded backscatter signal to increase the signal-to-noise ratio (SNR) [Curlander and McDonough, 1991].

The azimuth resolution of a RAR system is [Elachi and van Zyl, 2006]

$$\delta A = \frac{h\lambda}{D_A \cos(\theta)}, \tag{2.2}$$

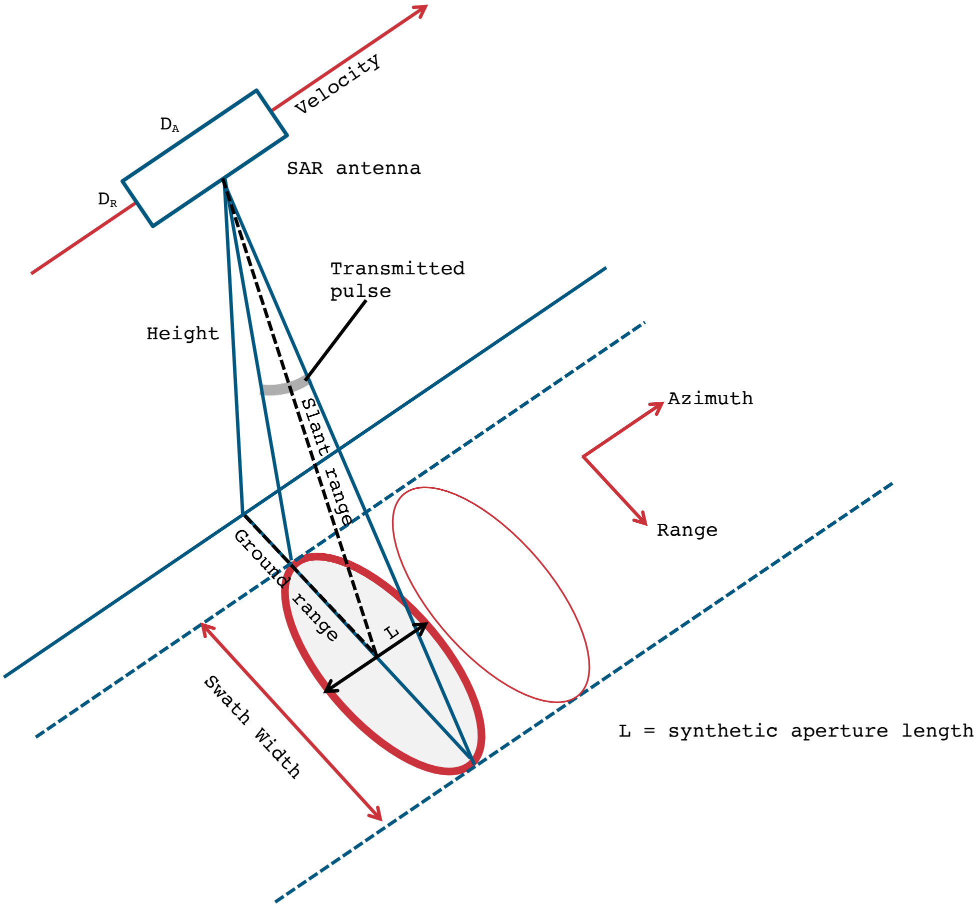

Figure 2.1: Simplified illustration of the SAR geometry (adapted from Figure 1.6 in [Curlander and McDonough, 1991]). D_A and D_R is the antenna length and width, respectively.

where h is the height between the sensor and ground, and λ is the wavelength of the transmitted EM pulse. The azimuth resolution is inversely proportional to the physical antenna length, and a fine azimuth resolution is achieved with a long RAR antenna. The fine azimuth resolution of SAR is achieved as a result of synthesizing a large antenna, hence the name SAR. In order to synthesize a larger antenna, the SAR sensor needs to be in motion while transmitting pulses. After advanced signal processing using the Doppler and phase history of the backscattered pulses the SAR azimuth resolution (δA) is [Curlander and McDonough, 1991]

$$\delta A = \frac{D_A}{2}, \tag{2.3}$$

where D_A is the antenna length. As seen from Equation 2.3, a small antenna results in fine resolution. Hence, the SAR is distinctive from other radar systems as it improves the azimuth resolution by synthesizing a longer antenna.

2.3 Temporal Resolution

The repeat cycle of a satellite is the time it takes for a satellite to pass over the same point on the Earth's surface. The repeat time varies along the latitude, and it can take several days for a spaceborne satellite to revisit the same area with the same orbit. For example, Sentinel-1 and RCM satellites have a repeat cycle of ~12 days, whereas Radarsat-2 has ~24 days [1].

The temporal resolution represents the time it takes for a satellite to cover the same location, i.e., overlap along adjacent orbits in the imaging swaths. The temporal resolution gets finer with distance from the equator. It can take less than one day for a spaceborne satellite to revisit a location in, for example, the Arctic. Combining different satellites will improve the temporal resolution. The same is true if an imaging mode with a large swath width (large coverage) is used. Furthermore, using an airborne instrument, e.g., Uninhabited Aerial Vehicle Synthetic Aperture Radar (UAVSAR) allows for fine temporal resolution. UAVSAR data with a temporal resolution of less than 20 minutes is explored in Papers I, II and III.

2.4 Polarimetry

SAR instruments transmit EM pulses towards the ground, and the EM pulses consist of electric and magnetic fields that are orthogonal to each other. The polarization of the EM wave is defined by the direction of the electric field, and direction and amplitude of the electric field may be described in terms of two orthogonal basis vectors [Elachi and van Zyl, 2006]. In general, the EM waves are elliptically polarized, and special cases are linear and circular polarization [Lee and Pottier, 2009].

Various polarizations and frequencies have different sensitivity to the physical properties of a given surface element, and polarization can therefore provide additional information. In SAR remote sensing, multiple polarization combinations on transmit and receive are available and one given combination is known as a polarization channel. Available polarization channels vary amongst sensors and also within imaging modes of a sensor. In the following subsections, a more detailed description of polarization and polarimetric target descriptors are presented. The concept of compact-polarimetry (CP) – one of the main topics of this thesis – is also introduced.

---

1. `https://earth.esa.int` (accessed 5 September 2019).

2.4.1 Polarization Diversity

SAR instruments can image the surface in different polarimetric modes, referred to as polarization diversity. Note that "mode" also is a common term when referring to the different acquisition modes, like the spotlight, stripmap, and scanSAR modes. There are three main polarimetric modes, namely the QP, DP, and SP mode. The SP mode transmits and receives using a single polarization. The DP mode employs two polarization channels, often one copolarization and one cross-polarization channel. The QP mode both transmits and receives in two polarization channels, resulting in four channels (HH, HV, VH, and VV).

Most satellites have linear polarizations on the transmitter and the receiver, either horizontal and/or vertical. In current satellite missions, there is a compromise between number of polarization channels, swath width, and spatial resolution. Over the last decades, CP has emerged, especially the HP mode [Raney, 2007]. The CP mode employs two channels, and is therefore categorized as a DP system.

There are three modes established in the CP architecture. The first was introduced by [Souyris et al., 2005], known as the $\pi/4$-polarization mode, which transmits diagonally polarized waves (orientated at 45°) and receives on two linear polarizations. The second mode, the HP mode, was suggested by [Raney, 2007]. In this case, circular polarization is transmitted while receiving linear horizontal and vertical polarizations. The third CP mode transmits in circular and measures the response in left- and right-hand circular polarizations, known as the dual-circular polarization (DCP) mode. In DCP and HP modes, both horizontal and vertical polarizations with different phases are transmitted simultaneously. The reasons for the large interest in the HP mode is that it provides the polarimetric benefits from the QP mode, the large swath width from the conventional co- and cross-polarimetric DP mode, and a simpler implementation of the radar design than the DCP mode [Raney, 2007].

In the literature, the HP mode has received the most attention, and has also been integrated in both previous and current satellites (RISAT-1, ALOS, and the RCM). This mode is explored throughout this thesis and in all the included papers. Papers I and IV are particularly focused on the HP mode.

2.4.2 The Scattering Coefficient

The scattering coefficients holds information about the unique target scattering signatures [Cloude, 2010]. The scattering coefficients are functions of both the sensor properties (frequency, incidence angle, and polarization) and the unique physical signatures of the target. In remote sensing, this unique signature is of special interest. Mathematically, the transformation between the transmitted and the received EM wave is [Lee and Pottier, 2009]

$$\boldsymbol{E}^{sc} = \begin{bmatrix} S_{HH} & S_{HV} \\ S_{VH} & S_{VV} \end{bmatrix} \boldsymbol{E}^{tr} = [S]\boldsymbol{E}^{tr}, \tag{2.4}$$

where $\boldsymbol{E}^{tr}$ is the transmitted electric field vector and $\boldsymbol{E}^{sc}$ is the received electric field vector. $[S]$ is the 2×2 complex scattering matrix that contains the scattering coefficients, where the first (second) subscript represents polarization on transmit (receive). Here, the H and V denotes horizontal and vertical polarizations. For a QP system the full 2×2 scattering matrix can be measured. For the DP system only two of the scattering coefficients are available, while the SP system only allows for one scattering coefficient to be measured. If the complete scattering matrix is known, one can synthesize any arbitrary combination of transmit and receive, for example synthesizing one of the CP modes [Cloude et al., 2012, Cloude, 2010]. This is done in Paper I, Paper II, and Paper IV presented in this thesis, which allows for testing and evaluating the potential of HP modes for applications such as oil spill and sea ice observation.

2.4.3 Covariance and Coherency Matrix

From the full scattering matrix, the target covariance and coherency matrices can be calculated. These matrices have been used frequently in various decomposition methods (for example the H/α decomposition [Lee and Pottier, 2009]) and as input to physical scattering models. Further, these matrices also form the fundamental basis of polarimetric feature retrieval. The full covariance and coherency matrix is derived from FP data. Reciprocity ($S_{HV} = S_{VH}$) is often assumed [Lee and Pottier, 2009], which reduces the covariance and coherency matrices by one dimension. The covariance matrix ($\boldsymbol{C}_3$) and the coherency matrix ($\boldsymbol{T}_3$) (with reciprocity) are [Lee and Pottier, 2009]

$$\boldsymbol{C}_3 = \langle \boldsymbol{s}_L \boldsymbol{s}_L^{\star T} \rangle = \begin{bmatrix} \langle |S_{HH}|^2 \rangle & \sqrt{2}\langle S_{HH} S_{HV}^{\star} \rangle & \langle S_{HH} S_{VV}^{\star} \rangle \\ \sqrt{2}\langle S_{HV} S_{HH}^{\star} \rangle & 2\langle |S_{HV}|^2 \rangle & \sqrt{2}\langle S_{HV} S_{VV}^{\star} \rangle \\ \langle S_{VV} S_{HH}^{\star} \rangle & \sqrt{2}\langle S_{VV} S_{HV}^{\star} \rangle & \langle |S_{VV}|^2 \rangle \end{bmatrix} \tag{2.5}$$

and

$$\begin{aligned} \boldsymbol{T}_3 &= \langle \boldsymbol{s}_P \boldsymbol{s}_P^{\star T} \rangle \\ &= \frac{1}{2} \left[\begin{matrix} \langle |S_{HH} + S_{VV}|^2 \rangle & \langle (S_{HH} + S_{VV})(S_{HH} - S_{VV})^\star \rangle & \\ \langle (S_{HH} - S_{VV})(S_{HH} + S_{VV})^\star \rangle & \langle |S_{HH} - S_{VV}|^2 \rangle & \cdots \\ 2\langle S_{HV}(S_{HH} + S_{VV})^\star \rangle & 2\langle S_{HV}(S_{HH} - S_{VV})^\star \rangle & \end{matrix} \right. \\ & \qquad \left. \begin{matrix} & 2\langle (S_{HH} + S_{VV})S_{HV}^\star \rangle \\ \cdots\cdots\cdots & 2\langle (S_{HV} - S_{VV})S_{HV}^\star \rangle \\ & 4\langle |S_{HV}|^2 \rangle \end{matrix} \right] \end{aligned} \tag{2.6}$$

where $\langle \ldots \rangle$ denotes spatial averaging, T is the transpose operator, and $\star$ denotes the complex conjugate. The scattering vector in the Lexicographic space, $\boldsymbol{s}_L$, is defined as [Lee and Pottier, 2009]

$$\boldsymbol{s}_L = [S_{HH}, \sqrt{2}S_{HV}, S_{VV}]^T, \tag{2.7}$$

while $\boldsymbol{s}_P$ is the scattering vector in the Pauli basis, defined as

$$\boldsymbol{s}_P = \frac{1}{\sqrt{2}}[S_{HH} + S_{VV}, S_{HH} - S_{VV}, \sqrt{2}S_{HV}]^T. \tag{2.8}$$

2.4.4 Hybrid-Polarity

Since the late 1980s research communities have synthesized various polarization on transmit and receive from a FP system. Kennaugh and Huynen first presented how to synthesize various polarization on transmit and receive using the unitary change of polarization state transformation [Huynen, 1970,Kennaugh, 1952]. The process of synthesizing various polarization channels is by multiplying the target scattering matrix with unitary matrices that contain information about the ellipticity angle (χ) and the orientation angle (ψ) of the transmitted and received EM wave. Figure 2.2 shows, at a given time-step and at a fixed point in space, an illustration of an elliptically polarized wave. For linear horizontal or vertical polarization the $\chi = 0$, whereas for perfect left- and right-hand circular polarized wave the $\chi = 45^\circ$ and $\chi = -45^\circ$, respectively [Lee and Pottier, 2009].

The HP SAR mode is a subgroup of CP, where the transmitted pulse is either left- or right-hand circular polarized, with linear horizontal and vertical polarizations on receive [Raney, 2007]. Touzi and Charbonneau [2014] pointed out the challenges with generating a perfectly circular polarized wave using current technology. A practical consequence of this is a more elliptically polarized wave rather than circularly polarized in an HP SAR system. This is known as the non-circularity property [Touzi and Charbonneau, 2014]. Paper IV briefly explores the impact of not having a perfect circularly polarized wave when separating different types of sea ice.

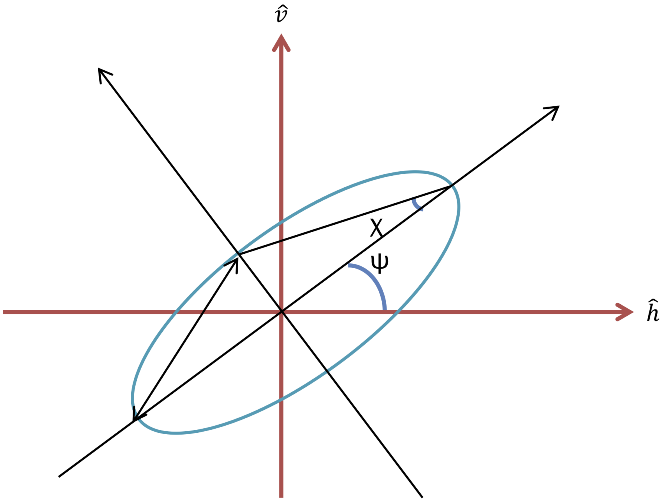

Figure 2.2: Geometry of an elliptical polarized wave described by the orientation angle (ψ) and ellipticity angle (χ). Illustration based on Figure 2.5 in [Lee and Pottier, 2009].

Figure 2.3 gives an overview of the three main CP modes, and three common ways of working with such modes. The three methods, namely reconstruction, feature retrieval, and decomposition, are ways of extracting information about the target. Espeseth et al. [2016] tested two existing reconstruction methods and suggest a new one for sea ice data. This paper is not included as one of the four main papers presented in this thesis. Decomposition has not been the focus of any of the included papers. This is because most of the explored targets usually are dominated by surface scattering, and not double-bounce and volume scattering. Feature retrieval is the method that has received the most attention in the four presented papers.

The Scattering Vector in HP mode

Any polarization can be synthesized on transmit and receive, as long as the full target scattering matrix is available. For example, the DP scattering vector of a general (G) transmit and horizontal (H) and vertical (V) polarizations on receive is defined as [Lee and Pottier, 2009, Sabry and Vachon, 2014];

$$\boldsymbol{k}_{(GH,GV)} = \begin{bmatrix} \cos(\chi_t)\left(\cos(\psi_t)S_{HH} + i\sin(\psi_t)S_{VH}\right) + i\sin(\chi_t)\left(\sin(\psi_t)S_{HH} + i\cos(\psi_t)S_{VH}\right) \\ \cos(\chi_t)\left(\cos(\psi_t)S_{HV} + i\sin(\psi_t)S_{VV}\right) + i\sin(\chi_t)\left(\sin(\psi_t)S_{HV} + i\cos(\psi_t)S_{VV}\right) \end{bmatrix}, \quad (2.9)$$

where χ_t and χ_r are the ellipticity angles, and ψ_t and ψ_r are the orientation angles. The superscripts t and r represents transmit and receive. The reason for fixing the receive is because present, current, and future DP SAR missions receive in vertical and horizontal

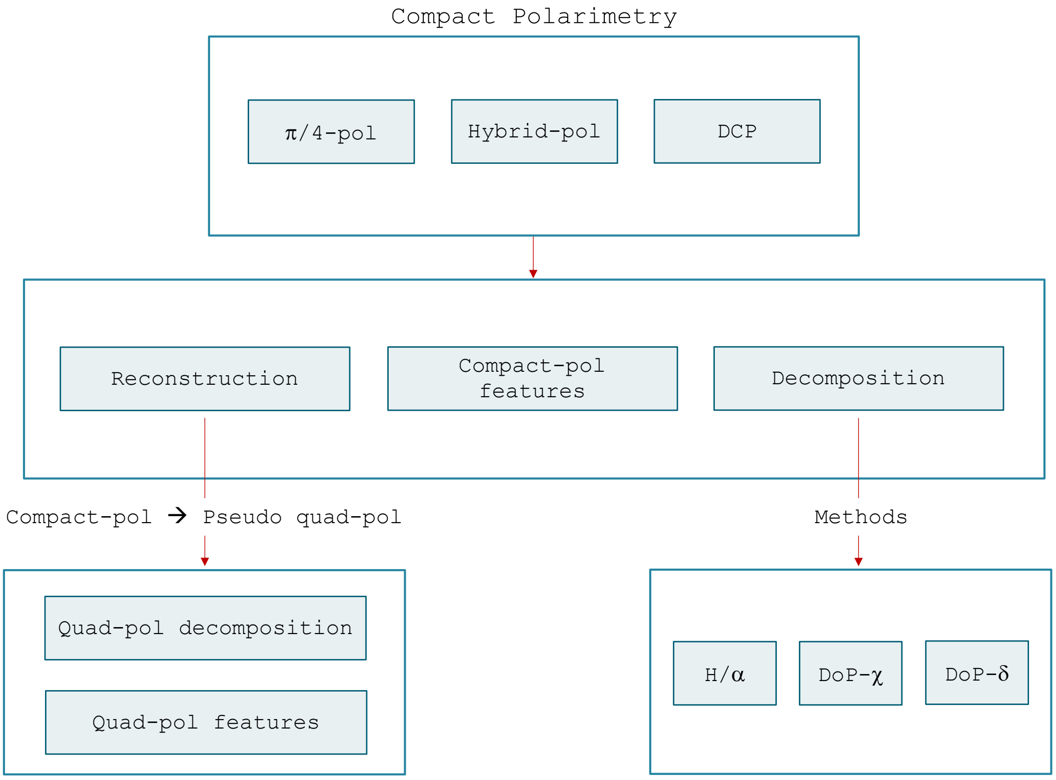

Figure 2.3: Compact polarimetry steps towards reconstruction, feature retrieval, or decomposition.

polarizations, while the transmit varies between vertical, horizontal, and circular. From Equation 2.9 several scattering coefficients can be synthesized, for example the HP mode with right-hand circular transmit and linear horizontal and vertical receive, i.e., $\chi_t = \pm 45$, $\psi_t = 0$, $\chi_r = \psi_t = 0$;

$$\boldsymbol{k}_{HP} = \begin{bmatrix} S_{RH} \\ S_{RV} \end{bmatrix} = \begin{bmatrix} S_{HH} & S_{VH} \\ S_{HV} & S_{VV} \end{bmatrix} \begin{bmatrix} \frac{1}{\sqrt{2}} \\ \pm\frac{j}{\sqrt{2}} \end{bmatrix} = \frac{1}{\sqrt{2}} \begin{bmatrix} S_{HH} \pm jS_{VH} \\ \pm jS_{VV} + S_{HV} \end{bmatrix}. \tag{2.10}$$

Equation 2.10 also demonstrates how the HP mode is simulated from the FP SAR system. This makes it possible to perform a direct comparison between various polarization modes, such as the FP versus HP SAR modes. Such a comparison is performed in most of the presented papers of this thesis. Equation 2.10 also serves as the starting point for feature extraction.

The Stokes Vector

The Stokes vector is a useful tool for representing the data collected by an HP system [Raney, 2007]. The polarization state of a wave can be described through the Stokes vector [Denbina, 2014]. The four real parameters given in the Stokes vector are incoherent, i.e., have no phase dependency. If the transmitted wave is either left- or right-circularly polarized, the Stokes vector becomes [Raney, 2007]:

$$\boldsymbol{q}_{LC} = \begin{bmatrix} |E_{RH}|^2 + |E_{RV}|^2 \\ |E_{RH}|^2 - |E_{RV}|^2 \\ 2\Re(E_{RH}E^{\star}_{RV}) \\ 2\Im(E_{RH}E^{\star}_{RV}) \end{bmatrix} \qquad \boldsymbol{q}_{RC} = \begin{bmatrix} |E_{LH}|^2 + |E_{LV}|^2 \\ |E_{LH}|^2 - |E_{LV}|^2 \\ 2\Re(E_{LH}E^{\star}_{LV}) \\ -2\Im(E_{LH}E^{\star}_{LV}) \end{bmatrix}, \tag{2.11}$$

where E is the complex electric field in the subscripted polarization [Raney, 2007], and L=left-hand circular and R=right-hand circular. Various polarimetric decomposition methods (see lower right box of Figure 2.3) describing scattering mechanisms have been suggested using the Stokes vector [Raney et al., 2012, Cloude et al., 2012]. Several features can be extracted from the Stokes vector, for example the Degree of Polarization (DoP) and ellipticity χ. The DoP has been connected to the entropy describing the scattering degree of randomness [Cloude et al., 2012]. Both DoP and χ have been used frequently in oil spill (see, e.g., [Shirvany et al., 2012, Zhang et al., 2017, Buono et al., 2016b, Nunziata et al., 2015, Nunziata et al., 2013]) and sea ice (see, e.g., [Li and Perrie, 2016, Dabboor and Geldsetzer, 2014b, Zhang et al., 2016, Geldsetzer et al., 2015]) studies. These features are used in three of the papers presented in this thesis.

2.5 Frequency

Frequency plays an important role in the physical interaction between the incident EM wave and the observed surface. The choice of frequency is controlled by the purpose of the SAR mission and its relevant applications. Table 2.1 shows different frequency bands that are commonly used in SAR. In this thesis, frequencies from X-, C-, and L-band have been explored. Ka- and Ku-bands suffer from high interference from the atmosphere due to the short wavelengths in these bands. Hence, these bands are not used frequently for surface studies using spaceborne radar systems.

Frequency band	**Ka**	**Ku**	**X**	**C**	**S**	**L**	**P**
Frequency [GHz]	40-25	17.6-12	12-7.5	7.5-3.75	3.75-2	2-1	0.5-0.25
Wavelength [cm]	0.75-1.2	1.7-2.5	2.5-4	4-8	8-15	15-30	60-120

Table 2.1: Microwave frequency bands [Chuvieco and Huete, 2010].

2.6 Speckle

Speckle is an inherent property in SAR and causes a grainy appearance and is a result of constructive and destructive interference between many scatterers within a resolution cell [Lee and Pottier, 2009]. Speckle is a multiplicative noise-like feature that is unavoidable in SAR images. Several advanced filter methods exist (see, e.g., [Lee and Pottier, 2009]) to reduce the speckle, but a simple method is averaging over a neighborhood of pixels in the spatial domain. The reduction of speckle is performed after the formation of the image, and when calculating the coherency or covariance matrix.

Figure 2.4 shows the effect of using a boxcar filter to reduce speckle. The left image in Figure 2.4 is the VV-intensity (σ^0_{VV}) without any speckle reduction, while the right image shows the improved visibility of the oil slicks after applying a boxcar filter with a 9×9 window.

Speckle also complicates image analysis like image segmentation and classification of various surfaces [Lee and Pottier, 2009]. Figure 2.5 shows the segmentation results (using a regular k-means clustering [Theodoridis and Koutroumbas, 2009]) without and with speckle reduction using a boxcar filter. A significant effect can be observed from applying speckle reduction, where most of the oil slick is segmented into one class and the surrounding clean sea is segmented as another.

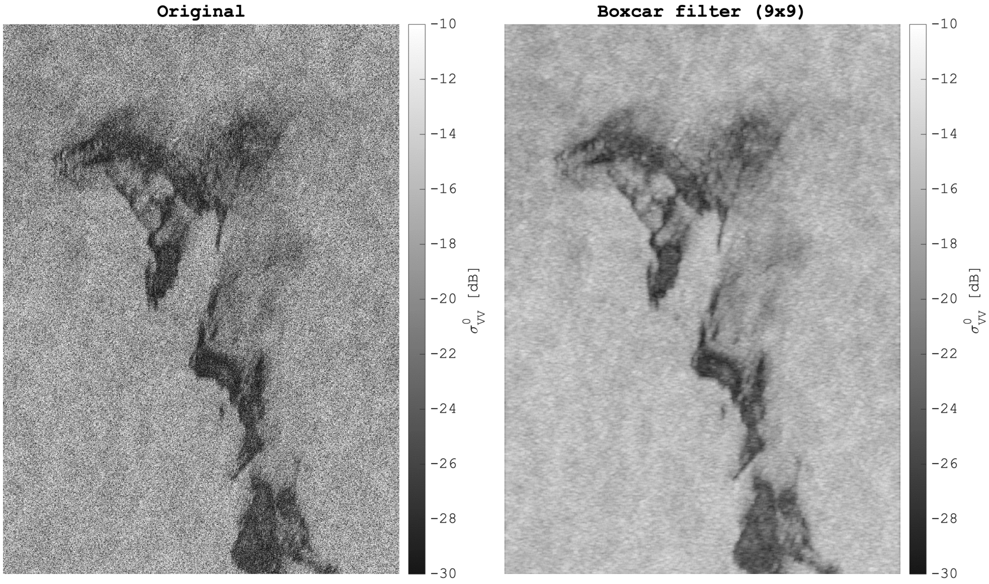

Figure 2.4: σ^0_{VV} images of an oil spill from the oil-on-water exercise in 2012. Left: the original σ^0_{VV} image. Right: σ^0_{VV} with a boxcar filter with a 9×9 window. The Radarsat-2 data and Products © MDA LTD. 2012 - All Rights Reserved.

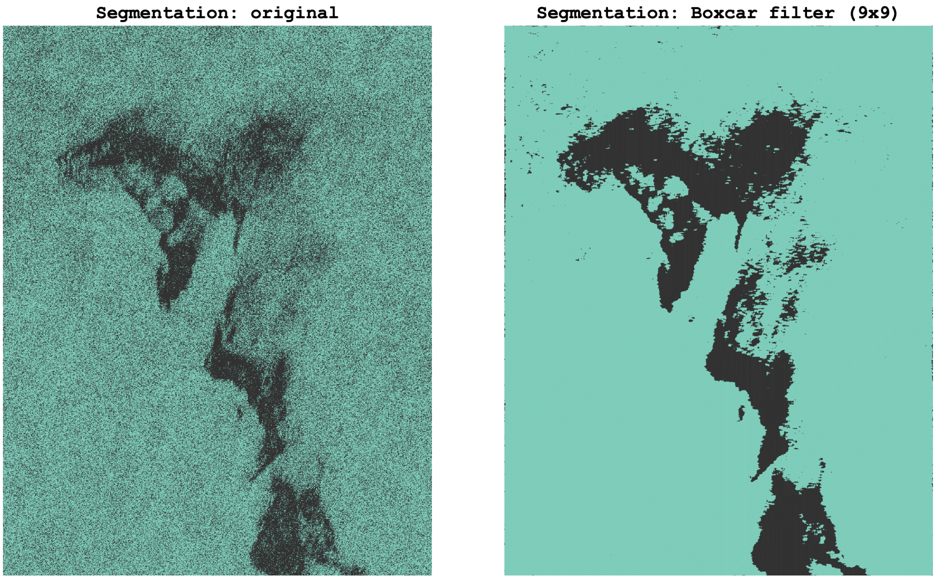

Figure 2.5: Left: Results of segmentation (k-means) on the original VV-intensity image. Right: The effect of speckle reduction (boxcar filter) when segmenting (k-means) the oil slick.

2.7 Noise Artifacts

Polarimetric SAR data contains a great deal of information about the physical interactions between the incident radar wave and the surface elements. Unfortunately, the measured and processed SAR signal contains various types of unwanted noise. As mentioned in Section 2.6, speckle is a multiplicative noise-like feature that is unavoidable in SAR. SAR images suffer not only from speckle noise, but also additive and multiplicative system noise sources. It is not possible to fully recover the RCS, but understanding the effects of various noise types is extremely important to avoid misinterpretations. Noise in SAR data might lead to degraded performance and accuracy of the intended application. The impact of both additive- and multiplicative instrumental noise is studied in Paper II for low-backscattering targets like oil slicks. The upcoming sections provide a brief overview of the various types of noise. This theory is necessary background for Paper II.

The measured scattering matrix can be expressed as [van Zyl, 1990]

$$\begin{aligned} \boldsymbol{M} &= \boldsymbol{R_s}^T \boldsymbol{S} \boldsymbol{T_s} + \boldsymbol{N} \\ &= \begin{bmatrix} 1 & \delta_2 \\ \delta_1 & \delta_{CI} \end{bmatrix} \begin{bmatrix} S_{HH} & S_{HV} \\ S_{VH} & S_{VV} \end{bmatrix} \begin{bmatrix} 1 & \delta_1 \\ \delta_2 & \delta_{CI} \end{bmatrix} + \begin{bmatrix} N_{HH} & N_{HV} \\ N_{VH} & N_{VV} \end{bmatrix}, \end{aligned} \tag{2.12}$$

where $\boldsymbol{S}$ is the complex scattering matrix of the target, $\boldsymbol{R_s}$ and $\boldsymbol{T_s}$ are effects of the receiving and transmitting system on the scattering matrix, and $\boldsymbol{N}$ is the complex additive (thermal) system noise [van Zyl, 1990]. δ_1 and δ_2 represent cross-talk, whereas δ_{CI} represents the channel imbalance [van Zyl, 1990]. Equation 2.12 only considers cross-talk and thermal noise, but there are several additional unwanted noise sources in the measured signal that reduces the SNR. Since the backscatter from oil slicks are low these noise sources might have a significant impact on the polarimetric SAR data covering such areas. The range and azimuth ambiguities, effects from sidelobes, and degradation due to quantization when compressing the measured voltage are not considered in Equation 2.12. These noise sources are just as important as the well known additive system noise when investigating the signal quality from an oil covered pixel. The upcoming subsections briefly discuss each of these noise/degradation sources in SAR, which are also used in Paper II.

2.7.1 Cross-talk and Channel Imbalance

Any SAR mode with more than one channel on either receive or transmit is exposed to cross-talk and channel imbalance. Cross-talk represents leakage between the polarization channels, both within the transmitting and receiving channels. Channel imbalance is inconsistency in amplitude and phase between the polarization channels [van Zyl and Kim, 2010]. Cross-talk and channel imbalance are both unavoidable. The response in the cross-polarization channels is much lower than that of the copolarization channels for most targets and certainly for oil slicks and ocean backscatter. Hence, the leakage is more serious for the cross-polarization channels.

There are ways of estimating and adjusting the cross-talk and channel imbalance using the imaging parameters with some assumptions about the scattering medium [van Zyl, 1990, Ainsworth et al., 2006, Quegan, 1994]. Adjusting the cross-talk and channel imbalance might be crucial when, for example, estimating physical parameters from models, interpreting the scattering physics, and synthesizing (simulating) different polarization modes.

Cross-talk calibration can only be performed on FP SAR data, since the full scattering matrix is required [Touzi et al., 2010, Freeman et al., 1992]. Cross-talk calibration is already performed on the FP Radarsat-2 products before being delivered to customers. Estimation of cross-talk values is not done for UAVSAR and TerraSAR-X in this thesis study. This is because the DP (HH-VV) mode is used in TerraSAR-X, and estimation of cross-talk values is not possible. Cross-talk calibration (see, e.g., [van Zyl, 1990, Ainsworth et al., 2006, Quegan, 1994]) relies on assumption about the scattering surface, and might introduce artifacts in the data. For the UAVSAR products, cross-talk calibration is not recommended for ocean applications, as this might introduce artifacts in the data [personal correspondence Cathleen E. Jones (JPL)]. Paper II highlights the unique cross-talk values in each of the investigated sensors.

2.7.2 Aliasing

Another noise artifact is ambiguity due to aliasing both in range and azimuth direction. These ambiguities appear as ghost images in the SAR data. For example, the ghost of ships might occur at an azimuth distance from the ship, and can in some unfortunate cases be located in an oil slick, corrupting the SAR data in that area. Azimuth ambiguities are affected by, e.g., wavelength, pulse repetition frequency (PRF), and azimuth antenna pattern [Cumming and Wong, 2005]. Range and mostly azimuth aliasing reduce the SNR by introducing unwanted signals that are repeated from other targets and mixed with the desired target signal, and is therefore an important factor to consider for low-backscattering areas such as oil slicks. Paper II briefly discusses the impact of aliasing in range and azimuth direction and how these effects can reduce the SNR.

2.7.3 Effects from Sidelobes

The signal around a target might be spatially smeared as a result of sidelobes of the antenna beam pattern. The terms established to measure these effects are the peak-to-sidelobe ratio (PSLR) and integrated sidelobe ratio (ISLR). These provide an indication of the SAR performance in resolving a weak target in the presence of a strong target (e.g., oil versus ships) [Cumming and Wong, 2005]. Most of the backscattered energy is measured in the mainlobe of the antenna beam pattern (see Figure 2.6). Unfortunately, some energy from adjacent areas will be measured in the sidelobes (like clean sea and ships). The energy from the sidelobes is unwanted signals, resulting in a reduction in the SNR.

The PSLR is defined as the ratio between the highest sidelobe value and the peak value of the mainlobe. The ISLR is the ratio between the total power in all the sidelobes and mainlobe [Cumming and Wong, 2005]. The signal is smeared out along and across track if the ratios of the PSLR and ISLR are high. The effects from the sidelobes can be mitigated by avoiding areas around ships. But the clean sea pixels surrounding the oil slick will have a significant effect on the measured signal from the oil slick if the ISLR is high. Hence low PSLR and ISLR values are desired, such that low-backscattering areas (e.g., oil slicks) have minor impacts caused by spillover from adjacent areas, such as clean sea and ships. The ISLR is therefore factored into the multiplicative noise ratio in the estimation of the SNR for Paper II.

2.7.4 Quantization Degradation

The SAR signal is digitized with an analog-to-digital converter followed by a compression technique (for example Block Adaptive Quantization (BAQ)) to improve the data storage and downlink rate [MDA, 2018]. This introduces degradation noise in the end-product. This could result in lower SNR values (see, e.g., [Vespe and Greidanus, 2012]) especially impacting low-backscattering surfaces like oil slicks and sea ice leads. In some sensors,

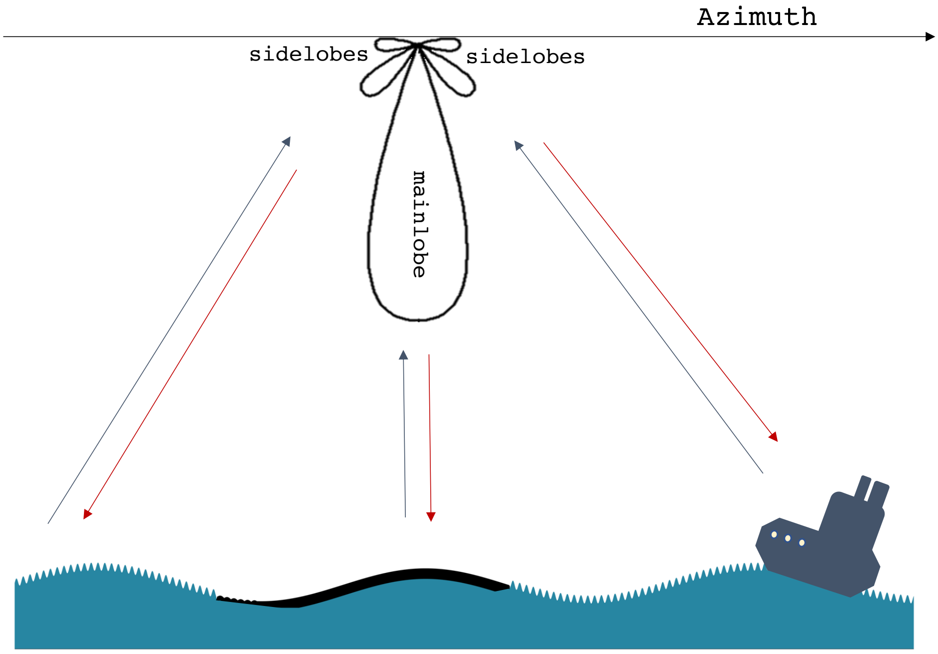

Figure 2.6: Backscattered signal from sidelobes can be captured by the sensor and cause errors in the measured signal from the mainlobe.

the Noise-Equivalent-Sigma-Zero (NESZ) values provided in the product file includes the quantization degradation in the estimation of the nominal NESZ values. One example is the nominal NESZ provided with TerraSAR-X products [Fritz and Eineder, 2010], which includes the quantization noise. On the other hand, Radarsat-2 (see [MDA, 2018]) and UAVSAR products do not include the quantization noise in the nominal NESZ. For example, as pointed out in [MDA, 2018], the quantization noise levels for Radarsat-2 are estimated -19dB times the mean signal level for 4-bit BAQ. This results in larger contributions from the BAQ noise for high values of the mean signal level. The quantization noise is therefore considered in the estimation of the SNR in Paper II.

2.7.5 Additive Noise

The additive noise power is contained in the NESZ, and consists of system and processing noise (e.g., thermal noise and in some cases quantization degradation) that is added to the observed signal from the target. The NESZ is defined as the value for which the radar backscatter coefficient has equal strength to the background noise. NESZ varies as a function of slant range due to the antenna elevation pattern, and also across different sensors and their imaging modes, as demonstrated in Figure 2.7. Examples of some noise

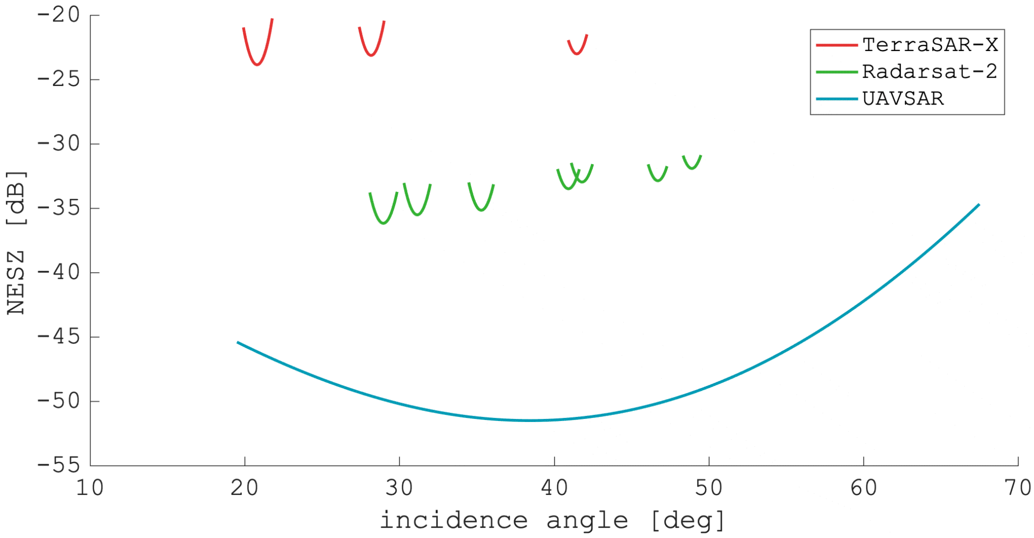

Figure 2.7: NESZ versus incidence angle (θ) for TerraSAR-X (SSC DP (HH-VV) strip-map mode), Radarsat-2 (strip-map fine FP mode), and the UAVSAR (FP mode).

profiles (NESZ) of TerraSAR-X, Radarsat-2, and the UAVSAR are displayed in Figure 2.7. Since the UAVSAR instrument operates in a wide range of incidence angles, only one NESZ profile is shown in Figure 2.7. The NESZ is lowest for the UAVSAR sensor, and this is one of several reasons for this instrument being particularly relevant for oil spill observation.

The SNR is the signal level above the noise floor, and is expressed as;

$$SNR = \frac{\sigma^0}{\sigma^n}, \tag{2.13}$$

where σ^0 is the RCS and σ^n, is the additive noise power. The SNR should be as large as possible. The SNR is often low for spaceborne radar instruments when monitoring low-backscattering targets like oil slicks, grease, or sea ice leads. This is because the smoothness of such surfaces reduces the backscatter response from the incident wave.

2.7.6 Additive and Multiplicative Noise

Most oil spill SAR studies ignore the noise issue or only considers additive noise power using the nominal NESZ when performing a noise analysis, which includes a comparison between the NESZ and the RCS. The impact of ISLR, mostly azimuth aliasing, and quantization noise depends on the mean signal level in the scene. These system noise sources are often left out, but should be included in order to achieve a realistic estimate of the SNR. Since these noise sources depend on the mean signal level in the scene, their effects increase with the mean signal level. These noise factors are called multiplicative system noise due to their dependency on the mean signal level in the scene, but are in fact another additive noise contribution to the measured signal. The multiplicative-noise-ratio (MNR) is a sum of ISLR, quantization-noise ratio (QNR), and ambiguity ratio (in linear units). Paper II demonstrates the negative impact these noise sources have on the SNR. Paper II suggests the following model (based on [Hensley et al., 2014]) for the measured RCS ($\sigma^{0,m}$)

$$\sigma_{pq}^{0,m} = \sigma_{pq}^{0} + \sigma_{pq}^{n} + \sigma_{pq}^{AVG} MNR, \tag{2.14}$$

and

$$MNR = ISLR + 1/QNR + AMB_t \tag{2.15}$$

where AMB$_t$ is the total ambiguity-to-signal ratio. Since oil slicks are usually surrounded by clean sea, the signals from clean sea areas are repeated (due to aliasing) in the oil-covered areas by a factor equal to AMB$_t$ × σ_{pq}^{AVG} (aliased power). A more accurate representation of the SNR should therefore include both the additive and multiplicative system noise, i.e;

$$SNR_{pq} = \frac{\sigma_{pq}^{0,m} - (\sigma_{pq}^{n} + \sigma_{pq}^{AVG} MNR)}{\sigma_{pq}^{n} + \sigma_{pq}^{AVG} MNR}. \tag{2.16}$$

Paper II demonstrates how Equation 2.16 is used and estimated from three different SAR sensors covering oil slicks and clean sea.

2.8 Surface Characteristics

The backscattering signature is highly dependent on the surface characteristics (e.g., roughness and dielectric constant) and sensor properties (e.g., frequency, polarization, incidence angle). The roughness and dielectric constant are discussed in the upcoming sections.

2.8.1 Roughness

High frequency EM waves, i.e., X-band (see Table 2.1), interacts with smaller surface elements than lower frequency waves. Scattering from a rough surface depends strongly on the frequency [Elachi and van Zyl, 2006]. Figure 2.8 shows an example of VV-intensity images from TerraSAR-X (X-band) and UAVSAR (L-band). For a constant roughness spectrum, the RCS increases with the fourth power of the frequency [Elachi and van Zyl, 2006]. The surface roughness and its relation to the incident frequency/wavelength is often described by the Rayleigh criterion, and the surface is considered rough if;

$$s_h \geq \frac{\lambda}{8} \cos(\theta) \tag{2.17}$$

where s_h is the standard deviation of the surface height, λ is the wavelength of the incident wave, and θ is the incidence angle.

The X-band radar observes a rougher sea and more pronounced wave pattern compared to the longer wavelength L-band UAVSAR (see Figure 2.8). The roughness plays an important role when monitoring both oil and sea ice. In oil spill remote sensing, the roughness of the sea is influenced by the wind and ocean conditions, which again will impact the oil-sea contrast. More theory of the roughness in relationship to oil spills and its dampening effects on surface waves is discussed in Chapter 3.

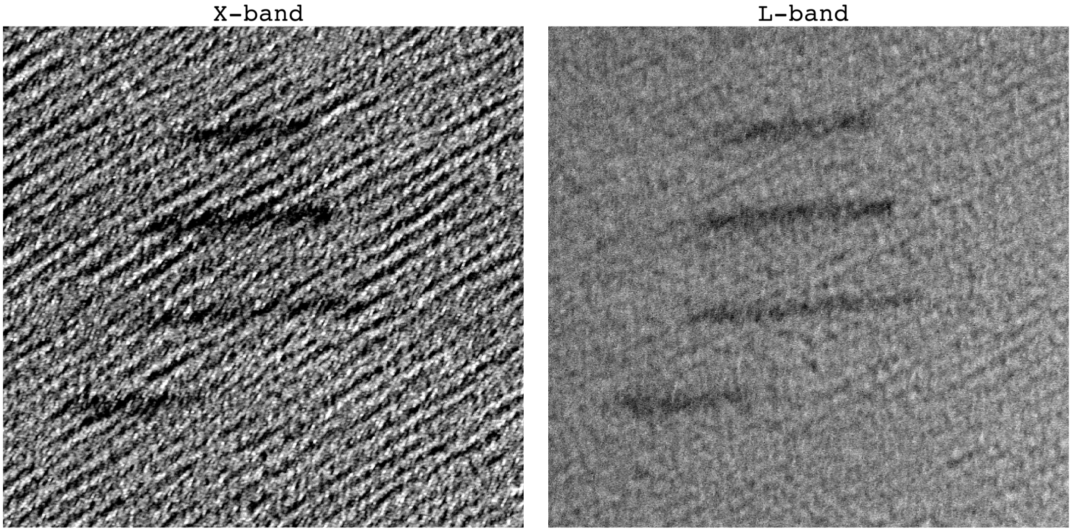

Figure 2.8: VV-intensity of TerraSAR-X (left) and UAVSAR (right) acquired over four oil slicks that were released during the oil-on-water exercise in 2015. TerraSAR-X ©2015 Distribution Airbus DS, Infoterra GmbH. UAVSAR data are courtesy of NASA/JPL-Caltech.

2.8.2 Dielectric Properties

The dielectric constant (ϵ_r) of the surface medium impacts the interaction between the incident EM pulse and the surface. The dielectric properties together with the frequency of the incident wave controls the penetration depth. Lower frequencies penetrate deeper into the surface than higher frequencies. The penetration depth (δ_p) is defined as the depth at which the EM signal is attenuated to $\frac{1}{e}$ [Cloude, 2010], i.e.,

$$\delta_p \approx -\frac{1}{2k\Im(\sqrt{\epsilon_r})} \tag{2.18}$$

where $\Im(\cdot)$ is the imaginary part, ϵ_r is the relative dielectric constant consisting of both a real and imaginary part, and k is the wavenumber defined as

$$k = \frac{2\pi f}{c} \tag{2.19}$$

where f is the frequency of the transmitted EM wave and c is the speed of light. For example, water has a high dielectric constant (both in real and the imaginary parts), and the penetration depth is therefore lower in water compared to pure ice, which has a much lower dielectric constant. Although the dielectric constant of oil is much lower than clean sea (see, e.g., [Minchew et al., 2012, Brekke et al., 2014]), most slicks are too thin for their dielectric properties to significantly influence the backscattered signal.

2.9 Scattering Mechanisms

The scattering mechanism defines how the incident EM wave from the satellite interacts with the target. In general, surface, double-bounce, and volume scattering are the three main scattering mechanisms. Within each category, more complex scattering models can be used that include for example physical interactions within multiple layers (air-snow-ice-water). The measured backscatter signal might be a mixture of one or more scattering types, as a result of several scattering mechanisms occurring within a single resolution cell.

The majority of the papers in this thesis focus on surfaces that are dominated by surface scattering, but some of the papers also discuss volume scattering in context of sea ice or as misinterpreted scattering from oil slicks. As such, only surface and volume scattering is presented in the upcoming sections.

2.9.1 Surface Scattering

Surface scattering, also known as single-bounce scattering, occurs when the incident wave has dispersed only once by the surface boundary between two media (often air and the surface element). There are three main surface scattering scenarios that are controlled by the roughness; (1) smooth surface; (2) slightly rough surface; and (3) a very rough surface [Chuvieco and Huete, 2010] (see Figure 2.9). In the smooth surface scenario, the incident wave is reflected away from the sensor (specular reflection). For a slightly rough surface, the incident wave is divided into two components; specular and diffuse (Lambertian). If the surface is very rough, the backscattered signal is completely diffuse, and a response is generated in all the polarization channels [Cloude, 2010]. No depolarization occurs for a perfectly smooth surface with no out-of-plane tilt [Cloude, 2010], which means no response in the cross-polarization channels. However, if the surface is slightly tilted, a depolarization effect is generated, and a response is introduced in the cross-polarization channel.

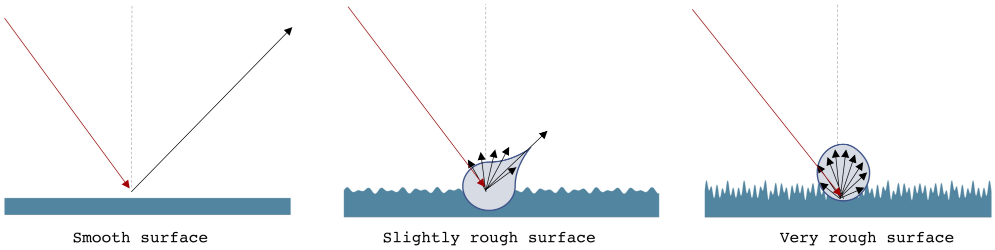

Figure 2.9: Scattering from surfaces with different roughness conditions.

Bragg scattering is a type of surface scattering where the backscatter return from the surface possesses the typical resonant scattering. This occurs when the incident wave's wavelength projected onto the surface is in resonance with the ocean waves [Valenzuela, 1978]. Bragg scattering is an important factor in several of the papers (Papers I-III), and is thus discussed further in Chapter 3. Further, sea ice with various roughness is also investigated (Paper IV), and surface scattering again plays an important role in the set of features that are selected and investigated throughout the papers.

2.9.2 Volume Scattering

Volume scattering occurs within heterogeneous bulk materials with varying particle density and particle distribution that contain local dielectric property variations [Cloude, 2010]. As discussed in Section 2.8.2, frequency, and dielectric properties are two important factors that control the penetration depth. The penetration depth lays the foundation for the dominant scattering type. If the dielectric constant of the scattering element is large, little transmission into the material occurs and thus little or no volume scattering takes place [Tucker III et al., 2013]. However, a higher penetration depth might allow for possible volume scattering to occur within the material, for example multi-year ice [Tucker III et al., 2013]. When volume scattering occurs, a response is generated in all the polarization channels.

There have been several studies within oil spill remote sensing claiming that volume scattering is part of the non-Bragg scattering occurring in oil slicks. One possible origin of volume scattering within the oil slick is breaking waves [Cloude, 2010], which often is classified as the non-polarized component in the non-Bragg scattering group [Alpers et al., 2017]. Unfortunately, system noise has often been misinterpreted as volume scattering measured in the backscattering response from oil slicks. This is the main topic of Paper II, where the influence of various system noise sources in the polarimetric measurements of radar-dark surfaces is explored.

3

SAR Remote Sensing of Oil Spill

Oil spills in the ocean due to human activities have a major and immediate impact on the marine ecosystem. Oil spills might originate from e.g., a pipeline leakage, illegal and legal discharge from vessels/platforms, or accidents. With approximately 8000 platforms and offshore facilitates in the World's oceans [Coleman, 2003], in addition to shipping, fishing, and tourism, there are many potential sources for oil spills. Another marine pollution is natural seeps from the seafloor, which are the largest source of oil entering the ocean [NOAA, nd].

Oil slicks are detected as dark spots in SAR images due to oil's damping effect on the capillary and small gravity waves. SAR is the main tool for oil spill monitoring, both operationally (see, e.g., [Ferraro et al., 2010]) and also within research (see, e.g., [Skrunes et al., 2014, Brekke et al., 2014, Migliaccio et al., 2009a, Wismann et al., 1998, Solberg et al., 2004]). For example, oil spill detection reports from KSAT are delivered daily to customers around the world. In research, most work has focused on the characterization aspect of the oil, i.e., investigating whether there is any additional information that can be extracted from oil slicks after detection.

The use of optical instruments has been valuable in terms of identifying different oil zones that can be connected to oil thickness according to the Bonn agreement oil appearance code [BAO, 2017]. Additionally, infrared (IR) sensors could potentially detect relative thickness variations within oil slicks [Fingas, 2011]. Unfortunately, one major disadvantage of optical instruments is the need for an external illumination source, like the Sun, and cloud-free view of the target area. SAR is independent of these factors, and therefore an extremely useful tool when monitoring oil slicks. Figure 3.1 demonstrates this and shows the Landsat-8 panchromatic band and the VV-intensity from the UAVSAR. It is impossible to see the oil in the Landsat-8 image due to clouds, cloud shadows, and/or sun glint conditions. The SAR image, on the other hand, clearly shows the oil slick.

It is well known that a single polarization channel system can detect oil slicks. Over the last decades, SAR polarimetry has been explored with the intention of extracting even more information from oil slicks and for improving the oil detection performance. The successive sections provide the necessary background for Papers I-III.

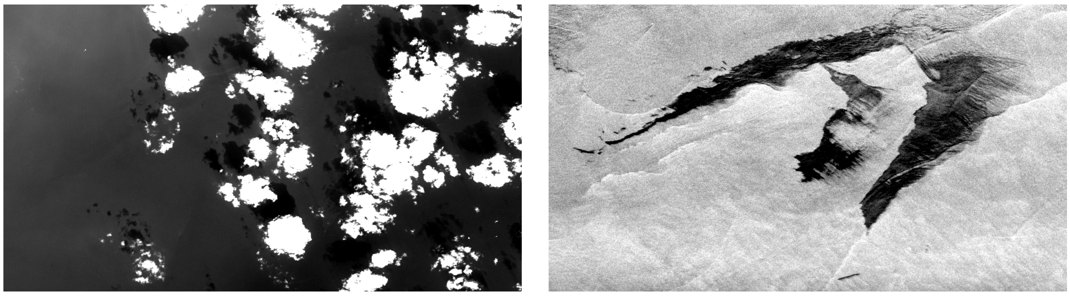

Figure 3.1: Left: Landsat-8 image (Landsat-8 product provided by USGS/NASA Landsat Program). Right: VV-intensity from UAVSAR. UAVSAR data courtesy of NASA/JPL-Caltech.

3.1 Oil Properties and Weathering Processes

The term "oil" is used to describe a wide variety of natural substances of plant, animal, and mineral origin. Crude oil and derived petroleum products contain dozens of major hydrocarbon compounds and thousands of minor ones [Coleman, 2003] generated by geological and geochemical processes. The fate and behaviour of oil in the marine environment are controlled by several physical properties like viscosity, density, solubility, and surface tension [Fingas, 2011]. Viscosity is the oil's resistance to flow, and low viscosity oils move readily compared to higher viscosity oils [Fingas, 2011]. High viscosity oils also tend to weather more slowly compared to low viscosity oils [Coleman, 2003]. The density is used by the petroleum industries to define light or heavy crude oil types and is an important property that indicates whether a certain oil will sink or float in water [Coleman, 2003]. Solubility in water is a measure of the amount of oil that will dissolve in the water on a molecular basis [Coleman, 2003].

These oil properties impact the efficiency of cleanup operations [Fingas, 2011] and change as the oil weathers on the sea surface. When crude oil is released onto the sea surface, it starts to undergo various physical (emulsification, evaporation, dissolution) and chemical (oxidation) weathering- and transport processes. These include spreading, dispersion and entrainment, sinking and sedimentation, partitioning and bioavailability, as well as stranding [Coleman, 2003]. Figure 3.2 illustrates these processes. All these processes alter the oil composition and oil thickness at the surface, which again influences the interaction process between the incoming SAR pulses and the oil.

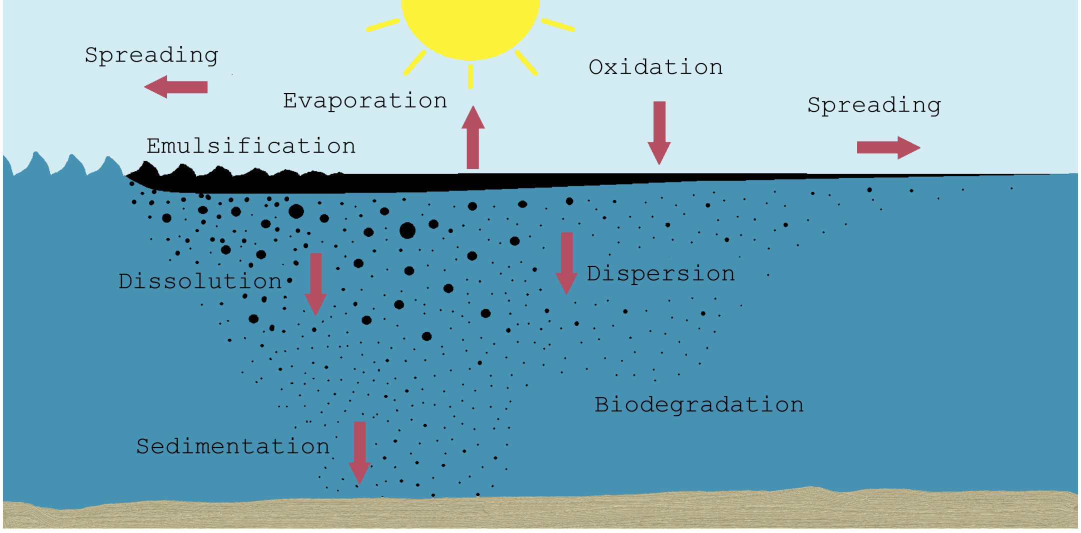

Figure 3.2: Weathering processes acting on an oil spill. The figure is from [Skrunes, 2014] and adapted from [ITOPF, 2002].

The wind and ocean currents play important roles in the oil slick transport (both horizontal and vertical movements) and weathering processes. The spreading of the oil is not necessarily uniform, and previous studies have found that more than 90% of the oil is located in less than 10% of the slick area [Hollinger and Mennella, 1973]. Furthermore, the weathering and wave actions cause the oil to mix with water. These factors might result in potential zoning within oil slicks. The wave-driven transport, known as the Stokes drift, as well as the ambient ocean current, transports the oil particles. Additionally, the oil slick drifts with approximately 3.5% of the wind speed [Schwartzberg, 1971]. Vertical movements contribute to mixing into the water column, which might lead to dispersion and break-up of the oil slick. Jones et al. [2018] compared a UAVSAR time series with an oil drift model (OpenDrift) to simulate the oil transport. Different oil types were released on a high-wind-driven sea surface. The authors discovered that by comparing the UAVSAR observations with the model simulations, one type of oil (biogenic oil) was shielded from the Stokes- and surface wind drift, and moved due to the Eulerian currents. This was a result of the vertical mixing into the water column, and only a few percents of the biogenic oil droplets were at the surface. On the other hand, a crude oil emulsion with 80% oil and 20% water drifted with the surface wind and Stokes drift, as well as the Eulerian currents. Based on the results from [Jones et al., 2018], it is clear that different types of oil react differently to these external drag forces.

3.2 Limitations of Oil Spill Observations by SAR

The SAR instrument is a valuable tool for oil spill monitoring, but there are several limitations associated with both detecting and characterizing the oil. Some examples are separating look-alikes from mineral oil, wind speed-, and sensor limitations.

3.2.1 Look-alikes

Mineral oil slicks produce a low-backscattering signature in SAR imagery. Unfortunately, several other phenomena also exhibit the same low-backscattering signatures. These are called oil spill look-alikes, and can be caused by low wind areas, natural biogenic slicks, wind shadowing due to coastal topography or man-made objects, rain cells, newly formed sea ice, upwelling, and internal waves [Clemente-Colón and Yan, 2000]. The most studied oil spill look-alike in SAR imagery is natural biogenic slicks (e.g., from algae and bacteria). As with mineral oil slicks, natural biogenic slicks will also dampen the capillary and small gravity waves [Fingas and Brown, 2014]. Therefore, several studies have explored SAR polarimetry and different sensors to separate the backscattered signal from mineral oil spills and biogenic surface films [Alpers et al., 2017], with various outcomes of success in specific cases. Natural biogenic slick areas are expected to form a monomolecular film on the sea surface due to their chemical composition [Hühnerfuss, 2006]. In contrast, crude oil or emulsified oil have a different composition than natural biogenic slicks, and the thickness of the crude oil is orders of magnitude higher than the monomolecular films [Hühnerfuss, 2006]. Efforts have been made in separating biogenic films from mineral oil spills using polarimetry (see, e.g., [Skrunes et al., 2014, Salberg and Larsen, 2018, Singha et al., 2013]), damping ratio (see, e.g., [Gade et al., 1998]), and multifrequency data (see, e.g., [Gade et al., 1998]). Figure 3.3 shows an example of an oil slick in near vicinity of an oil spill look-alike, which could either be a low wind area, ocean fronts, and/or a natural biogenic slick. The oil slick shown in Figure 3.3 was released close to this look-alike area, and identifying a way of separating the oil slick from the look-alike is extremely challenging. Paper I explores different polarimetric features as a function of time for one plant oil (simulant to biogenic slick) against three mineral oil emulsions.

3.2.2 Wind Speed Limitations

The wind is the main factor controlling the ocean surface roughness, and oil spill detection can only be performed in a limited range of wind speeds. If the wind speed is too low, the oil slicks are too similar to the calm smooth sea areas [Girard-Ardhuin et al., 2005]. If the wind is too strong, the oil might break and/or sink due to the turbulence of the upper surface layer. This might limit detection and also any discrimination between mineral oil and look-alikes. The optimal wind speed has been reported to be in the range 2-3 m/s to 10-14m/s [Alpers and Hühnerfuss, 1989, Singh et al., 1986].

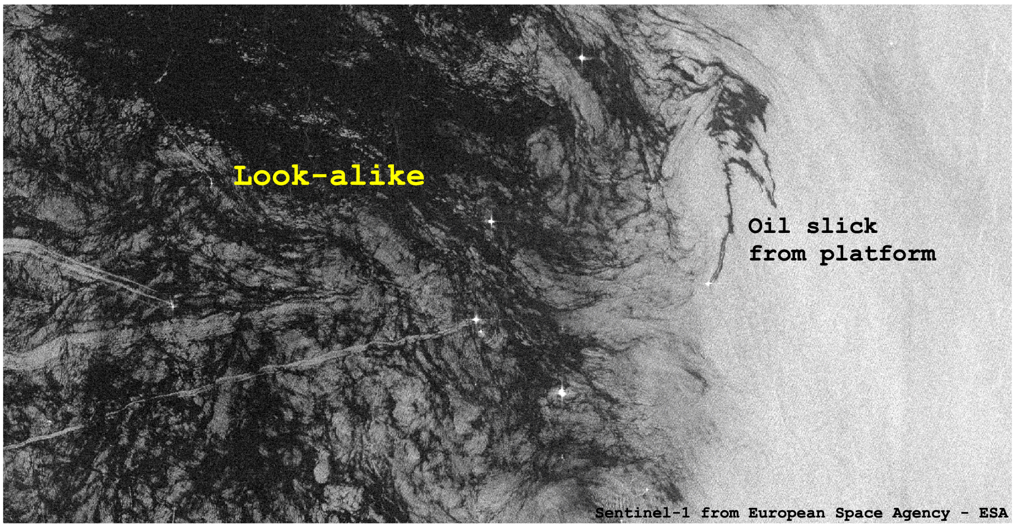

Figure 3.3: Sentinel-1 image of an oil slick in vicinity of oil spill look-alikes (most likely low wind areas, ocean fronts, or natural biogenic slicks).

3.2.3 Sensor Limitations

Each SAR sensor and its imaging modes have a variety of properties that impact the oil slick detection and characterization capabilities. It is well known that the backscatter response depends on the incidence angle. At low incidence angles specular reflection becomes important [Alpers et al., 2017, Gade et al., 1998], and the contrast between oil and the surrounding clean sea is low (see, e.g., [Minchew et al., 2012] for the copolarization channels). Low signal return from both oil slicks and clean sea occurs at high incidence angles [Minchew et al., 2012]. At higher incidence angles, less oil damping of the sea surface waves has been reported [Minchew et al., 2012], and sensor noise might also start to dominate the measured signal [Alpers et al., 2017]. As discussed in Section 2.7 several noise sources like thermal noise, quantization noise, sidelobe effects, and ambiguities will dilute the backscattered signal from oil slicks, and hamper any characterization and extraction of physical parameters like dielectric properties and volumetric fraction of oil.

Further, the temporal resolution of each satellite is poor, which limits the possibility of a high quality time series of drifting and evolving oil. However, due to the increasing number of active and planned satellites and microsatellites, the overall temporal resolution will improve if several sensors are combined. The search for oil spills requires a large swath width, which comes at a cost of few polarization channels and/or poorer spatial resolution. The use of HP modes can mitigate this as the polarimetric information level is somewhat comparable to a FP SAR system and offers twice the swath (or finer resolution) as a FP SAR system (see Section 2.4.4). The spatial resolution decides the minimum oil slick that is possible to detect, as coarse resolution modes might miss small oil slicks and also limit observation of internal variations within the slick.

3.3 Sea Surface Scattering

The dominant scattering mechanism from the ocean is Bragg scattering, i.e., surface scattering. This is the most important scattering mechanism of the interaction between the EM wave and the ocean surface [Valenzuela, 1978]. However, typical Bragg scattering from the ocean might be influenced if an oil slick pollutes the clean sea area and introduces other effects that must be included. The polarization of the incoming EM wave also plays an important role in the scattering process, as the return for vertical polarization is greater than for horizontal polarization [Wright, 1968]. Further, the backscattering response increases as the incidence angle decreases and with increasing wind, i.e., rougher sea surface [Wright, 1968, Valenzuela, 1978]. The upcoming sections discuss some of the most frequently used scattering models for ocean surface scattering.

3.3.1 Scattering Models

The backscattering response over the ocean comes from small- to large-scale roughness components controlled by several processes like the wind and wave-wave interactions [Holt, 2004]. According to the Bragg scattering theory, the incident EM wave is backscattered by the wind-generated short wave component (Bragg waves) of the ocean surface waves, whose wavelengths (λ_B) are on the same order as the EM signal (λ) with the following relation:

$$\lambda_B = \lambda/(2\sin\theta) \tag{3.1}$$

where θ is the incident angle of the radar. According to the first order Bragg scattering model (also known as the small perturbation model (SPM)) the backscattering coefficients are generated in the following manner;

$$\sigma^0_{pq}(\theta) = 4\pi k^4 \cos\theta |R_{pq}|^2 W(2k\sin\theta, 0) \tag{3.2}$$

where p and q denotes the polarization of the incident and backscattered signal, θ is the incidence angle of an untilted horizontal plane, $W(\cdot)$ is the two-dimensional ocean wave spectral density, and k is the wavenumber. The Bragg scattering coefficients R_{pq} are expressed as [Valenzuela, 1978]:

$$R_{HH}(\theta, \epsilon_r) = \frac{\cos\theta - \sqrt{\epsilon_r - \sin^2\theta}}{\cos\theta - \sqrt{\epsilon_r + \sin^2\theta}} \tag{3.3}$$

$$R_{VV}(\theta, \epsilon_r) = \frac{(\epsilon_r - 1)(\epsilon_r(1 + \sin^2\theta) - \sin^2\theta)}{(\epsilon_r \cos\theta + \sqrt{\epsilon_r - \sin^2\theta})^2} \tag{3.4}$$

where ϵ_r is the relative dielectric constant. The Bragg scattering model simulates the backscatter from small-scale ocean surface roughness (at the Bragg wavelength), and excludes any effects of tilted facets that model longer waves, also known as large-scale roughness. Therefore, no cross-polarization nor depolarization effects are generated with this model. The longer waves will modify these short Bragg waves which impact the measured SAR signal [Vachon et al., 2004]. Figure 3.4 illustrates this concept, where the short waves, i.e., Bragg waves, rides on the longer waves. Scattering from each rough facet is evaluated by the first-order Bragg scattering model [Iodice et al., 2011]. Various two-scale models have been suggested for modelling the backscatter of both small- and large-scale ocean surface roughness components as illustrated in Figure 3.4. Examples of two-scale models are the tilted Bragg [Valenzuela, 1978], X-Bragg [Hajnsek et al., 2003], and the polarimetric two-scale model [Iodice et al., 2011]. Each of these two-scale models has a different approach to modeling the tilts, slopes, and/or rotation of the surface facets. Only the intensities are generated in the tilted Bragg model, whereas the entire covariance/coherency matrix can be simulated from the X-Bragg and the polarimetric two-scale models. The tilted Bragg model has been the most frequently used for oil spill remote sensing, and in this case the backscattering response is modeled as [Valenzuela, 1978];

$$\begin{aligned}\sigma^0_{HH}(\theta_i) = 4\pi k^4 \cos^4\theta_i \left| \left(\frac{\sin(\theta+\psi_{ti})\cos\zeta_{ti}}{\sin\theta_i}\right)^2 R_{HH}(\theta_i) + \left(\frac{\sin\zeta_{ti}}{\sin\theta_i}\right)^2 R_{VV}(\theta_i)\right|^2 \times \\ W(2k\sin(\theta+\psi_{ti}), 2k\cos(\theta+\psi_{ti})\sin\zeta_{ti})\end{aligned} \tag{3.5}$$

$$\begin{aligned}\sigma^0_{VV}(\theta_i) = 4\pi k^4 \cos^4\theta_i \left| \left(\frac{\sin(\theta+\psi_{ti})\cos\zeta_{ti}}{\sin\theta_i}\right)^2 R_{VV}(\theta_i) + \left(\frac{\sin\zeta_{ti}}{\sin\theta_i}\right)^2 R_{HH}(\theta_i)\right|^2 \times \\ W(2k\sin(\theta+\psi_{ti}), 2k\cos(\theta+\psi_{ti})\sin\zeta_{ti})\end{aligned} \tag{3.6}$$

$$\begin{aligned}\sigma^0_{HV}(\theta_i) = \sigma^0_{VH}(\theta_i) = 4\pi k^4 \cos^4\theta_i \left(\frac{\sin(\theta+\psi_{ti})\sin\zeta_{ti}\cos\zeta_{ti}}{\sin^2\theta_i}\right)^2 \times \\ |R_{VV}(\theta_i) - R_{HH}(\theta_i)|^2 \times W(2k\sin(\theta+\psi_{ti}), 2k\cos(\theta+\psi_{ti})\sin\zeta_{ti})\end{aligned} \tag{3.7}$$

where θ_i is the local incidence angle relative to the tilted facet. The tilts are defined by ψ_{ti} and ζ_{ti}, where the normal to the facet deviates from the vertical by ψ_{ti} in the incidence plane and deviates by an angle ζ_{ti} in the plane perpendicular to the plane of incidence [Valenzuela, 1978]. It can be seen from Equations 3.5-3.6 that the ratio of $\sigma^0_{HH}/\sigma^0_{VV}$ cancels the ocean wave spectrum $W(\cdot)$, i.e., the small-scale ocean surface roughness. Unfortunately, the tilted Bragg model cannot be used for modelling the response from a HP SAR system, since the co- and cross-polarization intensity coefficients are no longer available in HP. The X-Bragg model in [Hajnsek et al., 2003] or the polarimetric two-scale model in [Iodice et al., 2011] outputs the 3×3 covariance/coherency matrix. The backscattering coefficients for a HP SAR can be modelled using the X-Bragg and the polarimetric two-scale models, since a connection between the HP and the covariance/coherency matrix exist [Raney, 2007]. The X-Bragg model is an extension of the SPM, where the complex scattering matrix is [Hajnsek et al., 2003, Iodice et al., 2011]:

$$\boldsymbol{S} = a_s \boldsymbol{R}(\phi) \begin{bmatrix} R_{HH}(\theta_i, \epsilon_r) & 0 \\ 0 & R_{VV}(\theta_i, \epsilon_r) \end{bmatrix} \boldsymbol{R}^T(\phi) \tag{3.8}$$

where $|a_s|^2 = k_r^4 \cos^4(\theta_i) W(\cdot)$ contains factors related to the small-scale roughness like the small-scale ocean surface roughness, incidence angle, and wave number. The tilt of the facet causes a rotation of the local plane of incidence around the look direction by an angle ϕ [Lee et al., 2000]. $\boldsymbol{R}(\phi)$ depends on the radar look angle and the surface slope (range and azimuth directions) or large-scale roughness [Cloude, 2010, Lee et al., 2000], and is expressed as:

$$\boldsymbol{R}(\phi) = \begin{bmatrix} \cos\phi & \sin\phi \\ -\sin\phi & \cos\phi \end{bmatrix} \tag{3.9}$$

Calculating the expression in Equation (3.8) gives:

$$\begin{aligned} \boldsymbol{S} &= \begin{bmatrix} S_{HH} & S_{HV} \\ S_{HV} & S_{VV} \end{bmatrix} \\ &= a_s \left[\begin{matrix} R_{HH}(\theta_i, \epsilon_r)\cos^2\phi + R_{VV}(\theta_i, \epsilon_r)\sin^2\phi \\ \cos\phi\sin\phi(-R_{HH}(\theta_i, \epsilon_r) + R_{VV}(\theta_i, \epsilon_r)) \end{matrix} \right. \quad \cdots \\ &\qquad \cdots \quad \left. \begin{matrix} \cos\phi\sin\phi(-R_{HH}(\theta_i, \epsilon_r) + R_{VV}(\theta_i, \epsilon_r)) \\ R_{VV}(\theta_i, \epsilon_r)\cos^2\phi + R_{HH}(\theta_i, \epsilon_r)\sin^2\phi \end{matrix} \right]. \end{aligned} \tag{3.10}$$

From Equation 3.8, the covariance and coherency can be estimated. The X-Bragg can be used to model the complex scattering vector for a HP system in the following manner [Salberg et al., 2014]:

$$\begin{aligned} \boldsymbol{k}_{(RH,RV)} = \begin{bmatrix} S_{RH} \\ S_{RV} \end{bmatrix} = \frac{a_s}{\sqrt{2}} &\left[\begin{matrix} R_{HH}(\theta_i, \epsilon_r)\cos^2\phi + R_{VV}(\theta_i, \epsilon_r)\sin^2\phi + \\ \cos\phi\sin\phi(R_{VV}(\theta_i, \epsilon_r) - R_{HH}(\theta_i, \epsilon_r)) - \end{matrix} \right. \\ &\qquad \left. \begin{matrix} j(\cos\phi\sin\phi(R_{HH}(\theta_i, \epsilon_r) - R_{VV}(\theta_i, \epsilon_r))) \\ j(R_{HH}(\theta_i, \epsilon_r)\sin^2\phi + R_{VV}(\theta_i, \epsilon_r)\cos^2\phi) \end{matrix} \right]. \end{aligned} \tag{3.11}$$

From Equation 3.11, the HP covariance matrix and the Stokes vector can be estimated. Both the tilted Bragg and X-Bragg are two-scale models that extend the SPM model with tilted/rotated facet, but the difference between tilted Bragg and X-Bragg is in how they model the tilt. X-Bragg uses a single rotation angle, whereas the tilted Bragg uses two tilt angles. There is a connection between the rotation angle in X-Bragg model and the two tilt angles in the tilted Bragg model, which was demonstrated in [Salberg et al., 2014]. Both the tilted Bragg and X-Bragg models are used in Paper I, and other studies using these models are [Minchew, 2012, Minchew et al., 2012, Salberg et al., 2014, Yin et al., 2015, Buono et al., 2019, Buono et al., 2016a].

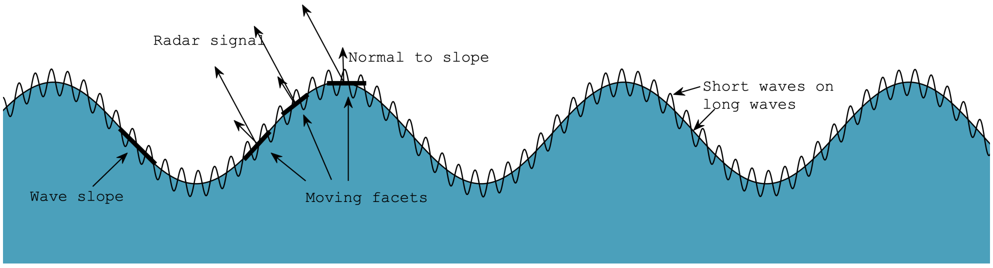

Figure 3.4: Illustration of small- and large-scale ocean surface roughness. The roughness within each facet is considered as the small-scale roughness, whereas the large-scale roughness is composed of many tilted facets. Figure adapted from [Holt, 2004, Shokr and Sinha, 1985].

3.4 Oil Slick Detection and Characterization

Oil slicks dampen the capillary and short gravity waves resulting in reduced backscatter compared to the surrounding sea [Fingas and Brown, 1997]. The oil slicks are seen as dark patches in SAR images, and the contrast is controlled by several factors like sensor properties (e.g., frequency, polarization, incidence angle), oil slick characteristics, weathering processes, and environmental conditions. As mentioned in Section 2.8.1, roughness and dielectric properties are two main factors impacted by oil slicks, i.e., through damping of the small scale ocean roughness and a change in the dielectric properties between the oil slick and clean sea, where both factors result in a reduction in the backscattered signal. Polarimetric features are a key tool when analyzing the detection capabilities within both FP and DP SAR products, as features vary in their detection and characterization properties. The upcoming section highlights the concept of polarimetric features and how these can be used in both detection and characterization of oil slicks.

3.4.1 Polarimetric Features

The traditional SP SAR system was first used when monitoring oil spills. Since the SP system provides only one polarization channel, information such as the geometry and shape of the oil patch, oil-sea contrast, contextual features (wind history, location relative to ships, oil rigs, and shore), and texture were used to describe the segmented low-backscattering regions [Brekke and Solberg, 2005]. Over the last decade, the use of multipolarization features for detection and characterization purposes of low-backscattering ocean areas has been discussed frequently in the literature [Skrunes et al., 2014, Brekke et al., 2014, Migliaccio et al., 2009a, Brekke et al., 2017, Migliaccio et al., 2005, Zhang et al., 2017, Skrunes et al., 2018, Salberg and Larsen, 2018, Singha et al., 2016, Li et al., 2016, Migliaccio et al., 2009b]. For several years, polarimetric features have been applied on all kinds of FP SAR data acquired under various wind- and ocean conditions and for different oil types. Polarimetric features are in general extracted from FP SAR products, but can also be extracted from DP SAR data when the two polarization channels are combined. Polarimetric features have seen extensive use when attempting to separate biogenic slicks from mineral oil slicks [Migliaccio et al., 2009b, Zhang et al., 2011, Skrunes et al., 2014, Zhang et al., 2017, Salberg and Larsen, 2018]. The polarimetric features are often used as input to various classification algorithms (see, e.g., [Salberg and Larsen, 2018, Zhang et al., 2017, Skrunes et al., 2014]), and/or separability measures when exploring the different polarimetric features' suitability for, e.g., detecting the oil and/or differentiating between types of surface films.

Polarimetric features extracted from HP SAR data have been increasingly discussed and studied in the literature [Nunziata et al., 2015, Salberg et al., 2014, Zhang et al., 2017, Brekke et al., 2017, Espeseth et al., 2017, Li et al., 2016]. The large interest is caused by the possibility of doubling the swath width compared to a FP SAR system, while at the same time retaining enough polarimetric information to describe the surface element. For oil slick monitoring this is beneficial as a large swath is necessary to cover a vast area. The FP features are extracted from both the sample covariance and coherency matrices, whereas the simulated HP features are extracted from the Stokes vector and the sample HP covariance matrix. Previous studies have investigated oil slick detection performance using features extracted from a simulated HP system and often compared the performance with features extracted from a FP system [Salberg et al., 2014, Zhang et al., 2017]. The results indicate a similar oil detection performance between a FP and HP system.

The features investigated in this thesis are grouped by their sensitivity to the physical parameters based on the two-scale Bragg models presented in Section 3.3. These are the small- and large-scale ocean surface roughness, incident angle, tilt angles, and the relative dielectric constant. Paper I identified two feature categories, shown in Table 3.1. In general, all the non-ratio-based features are found in category I and depends on small- and large-scale ocean surface roughness, relative dielectric constant, and incident angle, whereas the ratio-based belong to category II and depend on the large-scale ocean surface roughness, tilt angles, relative dielectric constant, and incident angle, i.e., they are independent of the small-scale roughness.

Figures 3.5 and 3.6 show examples of one feature from category I (the span), and one feature from category II (copolarization ratio). Here, based on visual inspection, the contrast between oil and the surrounding clean sea is higher for the span (category I) than the copolarization ratio (category II). In Figure 3.6, the top-most oil slick (a plant oil release during the oil-on-water exercise in 2013) is almost impossible to detect using the copolarization ratio, while it is visible using the span. The low visibility of the plant oil in the copolarization ratio is most likely due to the cancellation of the small-scale roughness (according to the two-scale Bragg models), which contains information about the damping

Table 3.1: Overview of the two categories that multipolarization features can be grouped into based on the two-scale Bragg models presented in Section 3.3.

Category I (non-ratio-based)	Large-scale roughness Small-scale roughness Incidence angle Dielectric properties
Category II (ratio-based)	Large-scale roughness Incidence angle Dielectric properties

of the small ocean waves. Since the plant oil forms a monomolecular layer, the EM wave penetrates the oil to scatter from the water. Hence, the dielectric constant of the plant oil will not influence the backscattered signal. The span (category I) shows higher contrast for the plant oil, indicating that the small-scale roughness is an important factor for detecting the plant oil.

Oil slicks seen in polarimetric SAR data are particularly susceptible to misinterpretation due to noise contamination, and the behaviour of these polarimetric features in the presence of noise contamination is explored in Paper II.

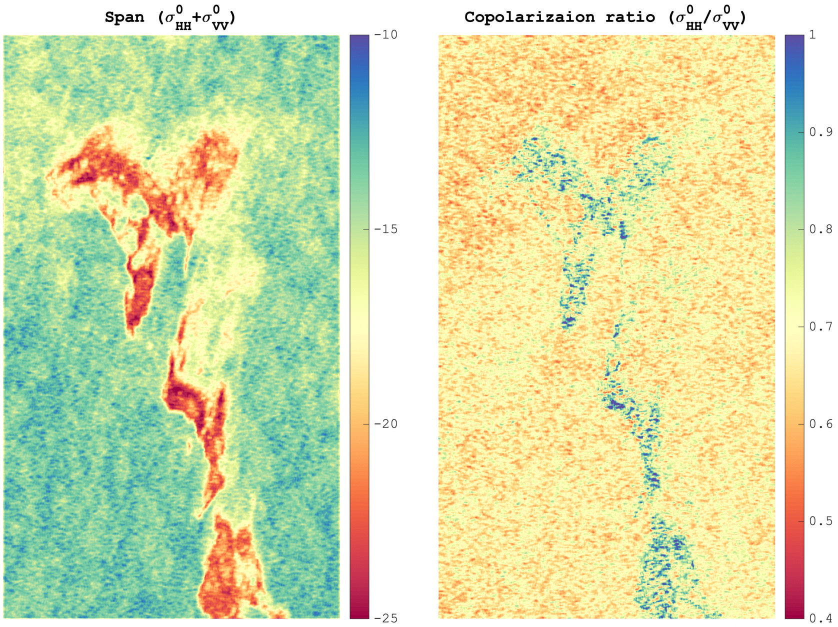

Figure 3.5: Pseudo-color images of the span (left panel) and copolarization ratio (right panel) of a Radarsat-2 acquisition (June 2012) covering mineral oil slicks from NOFO's oil-on-water exercise in 2012. The Radarsat-2 data and Products © MDA LTD. 2012– All Rights Reserved.

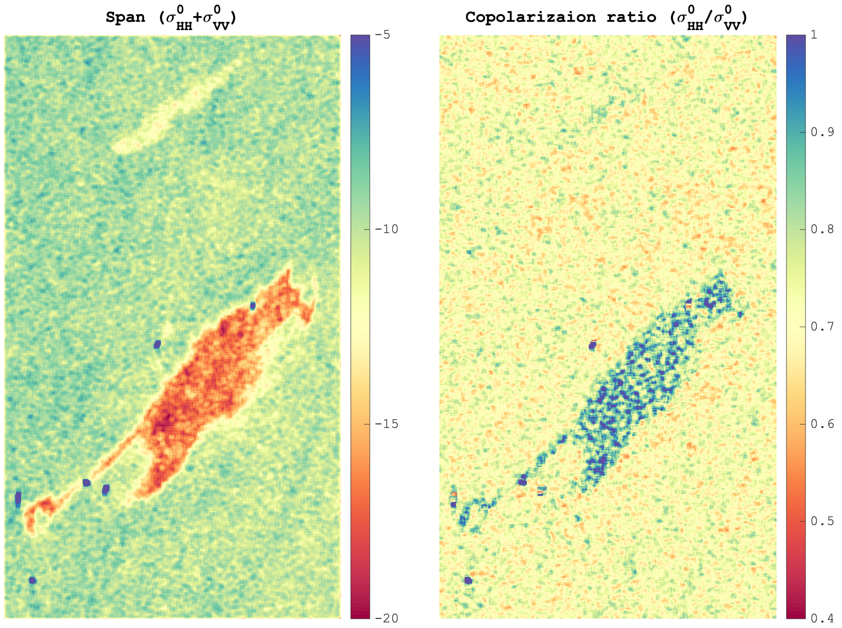

Figure 3.6: Pseudo-color images of the span (left panel) and copolarization ratio (right panel) of a Radarsat-2 acquisition (June 2013) covering plant oil (top-most slick) and mineral oil from NOFO's oil-on-water exercise in 2013. The Radarsat-2 data and Products © MDA LTD. 2013 – All Rights Reserved.

3.4.2 Damping Ratio

The damping ratio (DR) is a measure of the contrast between the oil and the surrounding clean sea [Gade et al., 1998], and is defined as

$$DR = \frac{\sigma^0_{clean\ sea}(\theta)}{\sigma^0(\theta)}. \tag{3.12}$$

The damping ratio has been reported to increase with wavenumber, oil viscosity, and thickness [Wismann et al., 1998, Gade et al., 1998, Pinel et al., 2014, Sergievskaya et al., 2019]. The wave damping of oil films are controlled by various physical parameters like for example the volume viscosity, surface and interfacial tensions, and elasticity [Sergievskaya et al., 2019, Jenkins and Jacobs, 1997]. Different oil types have unique physical and chemical compositions that might results in various damping ratio characteristics at different wavenumber and wind speed, allowing for discrimination of different oil types [Wismann et al., 1998, Gade et al., 1998, Jenkins and Jacobs, 1997]. A recent study [Sergievskaya et al., 2019] based on a laboratory experiment with two oil types (oil emulsion and crude oil) and different thicknesses demonstrated that the damping ratio increased with oil thickness, but reached a maximum value at a given oil thickness threshold that varied between the oil types. Higher damping was also reported for crude oil compared to oil emulsion in [Sergievskaya et al., 2019]. Figure 3.7 shows the VV-intensity and the damping ratio from a Radarsat-2 scene covering three different types of oil acquired during NOFO's oil-on-water exercise in 2011. In Figure 3.7, the damping ratio is lower for plant oil compared to the mineral oil films. The damping ratio image also reveals internal variations within the slicks, which might indicate thickness variations. Information about the relative thickness within an oil slick might aid in identifying actionable oil, monitoring the dispersion and evolution of the oil, and for discriminating between different oil types. Skrunes et al. [2017] used overlapping infrared (IR) observations and a SAR acquisition to demonstrate that the high damping ratio area corresponded to the IR white region indicating relatively thick oil.

The damping ratio has been widely explored in this work, especially in Papers I and III, and is also the key concept of the innovation project presented in Chapter 11.

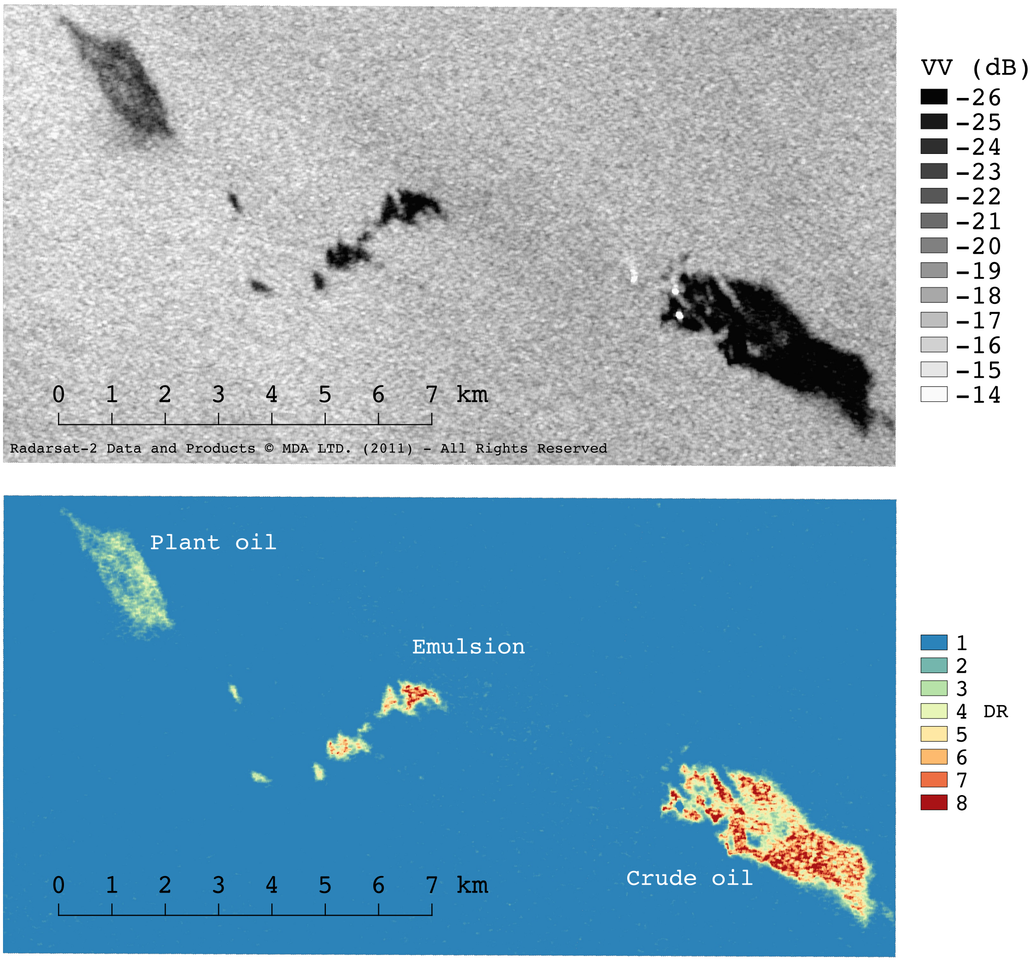

Radarsat-2 Data and Products © MDA LTD. (2011) – All Rights Reserved

Figure 3.7: Top: VV-intensity of Radarsat-2 covering three different types of oil. Bottom: VV damping ratio (DR). The three oil types are displayed in the DR image.

4

SAR Remote Sensing of Arctic Sea Ice

Sea ice is mostly located in remote areas with challenging conditions of heavy cloud cover and darkness for several months of the year. SAR satellites overcome these challenges, and are therefore an important tool for sea ice monitoring. Operational sea ice services around the world rely on SAR observations when creating various types of ice charts. These ice charts are then used, for example, for risk assessment and to make efficient decisions when operating in ice infested areas. This is one of the main goals and motivations for CIRFA; extracting information from remote sensing to aid decision making in Arctic operations. Another important reason for studying sea ice is its role in the global climate. Sea ice has an impact on the environment and global climate through its interactions with the ocean and atmosphere, and influence heat and gas exchange between the water and atmosphere [Onstott and Shuchman, 2004].

X-, C-, L-band SAR satellites have been used frequently for studying the radar signatures of sea ice (see, e.g., [Eriksson et al., 2010, Dierking and Busche, 2006, Johansson et al., 2017, Singha et al., 2018]). The FP SAR mode has been shown to improve classification of various sea ice types (see, e.g., [Moen et al., 2015, Singha et al., 2018, Dierking et al., 2003]) compared to SP or DP SARs. However, monitoring of vast areas requires large spatial coverage, which comes at a cost of coarse resolution and fewer polarization channels. Therefore, the HP SAR mode could be an important turning point, providing both large coverage and improved polarimetric information compared to the conventional SP and DP modes currently available in Radarsat-2 and Sentinel-1. Furthermore, integrating different sensors and modes will also increase the monitored area.

Paper IV focuses on sea ice from a HP perspective. Therefore, this chapter is limited to HP and provides the necessary background information for Paper IV.

4.1 Sea Ice Types

Sea ice generally consists of frozen water with inclusion of liquid brine pockets and gas bubbles. However, depending on atmospheric and ocean conditions, sea ice may appear in a large variety of forms. The sea ice is often labeled for classification purposes according to different properties such as thicknesses, sea ice concentration levels, sea ice age, or floe sizes [Onstott and Shuchman, 2004]. For example, sea ice classification from SAR data often uses sea ice labels defined by The World Meteorological Organization [WMO-No.574, 2010]. Various sea ice types have different EM signatures due to variations in surface roughness and composition. In the Norwegian Arctic, first-year ice, young ice, fast ice, and multi-year ice are the dominant types. The salinity content varies between these ice types and the brine pockets within the ice affect the radar signatures [Onstott and Shuchman, 2004]. The importance of volume- and multiple scattering will increase with snow thickness [Gill et al., 2015], resulting in different radar signatures between an ice layer with and without a snow layer. Figures 4.1 and 4.2 show example images of some sea ice types: nilas, lead, ridges, floes, multi-year-ice, and grey-white ice.

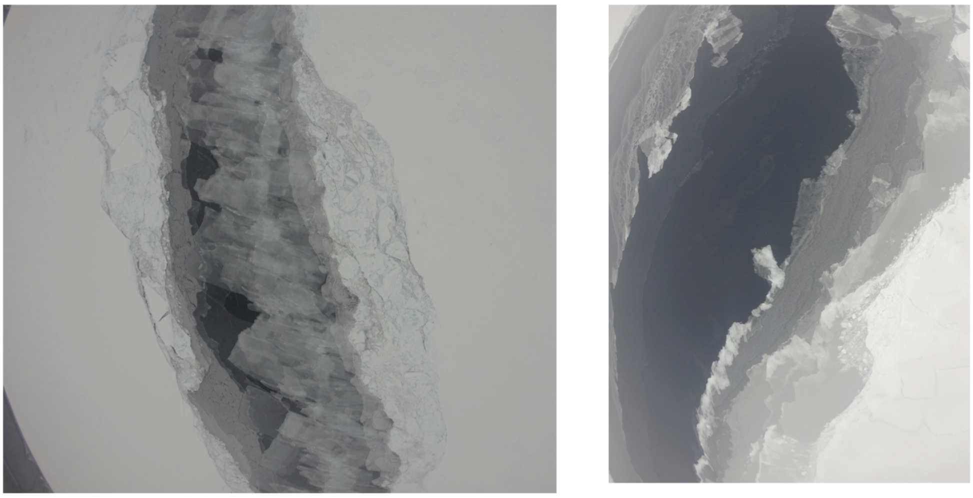

Nilas formed in calm water
Photographs courtesy Martine Espeseth, N-ICE 2015, Norweigan Polar Institute , Date: May 2015

Lead
Photographs courtesy Martine Espeseth, N-ICE 2015, Norweigan Polar Institute, Date: May 2015

Figure 4.1: Photos of different sea ice types in the Barents Sea acquired during the N-ICE project managed by the Norwegian Polar Institute.

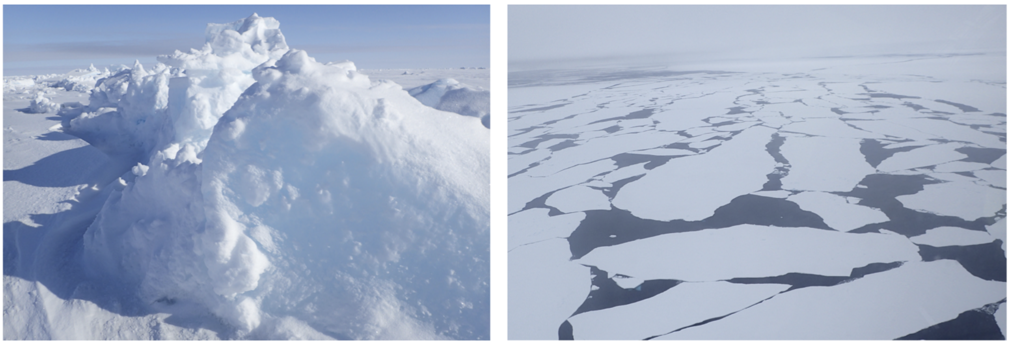

Ridges
Photographs courtesy Martine Espeseth, N-ICE 2015, Norweigan Polar Institute, Date: May 2015

Floes
Photographs courtesy Martine Espeseth, N-ICE 2015, Norweigan Polar Institute, Date: May 2015

Multi-year ice (left corner) and newly formed ice (right side of the photo)
Photographs courtesy Sebastian Sikora, UNIS, N-ICE 2015, Norweigan Polar Institute, Date: May 2015

Grey-white ice covered with 2-3 cm of snow (removed manually on the lower corner of the photo)
Photographs courtesy Martine Espeseth, N-ICE 2015, Norweigan Polar Institute, Date: May 2015

Figure 4.2: Photos of different sea ice types in the Barents Sea acquired during the N-ICE project managed by the Norwegian Polar Institute.

4.2 Scattering Characteristics of Sea Ice

The backscatter signature of sea ice depends on the ice type, the sensor properties (e.g., frequency, polarization, incidence angle), and other environmental factors like season, temperature, etc. The surface characteristics depend on a combination of four surface parameters: (1) surface roughness (both large and small scales); (2) the complex dielectric constant of sea ice; (3) dielectric discontinuities or discrete scatterers (e.g., gas bubbles in the ice); (4) orientation of the ice and its surface features to the radar [Onstott and Shuchman, 2004]. As mentioned in Section 2.8.1, the surface is considered rough if the Rayleigh criterion (see Equation 2.17) is satisfied. Hence, X-band SAR is more sensitive to small-scale roughness of sea ice than C- and L-band SAR. The roughness is a key parameter in the backscatter as compared to the dielectric properties [Spreen and Kern, 2016]. Figure 4.3 shows overlapping Sentinel-1 (C-band SAR) and Sentinel-2 (optical) images covering Arctic sea ice. The leads can be seen as dark features in both the optical and SAR image, whereas the other sea ice types have different visual appearance in the two images.

For EM scattering of sea ice and snow-covered surfaces, two main processes take place: surface and volume scattering [Spreen and Kern, 2016]. The penetration depth controls the scattering processes that might take place. Since L-band waves penetrate deeper than X- and C-band waves, more volume scattering might occur. Although the penetration depth depends on the frequency and incident angle of the EM wave, it also depends on the surface characteristics like the temperature, dielectric properties, and porosity of the ice and wet snow [Onstott and Shuchman, 2004, Spreen and Kern, 2016]. The penetration depth is low for sea ice and snow (but it is much lower for water), hence the surface scattering is considered to be the dominant scattering mechanism for sea ice, especially for young and first-year ice [Spreen and Kern, 2016]. Volume scattering within the sea ice might happen due to brine pockets (first-year ice), drainage structures, or air bubbles (multi-year ice) [Winebrenner et al., 1989]. The EM penetration depth and volume scattering are related to the age of the sea ice [Spreen and Kern, 2016].

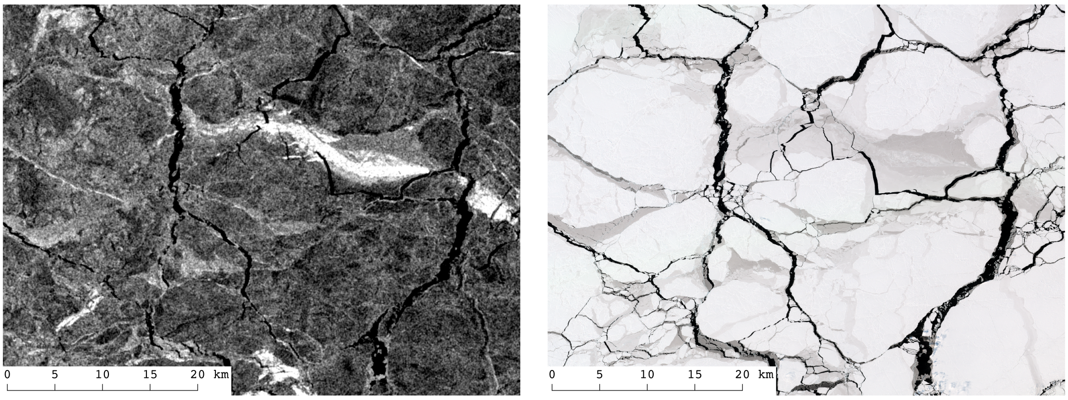

Figure 4.3: Left: Sentinel-1 HH-intensity image of Arctic sea ice acquired 5 April 2016 at 15:38 UTC. Right: RGB-image of Sentinel-2 over the same area acquired 5 April 2016 at 20:33 UTC. Sentinel-1 and Sentinel-2 data from European Space Agency - ESA.

4.3 Characterizing Sea Ice with Hybrid-Polarity SAR

The use of FP SAR data has been shown to enhance discrimination between various sea ice types as well as between open water and sea ice [Geldsetzer et al., 2015, Moen et al., 2015, Singha et al., 2018, Dierking et al., 2003]. This improvement comes at a cost of a limited swath width (25-50km) and is therefore unfit for most operational use cases. With the HP mode available, this compromise may no longer be necessary. The reason for the large interest in the HP mode for sea ice monitoring is the RCM (launched in 2019), which has HP capabilities. Understanding the benefit and limitations of the HP system can thus be granted some importance. Moreover, various polarimetric features retrieved from simulated HP SAR have been the main focus in multiple studies [Dabboor and Geldsetzer, 2014b, Dabboor and Geldsetzer, 2014a, Geldsetzer et al., 2015, Xi et al., 2016]. All have shown good performance of the HP mode. Most sea ice studies (see, e.g., [Dabboor and Geldsetzer, 2014b, Dabboor and Geldsetzer, 2014a, Geldsetzer et al., 2015, Xi et al., 2016]) with a focus on a HP SAR system simulate HP data from FP data, resulting in synthesizing of a perfectly transmitted circularly polarized wave. Transmitting a perfectly circular polarized wave is not possible using current technology, and the transmitted pulse will rather be more elliptical [Touzi and Charbonneau, 2014]. This is referred to as "the non-circularly" property of a HP system [Touzi and Charbonneau, 2014]. Hence, when simulating HP from FP this should be considered when exploring the polarimetric signatures of e.g., sea ice.

Another way of exploring HP SAR data is reconstruction of a pseudo FP covariance matrix [Souyris et al., 2005]. Espeseth et al. [2016] investigated various reconstruction methods for C- and L-band SAR covering overlapping areas of Arctic sea ice. This study discovered higher reconstruction accuracy for L- than C-band SAR data, which might have been because L-band is more exposed to volume scattering due it is higher penetration depth than C-band. The papers presented in this thesis do not perform any reconstruction. This makes it possible to avoid the scattering symmetry assumptions introduced in a reconstruction approach.

4.3.1 Hybrid-Polarity Features for Sea Ice Observations

The HP SAR features are derived from the HP 2×2 sample covariance matrix or the Stokes vector (see Section 2.4.4). A large feature set has been investigated for sea ice studies, but the majority of these studies have considered simulated- and not real HP data. Polarimetric features have proven to be sensitive to various surface characteristics like dielectric property, surface roughness, and amount of brine pockets and air bubbles. Geldsetzer et al. [2015] categorized several HP features into groups based on their sensitivity to a given scattering mechanism. This framework is also adopted in Paper IV and Table 4.1 shows the categorizes. The first distinct groups isolate sensitivity to strong surface scattering, depolarization due to volume scattering, depolarization due to multiscattering, and polarization differences in resonant Bragg scattering. The "independent" group corresponds to features that might

Group #	Scattering process
Group 1	Strong surface scattering
Group 2	Depolarization due volume scattering
Group 3	Depolarization due to multiscattering from rough surfaces
Group 4	Polarization differences in resonant Bragg scattering or in Fresnel coefficients
Independent	Complementary to other physical parameters

Table 4.1: Groups defined in [Geldsetzer et al., 2015] and their sensitivity to the scattering processes.

be sensitive to other characteristics that are not covered by Groups 1 - 4. Within each group, there exist several HP features. For example, most of the intensity features, like the first Stokes parameter and the single *RH* and *RV* intensities are found in Group 1, whereas, the degree of polarization (DoP) and the magnitude of the *RV* and *RH* cross-correlation are found in Group 3.

/5

Data Collection

Lack of ground truth information of an oil spill or sea ice can lead to speculations and misinterpretations of the remote sensing data. This is a major challenge for the scientific community working with remote sensing data. Therefore, data collection during the exercises and campaigns are unique opportunities to understand the SAR signatures of different types of oil and sea ice.

This chapter describes the exercises and campaigns from which the data used for this work originates. Section 5.4 gives an overview of the SAR data used for the papers presented in this thesis.

5.1 Oil-On-Water Exercise in the North Sea

The organization NOFO has conducted several exercises outside the abandoned Frigg field in the North Sea (see Figure 5.1) for several years, where oil is released under controlled supervision. NOFO is an oil spill response organization with members from all the oil companies operating in the Norwegian continental shelf. The main vision of NOFO is "keeping the sea clean", and the exercise is conducted with the purpose to both implement and test new clean-up systems and to ensure their oil recovery preparedness [NOFO, nd]. Norway is one of a few countries that conducts such experiments. Because of this, the exercises have gained international attention both within the research communities and various industries.

A SAR image of an oil spill is much more valuable if in-situ information about the spill is available. This is rarely the case, and remote sensing images from these oil-on-water exercises, where in-situ information is available, are extremely important to obtain knowledge about the development and properties of an oil spill. In-situ data such as the type and amount of oil, as well as the oil/water fraction, and release time and position are collected during these exercises. Additionally, wind information is collected, and in some cases drift buoys are released to record information about the ocean drift currents. Remote sensing data from these exercises have lead to several publications with scientific contributions. This includes studies on the polarimetry in terms of detection and characterization of the oil slicks (see, e.g., [Brekke et al., 2017, Angelliaume et al., 2018, Skrunes et al., 2014, Skrunes et al., 2015, Skrunes et al., 2018, Skrunes et al., 2016]), and oil drift models (see, e.g., [Röhrs et al., 2018, Jones et al., 2016]).

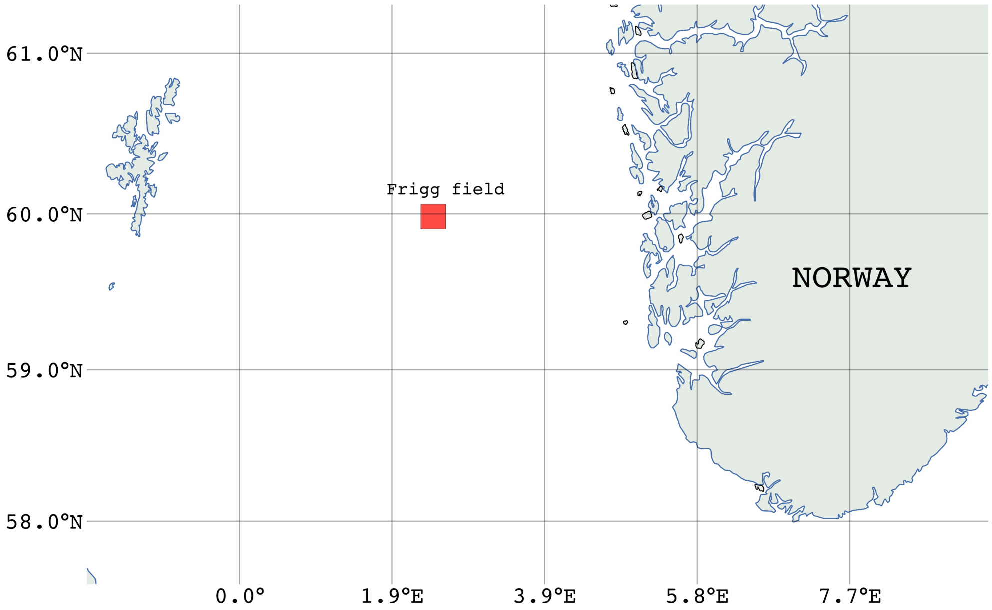

Figure 5.1: Map showing the location of the Frigg field where the oil-on-water exercise takes place.

Paper I and Paper II, presented in Chapter 6, used data that were collected during the oil-on-water exercises in the time period 2011-2018.

5.2 Seep in MC-20 block in the Gulf of Mexico

Oil seeps are a large source of oil entering the ocean. Oil seeps can be naturally occurring or a result of a leakage from oil and gas operations. The Gulf of Mexico is known to have a large number of seeps, and there have been numerous reports of oil slicks. One such event in the Gulf of Mexico occurred in the aftermath of a hurricane that destroyed the Taylor Energy platform in the Mississippi Canyon Block 20 (MC-20) in September 2004 [Sun et al., 2018]. In the following years, oil films were detected in the same area where the oil platform was located before the hurricane.

Several extensive campaigns investigating and collecting data from this particular site, known as the MC-20 oil spill, have taken place over the last years. This site is well studied, and several publications are available (see, e.g., [Sun et al., 2018, Asl et al., 2016, Androulidakis et al., 2018, Nunziata et al., 2019, Herbst et al., 2016, Warren et al., 2014, Jones and Holt, 2018]).

Figure 5.2 shows the area and oil slick masks extracted from the UAVSAR images used in Paper III. The coverage of the joint oil slick masks are shown in three different tones of grey from three UAVSAR time series (from dark to light respectively).

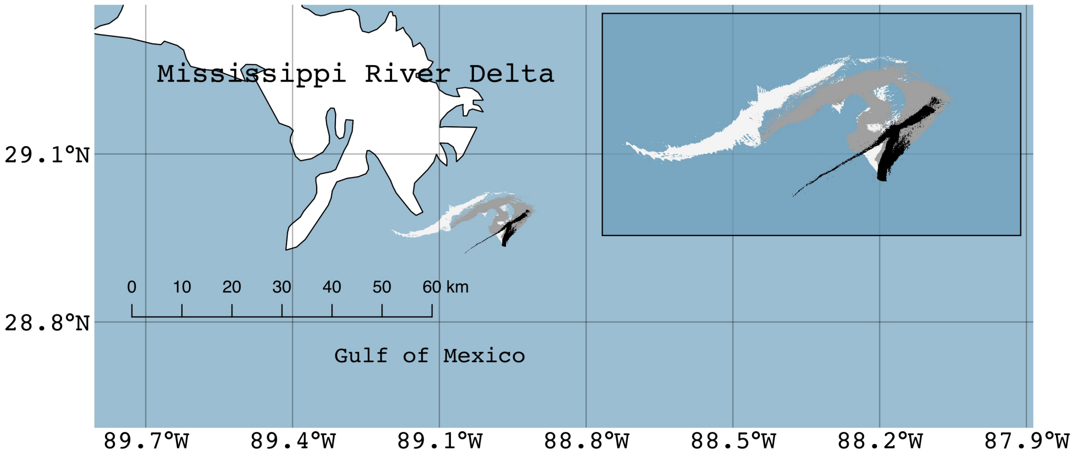

Figure 5.2: Map showing the location of the consistent seep in the MC-20 block in the Gulf of Mexico where the three UAVSAR time series (white, grey and black masks) were collected.

5.3 The Fram Strait Arctic Outflow Observatory

The Norwegian Polar Institute annually conducts a sea ice in-situ data collection in the Fram Strait. The main purpose of this campaign is to maintain an oceanographic mooring array that provides a time series of conditions, e.g., temperature, salinity, velocity, and sea ice thickness measurements in the Arctic Outflow. The ground truth information available in these remote areas allows for comparison of in-situ measurements with remote sensing data. During the 2015 Fram Strait campaign we had the opportunity to collect overlapping FP (Radarsat-2) and real HP (RISAT-1) C-band SAR data. A study (Paper IV) about the relationship between the two polarization modes using the overlapping SAR scenes together with the sea ice observations was conducted. Sea ice types, snow-, and ice thickness were some of the in-situ information collected. Three overlapping RISAT-1 and Radarsat-2 scenes with less than 20 minutes time difference were collected (see Figure 5.3).

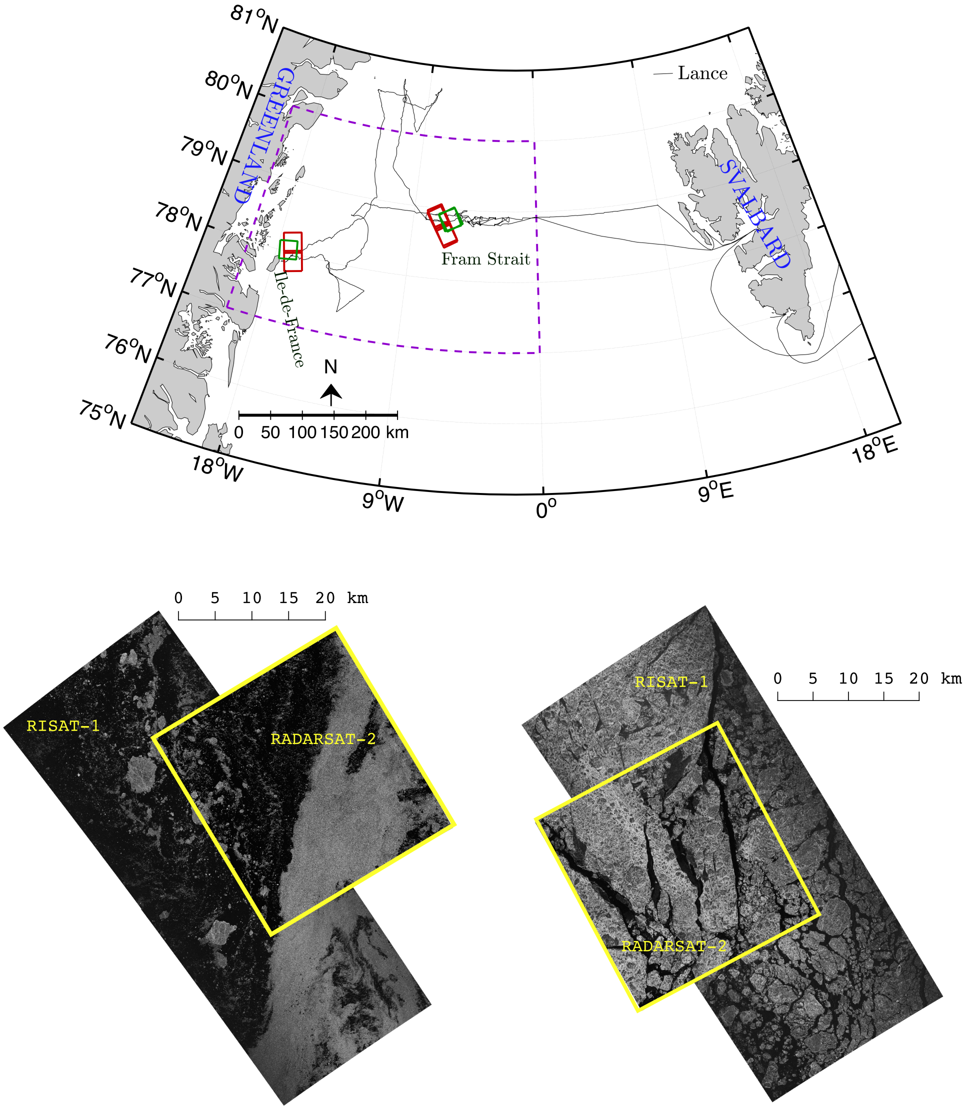

Figure 5.3: Top: Map with the locations of the overlapping scenes. The dashed square is the area of interest used in Paper IV. Bottom: Examples of two RISAT-1 and Radarsat-2 pairs used in Paper IV. The Radarsat-2 data and Products © MDA LTD. 2015 and RISAT-1 © 2015-Antrix-All rights reserved.

5.4 Remote Sensing Data Collection

Table 5.1 shows the different SAR sensors and imaging modes that are used in this thesis. UAVSAR (L-band sensor) and TerraSAR-X (X-band sensor) are only used for oil spill studies, whereas RISAT-1 (C-band sensor) is used only for the sea ice study presented in Paper IV. Radarsat-2 is used both for oil spill and sea ice studies. Note that RISAT-1 no longer is operational.

Table 5.1: Overview of the sensors used in this thesis and their properties [MDA, 2018] [Fritz and Eineder, 2010] [Fore et al., 2015] [Misra et al., 2013]. FRS-1 = Fine Resolution Stripmap. SSC = Single-look slant-range complex.

	TerraSAR-X	**Radarsat-2**	**RISAT-1**	**UAVSAR**
Frequency	X-band (9.65 GHz)	C-band (5.405 GHz)	C-band (5.35 GHz)	L-band (1.26 GHZ)
Mode	Stripmap SSC (Dual-pol)	Single Beam Fine Quad-pol	FRS-1 Dual-pol	Quad-pol
Polarization	HH,VV	HH,HV, VH,VV	RH, RV	HH,HV, VH,VV
Range swath[1]	15km	25km	25km	20km
Resolution[1] **(rg.**[2] **× az.)**	1.2 × 6.6m	5.2 × 7.6m	2 × 3m	2.5 × 1m
Incidence angle[1]	15°-60°	30°-50°	12°-55°	25°-65°
Paper #	II	I, II,IV	IV	I,II,III

[1] Nominal values.

[2] The range resolution is given in slant range.

6

Overview of Publications

This chapter provides an executive summary of the four publications presented in Chapters 7-10.

6.1 Paper Summaries

Paper I

M. M. Espeseth, S. Skrunes, C. E. Jones, C. Brekke, B. Holt, and A. P. Doulgeris. "**Analysis of Evolving Oil Spills in Full-Polarimetric and Hybrid-Polarity SAR**", IEEE Transactions on Geoscience and Remote Sensing, vol. 55, no. 7, pp. 4190-4210, July 2017.

This paper presents, for the first time, an investigation of the difference between FP and HP SAR for a time series with short revisit time (20 minutes). One of the main objectives of this thesis is to explore the potential of HP SAR data, and how this mode performs in comparison with the well known FP SAR mode. This study investigates several polarimetric features extracted from FP and simulated HP data. The investigation involves identifying and comparing the features ability to separate various oil types from the surrounding clean sea. The two-scale Bragg models, namely the X-Bragg [Hajnsek et al., 2009] (referred to as the two-scale Bragg model in the paper) and the tilted Bragg [Valenzuela, 1978] are used when grouping the investigated FP and HP features into two categories that are either independent or dependent of the small-scale ocean surface roughness.

Short time series of the oil slick evolution is challenging to obtain using spaceborne SARs with and without full polarimetric capabilities. Since oil changes and evolves rapidly at the sea surface, short time difference between scenes is advantageous. Using airborne SAR, such as the UAVSAR, time series of SAR images can be gathered with high temporal resolution and full polarimetric capabilities. As a result of the low noise floor of the UAVSAR instrument, polarimetric features, and simulation of HP data can be used without too much noise contamination.

The overall conclusion is that the HP mode is comparable to the FP mode for oil versus sea separability. Furthermore, the features dependent on the small-scale roughness are the ones which exhibit highest separability between the various slick types and clean sea. It was not possible to separate the various types of oil using any of the investigated features. In general, the plant oil had higher detectability than the three emulsions across the time series. Furthermore, the features that contain the cross-polarization component are better for distinguishing the various oil slicks from clean sea. These cross-polarization features are not available in the HP mode, and alternative HP features are suggested in Paper I.

Errata

Some minor mistakes were discovered after publication of this paper, and these are listed here.

- Typo in the Bhattacharyya distance equation. The $\Sigma_i^{-1} + \Sigma_j^{-1}$ should have been $(\Sigma_i + \Sigma_j)^{-1}$.
- The calculation of the mean alpha angle was based on the coherency matrix, but the paper erroneously referred to this as the covariance matrix.

Paper II

M. M. Espeseth, C. Brekke, C. E. Jones, B. Holt, and A. Freeman "**Interpreting backscattering from oil spills in view of system noise in polarimetric SAR imagery**", IEEE Transactions on Geoscience and Remote Sensing, 2019, in review.

Several studies have argued that polarimetry can aid in understanding the scattering types within oil slicks, and use polarimetry for characterization. This can only be done if the signal is well above the noise floor. The limitation of polarimetric features and their behaviour with respect to system noise is evaluated in this paper. The motivation behind this study originates from several articles (see, e.g., [Alpers et al., 2017, Minchew et al., 2012, Skrunes et al., 2018]) showing their concerns on the influence of system noise on several polarimetric features. Both multiplicative and additive system noise is investigated in this paper unlike several previous studies on SAR remote sensing of oil. The multiplicative system noise factors are quantization noise, ISLR effect, azimuth and range ambiguity and these are treated as another additive noise contribution in the measured signal. These sources are considered multiplicative since they depend on the mean signal level as opposed to the thermal noise.

This study shows a high correlation between the polarimetric feature values and system noise. The results demonstrate a significant reduction of the SNR when including the multiplicative system noise factors, which are usually not considered when estimating the SNR. Further, the authors recommend an SNR=10dB prior to any scattering analysis.

Several polarimetric features are investigated in this paper, and amongst these are the entropy and mean alpha angle commonly used in oil spill studies. This study confirms (also mentioned in e.g., [Minchew et al., 2012, Alpers et al., 2017]) that high entropy and high mean alpha angle for oil slicks are related to system noise and not a different scattering mechanism than the surrounding clean sea. In this study, we recommend not using H/α for oil spill scattering analysis. We also recommend a noise subtraction before any polarimetric analysis when characterizing the oil. However, the noise subtraction reduces the oil-sea contrast and should be avoided for oil slick detection purposes.

Paper III

M. M. Espeseth, C. E. Jones, B. Holt, C. Brekke, and S. Skrunes "**Oil Spill Response-Oriented Information Products Derived from a Rapid Repeat Time-Series of SAR Images**", IEEE Journal of Selected Topics in Applied Earth Observations and Remote Sensing, 2019, submitted.

This paper focuses on oil spill response-oriented information products derived from SAR data from an operational perspective. The study introduces two semi-automatable methods for investigating oil slick evolution using a time series of UAVSAR images. The methods show two ways of acquiring information about the changes and stability within an oil slick over a short time period using the damping ratio. The damping ratio is based on the VV-channel, and a single-polarization could therefore be used as input for the two methods. These methods are straightforward to implement and could potentially be used in an oil spill recovery process when time is of the essence. One method is used to identify locations within the slick that consistently exhibit a high damping ratio over a period of time, which might be categorized as actionable oil.

The other method provides an overview of the small-scale oil drift pattern using the mean difference between pairs of damping ratio images acquired with small time difference. Here, information about both oil movement and the change in backscatter within the oil slick can be obtained. The two methods are complementary in terms of identifying internal variations within a slick, the oil drift pattern, and the weathering and accumulation of oil to form higher damping surface layers. These are important aspects in the planning and execution of a clean-up process.

Paper IV

M. M. Espeseth, C. Brekke, and M. Johansson, "**Assessment of RISAT-1 and Radarsat-2 for Sea Ice Observations from a Hybrid-Polarity Perspective**", Remote Sensing, vol. 9, no. 11, September 2017.

Paper I compares FP and simulated HP for oil spill detection. Similarly, Paper IV compares simulated HP with real HP for separating various sea ice types. Sea ice classification is important from a maritime perspective in ice infested waters to ensure safe and fuel-efficient passages. The heat and gas exchange is influenced by the sea ice types and their respective abundances. In this paper a unique data set of overlapping FP (Radarsat-2) and real HP (RISAT-1) are used. This data set provides the opportunity to test simulated HP with the real HP. The main objective of this study is to identify the dissimilarities and similarities between simulated and real HP data for different sea ice types. The analysis is based on 13 HP features that are sensitive to various scattering properties within the sea ice.

The results indicate a similar separability between the sea ice types using the real HP system in RISAT-1 and the simulated HP system from Radarsat-2. The HP features that are sensitive to surface scattering and depolarization due to volume scattering showed great potential for separating various sea ice types. A subset of features are affected, in terms of sea ice separability, by the non-circularity property of the transmitted wave in the simulated HP system across all the scene pairs. Overall, the best features, showing high separability between various sea ice types and which are invariant to the non-circularity property of the transmitted wave, are the RH- and RV-intensity coefficients and the first parameter in the Stokes vector.

6.2 Other Publications

As first author

1. M. Espeseth, C. Brekke, and S. N. Anfinsen, "**Hybrid-Polarity and Reconstruction Methods for Sea Ice With L- and C-Band SAR**", IEEE Geoscience and Remote Sensing Letters, vol. 13, no. 3, pp. 467-471, February, 2016.

2. M. Espeseth, S. Skrunes, C. Brekke, and A. B. Salberg, C. Jones, and B. Holt, "**Oil spill characterization in the hybrid-polarity SAR domain using log-cumulants**".

Proceedings of SPIE, the International Society for Optical Engineering, vol. 10004, 2016.

As co-author

3. A. Marinoni, M. Johansson, M. Espeseth, and C. Brekke, "**Multidi-mensional distance geometry analysis for classification of PolSAR images in Arctic scenarios.** Polarimetric Interferometric SAR (PolInSAR) conference, 2019.
4. S. Skrunes, C. Brekke, C. E. Jones, M. Espeseth, and B. Holt, "**Effect of Wind Direction and Incidence Angle on Polarimetric SAR Observations of Slicked and Unslicked Sea Surfaces**", Remote Sensing of Environment, vol. 213, pp. 73-91, 2018.
5. C. E. Jones, M. Espeseth, B. Holt, C. Brekke, "**Measurement of Oil Slick Transport and Evolution in the Gulf of Mexico using L-band Synthetic Aperture Radar**", 12th European Conference on Synthetic Aperture Radar (EUSAR), 2018.
6. S. Skrunes, C. Brekke, and M. Espeseth. "**Assessment of the RISAT-1 FRS-2 Mode for Oil Spill Observation.**" IEEE International Geoscience and Remote Sensing Symposium (IGARSS) proceedings, 2017.
7. C. Brekke, S. Skrunes, and M. Espeseth. "**Oil Spill Dispersion in Full-polarimetric and Hybrid-polarity SAR**". IEEE International Geoscience and Remote Sensing Symposium (IGARSS) Proceedings, 2017.
8. C. Brekke, C. E. Jones, S. Skrunes, B. Holt, M. Espeseth, and T. Eltoft, "**Cross-Correlation Between Polarization Channels in SAR Imagery Over Oceanographic Features.**" IEEE Geoscience and Remote Sensing Letters 2016, Volum 13 (7).
9. C. E. Jones, K.-F. Dagestad, Ø. Breivik, B. Holt, J. Röhrs, K. H. Christensen, M. Espeseth, C. Brekke, and S. Skrunes, "**Measurement and modeling of oil slick transport.**" Journal of Geophysical Research - Oceans, 2016, Volum 121 (10).
10. S. Skrunes, C. E. Jones, C. Brekke, B. Holt, and M. Espeseth, "**On the effect of imaging geometry on multipolarization SAR features for oil spill observation**". Proceedings of Living Planet Symposium, European Space Agency, 2016.
11. C. E. Jones, M. M. Espeseth, B. Holt, C. Brekke, and S. Skrunes, "**Characte-rization and discrimination of evolving mineral and plant oil slicks based on L-band synthetic aperture radar (SAR)**", Proceedings of SPIE, the International Society for Optical Engineering 2016; Volum 10003.

12. K. Blix, M. Espeseth, and E. Eltoft, "**Up-Scaling From Quad-polarimetric To Dual-polarimetric SAR Data Using Machine Learning Gaussian Process Regression**", IEEE International Geoscience and Remote Sensing Symposium (IGARSS) Proceedings, 2018.

13. K. Blix, M. Espeseth, and T. Eltoft, "**Machine Learning simulations of quad-polarimetric features from dual-polarimetric measurements over sea ice**", 12th European Conference on Synthetic Aperture Radar (EUSAR), 2018.

14. C. E. Jones, C. Brekke, Ø. Breivik, B. Holt, S. Skrunes, M. Espeseth, "**NORSE2015 - A Focused Experiment On Oil Emulsion Characterization Using PolSAR During the 2015 Norwegian Oil-On-Water Exercise**, AGU Oceans, 2016.

15. M. Johansson, M. Espeseth, C. Brekke, and S. Skrunes. "**Separation and characterisation of mineral oil slicks and newly formed sea ice in L-band synthetic aperture radar.**" IEEE International Geoscience and Remote Sensing Symposium (IGARSS) Proceedings, 2019.

16. A. Marinoni, M. Espeseth, P. Gamba, C. Brekke, and T. Eltoft. "**Assessment of Polarimetric Variability by Distance Geometry for Enhanced Classification of Oil Slicks Using SAR**". IEEE International Geoscience and Remote Sensing Symposium (IGARSS) Proceedings, 2019.

17. M. Espeseth, S. Skrunes, C. Brekke, and M. Johansson. "**The Impact of Additive Noise on Polarimetric RADARSAT-2 Data Covering Oil Slicks**". IEEE International Geoscience and Remote Sensing Symposium (IGARSS) Proceedings, 2019.

7

Paper I:

Analysis of Evolving Oil Spills in Full-Polarimetric and Hybrid-Polarity SAR

M. M. Espeseth, S. Skrunes, C. E. Jones, C. Brekke, B. Holt, and
A. P. Doulgeris

Published in:
IEEE Transactions on Geoscience and Remote Sensing, vol. 55,
no. 7, July 2017.

Analysis of Evolving Oil Spills in Full-Polarimetric and Hybrid-Polarity SAR

Martine M. Espeseth, Stine Skrunes, *Member, IEEE*, Cathleen E. Jones, *Member, IEEE*,
Camilla Brekke, *Member, IEEE*, Benjamin Holt, *Member, IEEE*,
and Anthony P. Doulgeris, *Member, IEEE*

***Abstract*—Oil spill detection using a time series of images acquired off Norway in June 2015 with the uninhabited aerial vehicle synthetic aperture radar is examined. The relative performance of a set of features derived from quad-polarization versus hybrid-polarity (HP) modes in detection of various types of slicks as they evolve on a high wind driven sea surface is evaluated. It is shown that the HP mode is comparable with the full-polarimetric mode in its ability to distinguish the various slicks from open water (OW) for challenging conditions of high winds (9–12 m/s), small release volumes (0.2–0.5 m^3), and during the period 0–9 h following release. The features that contain the cross-polarization component are better for distinguishing the various slicks from open water at later and more developed stages. Although these features are not available in the HP mode, we identify alternative features to achieve similar results. In addition, a clear correlation between the results of individual features and their dependence on particular components within the two-scale Bragg scattering theory is identified. The features that show poor detectability of the oil slicks are those that are independent of the small-scale roughness, while the features resulting in good separability were dependent on several factors in the two-scale Bragg scattering model. We conclude that the HP mode is a viable alternative for SAR-based oil spill detection and monitoring that provides comparable results to those from the quad-polarimetric SAR.**

***Index Terms*—Hybrid polarity (HP), NORSE2015, oil spill observation, synthetic aperture radar (SAR), time series, uninhabited aerial vehicle synthetic aperture radar (UAVSAR).**

I. INTRODUCTION

SPACEBORNE and airborne remote sensing instruments are the key tools for an operational oil pollution monitoring program. Spaceborne instruments offer the unique capabilities of large swath widths and for some satellite constellation missions improved temporal coverage. Aircraft surveillance flights are flexible and allow monitoring of evolving oil with time, as well as verifying the oil in some cases. In recent years, characterizing oil spills in the marine environment using the full-polarimetric (FP) synthetic aperture radar (SAR) has intensified (see, e.g., [1]–[4]). During the Deepwater Horizon accident, the National Aeronautics and Space Administration (NASA) uninhabited aerial vehicle synthetic aperture radar (UAVSAR) provided the valuable observations of the major oil spill with fine resolution and a system that has a low noise floor [5]. An analysis of the FP SAR acquisitions revealed a potential in retrieval of quantitative slick properties [1].

FP SAR systems provide a unique capability of measuring the complete scattering matrix and allow identification and extraction of the scattering properties within a given resolution cell. However, the FP SAR system comes at a cost, typically a smaller spatial coverage or reduced spatial resolution compared with the dual-polarization (DP) and single-polarization SAR modes. A DP SAR transmits in one polarization and receives in two polarization channels. The choice of polarization for the conventional linear–linear DP SAR systems is horizontal (H) or vertical (V) linear polarization on transmit, and the backscattered response is measured in the horizontal and vertical linearly polarized channels. The drawback of using a DP SAR system is the reduced polarimetric information compared with FP. Raney [6] suggested that changing the polarization of the transmitted wave to circular polarization (resulting in a circular–circular system) gave a simpler instrument and improved the quality of the radar measurements in terms of minimizing sensitivity to relative errors and crosstalk, straightforward calibration of the radar signals, and decreasing the on-board resource requirements. This mode was named hybrid-polarity (HP) or compact-polarimetric (CP) mode. In addition, the polarimetric information given in the HP (CP) mode is in some cases reported to be close to that of FP SARs (see, e.g., [7]–[10]). The HP mode belongs to the DP SAR group, with wider swath and equal spatial resolution or improved spatial resolution and equal swath compared with the conventional FP SARs.

There exist a few studies on oil spill detection related to the use of simulated HP UAVSAR data from the Deepwater Horizon in the Gulf of Mexico from 2010 (see, e.g., [11], [12]). Collins *et al.* [11] investigated the reconstruction of a pseudo-FP covariance matrix from simulated HP data and computed the oil-water mixing index suggested in [13]. Shirvany *et al.* [12] investigated some simulated HP features and analyzed the appearance of the oil in the Deepwater

Manuscript received February 6, 2017; accepted March 9, 2017. Date of publication April 25, 2017; date of current version June 22, 2017. This work was supported in part by the Jet Propulsion Laboratory, California Institute of Technology under contract with the National Aeronautics and Space Administration, in part by the Centre for Integrated Remote Sensing and Forecasting for Arctic Operations (CIRFA) under Research Council of Norway (RCN) Grant 237906, and in part by the NORRUSS Program under RCN under Grant 233896. *(Corresponding author: Martine M. Espeseth.)*

M. M. Espeseth, S. Skrunes, C. Brekke, and A. P. Doulgeris are with the Department of Physics and Technology, UiT The Arctic University of Norway, 9019 Tromsø, Norway (e-mail: martine.espeseth@uit.no; stine.skrunes@uit.no; camilla.brekke@uit.no; anthony.p.doulgeris@uit.no).

C. E. Jones and B. Holt are with the Jet Propulsion Laboratory, California Institute of Technology, Pasadena, CA 91125 USA (e-mail: cathleen.e.jones@jpl.nasa.gov; benjamin.m.holt@jpl.nasa.gov).

Color versions of one or more of the figures in this paper are available online at http://ieeexplore.ieee.org.

Digital Object Identifier 10.1109/TGRS.2017.2690001

$$\sigma^0_{\mathrm{HH}} = 4\pi k_r^4 \cos^4(\theta_i) \left| \left(\frac{\sin(\theta+\psi)\cos(\xi)}{\sin(\theta_i)}\right)^2 R_{\mathrm{HH}}(\theta_i,\epsilon_r) + \left(\frac{\sin(\xi)}{\sin(\theta_i)}\right)^2 R_{\mathrm{VV}}(\theta_i,\epsilon_r) \right|^2 W(2k_r\sin(\theta+\psi), 2k_r\cos(\theta+\psi)\sin(\xi)) \quad (1)$$

$$\sigma^0_{\mathrm{VV}} = 4\pi k_r^4 \cos^4(\theta_i) \left| \left(\frac{\sin(\theta+\psi)\cos(\xi)}{\sin\theta_i}\right)^2 R_{\mathrm{VV}}(\theta_i,\epsilon_r) + \left(\frac{\sin(\xi)}{\sin(\theta_i)}\right)^2 R_{\mathrm{HH}}(\theta_i,\epsilon_r) \right|^2 W(2k_r\sin(\theta+\psi), 2k_r\cos(\theta+\psi)\sin(\xi)) \quad (2)$$

$$\sigma^0_{\mathrm{HV}} = 4\pi k_r^4 \cos^4(\theta_i) \left(\frac{\sin(\theta+\psi)\cos(\xi)\sin(\xi)}{\sin^2(\theta_i)}\right)^2 |R_{\mathrm{VV}}(\theta_i,\epsilon_r) - R_{\mathrm{HH}}(\theta_i,\epsilon_r)|^2 W(2k_r\sin(\theta+\psi), 2k_r\cos(\theta+\psi)\sin(\xi)) \quad (3)$$

Horizon slick using one UAVSAR scene covering a relatively thick oil slick under low wind conditions.

The backscattered response from clean seas and oil slicks within SAR scenes is complex and dependent on several factors, including amongst others the slick characteristics (dielectric properties, viscosity, extent, and composition), environmental conditions (wind, sea state, and temperature), and sensor properties [frequency, resolution, coverage, and signal-to-noise ratio (SNR)]. In general, oil spills will spread to form a thin layer on the water surface, and this layer will dampen the small-scale roughness on the ocean surface, resulting in reduced backscattered power [14]. Another factor that can reduce the backscattered power is a reduction in the dielectric constant within the slick compared with the clean sea. This factor will contribute to the detectability if the oil slick is thick enough and/or the concentration of the oil droplets within the water column is high enough [13]. The backscattering of microwaves from a clean sea surface is usually described using the Bragg scattering theory, in which the incoming wave is in resonance with the ocean waves (resonant scattering) [15], [16]. The Bragg waves can further be modulated by the longer waves on which they ride through tilt and hydrodynamic effects [17].

For the first time, in this paper, we investigate the difference between FP and HP for a series of UAVSAR scenes covering various types of oil slicks under high wind condition as they evolve following release. This paper investigates and compares FP and simulated HP data acquired over slicks using a unique UAVSAR time series acquired in the FP mode. The UAVSAR time series was collected from a controlled oil spill experiment, the NOrwegian Radar oil Spill Experiment 2015 (NORSE2015), that took place in the North Sea at the Frigg field in June 2015. This experiment was a collaboration between UiT The Arctic University of Norway, the Jet Propulsion Laboratory (JPL)/NASA, and the Norwegian Clean Seas Association for Operating Companies. The UAVSAR time series was collected during two flights during a single day with approximately 3 h between the end of data acquisition in the first and the beginning of data acquisition in the second. There were 16 and 6 acquisitions in the first and second flights, respectively, obtained over an 8-h total time span. The UAVSAR was used to image four different oil slicks as they evolved and weathered on a high wind sea surface (approximately 12 m/s). In addition, X-, C-, and L-band SAR data were also collected from satellite SAR sensors coincident with one of the UAVSAR images. The reader is referred to [18]–[20] for additional information and analysis from the experiment.

The main objectives of this paper are: 1) to study the performance of a set of well-known FP and HP features to detect oil slicks; 2) to identify and compare the best FP and HP features for detecting the evolving oil slicks; 3) to identify the dominating components in the Bragg scattering theory to which the investigated FP and HP polarimetric features are sensitive; and 4) to study the difference in detectability of the various oil slicks as they developed.

The Bragg scattering theory and the HP theory are described in Section II, the experiment is described in Section III, the preprocessing steps are described in Section IV and in the Appendix, and Section V contains the information about the polarimetric features used in this paper. Section VI presents the time series results, and Section VII presents the conclusions of this paper.

II. THEORY

In this section, we introduce the tilted Bragg scattering model used for the FP data, the theory of the HP SAR mode, and the two-scale Bragg model that is adapted for the HP mode.

A. Tilted Bragg Model

The backscatter from the ocean surface can be described through the theory of Bragg. Bragg scattering is caused by small-scale surface roughness whose height is small compared with the radar wavelength [15]. In addition, the in-plane tilt and the out-of-plane tilt of the facet, caused by the large-scale gravity waves on the ocean surface, will alter a response in the like-polarized channel and add a response in the cross-polarized channel. Including this tilt of the surface in the Bragg model leads to the tilted Bragg model (also known as the Valenzuela model) [15]. From this model, the equations of the normalized radar cross sections from an FP SAR system are given in (1)–(3), as shown at the top of the page. In these equations, k_r is the wavenumber, θ is the incidence angle relative to the untilted horizontal plane [1], and $\theta_i = \cos^{-1}[\cos(\theta+\psi)\cos(\xi)]$ is the local incidence angle. ψ is the angle between the vertical and the normal to the patch projected into the plane of incidence, and ξ is the angle between the vertical and the normal to the patch projected into the plane perpendicular to the plane of incidence [15]. $W(\cdot)$ is the 2-D wavenumber spectral density of the ocean surface roughness, and R_{HH} and R_{VV} are the Bragg scattering coefficients defined as [1]

$$R_{\mathrm{HH}}(\theta_i,\epsilon_r) = \frac{\cos(\theta_i) - \sqrt{\epsilon_r - \sin^2(\theta_i)}}{\cos(\theta_i) + \sqrt{\epsilon_r - \sin^2(\theta_i)}} \quad (4)$$

and

$$R_{\mathrm{VV}}(\theta_i, \epsilon_r) = \frac{(\epsilon_r - 1)(\sin^2(\theta_i) - \epsilon_r(1 + \sin^2(\theta_i)))}{(\epsilon_r \cos(\theta_i) + \sqrt{\epsilon_r - \sin^2(\theta_i)})^2} \quad (5)$$

where ϵ_r is the relative dielectric constant, and the subscripts of R_{HH} and R_{VV} represent the transmit and the receive polarizations. As can be observed from (4) and (5), the backscattered radar cross sections are dependent on several components, namely, the wave spectrum, the imaging geometry, and the dielectric properties of the media.

B. Hybrid-Polarity Theory

In this paper, we investigate the HP system with right circular transmit and linear receive architecture. This configuration is already integrated in current satellite missions, such as RISAT-1 and ALOS-2, and will also be incorporated in several upcoming spaceborne SARs. Recognizing its great potential for oil spill detection identified in [10] and [11], we choose HP as a comparing system to FP SAR in this paper. The fundamental quantities measured by a polarimetric SAR system are the complex backscattering terms S_{ij}. Here, i and j define the polarizations of the transmit and receive channels in the radar system. The HP mode transmits only one circular polarization, either left (L) or right (R), and receives two orthogonal linear polarizations, namely, horizontal and vertical [6]. For the right circular HP mode, the scattering vector is defined as

$$\bar{k}_{(\mathrm{RH,RV})} = [S_{\mathrm{RH}}, S_{\mathrm{RV}}]^T \quad (6)$$

where T denotes the transpose operator. The right circularly polarized transmit mode is used throughout this paper. In the linear horizontal and vertical basis, the scattering vector is expressed as [21]

$$\bar{k}_{(\mathrm{RH,RV})} = \frac{1}{\sqrt{2}}[S_{\mathrm{HH}} - iS_{\mathrm{HV}}, -iS_{\mathrm{VV}} + S_{\mathrm{HV}}]^T \quad (7)$$

where reciprocity is assumed ($S_{\mathrm{HV}} = S_{\mathrm{VH}}$). The UAVSAR instrument is an FP radar, and the HP scattering vector is simulated based on (7). In the FP SAR data, we have both co- and cross-polarized channels. By looking at the scattering vector $\bar{k}_{(\mathrm{RH,RV})}$, we can observe that the co- and cross-polarized components are not possible to isolate, since the HP scattering components are a mix of co- and cross-polarized terms. Combining the two measured linear horizontal and vertical polarization values, we can also form orthogonal components in the circular–circular polarization basis as [22]

$$\begin{aligned}\bar{k}_{(\mathrm{RR,RL})} &= [S_{\mathrm{RR}}, S_{\mathrm{RL}}]^T\\ &= \frac{1}{\sqrt{2}}[-S_{\mathrm{RH}} + iS_{\mathrm{RV}}, iS_{\mathrm{RH}} - S_{\mathrm{RV}}]^T\\ &= \frac{1}{2}[S_{\mathrm{VV}} - S_{\mathrm{HH}} + 2iS_{\mathrm{HV}}, i(S_{\mathrm{HH}} + S_{\mathrm{VV}})]^T. \quad (8)\end{aligned}$$

The expected sense of received circular polarization is opposite to the transmitted sense [23]. Therefore, S_{RR} becomes the cross-polarization state, while S_{RL} is the like-polarization state [23]. This corresponds to the CP SAR group, where the antenna transmits on right circular and receives in both right-hand circular and left-hand circular. Note, our initial starting point is still a simulated HP SAR system, but the HP scattering vector is in this case projected onto the circular basis at the receiver. Polarimetric features extracted from $\bar{k}_{(\mathrm{RH,RV})}$ and $\bar{k}_{(\mathrm{RR,RL})}$ will in Sections V and VI be investigated.

The polarimetric sample covariance matrix can be calculated from the target vector for each polarimetric system. The sample FP covariance matrix is given as

$$\boldsymbol{C}_{\mathrm{FP}} = \frac{1}{L}\sum_{j=1}^{L} \bar{k}_{\{j,(\mathrm{FP})\}}\bar{k}^{\star T}_{\{j,(\mathrm{FP})\}} \quad (9)$$

where $\star$ represents complex conjugate, $\bar{k}_j$ is the jth lexicographic scattering vector $\bar{k}_j = [S_{\mathrm{HH}}, S_{\mathrm{HV}}, S_{\mathrm{VH}}, S_{\mathrm{VV}}]^T$, and L is the number of samples included in the computation of the covariance matrix (the number of looks). Similarly, the sample HP covariance matrices in the circular–linear and circular–circular basis are given as

$$\boldsymbol{C}_{(\mathrm{RH,RV})} = \frac{1}{L}\sum_{j=1}^{L} \bar{k}_{\{j,(\mathrm{RH,RV})\}}\bar{k}^{\star T}_{\{j,(\mathrm{RH,RV})\}} \quad (10)$$

and

$$\boldsymbol{C}_{(\mathrm{RR,RL})} = \frac{1}{L}\sum_{j=1}^{L} \bar{k}_{\{j,(\mathrm{RR,RL})\}}\bar{k}^{\star T}_{\{j,(\mathrm{RR,RL})\}}. \quad (11)$$

Several studies have attempted to reconstruct a pseudo-FP covariance matrix, i.e., transforming from (10) to (9) (see, e.g., [21]–[24]). To do so, it is necessary to make some assumptions about the backscattering properties. As highlighted in [25], the appropriate methodology is to directly compare the HP with the FP mode without transforming to a pseudo-FP covariance matrix, thus avoiding any assumptions. In this paper, we follow Raney's methodology [25] and perform the study on features extracted directly from the simulated HP data. It is important to be aware that the use of HP mode in the UAVSAR instrument will not increase the swath width due to the design of the system. Also, when simulating the HP data from the FP data, a 3-dB power loss is introduced due to $\sqrt{2}$ in (7) [8].

Only the radar cross section of the HH, HV, and VV channels are estimated in the tilted Bragg model discussed in Section II-A. In order to have model estimates of the HP data, another model containing the complex backscattering coefficients is needed. In addition, a similar model is also necessary when evaluating polarimetric features from the FP covariance matrix. Therefore, Salberg *et al.* [10] suggested to use the two-scale Bragg for the HP mode. This model is similar to the tilted Bragg model in terms of containing two scales of the surface roughness, namely, the small- and the large-scale roughness. Salberg *et al.* [10] used the two-scale model by first simulating the HP scattering vector followed by a projection to the circular basis. The matrix ($\boldsymbol{S}$) of scattering coefficients denotes the Sinclair scattering matrix. Following the two-scale model, $\boldsymbol{S}$ can be expressed as [10], [26]:

$$\boldsymbol{S} = a_s\boldsymbol{R}(\phi)\begin{bmatrix} R_{\mathrm{HH}}(\theta_i, \epsilon_r) & 0 \\ 0 & R_{\mathrm{VV}}(\theta_i, \epsilon_r)\end{bmatrix}\boldsymbol{R}^T(\phi) \quad (12)$$

where $|a_s|^2 = k_r^4 \cos^4(\theta_i) W(\cdot)$ contains the factors related to the small-scale roughness, such as the ocean wave spectrum, incidence angle, and wavenumber. The rotation matrix $\boldsymbol{R}(\phi)$ is given as

$$\boldsymbol{R}(\phi) = \begin{bmatrix} \cos(\phi) & \sin(\phi) \\ -\sin(\phi) & \cos(\phi) \end{bmatrix}. \tag{13}$$

The tilt of the facet causes a rotation of the local plane of incidence around the look direction by an angle ϕ [27]. $\boldsymbol{R}(\phi)$ depends on the surface slope (azimuth and range directions) or large-scale roughness and the radar look angle [22], [27]. Calculating the expression in (12) gives (14), as shown at the bottom of the page. Inserting (14) into (7) gives (15), as shown at the bottom of the page. Both S_{RH} and S_{RV} depend on the rotation angle (ϕ), so Salberg *et al.* [10] suggested to consider the following quantities:

$$\begin{aligned} S_{\text{RH}} - iS_{\text{RV}} &= \frac{1}{\sqrt{2}}(S_{\text{HH}} - S_{\text{VV}} - 2iS_{\text{HV}}) \\ &= \frac{a_s}{\sqrt{2}}(R_{\text{HH}}(\theta_i, \epsilon_r) - R_{\text{VV}}(\theta_i, \epsilon_r)) \exp(2\phi i) \\ S_{\text{RH}} + iS_{\text{RV}} &= \frac{1}{\sqrt{2}}(S_{\text{HH}} + S_{\text{VV}}) \\ &= \frac{a_s}{\sqrt{2}}(R_{\text{HH}}(\theta_i, \epsilon_r) + R_{\text{VV}}(\theta_i, \epsilon_r)). \end{aligned} \tag{16}$$

Note the similarity to (8), where the

$$\begin{aligned} \bar{k}_{(\text{RR},\text{RL})} &= \begin{bmatrix} S_{\text{RR}} \\ S_{\text{RL}} \end{bmatrix} = \frac{1}{\sqrt{2}} \begin{bmatrix} -(S_{\text{RH}} - iS_{\text{RV}}) \\ i(S_{\text{RH}} + iS_{\text{RV}}) \end{bmatrix} \\ &= \frac{a_s}{2} \begin{bmatrix} (R_{\text{VV}}(\theta_i, \epsilon_r) - R_{\text{HH}}(\theta_i, \epsilon_r)) \exp(2\phi i) \\ i(R_{\text{HH}}(\theta_i, \epsilon_r) + R_{\text{VV}}(\theta_i, \epsilon_r)) \end{bmatrix}. \end{aligned} \tag{17}$$

The intensity of S_{RR} and S_{RL} becomes

$$\begin{aligned} |S_{\text{RR}}|^2 &= \left| -\frac{1}{\sqrt{2}}(S_{\text{RH}} - iS_{\text{RV}}) \right|^2 \\ &= \frac{|a_s|^2}{4} |R_{\text{VV}}(\theta_i, \epsilon_r) - R_{\text{HH}}(\theta_i, \epsilon_r)|^2 \end{aligned} \tag{18}$$

and

$$\begin{aligned} |S_{\text{RL}}|^2 &= \left| \frac{i}{\sqrt{2}}(S_{\text{RH}} + iS_{\text{RV}}) \right|^2 \\ &= \frac{|a_s|^2}{4} |R_{\text{HH}}(\theta_i, \epsilon_r) + R_{\text{VV}}(\theta_i, \epsilon_r)|^2. \end{aligned} \tag{19}$$

We observe that S_{RL} is independent of the rotation angle and so are $|S_{\text{RR}}|^2$ and $|S_{\text{RL}}|^2$. Note, however, that all of these include the Bragg coefficients, which are dependent on the tilt angles. The theory of tilted Bragg and the two-scale Bragg models will be used as a fundamental theory both when presenting the polarimetric features investigated and when evaluating the results from the UAVSAR data (Sections V and VI).

TABLE I

PROPERTIES OF THE EXPERIMENTAL OIL RELEASES DURING NORSE2015 [18], [19]

Release	Time (UTC)	Substance	Volume
PO	04:48	Plant Oil: Radiagreen ebo	0.2 m^3
E40	04:59	Emulsion (40% oil) 300 L water + 100 L Troll + 100 L Oseberg + 0.2 L One-Mul	0.5 m^3
E60	05:15	Emulsion (60% oil) 200 L water + 150 L Troll 150 L Oseberg + 0.2 L One-Mul	0.5 m^3
E80	05:30	Emulsion (80% oil) 100 L water + 200 L Troll + 200 L Oseberg + 0.2 L One-Mul	0.5 m^3

III. NORSE2015 EXPERIMENT

An extensive SAR data set was collected from both the airborne and spaceborne platforms during the NORSE2015 experiment at the abandoned Frigg field in the North Sea. *In situ* data, including wind, temperature, and oil-to-water ratios of the released oils, were collected and have been described in detail previously [18], [19]. The main motivation behind the NORSE2015 experiment was to collect the multisensor and multifrequency SAR data to study the polarization-dependent electromagnetic signals and their relationship to varying oil–water mixtures and dielectric properties, as well as study the evolving oil slicks' drift and characteristics as a function of time using SAR [18]–[20], [28], [29]. Table I summarizes the information about the released oil, which was three emulsions based on the same crude oil but with different volumetric oil concentrations, i.e., 40% oil (E40), 60% oil (E60), 80% oil (E80), and release of plant oil (PO) for the simulation of a natural biogenic slick.

The VV-intensity images for the UAVSAR scenes are shown in Fig. 1. These intensity images are geocoded, smoothed, and scaled for displaying purposes, and the ships are masked out and colored red. Note that the true width (number of pixels in the subsection displayed) of the images varies across the time series as the oil slicks evolve and spread out. The release of the E80 slick was not complete in the first UAVSAR acquisition, so this scene is not used in the analysis of the E80 slick. The PO and the three emulsion slicks are shown in Fig. 1, with the PO as the southern-most slick, and E40, E60, and E80 to the north. The properties of the UAVSAR sensor are given in Table II.

The oils were released along a line approximately parallel to the spaceborne SAR flight directions to obtain similar incidence angles for all slicks. In order to maximize the SNRs, the releases were done close to the center of the swaths. The UAVSAR acquisitions were then adapted to this setup

$$\boldsymbol{S} = \begin{bmatrix} S_{\text{HH}} & S_{\text{HV}} \\ S_{\text{HV}} & S_{\text{VV}} \end{bmatrix} = a_s \begin{bmatrix} R_{\text{HH}}(\theta_i, \epsilon_r)\cos^2(\phi) + R_{\text{VV}}(\theta_i, \epsilon_r)\sin^2\phi & \cos(\phi)\sin(\phi)(R_{\text{VV}}(\theta_i, \epsilon_r) - R_{\text{HH}}(\theta_i, \epsilon_r)) \\ \cos(\phi)\sin(\phi)(R_{\text{VV}}(\theta_i, \epsilon_r) - R_{\text{HH}}(\theta_i, \epsilon_r)) & R_{\text{VV}}(\theta_i, \epsilon_r)\cos^2(\phi) + R_{\text{HH}}(\theta_i, \epsilon_r)\sin^2\phi \end{bmatrix} \tag{14}$$

$$\bar{k}_{(\text{RH},\text{RV})} = \begin{bmatrix} S_{\text{RH}} \\ S_{\text{RV}} \end{bmatrix} = \frac{a_s}{\sqrt{2}} \begin{bmatrix} R_{\text{HH}}(\theta_i, \epsilon_r)\cos^2(\phi) + R_{\text{VV}}(\theta_i, \epsilon_r)\sin^2(\phi) + i(\cos(\phi)\sin(\phi)(R_{\text{HH}}(\theta_i, \epsilon_r) - R_{\text{VV}}(\theta_i, \epsilon_r))) \\ \cos(\phi)\sin(\phi)(R_{\text{VV}}(\theta_i, \epsilon_r) - R_{\text{HH}}(\theta_i, \epsilon_r)) - i(R_{\text{HH}}(\theta_i, \epsilon_r)\sin^2(\phi) + R_{\text{VV}}(\theta_i, \epsilon_r)\cos^2\phi) \end{bmatrix} \tag{15}$$

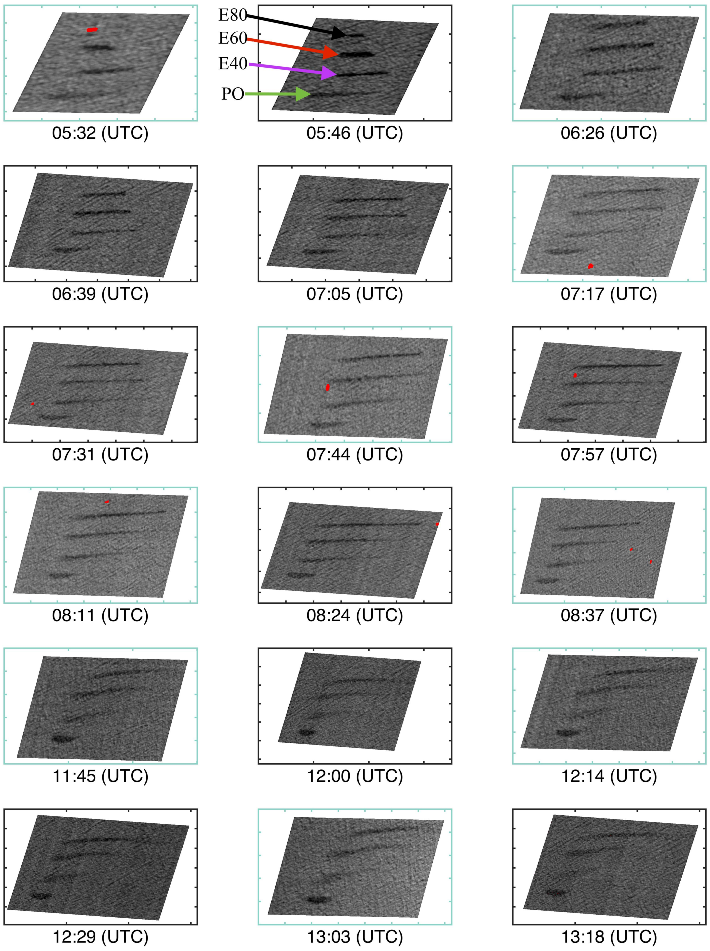

Fig. 1. Geocoded VV-intensity for the ascending (blue box) and descending (black box) UAVSAR scenes. The images are oriented with north pointing upward, and the ships are masked out and colored red. UAVSAR data are the courtesy of NASA/JPL-Caltech.

TABLE II

PROPERTIES OF THE UAVSAR SENSOR [5] AND THE UAVSAR SLC DATA PRODUCTS FOR THE ACQUIRED TIME SERIES OF IMAGES

Date	Time[a] (UTC)	Mode	Polarization	Frequency [GHz]	Incidence angle	NESZ [dB]	Resolution (rg[b] × az[c])	Swath width	Look direction
10th June 2015	05:32 - 13:18	PolSAR	Full-pol (HH,HV,VH,VV)	L-band (1.26)	19.5° to 67.5°	∼ -48 to -33	2.5 m × 1 m	20 km	Left

[a]Time when starting the acquisition to the end of the acquisition (including both flight 1 and 2), [b]rg: range, [c]az: azimuth

and the research team onboard the aircraft selected the flight lines so that the oil slicks were located where the antenna gain was near its maxima. The noise floor as a function of incidence angle (along the range direction) is shown for the UAVSAR instrument in [5, Fig. 1]. Here, the minimum noise is found near mid-swath in the range direction. Fig. 2 shows the incidence angle span for each slick along the UAVSAR time series. The UAVSAR monitored the evolving slicks in three different look directions and five different imaging geometries. In order to limit the effect from the imaging geometry on the polarimetric features, only ID numbers 00709 (ascending) and 18709 (descending) are used in this paper, with white background in Fig. 2. This is because these two data sets of imaging geometries contain the most scenes and the oil slicks are located at approximately the same incidence angles across the two subsets. The gray background denotes the scenes that are left out of this analysis and are the ones with slightly different imaging geometries. However, these scenes will be included in a future study that analyzes the effects from the imaging geometry on several polarimetric features.

IV. PREPROCESSING

In this section, we introduce the separability measure that is used when evaluating the performance in the preprocessing steps and the different polarimetric features. Furthermore, we discuss each of the steps that are performed on the UAVSAR data prior to the polarimetric analysis.

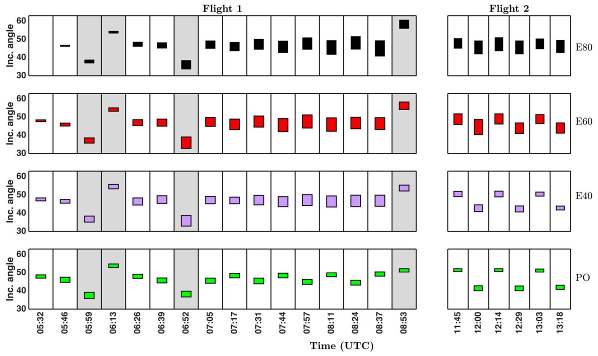

Fig. 2. Overview of the incidence angle range for each slick along the UAVSAR time series. The white colored sections (a total of 18 UAVSAR scenes) are used in this analysis, and the gray colored sections are not included.

A. Separability Measure

In this paper, several polarimetric features are compared in terms of how well they separate the various oil slicks from each other as well as from open water (OW). In the literature, several statistical metrics are described that can be used to accomplish this task. We want to use a statistical distance measure that can be applied across the UAVSAR time series for the range of polarimetric features investigated. The Bhattacharyya distance in the closed-form expression [30] has been used in [10] for evaluating the separability between various oil slicks and open water using some selected polarimetric features. Similarly, the normalized distance between the means was used in [31]. Evaluating the mean and standard deviations for each polarimetric feature relative to each other has been done in several studies (see, e.g., [3], [32]). In our case, we choose to use a distance measure that captures both the mean and the standard deviation of the polarimetric feature and, at the same time, is defined on an interval with discrete boundaries. We use the closed-form expression of the Bhattacharyya distance and assume Gaussian distributed data. This distance measure is defined as [30]

$$d_{ij} = \frac{1}{4}(\mu_j - \mu_i)^T \left(\Sigma_i^{-1} + \Sigma_j^{-1}\right)(\mu_j - \mu_i) + \frac{1}{2}\log\left(\frac{|\Sigma_i + \Sigma_j|}{2\sqrt{|\Sigma_i \Sigma_j|}}\right) \tag{20}$$

where μ_i and μ_j are the mean values and Σ_i and Σ_j denote the covariance matrices of the classes i and j, respectively. Superscript T denotes the transpose operator. In this paper, we apply this measure to each of the 1-D polarimetric features, i.e., Σ_i is the marginal variance and the transpose operator is not necessary. This distance spans from 0 (high similarity) to infinity (low similarity). To obtain a distance measure with discrete boundaries, we apply the Jeffries–Matusita (JM) distance, which takes values in the interval 0 (high similarity) to 2 (low similarity) [33]. The JM distance is defined as [33], [34]

$$\text{JM}_{ij} = 2(1 - e^{-d_{ij}}) \tag{21}$$

where d_{ij} is the Bhattacharyya distance given in (20). The JM_{ij} distance is well described in [33], and has been used for the sea ice classification in SAR data [35]. This measure is a function of the mean and standard deviation between feature values representing two given classes in our case the various oil slicks and open water. Dabboor and Geldsetzer [35] defined a JM of $\geq$1 to indicate that two classes are considered to be separable. Fig. 3 shows the examples on the sensitivity of the JM distance, where the histograms of four slicks and open water regions and their corresponding intensity images are displayed. We note that the boundary around the edges of the slick is partially composed of both oil and water, and the pixels will therefore be a mix of these. In two of the examples in Fig. 3, the JM distance is slightly above 0.8. These slicks are visible from the surrounding clean sea, and we therefore define JM values to be "acceptable" at a threshold of 0.8 and "confident" at 1.

B. Speckle Filtering

The backscattered signals from the surface can interfere constructively or destructively to produce bright and dark pixels in the SAR scene, known as speckle variation. Prior to calculating the polarimetric features used in this paper, speckle filtering is performed using a box-car filter. Following the selection of the filter, we select the window size (also known as the number of looks). The choice of number of looks has a great impact on the spatial resolution and on the contrast between the oil slicks and the clean sea. With the high resolution of the UAVSAR scenes, we can afford to have a coarser resolution with the gain of reducing speckle. The UAVSAR ground range resolution is 2.5 m (the slant range resolution is 1.7 m) and the azimuth resolution is 1 m [1], [5]. In the multilooking process, Minchew *et al.* [1] chose the relation to be one to four between the looks in the range and azimuth directions. We apply the same relation in this analysis when multilooking the data. Additionally, to achieve a good compromise between speckle reduction and preservation of details, a sliding window is used in the feature computations.

The single-look complex (SLC) images are smoothed with a mask of 15 × 60 pixels (range × azimuth). Fig. 4 shows the effect of smoothing on the JM separability of the VV-damping ratio between open water and between the four slicks as the total number of looks (both in range and azimuth) increases. The effect of increasing the number of looks in the averaging process is significant for all the JM distances of the four slicks and open water. In this case, we show the effect on two scenes, but similar results have been obtained for the other scenes as well. It is already known that increasing the mask size will enhance interpretability [36], but the small oil slicks might hamper detectability. From Fig. 4, the minimum mask size for separating the four slicks from the open water varies depending on the oil type. For these two scenes, less averaging is necessary to separate the PO from the open water compared to separating the emulsion slicks from the open water regions. Less averaging is needed for the E80 followed by E60 and E40. Because our main goal is to study the

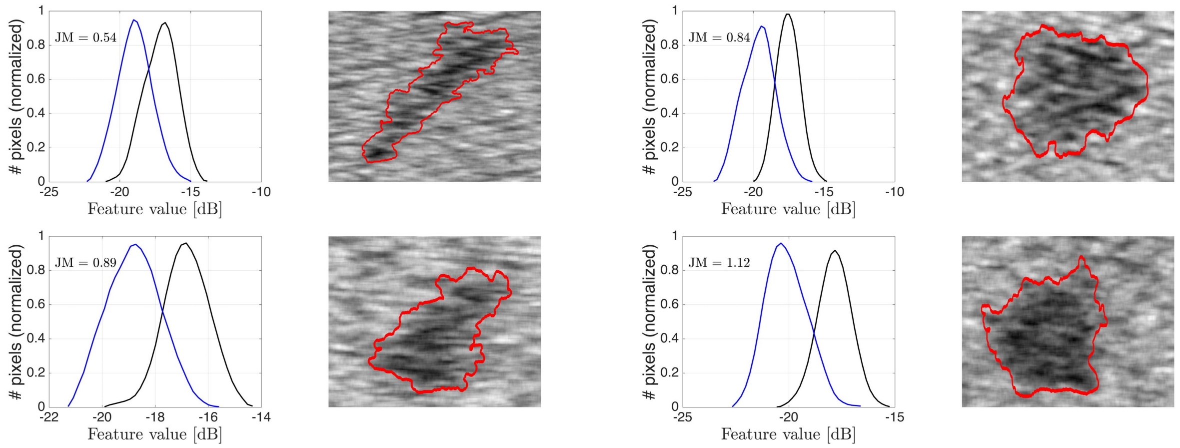

Fig. 3. Sensitivity of various values of the JM distance using the VV-intensity is illustrated using the histograms of the VV-intensity of four oil slicks (black color) and open water (blue color) with the same incidence angle range. The JM distance is calculated between the oil slick region and the open water region. Intensity images with the outline of the segmented masks are given to the right of their corresponding histograms.

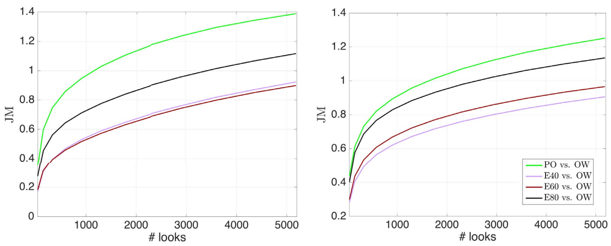

Fig. 4. Effect of increasing the number of looks in the speckle filtering on the JM separability between the four slicks and the open water using the VV-damping ratio. (Left) UAVSAR acquisition taken at 07:17 UTC. (Right) Scene acquired at 07:44 UTC.

evolution of different oil slicks, it is important to enhance interpretability of the oil slicks and, at the same time, keep a high spatial resolution.

C. Segmentation

Our goal is to evaluate the detectability of several polarimetric features for the various slick types over the UAVSAR time series. To be able to compare detectability, we need to segment out the different slicks. The same segmentation method should be applied on each scene for consistency and to avoid errors introduced by manual selection. Several segmentation methods for oil spill detection have already been extensively studied in the literature (see, e.g., [37], [38]). In our case, we choose a method that is generic and relatively simple to use, namely, the "extended polarimetric feature space" (EPFS) unsupervised method described in [39] and [40]. This unsupervised segmentation method includes both the polarimetric information and the textural information from the SAR data and groups all pixels with similar statistical properties in the same clusters.

The intensity variation related to incidence angle can be larger than the intensity difference between the classes, and hence, the oil slicks might be neglected in the original segmentation. Furthermore, the oil slicks spread out in the range direction with time, increasing the incidence angle span across the slicks. Therefore, an incidence angle correction (described in the Appendix) is applied on the scattering vector prior to segmentation.

The EPFS method can be split into four stages. The first is extraction of input features from the SAR data. Here, we use the span and the relative kurtosis [40] as an input. This stage also includes transforming the extracted features to partially remove non-Gaussian spreading and improve symmetry of the clusters, which is often achieved with the log operator. The second stage is to subsample the input features to speed up the segmentation process. In the third stage, the clusters are created using the expectation–maximization (EM) algorithm, assuming a multivariate Gaussian model for the transformed features. The number of classes (clusters) is usually a necessary input choice when segmenting, but this approach instead automatically determines the number of clusters using a goodness-of-fit test stage and sequentially applies the EM algorithm. Finally, a discrete Markov random field contextual smoothing stage completes the segmentation by integrating contextual information to improve the connectivity within the image segments. After the unsupervised segmentation approach, the oil slick regions are manually chosen from the output segments and labeled based on the *in situ* data.

Fig. 5 shows the segmentation results for the different slicks in the UAVSAR acquisition at 06:26 UTC. The green mask is PO, pink is E40, red is E60, and black is E80. Several open water regions are selected to determine the variance in the clean water properties and to enable a reasonable representation of the polarimetric features representing the open water class under the same environmental conditions as the slicks. These are selected based on the same shape for each slick, as shown in Fig. 5. This is done in order to have an equal number of open water samples as the oil slick as well as an equal number of pixels in both the range and azimuth directions, which matches the incidence angles of the slick pixels.

TABLE III

OVERVIEW OF THE INVESTIGATED FP POLARIMETRIC FEATURES (COMPUTED USING A MASK OF 15 × 60 PIXELS). THE REFERENCES INCLUDED ARE THE EXAMPLES OF STUDIES WHERE THE FEATURES HAVE BEEN STUDIED FOR OIL SPILL OBSERVATION

FP Features	
Name	Formula
Damping ratio ([1] [3] [41] [42])	$\zeta_{ij} = 10 \log_{10} \left(\frac{\langle I_{ij}^{(sea)} \rangle}{\langle I_{ij}^{(slick)} \rangle} \right), I_{ij} = \lvert S_{ij} \rvert^2$ $(i, j) \in \{(\mathrm{H,H}) \vee (\mathrm{H,V}) \vee (\mathrm{V,H}) \vee (\mathrm{V,V})\}$
Copolarization power ratio ([1] [2])	$\gamma_{CO} = \frac{\langle I_{VV} \rangle}{\langle I_{HH} \rangle}$
Real and imaginary part of the copolarization cross product ([2] [3] [19])	$r_{CO} = \lvert \Re(\langle S_{HH} S_{VV}^{\star} \rangle) \rvert, i_{CO} = \lvert \Im(\langle S_{HH} S_{VV}^{\star} \rangle) \rvert$
Standard deviation of the copolarization phase difference ([4] [43])	$\phi_{CO} = \sqrt{\langle (\phi_{HH} - \phi_{VV})^2 \rangle + (\langle \phi_{HH} - \phi_{VV} \rangle)^2}$
Magnitude of the copolarization correlation coefficient ([2] [9] [44] [45] [44])	$\rho_{CO} = \frac{\lvert (S_{HH} S_{VV}^{\star}) \rvert}{\sqrt{\langle \lvert S_{HH} \rvert^2 \rangle \langle \lvert S_{VV} \rvert^2 \rangle}}$
Conformity coefficient ([46])	$\mu_{FP} = \frac{2\left(\Re(\langle S_{HH} S_{VV}^{\star} \rangle) - \langle \lvert S_{HV} \rvert^2 \rangle\right)}{\langle \lvert S_{HH} \rvert^2 \rangle + 2 \langle \lvert S_{HV} \rvert^2 \rangle + \langle \lvert S_{VV} \rvert^2 \rangle}$
Determinant of the sample covariance matrix ([2] [3])	$\det(\boldsymbol{C}_{(FP)})$
Span of the sample covariance matrix ([45])	$\mathrm{span}(\boldsymbol{C}_{(FP)})$
Copolarization difference ([3] [47])	$\mathrm{PD} = \langle \lvert S_{HH} \rvert^2 \rangle - \langle \lvert S_{VV} \rvert^2 \rangle$
Cross-polarization ratio	$P_X = \frac{\langle \lvert S_{HV} \rvert^2 \rangle}{\langle \lvert S_{HH} \rvert^2 \rangle + \langle \lvert S_{VV} \rvert^2 \rangle}$
Eigenvalues of the sample covariance matrix	$\lambda_1 > \lambda_2 > \lambda_3$
Entropy ([9] [46] [45] [48] [49] [50] [51])	$H = -\sum_{i=1}^{3} p_i \log_3 p_i, \quad p_i = \frac{\lambda_i}{\sum_{i=1}^{3} \lambda_i}$
Mean α angle of eigenvectors	$\langle \alpha \rangle = \sum_{i=1}^{3} p_i \cos^{-1}(\boldsymbol{e}_i(1))$
Anisotropy	$A = \frac{\lambda_2 - \lambda_3}{\lambda_2 + \lambda_3}$
Polarization fraction	$PF = 1 - \frac{\lambda_3}{\lambda_1 + \lambda_2 + \lambda_3}$
Pedestal height	$PH = \frac{\lambda_3}{\lambda_1}$

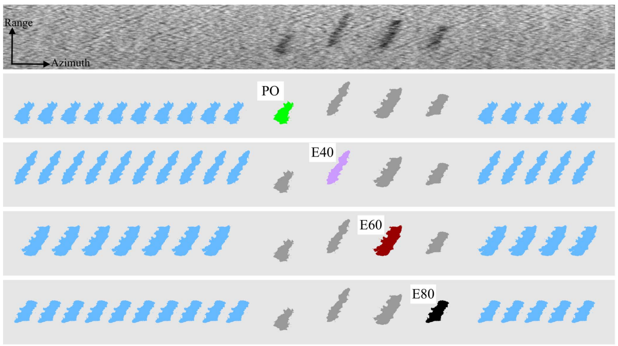

Fig. 5. Top-most figure is the VV-damping ratio of the UAVSAR acquisition taken at 06:26 UTC. The figures below show the segmentation results for each of the four slicks, and the manually selected open water regions to which they are compared. Multiple water regions are used to determine the variance in the clean water properties. The green color represents the PO, and the pink, red, and black colors represent E40, E60, and E80, respectively. Blue color represents open water regions.

V. POLARIMETRIC FEATURES FOR SLICK OBSERVATION

There exists several studies of the performance of oil slick characterization based upon various polarimetric features extracted from the FP and linear–linear DP SAR data evaluated for different ocean and wind conditions, various oil types, and different sensors with various incidence angles and frequencies (see, e.g., [1], [3], [32]). The sensitivity of polarimetric features to the different factors varies. This section presents the most frequently evaluated polarimetric features extracted from the FP and HP SAR data based on previous studies. A rigorous analysis is presented, connecting the Bragg scattering theory discussed in Section II and the polarimetric features here investigated (from both the FP and simulated HP modes).

A. Full-Polarimetric Features

The FP features used in this analysis are given in Table III and their corresponding relation to the components of the Bragg scattering theory is shown in Table IV. Table IV shows all the polarimetric features investigated (both FP and HP) and their dependence on factors in the Bragg scattering theory discussed in Section II. The FP features have all been extensively tested for oil spill characterization and detection, and some corresponding references for these studies are given in parentheses in Table III. In this paper, we observe oil slicks with different chemical and physical properties under high wind conditions and with relatively small volumes of slick material. Hence, some of the FP features reported as having the best performance in the literature may not fulfill their

TABLE IV

POLARIMETRIC FEATURES RELATED TO FACTORS IN THE TWO-SCALE BRAGG SCATTERING THEORY DISCUSSED IN SECTION II. THIS SETUP IS BASED ON THE DISCUSSION OF POLARIMETRIC FEATURES IN SECTION V. NOTE THE INCIDENCE ANGLE IS EITHER θ AND/OR THE LOCAL θ_i (SEE SECTION II)

Factors	Polarimetric features	
- Large-scale roughness - Small-scale roughness - Incidence angle - Dielectric properties	FP	ζ_{HH}, ζ_{VV}, ζ_{HV}, r_{CO}, i_{CO}, det($\boldsymbol{C}_{(FP)}$), span($\boldsymbol{C}_{(FP)}$), PD, λ_1, λ_2, λ_3
	HP	ζ_{RH}, ζ_{RV}, ζ_{RR}, ζ_{RL}, q_0, q_1, q_2, q_3, λ_1^{HP}, λ_2^{HP}, det($\boldsymbol{C}_{(RH,RV)}$), det($\boldsymbol{C}_{(RR,RL)}$)
- Large-scale roughness - Incidence angle - Dielectric properties	FP	γ_{CO}, ρ_{CO}, μ_{FP}, P_X, ϕ_{CO}, H, $\langle\alpha\rangle$, A, PF, PH
	HP	DoP, χ, δ, α, μ_E, $\gamma_{RV/RH}$, $\rho_{(RH,RV)}$, $\phi_{(RR,RL)}$, $\rho_{(RR,RL)}$, $\phi_{(RH,RV)}$, H_w, μ_{HP}

potential in our case, as already highlighted in [19]. Using one of the UAVSAR acquisitions, Skrunes *et al.* [19] showed that the best features for separating the various oil slicks from the open water region were the VV-intensity, the geometric intensity, the largest eigenvalue of the polarimetric decomposition, the real part of the copolarization cross product, and the span (as defined in Table III). These features had the highest separability (the Fisher discriminant ratio) between the four slicks and the open water.

The damping ratios have been shown to be good features for evaluating the contrast between the slick-free and slick covered surfaces in SAR imagery (see, e.g., [1], [3], [41], [42]). Both measured and simulated damping ratios are reported to decrease with increasing wind speed and to increase with frequency (Bragg wavenumber), oil viscosity, and thickness [41], [42]. The damping ratio is a function of the Bragg coefficients and the 2-D wavenumber spectral density of the ocean surface roughness [1]. The change in the effective dielectric constant decreases the backscatter power only if the oil spill is sufficiently thick or if the oil slick is mixed into the water in high enough concentration in a layer below the surface [13]. The oil slicks in our case are quite small in volume and areal extent. Skrunes *et al.* [19] estimated the thickness of the emulsion slicks to be in the range of 1.3–1.7 and 0.7 μm for the PO in the UAVSAR scene acquired at 06:26 UTC. The expected penetration depth for the L-band radar is much higher than these thicknesses. The radiation penetrates to the underlying seawater surface from which it scatters, and the ratio between the Bragg coefficients between the open water and the oil slick is approximately unity, because the scattering occurs mainly from the water interface [1]. The damping ratios are located in the first frame in Table IV. Damping ratios extracted from L-band UAVSAR imagery covering the Deepwater Horizon oil spill were discussed in [1]. It was shown that the HH was dampened slightly less than the VV and HV.

The copolarization power ratio is the ratio between the intensity of the complex scattering coefficients in the HH and VV channels. This feature has been found useful in several studies [1], [2]. In the tilted Bragg model, the copolarization power ratio is independent of the damping of gravity-capillary waves by the oil and is sensitive to the dielectric constant, the large-scale roughness, and the incidence angle [1]. Based on this, the copolarization power ratio is placed in the last frame in Table IV. In general, the ocean wave spectrum is independent of the polarizations. Following this, all the polarimetric features that are composed of ratios are independent of the ocean wave spectrum and depend only on the angles related to the slope and tilt, the incidence angle, and the dielectric properties.

The real part of the copolarization cross product has been shown to be a useful feature for detecting oil. Skrunes *et al.* [2] observed a decrease in correlation when moving from slick-free to slick-covered areas when using spaceborne SAR data. A difference in correlation was also observed using one of the UAVSAR scenes from the NORSE2015 experiment [19]. The physical mechanism behind the change in the correlation of the copolarization channels is yet unknown, but Bragg versus non-Bragg scattering, lower backscatter response for slick-covered surface, and change in scattering mechanism are some theories related to this feature. In the tilted Bragg model, no terms cancel out for this feature, and hence, this feature is in the top row of Table IV, depending on all the factors in the tilted Bragg model.

Another feature frequently used for slick detection is the standard deviation of the phase difference between the copolarization scattering coefficients. This feature is related to the target's properties and measures the degree of correlation between S_{HH} and S_{VV} [52]. Migliaccio *et al.* [4] used this feature to characterize the scattering return from oil spills and biogenic slicks. They differentiated the mineral oil from the clean sea under low-to-moderate wind conditions, and found higher values of the standard deviation of the phase difference for the mineral oil. Migliaccio *et al.* [4] and Schuler *et al.* [43] observed that the low values of this feature represented the presence of Bragg scattering and that an increase in this feature indicated departure from the Bragg regime. However, there is a lack of research on how this feature behaves when using high SNR SAR data. As discovered in [1] and [19], Bragg scattering was observed for the oil slick regions as well as in the open water areas. Therefore, using this feature to separate the oil from open water could be a challenging task, as a similar scattering mechanism might be present in both the regions. The phase difference is located in the bottom panel in Table IV, and this is because this feature contains a ratio between the imaginary and real part of the copolarization correlation coefficients (see, e.g., [53]), making it independent of the ocean wave spectrum.

The magnitude of the copolarization correlation coefficient ($\rho_{(\mathrm{CO})}$) is a multipolarization feature with values between 0 and 1. The low values of $\rho_{(\mathrm{CO})}$ indicate depolarization effects. These effects are sensitive to the presence of a complex surface, multiple scattering surface layers, and/or system noise [53]. This feature will be a function of the root mean square slope (large-scale roughness), the dielectric constant, and the incidence angle [2] (as shown in Table IV).

Studies related to this feature have found low values (low HH–VV correlation) for oil covered areas, and high values for open water regions using both the C- and X-band SARs [2], [44].

Another polarimetric feature that uses multipolarization data is the determinant of the sample covariance matrix. This feature is also similar to the geometric intensity (defined in [2]). Skrunes *et al.* [2] discovered that the geometric intensity gives good contrast between oil slicks and sea for both the X- and C-band SAR data with relatively high incidence angles. They also discovered lower values of this feature for slick-covered areas compared with slick-free areas. Neither the span nor the determinant of the sample covariance matrix contains the ratios of scattering coefficients, and hence, these features are given in the top row in Table IV.

Features related to the eigenvalues and the eigenvectors of the FP sample covariance matrix are also considered. The ones evaluated in this paper, for the FP case, are the eigenvalues, entropy (H), anisotropy (A), polarization fraction (PF), and mean alpha angle ($\langle\alpha\rangle$). The entropy contains information regarding the degree of randomness of the scattering process, while the anisotropy represents the relative importance of the second and third eigenvalues [54]. These features are all composed of ratios of eigenvalues extracted from the covariance matrix, and we can therefore assume, following the two-scale Bragg model, that these features are independent on the small-scale roughness and are only a function of the large-scale roughness, dielectric properties, and incidence angle (as reflected in the second frame in Table IV).

B. Hybrid-Polarity Features

The polarimetric features extracted from the simulated HP data used in this analysis are given in Table V, with the corresponding references given in parentheses. The Stokes vector is a popular feature when analyzing HP data. The expression for the Stokes vector for linear receive polarization is given in Table V. Each of the Stokes parameters is tested in this paper, where the first Stokes parameter (q_0) is the total power, the second, q_1, is the power in the linear horizontal or vertical polarization, q_2 is the power in the linearly polarized components at tilt angles 45° and 135°, and q_3 is equal to the power in the left-handed and right-handed circular polarizations [54]. Brekke *et al.* [18] showed that the imaginary part of the RH and RV (q_3) follows the same trend as the copolarization cross product, which has lower correlation for the oil slicks than for clean water. Following the two-scale Bragg model of the HP data, q_0 and q_3 are a function of the tilt angles, wave spectrum, incidence angle, and the dielectric properties, while q_1 and q_2 depend on the same terms, in addition to the rotation angle (as shown in Section II-B).

Child parameters of the Stokes vector evaluated in this paper are the degree of polarization (DoP), the ellipticity angle (χ), the circular-polarization ratio (μ_E), the relative phase (δ), and the alpha angle (α). The DoP has been extensively used in the literature [10], [12], [56], and describes the degree of depolarization in the measured signal backscattered from a given surface element. The DoP has been extensively used in the literature (see, e.g., [10], [12], [56]). The χ feature is used in the $m - \chi$ (where m is DoP) decomposition [58], and this feature could help in distinguishing the even versus odd bounce scattering. If the open water and the oil slicks posses different scattering mechanisms, the resulting separability would be high for this feature. The features χ, μ_E, δ, and α are ratios of the Stokes parameters. In the two-scale Bragg model (see Section II), these features are independent of the ocean wave spectrum (the damping of the gravity-capillary waves by oil). This indicates that these features are the function of the dielectric constant, the incidence angle, and the large-scale roughness (see second frame in Table IV).

The hybrid-polarization power ratio is the ratio between the intensity of the simulated complex scattering coefficients in the RH and RV channels. Since the copolarization intensities have higher response than the cross-polarization intensity, the hybrid-polarization ratio is expected to have approximately the same behavior as the copolarization ratio discussed in Section V-A. Hence, this feature is also independent of the ocean wave spectrum. The standard deviation of the phase difference between the RH and RV scattering coefficients has been found to be a good feature for oil spill detection [10]. We also test the standard deviation of the phase difference between the RR and RL scattering coefficients.

The magnitude of the hybrid-polarization correlation coefficients are also considered, both in circular–linear and circular–circular basis, i.e., $\rho_{(\mathrm{RH,RV})}$ and $\rho_{(\mathrm{RR,RL})}$. $\rho_{(\mathrm{RR,RL})}$ was introduced in [10], and they named it the HP coherence measure. The authors in the same article demonstrated this feature on five Radarsat-2 scenes covering various types of oil. From the figures in [10], one can see that the low values of $\rho_{(\mathrm{RR,RL})}$ are present for the oil slick regions and high values for the open water areas, which is the same behavior as $\rho_{(\mathrm{CO})}$. We concluded that this feature could suppress some lookalikes caused by low wind and also generated good slick-sea contrast. Zhang *et al.* [9] also found the low values of $\rho_{(\mathrm{RH,RV})}$ for oil covered areas and high values for open water using both the L- and C-band SARs. These features are located in the last row of Table IV, where $\rho_{(\mathrm{RH,RV})}$ and $\rho_{(\mathrm{RR,RL})}$ are independent of the small-scale roughness, since these features are composed of ratios.

The conformity coefficient is a multipolarization feature containing both cross- and co-polarization intensities and correlation. The FP variant of this feature can be seen in Table III, and to calculate this feature, the reflection symmetry assumption must be made. Zhang *et al.* [46] stated that this feature can be used to distinguish different scattering mechanisms of ambient sea surfaces and slicks. They concluded that when μ was positive, Bragg scattering took place, and the pixels producing such values were classified as slick free area. Negative values was defined as non-Bragg scattering and thus classified as slick-covered areas. However, Minchew *et al.* [1] discovered that Bragg scattering was present within the slick-covered areas, and this feature might therefore not follow the theory suggested in [46] for separating the oil slicks from open water using the UAVSAR data. The conformity coefficients, $\rho_{(\mathrm{RH,RV})}$ and $\rho_{(\mathrm{RR,RL})}$, contain the ratios of scattering coefficients, and since the ocean wave spectrum is polarization

TABLE V

OVERVIEW OF THE INVESTIGATED HP (WITH RIGHT CIRCULAR TRANSMITS AND LINEAR RECEIVE) FEATURES (COMPUTED USING A MASK OF 15 × 60 PIXELS). THE REFERENCES INCLUDED ARE THE EXAMPLES OF STUDIES WHERE THE FEATURES HAVE BEEN INVESTIGATED FOR OIL SPILL OBSERVATION. THE "CIRCULAR-LINEAR" BASIS DENOTES THE HP FEATURES, WHILE THE "CIRCULAR–CIRCULAR" DENOTES THE HP FEATURES PROJECTED INTO THE CIRCULAR TRANSMIT AND CIRCULAR RECEIVE BASIS

HP Features (based on measuring RH and RV)	
Name	Formula
Stokes vector ([6] [56])	$\boldsymbol{q} = \begin{bmatrix} q_0 \\ q_1 \\ q_2 \\ q_3 \end{bmatrix} = \underset{\text{(circular-linear)}}{\begin{bmatrix} \langle \lvert S_{RH}\rvert^2 + \lvert S_{RV}\rvert^2 \rangle \\ \langle \lvert S_{RH}\rvert^2 - \lvert S_{RV}\rvert^2 \rangle \\ 2\Re\langle (S_{RH} S_{RV}^\star) \rangle \\ -2\Im\langle (S_{RH} S_{RV}^\star) \rangle \end{bmatrix}} = \underset{\text{(circular-circular)}}{\begin{bmatrix} \langle \lvert S_{RR}\rvert^2 + \lvert S_{RL}\rvert^2 \rangle \\ 2\Re\langle (S_{RR} S_{RL}^\star) \rangle \\ 2\Im\langle (S_{RR} S_{RL}^\star) \rangle \\ -\langle \lvert S_{RL}\rvert^2 - \lvert S_{RR}\rvert^2 \rangle \end{bmatrix}}$
Degree of polarization ([10] [12] [57])	$\text{DoP} = \frac{\sqrt{q_1^2+q_2^2+q_3^2}}{q_0}$
Ellipticity angle ([10] [57])	$\chi = \frac{1}{2}\sin^{-1}(-\frac{q_3}{DoP\ q_0})$
Relative phase ([7]) and alpha angle ([58])	$\delta = \frac{1}{2}\tan^{-1}(\frac{q_3}{q_2}) \quad \alpha = \frac{1}{2}\tan^{-1}(\frac{q_1+q_2}{q_3})$
Damping ratio	$\zeta_{ij} = 10\ \log_{10}\left(\frac{\langle I_{ij}^{(sea)}\rangle}{\langle I_{ij}^{(slick)}\rangle}\right)$, where $I_{ij} = \lvert S_{ij}\rvert^2$ $(i,j) \in (\underset{\text{(circular-linear)}}{(\text{R,H}) \vee (\text{R,V})}) \vee (\underset{\text{(circular-circular)}}{(\text{R,R}) \vee (\text{R,L})})$
Circular-polarization ratio ([9])	$\mu_E = \frac{q_0-q_3}{q_0+q_3}$ $\left(\text{also equal to: } \gamma_{RR/RL} = \frac{\langle I_{RR}\rangle}{\langle I_{RL}\rangle}\right)$
Hybrid-polarization power ratio ([35])	$\gamma_{RV/RH} = \frac{\langle I_{RV}\rangle}{\langle I_{RH}\rangle}$
Correlation coefficient ([10] [9])	$\rho_{(RH,RV)} = \frac{\lvert\langle S_{RH} S_{RV}^\star\rangle\rvert}{\sqrt{\langle \lvert S_{RH}\rvert^2\rangle\langle \lvert S_{RV}\rvert^2\rangle}}$ (circular-linear) $\rho_{(RR,RL)} = \frac{\lvert\langle S_{RR} S_{RL}^\star\rangle\rvert}{\sqrt{\langle \lvert S_{RR}\rvert^2\rangle\langle \lvert S_{RL}\rvert^2\rangle}}$ (circular-circular)
Standard deviation of the phase difference	$\phi_{(RH,RV)} = \sqrt{\langle(\phi_{RH} - \phi_{RV})^2\rangle + (\langle\phi_{RH} - \phi_{RV}\rangle)^2}$ (circular-linear) $\phi_{(RR,RL)} = \sqrt{\langle(\phi_{RR} - \phi_{RL})^2\rangle + (\langle\phi_{RR} - \phi_{RL}\rangle)^2}$ (circular-circular)
Eigenvalues	$\lambda_{1,2}^{HP} = q_0 \pm \sqrt{q_1^2 + q_2^2 + q_3^2}$
Entropy (wave entropy) ([9])	$H_w = -\sum_{i=1}^2 p_i \log_2 p_i, \qquad p_i = \frac{\lambda_i^{HP}}{\sum_{i=1}^2 \lambda_i^{HP}}$
Conformity coefficient ([10] [46])	$\mu_{HP} = \frac{2\Im\langle S_{RH} S_{RV}^\star\rangle}{\langle \lvert S_{RH}\rvert^2\rangle + \langle \lvert S_{RV}\rvert^2\rangle}$
Determinant of the covariance matrix	$\det(\boldsymbol{C}_{(RH,RV)}) = \det\left(\begin{bmatrix} \langle \lvert S_{RH}\rvert^2\rangle & \langle S_{RH} S_{RV}^\star\rangle \\ \langle S_{RV} S_{RH}^\star\rangle & \langle \lvert S_{RV}\rvert^2\rangle \end{bmatrix}\right)$ (circular-linear) $\det(\boldsymbol{C}_{(RR,RL)}) = \det\left(\begin{bmatrix} \langle \lvert S_{RR}\rvert^2\rangle & \langle S_{RR} S_{RL}^\star\rangle \\ \langle S_{RL} S_{RR}^\star\rangle & \langle \lvert S_{RL}\rvert^2\rangle \end{bmatrix}\right)$ (circular-circular)

independent, these features become independent of the ocean wave spectrum, as given in the second frame in Table IV.

The determinant of the simulated sample HP covariance matrix, both in the circular–linear and circular–circular basis, is also evaluated. We did not find studies related to these two features in the HP scenario. Unfortunately, the HP sample covariance matrix is 2-D, and the anisotropy is not available, since it requires the two minimum eigenvalues from a 3-D matrix. This is only possible if a reconstruction of a pseudo-FP covariance matrix is performed. The HP entropy (known as the wave entropy), however, can be calculated from the Stokes vector. This was done for an oil spill study in [9], and was found to have the same behavior as the FP entropy, that is, large for slick-covered areas and low for slick-free areas.

VI. RESULTS AND DISCUSSION

In Sections VI-A–VI-D, the results obtained from the analysis of the UAVSAR time series are presented. The simulated HP features are compared with the FP features in terms of slick detectability. The change in separability based upon the best FP and HP features as a slick evolves naturally on the sea surface is also discussed. The results obtained from the simulated HP features are also compared with the previous findings.

A. Noise Analysis

As is already known, the returns from the oil slicks are low, and hence, a noise analysis of the data used is important. The minimum backscattered signal that can be detected from a given surface element is dependent on the system's *noise floor*. The noise floor, related to the *noise equivalent sigma zero* (NESZ), is extremely low for the UAVSAR instrument (NESZ in the range of −48 to −33 dB [5]) compared with other sensors such as Radarsat-2 (NESZ in the range of −27.5 to −43 dB [59]) and TerraSAR-X (NESZ in the range of −19 to −26 dB [60]). Several studies of the effect

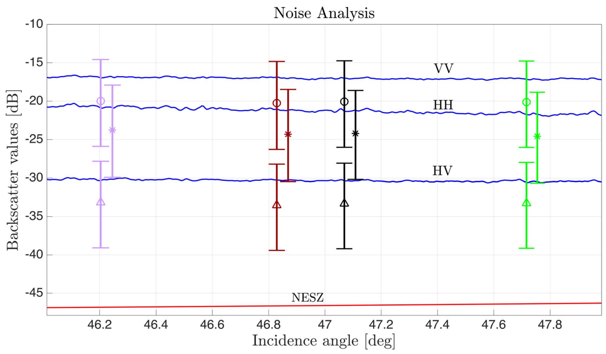

Fig. 6. Noise analysis from the UAVSAR scene taken at 06:26 UTC (ascending). The 5th, 50th, and 95th percentiles are calculated for each slick region, and plotted with a vertical line from the 5th to the 95th percentile, and a symbol indicating the 50th percentile: a circle for VV, a star for HH, and a triangle for HV. The lines for HH are slightly shifted to higher incidence angle to improve the discrimination in the plot. The blue continuous lines show the 50th percentile for clean sea samples selected along the range direction.

of the NESZ on radar-dark surfaces, such as oil slicks, have been conducted using spaceborne SAR sensors [2], [3], [61], and have shown that a large part of the cross-polarization return and also some part of the copolarization return from oil slicks are near or even below the instrument noise floor. RISAT-1 is the first spaceborne satellite that offers the circular or HP imaging mode. Unfortunately, the NESZ is high, -17 dB, for the RISAT-1 FRS-1 mode [62]. A consequence of returns below the NESZ is loss of information, and even though the slick can be detected through comparison with clean water signals above the NESZ, oil spill characterization may not be possible.

The NESZ for the UAVSAR varies between -48 dB at the point of maximal antenna gain and -33 dB in the far range [5]. Such a low NESZ is important for our application as our goal is analyzing the backscattered response from the various slicks, in addition to simulating the HP data from the FP data, resulting in a mix of co- and cross-polarization channels and a 3-dB power loss when simulating the HP scattering vector [8]. The HP intensities are still above the noise floor for all the UAVSAR scenes used in this analysis. We demonstrate this using one scene in Fig. 6, and the other scenes show a similar trend.

Fig. 6 shows an example of the noise analysis we performed. The 5th, 50th, and 95th percentiles of the HH, VV, and HV intensities are calculated for each region. No multilooking and incidence angle correction has been done prior to the noise analysis in order to show the characteristics of the different intensities of the actual measured values at the highest instrument resolution. The 50th percentiles are indicated by various symbols depending on the polarization used. The blue continuous lines show the 50th percentile for clean sea samples selected along the range direction for the three intensities. Following [1], an acceptable return was suggested to be 6 dB above the noise floor, i.e., 20% of the measured signal is noise, and 80% is the signal backscattered. The NESZ is indicated by the red continuous line in Fig. 6. The NESZ as a function of incidence angle is found in [5]. The HH intensities are slightly below the VV intensities but well above the NESZ + 6 dB limit. This is also the case for the other UAVSAR scenes used in this analysis. Hence, the noise should not have a significant impact on the various polarimetric features extracted from the UAVSAR scenes. Similar results are found in [19] for one UAVSAR acquisition from the NORSE2015 experiment.

B. Slick Separability Based on FP and HP Features

The polarimetric feature values are calculated for each region (different slicks and open water), and their statistical properties used as an input in the calculation of the JM separability measure. Figs. 7–10 show the charts of the mean JM separability for all of the polarimetric features for slick versus open water. The separability between the various slicks is not shown, because the JM separability is below 0.6 for all cases. Note that the JM separability is calculated between each slick and its corresponding subset of open water regions (as shown in Fig. 5). This result in several JM distances, and the average of these are shown in the color charts in Figs. 7–10. Due to space limitation, the standard deviation of the JM measures is left out, but these are shown later for the features with the maximum JM separability. Note that the features in the color charts are sorted so that the JM separability decreases from the top of the chart to the bottom. In Figs. 7–10, the red color indicates the highest separability between the slick and the open water. Red, orange, yellow, green, dark, and light blue colors indicate separability, in decreasing order. Using color charts, we obtain a good overview of all the polarimetric features, and can more easily identify the best ones.

The FP color chart in Fig. 7, representing the average separability between PO and the OW regions, is the one that contains highest separability for the various features along the time series compared with the other emulsion slicks and open water (both for FP and HP). The FP features that provide high separability between the PO and open water are ζ_X (damping ratio) with seven red and ten orange cells along the time series, and second is the λ_3 (minimum eigenvalue) with nine red and seven orange cells. In other words, using the ζ_X feature, the PO can be differentiated from open water in 17 out of 18 scenes with relatively high separability.

These two features are also among the best at providing high separability for the emulsion slicks. Considering the FP separability color charts for E40, both the ζ_X and λ_3 features give high separability for three scenes in the times series. For the two first scenes, several FP features can be used to distinguish either E40 or E60 from the open water regions. The E40 has high separability (JM > 0.8) in 8 out of 18 scenes using various features, while the E60 has high separability in 9 out of 18 scenes. The ζ_{VV} and the PF features provide higher detectability of E60 than E40. The FP color chart representing the separability between E80 and OW is shown in Fig. 10. Here, the first acquisition at 05:32 UTC is not included, because this oil had not been released. This color chart contains several orange cells, more than the E40 and E60 FP color charts, which indicates higher overall detectability of E80 than E60 and E40. Again, ζ_X and λ_3 stand out, followed

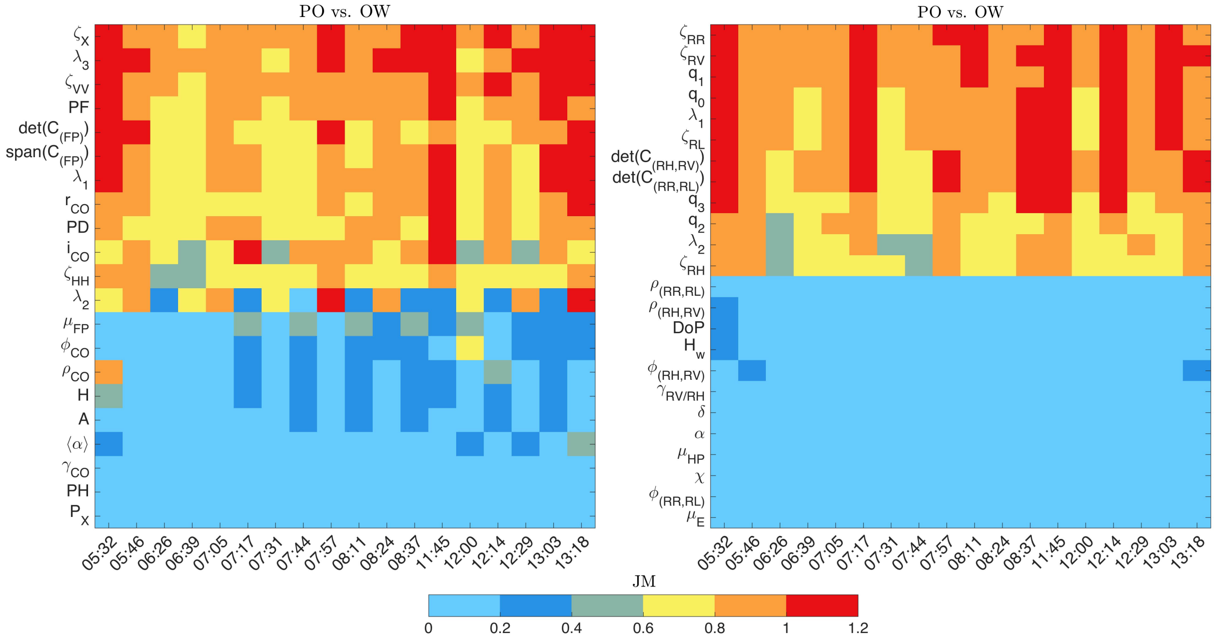

Fig. 7. Color charts of the JM separability between PO and OW for the FP (left chart) and the HP (right chart) features. Red, orange, yellow, green, dark, and light blue indicate separability, in decreasing order. The x-axis represents the acquisition time (in UTC).

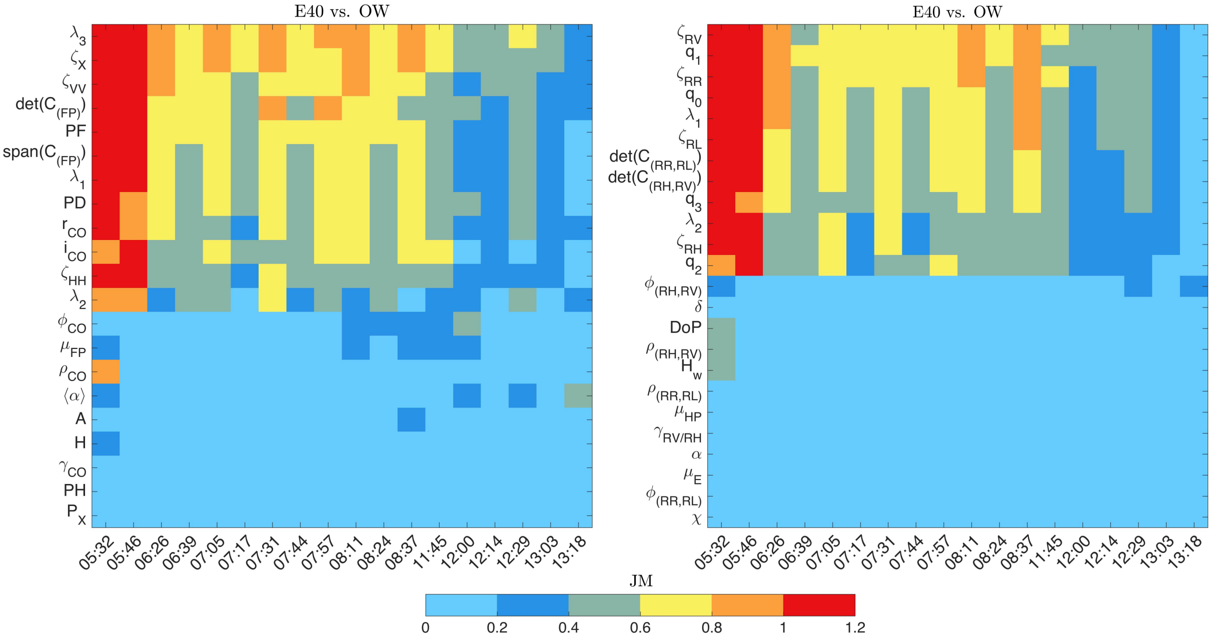

Fig. 8. Color charts of the JM separability between E40 and OW for the FP (left chart) and the HP (right chart) features. Red, orange, yellow, green, dark, and light blue indicate separability, in decreasing order. The x-axis represents the acquisition time (in UTC).

by det($\boldsymbol{C}_{(\mathrm{FP})}$), PF, and PD. A more in-depth analysis of how the JM changes with time for the various oil slicks is given in Section VI-C. The FP features that are not able to separate the various slicks from open water are γ_{CO}, P_X, ϕ_{CO}, ρ_{CO}, PH, μ_{FP}, H, $\langle\alpha\rangle$, and A, according to the threshold that is set for the JM distance. One previous study related to the use of UAVSAR L-band for oil spill observation (Deepwater Horizon oil spill) was presented in [1]. Minchew *et al.* [1] discovered that $\langle\alpha\rangle$ was sensitive to the change in the dielectric constant rather than damping of the ocean waves. To detect the oil using $\langle\alpha\rangle$,

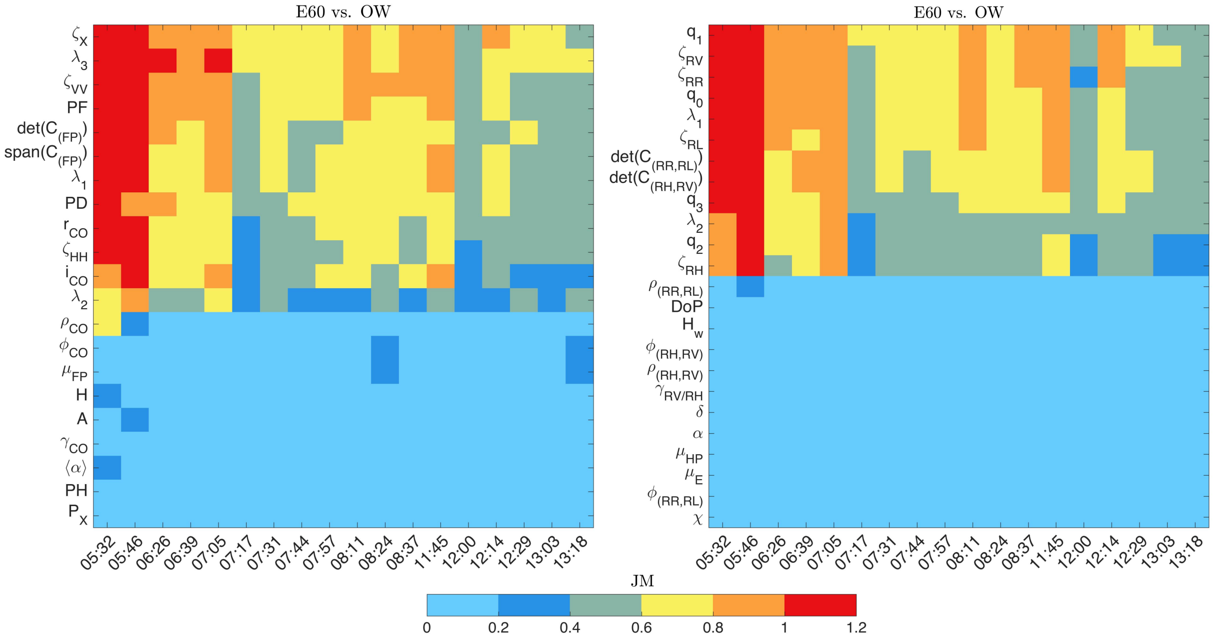

Fig. 9. Color charts of the JM separability between E60 and OW for the FP (left chart) and the HP (right chart) features. Red, orange, yellow, green, dark, and light blue indicate separability, in decreasing order. The x-axis represents the acquisition time (in UTC).

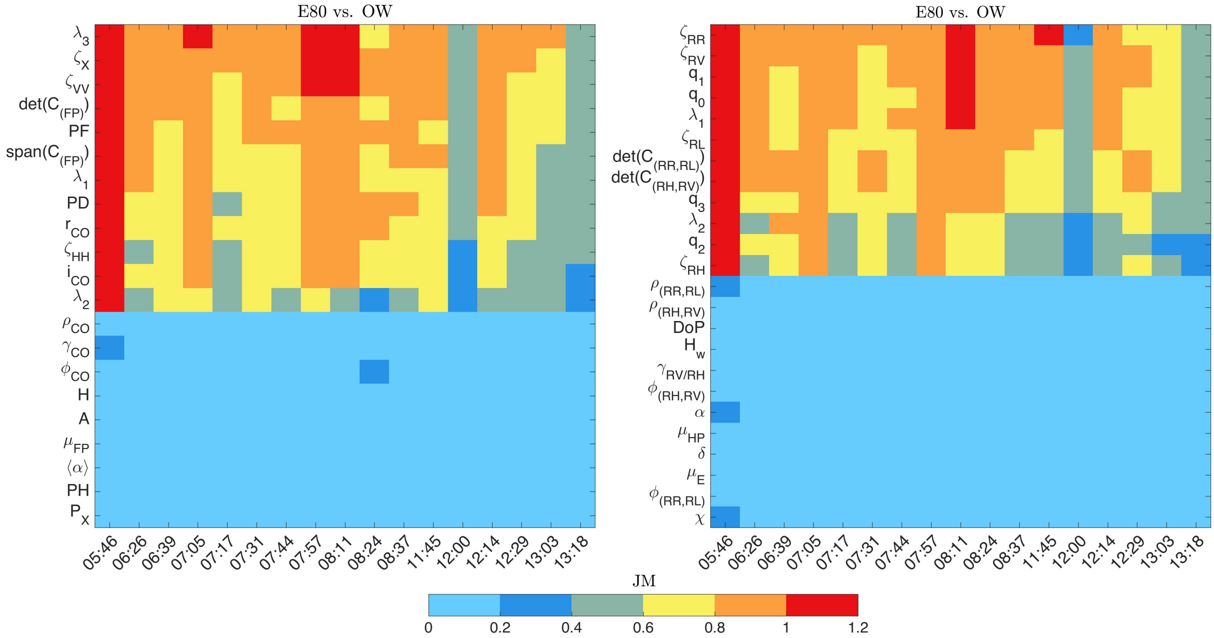

Fig. 10. Color charts of the JM separability between E80 and OW for the FP (left chart) and the HP (right chart) features. Red, orange, yellow, green, dark, and light blue indicate separability, in decreasing order. The x-axis represents the acquisition time (in UTC).

it is required that the oil must mix with the ocean to create an intermediate dielectric layer and/or the oil slick is sufficient thick enough (see Section I). The low separability values of $\langle\alpha\rangle$ in our case might indicate that such a layer was not presented. Minchew *et al.* [1] also discovered, based on the entropy (H), that both the oil slicks and open water had one dominant scattering mechanism, namely, the Bragg scattering. Therefore, it is challenging to use the entropy to separate the oil slicks from the clean sea, as the same scattering characteristics might be present. Although it has been suggested that the entropy is sensitive to slick-covered surfaces (high entropy for slick-covered surface and low entropy for slick-free surface) in several studies using spaceborne SAR data under various wind conditions [32], [45], [48], [51], this is not the case for our data set. The set of features that are incapable of separating the four oil slicks from the open water region are all located in the bottom panel in Table IV. The top best features for detecting the various oil slicks are located in the top panel in Table IV. This indicates that the features independent on the small-scale roughness show poor detection capabilities, while features containing the small-scale roughness show good detectability.

Previous studies have found that $\det(\boldsymbol{C}_{(\mathrm{FP})})$ (only using co-polarization products) and r_{CO} are best at distinguishing biogenic slicks from mineral oil under low wind conditions, in this case using Radarsat-2 C-band data [2]. $\det(\boldsymbol{C}_{(\mathrm{FP})})$ and r_{CO} in our case have JM above 0.5 in all scenes, but they do not separate as well as the ζ_X and λ_3 features. The same study [2] did exclude features that contained the cross-polarization scattering coefficients, because they had a large part of the signal below the noise floor. Using the UAVSAR data, the noise is no longer an issue for the cross-polarization scattering components, and we are now able to see the usefulness of the cross-polarization feature, for example, the high separability of the ζ_X and λ_3 features. The reasons why the cross-polarization feature is the best for detecting the oil should be further investigated. One theory could be that the cross-polarization intensity is closer to the noise floor compared with the copolarization intensities. Other theories could be related to the depolarization effects caused by the dielectric properties within the oil or that the tilt angles are larger for high wind conditions. The good potential of the cross-polarization feature was also highlighted using UAVSAR data from the Deepwater Horizon oil spill [1], and also in one of the UAVSAR scenes from the NORSE2015 experiment [63].

The right panels in Figs. 7–10 show the color charts for the HP features along the time series. Fewer red colored cells are observed for the PO versus OW HP color chart compared with the PO versus OW FP color chart. Unfortunately, the polarimetric features containing the cross-polarization component are no longer possible to separate out in the HP mode. The HP features that have high separability between PO and OW, in decreasing order, are ζ_{RR}, ζ_{RV}, q_1, q_0, λ_1, ζ_{RL}, $\det(\boldsymbol{C}_{(\mathrm{RH,RV})})$, $\det(\boldsymbol{C}_{(\mathrm{RR,RL})})$, and q_3, respectively. The same features also provide high separability for the emulsion slicks. The HP features that are comparable with the FP features show similar colors of the JM separability, for example, ζ_{RV} and ζ_{RH} show similar separability values as ζ_{VV} and ζ_{HH} for all the various slicks. $\gamma_{\mathrm{RV/RH}}$, $\phi_{(\mathrm{RH,RV})}$, $\phi_{(\mathrm{RR,RL})}$, $\rho_{(\mathrm{RR,RL})}$, $\rho_{(\mathrm{RH,RV})}$, μ_{HP}, H_w, DoP, χ, and μ_E are features that achieve low separability between the various slicks and open water for all the UAVSAR scenes. This corresponds well with the setup in Table IV, where the features resulting in high separability are dependent on, amongst other, the small-scale roughness, and the features showing low separability are independent of this factor. This was also found for the corresponding FP features, namely, γ_{CO}, ϕ_{CO}, μ_{FP}, and H. Hence, we are left with 12 HP features that perform reasonably well at separating the various oil types from the open water regions. For the emulsions slicks, the E40 versus OW HP color chart has the minimum number of orange colored cells, followed by E60 versus OW and E80 versus OW HP color charts. This is the same behavior as the FP color charts for the emulsion slicks.

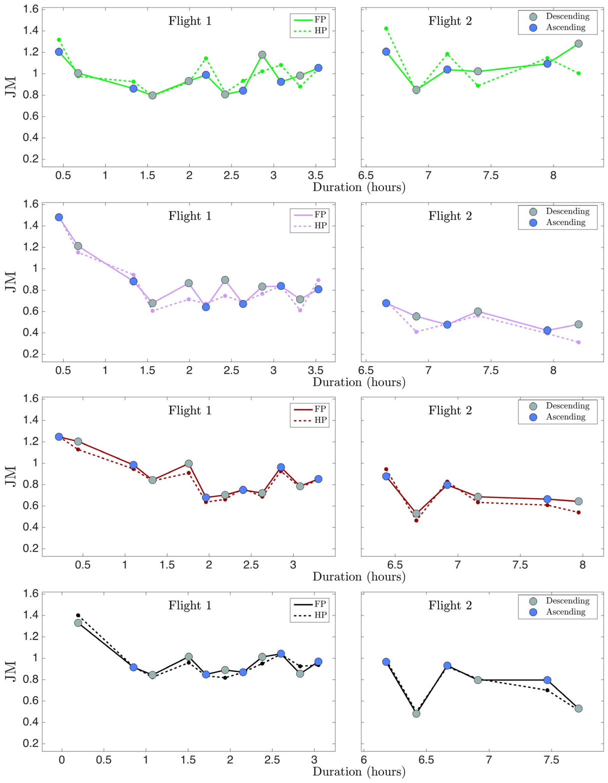

Fig. 11. Maximum JM distance obtained from all the polarimetric features along the time series. The points represent the maximum mean JM distance, and the solid (dashed) lines represent the values between these for the FP (HP) features. The green, pink, red, and black colors represent the JM separability between the PO versus OW, E40 versus OW, E60 versus OW, and E80 versus OW. The blue and gray markers represent the ascending and descending scenes.

Previous studies related to the HP features simulated from spaceborne FP SAR have obtained different results. Salberg *et al.* [10] used the same data set as [2], and discovered that $\rho_{(\mathrm{RR,RL})}$ (Salberg *et al.* [10] named this feature Coh), the conformity index μ_{HP}, and the DoP can be used to detect various types of oil (plant, emulsion, and crude oil), using C-band data under low-to-moderate wind condition. Nunziata *et al.* [9] concluded based on L- and C-band spaceborne SAR data that the wave entropy (H_w), circular-polarization ratio (μ_E), $\rho_{(\mathrm{RR,RL})}$, and the relative intensity of the polarized component to the intensity of the total field could discriminate slick-free, weak-damping slick covered, and strong-damping slick-covered sea surfaces. Additionally, [64] also concluded that the DoP could be used to detect the oil spills from the ocean surface using both C-band SAR and L-band UAVSAR data. The separability observed in our color charts do not agree with the findings in [9], [10], and [65], which may be due to several factors, including the high wind, the small slicks, and the fact that the data used in this paper are well above the noise floor.

The highest JM separabilities obtained from both the FP and HP features across the entire UAVSAR time series are shown in Fig. 11. The green, pink, red, and black colors represent the highest mean JM separability for the PO versus OW, E40 versus OW, E60 versus OW, and E80 versus OW, respectively. The FP and HP features that provide the highest mean JM and the corresponding standard deviation of the JM between the slick and the open water regions (see Fig. 5) are given in Table VI. Note that the feature for which the JM separability is highest can change as the slick evolves. For comparison, the highest JM separability obtained using the HP features is plotted as a dashed line in the same figure as the highest JM separability using the FP features. The x-axis represents the time since release of each slick, not the time since the first image was acquired. Because the slicks were not all released simultaneously, the x-axis is shifted for each of the slicks. The UAVSAR time series was collected in two flights, and hence, each panel in Fig. 11 is divided into two subplots. Additionally, the difference between the ascending and the descending scenes are marked with green and gray colored dots.

There are two ways to evaluate the information in Table VI and Fig. 11. The first is to study how the separability between the various slicks and the open water regions varies with time and how the weathering process of the emulsion and PO slicks affects the detectability. The second way is to identify the polarimetric features that give the highest JM separability as a function of time for the various slicks. Each of these two evaluations will be discussed in Sections VI-C and VI-D.

C. Separability as a Function of Time

The first flight covers approximately the first 4 h after release, while the second flight covers approximately 6.5–8.5 h following release of the oils, with some variation, because the PO was released first and the E80 last. From Fig. 11, we find that the JM separability between the PO and the open water regions starts off at 1.2 and then decreases over the next 2 h. The separability increases again during the next half an hour. During the remaining hours of flight 1, the separability fluctuates, and in the last hour of flight 2, the separability increases again. From the intensity images in Fig. 1, the PO reaches an equilibrium in terms of shape and size in the beginning of flight 2 and remains visible throughout the time series.

The separability of the emulsion oils from the open water regions generally decreases with time with some fluctuations along the way. The separability is higher between the E80 and the open water regions along the time series compared with the other emulsion slicks. This might be a result of the higher oil fraction in E80 compared with E60 and E40. The viscosities of the emulsion slicks are characterized by higher viscosity than the natural film [65]. Hence, the emulsion slicks should have a stronger damping of the ocean waves and thus be more detectable than the PO. Both Figs. 7 and 11 show that this is not the case, and the PO is visible longer on the sea surface than the emulsion slicks. Hence, the PO compound used, Radiogreen EBO, might therefore not be a good indicator for simulating biogenic slicks, as already stated in [20].

It is challenging to segment out the emulsion slicks for the UAVSAR scenes in flight 2, which results in higher presence of the open water in these segments. This might be because of the emulsion slicks have a higher area and higher westerly extent than the PO (see Fig. 1). Immediately after release, the emulsion slicks might undergo emulsification, i.e., take in additional water molecules into the oil–water mix [66]. Hence, more water can be mixed with the E80, and higher volume over time. Parts of the oil spill might also break up into drops of varying sizes that are mixed down into the water column (dispersion), and the oil droplets might also resurface. A parallel study investigated the oil slicks' drift using two different oil drift models [20]. The model results indicated that the PO entrained more quickly and deeper into the water column compared with the emulsion slicks. Additionally, the PO droplets resurfaced to maintain the observable slick. As a result of the entrainment into the water column, the PO was shielded from the wind drag and Stokes drift, which resulted in longer visibility on the sea surface compared with the emulsion slicks. The same study also compared the E80 slick with the model simulations, and the model results showed that the simulated E80 had $\sim$50% or more of the oil on the surface throughout the simulation, and relatively little penetrated deeper than 10 m. Hence, the emulsion slicks are more exposed to wind drag and Stokes drift, which results in more spreading than the PO experienced.

The separability as a function of time can be affected by several factors, which include the imaging geometry (the difference between ascending and descending), changing wind and ocean state over the time series, weathering processes, and the accuracy of the segmentation for all the scenes. The incidence angle of the PO within the scene varies across the times series (see Fig. 2). The incidence angle has a higher variation in flight 2 scenes compared with flight 1 scenes, which might be the reason for the fluctuations in the separability between the descending and ascending scenes in flight 2. In the Appendix, the incidence angle correction applied to the complex scattering vector in the preprocessing of the UAVSAR scenes was discussed. The fact that the incidence angle affects the separability of the PO might be a result of the texture variation with incidence angle (which is not corrected for), and difference in the imaging geometry between ascending and descending. Finding the best incidence angle correction method that can allow comparison across several scenes (especially the ascending and descending in our case) with slightly different incidence angle is a study in itself and should be further investigated.

The PO is released to simulate biogenic slicks, and the biogenic slick forms a monomolecular layer [67]. Previous studies have found that biogenic surface films disappear in high wind condition (typically above 7–10 m/s) due to entrainment into the underlying water by the breaking waves [16], [67]. The reader is referred to [20] for additional information on how the various oil slicks were transported. In addition, a study on how the polarimetric features are affected by the imaging geometry is on-going.

TABLE VI

MEAN AND STANDARD DEVIATION OF THE JM FROM THE BEST FP (TOP) AND THE BEST HP (BOTTOM) FEATURE ALONG THE TIME SERIES FOR THE VARIOUS OIL SLICKS AND THE OPEN WATER REGIONS

Time (UTC)	PO vs. OW	E40 vs. OW	E60 vs. OW	E80 vs. OW
05:32	ζ_{VV} (1.2 ± 0.1) ζ_{RV} (1.32 ± 0.12)	λ_3 (1.48 ± 0.08) ζ_{RV} (1.49 ± 0.1)	λ_3 (1.25 ± 0.07) ζ_{RV} (1.25 ± 0.09)	ζ_{VV} (0.93 ± 0.1) ζ_{RR} (1.15 ± 0.15)
05:46	λ_3 (1.01 ± 0.11) $\det(C_{(RH,RV)})$ (0.98 ± 0.1)	λ_3 (1.21 ± 0.07) $\det(C_{(RH,RV)})$ (1.15 ± 0.07)	ζ_X (1.2 ± 0.04) ζ_{RR} (1.13 ± 0.07)	$\det(C_{(FP)})$ (1.33 ± 0.07) $\det(C_{(RR,RL)})$ (1.4 ± 0.11)
06:26	ζ_{VV} (0.86 ± 0.06) ζ_{RV} (0.93 ± 0.1)	λ_3 (0.88 ± 0.07) q_1 (0.94 ± 0.1)	λ_3 (0.98 ± 0.06) q_1 (0.95 ± 0.07)	λ_3 (0.92 ± 0.07) ζ_{RR} (0.92 ± 0.08)
06:39	λ_3 (0.8 ± 0.1) q_1 (0.79 ± 0.1)	ζ_X (0.68 ± 0.08) q_1 (0.61 ± 0.09)	ζ_{VV} (0.84 ± 0.06) ζ_{RR} (0.83 ± 0.08)	λ_3 (0.84 ± 0.09) $\det(C_{(RR,RL)})$ (0.82 ± 0.12)
07:05	$\det(C_{(FP)})$ (0.93 ± 0.12) ζ_{RR} (0.92 ± 0.14)	λ_3 (0.86 ± 0.12) $\det(C_{(RH,RV)})$ (0.71 ± 0.12)	λ_3 (1 ± 0.12) $\det(C_{(RR,RL)})$ (0.91 ± 0.12)	λ_3 (1.01 ± 0.1) ζ_{RR} (0.96 ± 0.11)
07:17	i_{CO} (0.99 ± 0.08) ζ_{RR} (1.14 ± 0.07)	ζ_X (0.64 ± 0.13) q_1 (0.67 ± 0.09)	λ_3 (0.68 ± 0.13) q_1 (0.64 ± 0.13)	λ_3 (0.85 ± 0.12) q_1 (0.83 ± 0.14)
07:31	ζ_X (0.81 ± 0.06) q_1 (0.82 ± 0.13)	λ_3 (0.89 ± 0.07) $\det(C_{(RH,RV)})$ (0.75 ± 0.11)	λ_3 (0.7 ± 0.07) q_1 (0.66 ± 0.08)	ζ_X (0.89 ± 0.04) $\det(C_{(RH,RV)})$ (0.82 ± 0.09)
07:44	ζ_X (0.84 ± 0.06) ζ_{RR} (0.93 ± 0.13)	ζ_X (0.67 ± 0.06) q_1 (0.69 ± 0.09)	ζ_X (0.75 ± 0.05) q_1 (0.76 ± 0.1)	ζ_X (0.87 ± 0.05) q_1 (0.87 ± 0.04)
07:57	λ_3 (1.18 ± 0.06) $\det(C_{(RR,RL)})$ (1.02 ± 0.1)	λ_3 (0.83 ± 0.06) ζ_{RR} (0.77 ± 0.1)	ζ_{VV} (0.72 ± 0.06) q_1 (0.69 ± 0.08)	λ_3 (1.01 ± 0.05) ζ_{RR} (0.95 ± 0.1)
08:11	ζ_{VV} (0.92 ± 0.1) ζ_{RR} (1.08 ± 0.09)	λ_3 (0.84 ± 0.12) ζ_{RR} (0.84 ± 0.12)	λ_3 (0.96 ± 0.11) q_1 (0.93 ± 0.12)	λ_3 (1.04 ± 0.1) ζ_{RV} (1.04 ± 0.1)
08:24	λ_3 (0.98 ± 0.06) q_1 (0.88 ± 0.09)	λ_3 (0.71 ± 0.06) q_1 (0.61 ± 0.08)	ζ_{VV} (0.79 ± 0.06) q_1 (0.77 ± 0.07)	ζ_{VV} (0.85 ± 0.05) ζ_{RV} (0.92 ± 0.08)
08:37	ζ_X (1.05 ± 0.08) q_0 (1.04 ± 0.15)	λ_3 (0.81 ± 0.09) ζ_{RV} (0.89 ± 0.16)	λ_3 (0.85 ± 0.09) ζ_{RV} (0.84 ± 0.09)	λ_3 (0.97 ± 0.07) q_1 (0.94 ± 0.07)
11:45	ζ_{VV} (1.21 ± 0.08) ζ_{RR} (1.42 ± 0.13)	ζ_X (0.68 ± 0.08) ζ_{RR} (0.7 ± 0.16)	ζ_X (0.88 ± 0.07) ζ_{RR} (0.94 ± 0.12)	λ_3 (0.97 ± 0.08) ζ_{RR} (0.98 ± 0.14)
12:00	ζ_X (0.85 ± 0.06) q_1 (0.83 ± 0.08)	λ_3 (0.55 ± 0.07) q_1 (0.41 ± 0.1)	λ_3 (0.53 ± 0.06) ζ_{RV} (0.46 ± 0.11)	ζ_X (0.48 ± 0.07) ζ_{RV} (0.5 ± 0.1)
12:14	ζ_X (1.04 ± 0.05) ζ_{RV} (1.18 ± 0.07)	ζ_X (0.48 ± 0.05) ζ_{RV} (0.48 ± 0.09)	ζ_X (0.8 ± 0.06) ζ_{RR} (0.83 ± 0.06)	λ_3 (0.93 ± 0.06) q_1 (0.92 ± 0.08)
12:29	λ_3 (1.02 ± 0.07) q_1 (0.89 ± 0.1)	λ_3 (0.6 ± 0.08) q_1 (0.56 ± 0.11)	λ_3 (0.69 ± 0.08) $\det(C_{(RR,RL)})$ (0.63 ± 0.06)	λ_3 (0.8 ± 0.08) $\det(C_{(RH,RV)})$ (0.81 ± 0.1)
13:03	ζ_X (1.09 ± 0.07) ζ_{RV} (1.15 ± 0.15)	ζ_X (0.42 ± 0.09) ζ_{RV} (0.39 ± 0.11)	ζ_X (0.66 ± 0.09) ζ_{RV} (0.61 ± 0.14)	λ_3 (0.8 ± 0.09) q_1 (0.7 ± 0.15)
13:18	λ_3 (1.28 ± 0.06) $\det(C_{(RH,RV)})$ (1 ± 0.09)	μ_C (0.78 ± 0.32) $\phi_{(RH,RV)}$ (0.31 ± 0.36)	λ_3 (0.64 ± 0.07) q_1 (0.54 ± 0.08)	λ_3 (0.53 ± 0.07) q_1 (0.51 ± 0.03)

D. Polarimetric Features With the Highest Separability

The highest JM separability between the slicks and the open water regions (see Table VI) is provided by λ_3, ζ_{VV}, $\det(\boldsymbol{C}_{(\mathrm{FP})})$, PD, $\mathrm{span}(\boldsymbol{C}_{(\mathrm{FP})})$, and ζ_X in FP. λ_3 is the feature that provides the highest JM separability most frequently. The majority of the mean JM is around 0.9–1.1, while the standard deviation is around 0.1, which indicates that the JM has a small variation within the open water subsets that are used. The best polarimetric FP features, i.e., λ_3, ζ_{VV}, $\det(\boldsymbol{C}_{(\mathrm{FP})})$, and ζ_X, were also evaluated as a function of time. All showed a similar trend with time as in Fig. 11, but are left out due to space limitation. The best HP features to detect the various oil slicks are ζ_{RR}, ζ_{RV}, $\det(\boldsymbol{C}_{(\mathrm{RH,RV})})$, $\det(\boldsymbol{C}_{(\mathrm{RR,RL})})$, q_0, and q_1, and they all have a similar separability trend as a function of time to the best FP features. ζ_{RV} and ζ_{RR} are the HP features that provide the highest JM separability along the time series.

Overall, the best FP features are 0.6% better for detecting the E80 compared with the simulated HP features. For E60 and E40, the best FP features are 1.6% and 3.3% better than the HP features for detection. However, for the detection of the PO, the best HP features showed 0.8% better detection ability compared with the FP.

VII. CONCLUSION

A comparison between FP and simulated HP data from a UAVSAR time series of recently released and evolving oil slicks has been presented. The relative performance of FP and simulated HP in slick detection capability using a wide range of polarization-dependent features has been carefully evaluated using the JM separability.

Overall, the FP features were estimated to be 0%–3.3% better at distinguishing the various emulsion oil slicks from the ambient sea surface compared with the simulated HP features, while the best simulated HP features were 0.8% better than the FP features to distinguish the PO from the open water region. The best HP features show lower separability than the best FP features in the end of the ~8 h time series compared with the beginning for the emulsion slicks. The FP features containing the cross-polarization scattering component are found to be best at distinguishing the various slicks from open water, and however, these cross-polarization features are not possible to isolate when using the HP mode. ζ_{RR}, ζ_{RV}, q_1, and q_0 are good alternatives to separate the slicks from the open water regions using the HP mode. High separability values between the oil slicks and the open water were also obtained using det($\boldsymbol{C}_{(\mathrm{RH,RV})}$) and det($\boldsymbol{C}_{(\mathrm{RR,RL})}$), and their potential should be further investigated for other types of oil under various wind and ocean conditions. Overall, the best FP features are ζ_X, det($\boldsymbol{C}_{(\mathrm{FP})}$), λ_3, and ζ_{VV}.

This paper reveals a high correspondence between the results and the scattering theory of the two-scale Bragg model. All the features that showed poor detectability of the oil slicks are independent of the ocean wave spectrum (the small-scale roughness), while the features resulting in good separability were dependent, amongst other factor, on the ocean wave spectrum.

This paper highlights the importance of performing an incidence angle correction on the complex scattering vector prior to segmentation.

In general, the PO has the highest detectability across the full time series for both the FP and the HP modes, and its detectability does not decrease at the end of the UAVSAR time series, as is the case for the emulsion slicks. It was not possible to discriminate the PO from the emulsion slicks, which might be a result of the high wind and the relatively small volume of the released oils.

Our findings suggest that a similar slick-sea separability performance can be achieved using either HP or FP data at high wind conditions and for small slicks in volume. However, this paper should be repeated for data collected in other wind conditions and for various oil thicknesses. Further investigation should be conducted to determine whether real HP data could achieve the same results as both the FP and simulated HP data. Real HP data would reduce complexity (compared with the FP mode) of the sensor in terms of average power, on-board mass, and data volume, and provide more design flexibility.

APPENDIX
INCIDENCE ANGLE CORRECTION

The UAVSAR instrument images at incidence angles between 20° and 65° [5], and the ocean backscatter is known to decrease with increasing incidence angle. The oil slick regions in the UAVSAR time series are selected based on a segmentation method that is discussed in Section IV-C. The intensity variation related to incidence angle can be larger than the intensity difference between the classes, and hence, the oil slicks might be neglected in the original segmentation. Furthermore, the oil slicks spread out in the range direction with time, increasing the incidence angle span across the slicks. Hence, the effects from the incidence angle on the output regions are more significant in the last passes of the UAVSAR time series when the slicks have spread out. Therefore, to avoid the incidence angle effect dominating the segmentation, and to allow incidence angle independent comparison across the time series, an incidence angle correction is performed on the scattering vector prior to multilooking, segmentation, and feature computation. The incidence angle correction is obtained from the following expression [68]:

$$\boldsymbol{S}(\theta) = \boldsymbol{S}'\sqrt{\frac{\sin(\theta)}{\sin(\theta_{ref})}} \implies \boldsymbol{S}' = \boldsymbol{S}(\theta)\sqrt{\frac{1}{\gamma(\theta)}} \tag{22}$$

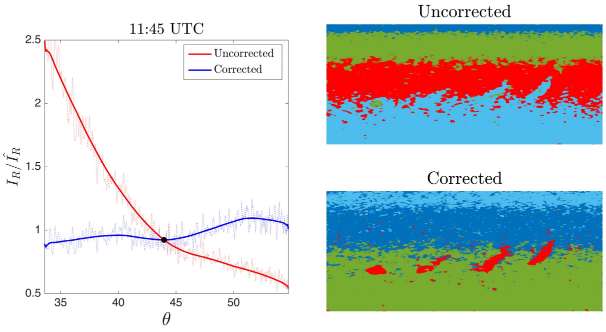

Fig. 12. Illustration of the incidence angle correction applied to the UAVSAR scene acquired at 11:45 UTC. (Left) Smoothed mean VV-intensity profiles normalized to the mean of the span profile using the clean sea region before (red line) and after correction (blue line). Dotted lines: unsmoothed mean intensity profiles. Black marker: reference level, i.e., the mean of the span along the range direction. (Right) Results of the segmentation with and without incidence angle correction. Colors: various output segments.

where $\boldsymbol{S}(\theta)$ is the measured scattering vector dependent on the incidence angle, θ is the incidence angle, θ_{ref} is the reference angle, $\boldsymbol{S}'$ is the corrected scattering vector independent of the incidence angle, and $\gamma(\theta)$ is the $((\sin(\theta))/(\sin(\theta_{\mathrm{ref}})))$ fraction. Because we are dealing with the complex scattering vector, rather than intensities, the square root is applied. Range and incidence angle are related in a one-to-one correspondence, and hence, $\gamma(r)$ rather than $\gamma(\theta)$ is used.

To preserve the polarimetry in the data, the same $\gamma(r)$ value should be used when correcting the different complex scattering components, i.e., S_{HH}, S_{HV}, and S_{VV}. Selecting different $\gamma(r)$ values for each complex scattering component could influence the various multivariate polarimetric features, such as the determinant of the covariance matrix. Rather than determining the relation between range and incidence angle, we estimate $\gamma(r)$ empirically from the span of the intensities (span $= I_{\mathrm{HH}} + I_{\mathrm{VV}} + I_{\mathrm{HV}}$) by considering a region of clean water (no ships nor oil slicks), and assuming that this region is homogenous and has no texture. For this paper, the region along the range direction was selected from the span, and contained 1000 pixels in the azimuth direction. An intensity profile ($I_{\mathrm{Rg}}^{\mathrm{span}}$) from the span was created by taking the average of that region, and these values were further smoothed in the range direction. The reference level was chosen to be the mean value of the total power along the range direction ($\hat{I}_{\mathrm{Rg}}^{\mathrm{span}}$). $\gamma(r)$ can be estimated as

$$\gamma(r) \approx \frac{I_{Rg}^{\mathrm{span}}}{\hat{I}_{Rg}^{\mathrm{span}}}. \tag{23}$$

Fig. 12 shows the incidence angle correction applied to an ascending UAVSAR scene. The blue line is the corrected smoothed mean VV-intensity along the range direction (normalized to the mean intensity value), and the dashed blue line is the unsmoothed corrected mean intensity value along the range direction, also normalized. Here, we use the incidence angle (covering the location of the oil slicks) on the x-axes. The red line is the smoothed uncorrected mean VV-intensity profile, and the dashed red line is the unsmoothed version of that profile. Only the VV-intensity is used to demonstrate this, but the same behavior was observed for the

HH and HV intensities. After applying this correction method, the incidence angle dependence of the scattering components is reduced.

The corrected intensity profile is not a perfectly flat curve in any of the individual channels, which might be because they are corrected based on span, and the visible polarimetric variation indicates that there is some local variations.

From visual inspection of the right panel in Fig. 12, it is clear that the intensities are significantly affected by the incidence angle. One example of how the incidence angle effects the segmentation results is also shown in Fig. 12. Here, the top-right figure displays the results of the segmentation using uncorrected data as input, while the bottom-right image is when the incidence angle correction is applied prior to the segmentation method. Clearly, the segmentation method did not successfully locate the oil slicks in the uncorrected case. However, if the corrected data are used, the segmentation algorithm successfully identifies the oil slicks. These segmentation results highlight how important it is to perform the incidence angle correction prior to segmentation. This correction is done on all the UAVSAR scenes prior to segmentation and feature computation.

Calculating the intensity values from the corrected scattering vector yields an approximation of the damping ratio. This is because the entire intensity image is normalized using the mean of a chosen open water region ($I_{\mathrm{Rg}}^{\mathrm{span}}$). The corrected intensities are named damping ratios (see Tables III and V), and are labeled ζ, for example

$$\zeta_{\mathrm{VV}} = \left\langle \left| S'_{\mathrm{VV}} \right|^2 \right\rangle \tag{24}$$

where $\langle\cdot\rangle$ represents the averaging (multilooking).

ACKNOWLEDGMENT

The authors would like to thank NOFO for hosting NORSE2015 and MET Norway for collecting the meteorological and ocean observations. They would also like to thank the reviewers for their useful comments and suggestions. UAVSAR data are the courtesy of NASA/JPL Caltech.

REFERENCES

[1] B. Minchew, C. E. Jones, and B. Holt, “Polarimetric analysis of backscatter from the deepwater horizon oil spill using L-band synthetic aperture radar,” *IEEE Trans. Geosci. Remote Sens.*, vol. 50, no. 10, pp. 3812–3830, Oct. 2012.

[2] S. Skrunes, C. Brekke, and T. Eltoft, “Characterization of marine surface slicks by Radarsat-2 multipolarization features,” *IEEE Trans. Geosci. Remote Sens.*, vol. 52, no. 9, pp. 5302–5319, Sep. 2014.

[3] S. Skrunes, C. Brekke, T. Eltoft, and V. Kudryavtsev, “Comparing near-coincident C- and X-band SAR acquisitions of marine oil spills,” *IEEE Trans. Geosci. Remote Sens.*, vol. 53, no. 4, pp. 1958–1975, Apr. 2015.

[4] M. Migliaccio, F. Nunziata, and A. Gambardella, “On the co-polarized phase difference for oil spill observation,” *Int. J. Remote Sens.*, vol. 30, no. 6, pp. 1589–1602, Mar. 2009.

[5] A. G. Fore *et al.*, “UAVSAR polarimetric calibration,” *IEEE Trans. Geosci. Remote Sens.*, vol. 53, no. 6, pp. 3481–3491, Jun. 2015.

[6] R. K. Raney, “Hybrid-polarity SAR architecture,” *IEEE Trans. Geosci. Remote Sens.*, vol. 45, no. 11, pp. 3397–3404, Nov. 2007.

[7] F. J. Charbonneau *et al.*, “Compact polarimetry overview and applications assessment,” *Can. J. Remote Sens.*, vol. 36, no. S2, pp. S298–S315, 2010.

[8] J.-C. Souyris, P. Imboa, R. Fjørtoft, S. Mingot, and J.-S. Lee, “Compact polarimetry based on symmetry properties of geophysical media: The $\pi/4$ mode,” *IEEE Trans. Geosci. Remote Sens.*, vol. 43, no. 3, pp. 634–646, Mar. 2005.

[9] F. Nunziata, M. Migliaccio, and X. Li, “Sea oil slick observation using hybrid-polarity SAR architecture,” *IEEE J. Ocean. Eng.*, vol. 40, no. 2, pp. 426–440, Apr. 2015.

[10] A.-B. Salberg, O. Rudjord, and A. H. S. Solberg, “Oil spill detection in hybrid-polarimetric SAR images,” *IEEE Trans. Geosci. Remote Sens.*, vol. 52, no. 10, pp. 6521–6533, Oct. 2014.

[11] M. J. Collins, M. Denbina, B. Minchew, C. E. Jones, and B. Holt, “On the use of simulated airborne compact polarimetric SAR for characterizing oil–water mixing of the deepwater horizon oil spill,” *IEEE J. Sel. Topics Appl. Earth Observat. Remote Sens.*, vol. 8, no. 3, pp. 1062–1077, Mar. 2015.

[12] R. Shirvany, M. Chabert, and J.-Y. Tourneret, “Ship and oil-spill detection using the degree of polarization in linear and hybrid/compact dual-pol SAR,” *IEEE J. Sel. Topics Appl. Earth Observat. Remote Sens.*, vol. 5, no. 3, pp. 885–892, Jun. 2012.

[13] B. Minchew, “Determining the mixing of oil and sea water using polarimetric synthetic aperture radar,” *Geophys. Res. Lett.*, vol. 39, no. 16, Aug. 2012.

[14] W. Alpers and H. Hühnerfuss, “Radar signatures of oil films floating on the sea surface and the Marangoni effect,” *J. Geophys. Res.*, vol. 93, no. C4, pp. 3642–3648, Apr. 1988.

[15] G. R. Valenzuela, “Theories for the interaction of electromagnetic and oceanic waves—A review,” *Boundary-Layer Meteorol.*, vol. 13, no. 1, pp. 61–85, Jan. 1978.

[16] B. Holt, “SAR imaging of the ocean surface,” in *Synthetic Aperture Radar Marine User’s Manual*, C. R. Jackson and J. R. Apel, Eds. Washington, DC, USA: NOAA NESDIS Office of Research and Applications, 2004, pp. 25–79

[17] R. Romeiser, V. Wismann, and W. Alpers, “An improved composite surface model for the radar backscattering cross section of the ocean surface: 1. Theory of the model and optimization/validation by scatterometer data,” *J. Geophys. Res.*, vol. 102, no. C11, pp. 25237–25250, Nov. 1997.

[18] C. Brekke, C. E. Jones, S. Skrunes, B. Holt, M. Espeseth, and T. Eltoft, “Cross-correlation between polarization channels in SAR imagery over oceanographic features,” *IEEE Geosci. Remote Sens. Lett.*, vol. 13, no. 7, pp. 997–1001, Jul. 2016.

[19] S. Skrunes, C. Brekke, C. E. Jones, and B. Holt, “A multisensor comparison of experimental oil spills in polarimetric SAR for high wind conditions,” *IEEE J. Sel. Topics Appl. Earth Observat. Remote Sens.*, vol. 9, no. 11, pp. 4948–4961, Nov. 2016.

[20] C. E. Jones *et al.*, “Measurement and modeling of oil slick transport,” *J. Geophys. Res. Oceans*, vol. 121, no. 10, pp. 7759—7775, 2016.

[21] M. E. Nord, T. L. Ainsworth, J.-S. Lee, and N. J. S. Stacy, “Comparison of compact polarimetric synthetic aperture radar modes,” *IEEE Trans. Geosci. Remote Sens.*, vol. 47, no. 1, pp. 174–188, Jan. 2008.

[22] S. R. Cloude, *Polarisation Applications in Remote Sensing*, 1st, ed. Oxford, U.K.: Oxford Univ. Press, 2010.

[23] R. K. Raney, “A perspective on compact polarimetry,” *IEEE Geosci. Remote Sens. Newslett.*, no. 160, pp. 12–18, Sep. 2010.

[24] M. J. Collins, M. Denbina, and G. Atteia, “On the reconstruction of quad-Pol SAR data from compact polarimetry data for ocean target detection,” *IEEE Trans. Geosci. Remote Sens.*, vol. 51, no. 1, pp. 591–600, Jan. 2013.

[25] R. K. Raney, “Comparing compact and quadrature polarimetric SAR performance,” *IEEE Geosci. Remote Sens. Lett.*, vol. 13, no. 6, pp. 861–864, Jun. 2016.

[26] A. Iodice, A. Natale, and D. Riccio, “Retrieval of soil surface parameters via a polarimetric two-scale model,” *IEEE Trans. Geosci. Remote Sens.*, vol. 49, no. 7, pp. 2531–2547, Jul. 2011.

[27] J.-S. Lee, D. L. Schuler, and T. L. Ainsworth, “Polarimetric SAR Data Compensation for Terrain Azimuth Slope Variation,” *IEEE Trans. Geosci. Remote Sens.*, vol. 38, no. 5, pp. 2153–2163, Sep. 2000.

[28] M. M. Espeseth, S. Skrunes, C. Brekke, A.-B. Salberg, C. E. Jones, and B. Holt, “Oil spill characterization in the hybrid polarity SAR domain using log-cumulants,” *Proc. SPIE*, vol. 10004, p. 1000414, Oct. 2016.

[29] C. E. Jones, M. M. Espeseth, B. Holt, C. Brekke, and S. Skrunes, “Characterization and discrimination of evolving mineral and plant oil slicks based on L-band synthetic aperture radar (SAR),” *Proc. SPIE*, vol. 10003, p. 100030K, Oct. 2016.

[30] M. Basseville, “Distance measures for signal processing and pattern recognition,” *Signal Process.*, vol. 18, no. 4, pp. 349–369, 1989.

[31] Y. Li, H. Lin, Y. Zhang, and J. Chen, "Comparisons of circular transmit and linear receive compact polarimetric SAR features for oil slicks discrimination," *J. Sensors*, vol. 2015, 2015, Art. no. 631561.

[32] M. Migliaccio, A. Gambardella, and M. Tranfaglia, "SAR polarimetry to observe oil spills," *IEEE Trans. Geosci. Remote Sens.*, vol. 45, no. 2, pp. 506–511, Feb. 2007.

[33] M. Dabbor, S. Howell, M. Shokr, and J. Yackel, "The Jeffries–Matusita distance for the case of complex Wishart distribution as a separability criterion for fully polarimetric SAR data," *Int. J. Remote Sens.*, vol. 35, no. 19, pp. 6859–6873, Oct. 2014.

[34] P. H. Swain and S. M. Davis, *Remote Sensing: The Quantitative Approach*. New York, NY, USA: McGraw-Hill, 1978.

[35] M. Dabboor and T. Geldsetzer, "On the classification of sea ice types using simulated radarsat constellation mission (RCM) compact polarimetric SAR parameters," in *Proc. ASPRS Annu. Conf.*, Louisville, KY, USA, Mar. 2014.

[36] M. Migliaccio, M. Tranfaglia, and S. A. Ermakov, "A physical approach for the observation of oil spills in SAR images," *IEEE J. Ocean. Eng.*, vol. 30, no. 3, pp. 496–507, Jul. 2005.

[37] F. Galland, P. Réfrégier, and O. Germain, "Synthetic aperture radar oil spill segmentation by stochastic complexity minimization," *IEEE Geosci. Remote Sens. Lett.*, vol. 1, no. 4, pp. 295–299, Oct. 2014.

[38] S. Derrode and G. Mercier, "Unsupervised multiscale oil slick segmentation from SAR images using a vector HMC model," *Pattern Recognit.*, vol. 40, no. 3, pp. 1135–1147, Mar. 2007.

[39] A. P. Doulgeris and T. Eltoft, "Scale mixture of Gaussian modelling of polarimetric SAR data," *EURASIP J. Adv. Signal Process.*, vol. 2010, p. 12, Dec. 2009.

[40] A. P. Doulgeris, "A simple and extendable segmentation method for multi-polarisation SAR images," in *Proc. POLINSAR*, Frascati, Italy, 2013.

[41] V. Wismann, M. Gade, W. Alpers, and H. Huhnerfuss, "Radar signatures of marine mineral oil spills measured by an airborne multi-frequency radar," *Int. J. Remote Sens.*, vol. 19, no. 18, pp. 3607–3623, 1998.

[42] N. Pinel, C. Bourlier, and I. Sergievskaya, "Two-dimensional radar backscattering modeling of oil slicks at sea based on the model of local balance: Validation of two asymptotic techniques for thick films," *IEEE Trans. Geosci. Remote Sens.*, vol. 52, no. 5, pp. 2326–2338, May 2014.

[43] D. L. Schuler, J.-S. Lee, and K. W. Hoppel, "Polarimetric SAR image signatures of the ocean and Gulf Stream features," *IEEE Trans. Geosci. Remote Sens.*, vol. 31, no. 6, pp. 1210–1221, Nov. 1993.

[44] D. Velotto, M. Migliaccio, F. Nunziata, and S. Lehner, "Dual-polarized TerraSAR-X data for oil-spill observation," *IEEE Trans. Geosci. Remote Sens.*, vol. 49, no. 12, pp. 4751–4762, Dec. 2011.

[45] W. Wenguang, L. Fei, W. Peng, and W. Jun, "Oil spill detection from polarimetric SAR image," in *Proc. ICSP*, 2010, pp. 823–835.

[46] B. Zhang, W. Perrie, X. Li, and W. G. Pichel, "Mapping sea surface oil slicks using RADARSAT-2 quad-polarization SAR image," *Geophys. Res. Lett.*, vol. 38, no. 10, May 2011.

[47] V. N. Kudryavtsev, B. Chapron, A. G. Myasoedov, F. Collard, and J. A. Johannessen, "On dual co-polarized SAR measurements of the ocean surface," *IEEE Geosci. Remote Sens. Lett.*, vol. 10, no. 4, pp. 761–765, Jul. 2013.

[48] W. Tian, Y. Shao, J. Yuan, S. Wang, and Y. Liu, "An experiment for oil spill recognition using RADARSAT-2 image," in *Proc. IEEE Int. Geosci. Remote Sens. Symp.*, Jul. 2010, pp. 2761–2764.

[49] M. Migliaccioa, F. Nunziata, and A. Buono, "SAR polarimetry for sea oil slick observation," *Int. J. Remote Sens.*, vol. 36, no. 12, pp. 3243–3273, Jun. 2015.

[50] D. L. Schuler and J. S. Lee, "Mapping ocean surface features using biogenic slick-fields and SAR polarimetric decomposition techniques," *IEE Proc.-Radar, Sonar Navigat.*, vol. 153, no. 3, pp. 260–270, Jun. 2006.

[51] M. Migliaccio, A. Gambardella, F. Nunziata, M. Shimada, and O. Isoguchi, "The PALSAR polarimetric mode for sea oil slick observation," *IEEE Trans. Geosci. Remote Sens.*, vol. 47, no. 12, pp. 4032–4041, Dec. 2009.

[52] F. T. Ulaby, K. Sarabandi, and A. Nashashibi, "Statistical properties of the Müller matrix of distributed targets," *IEE Proc. F-Radar Signal Process.*, vol. 139, no. 2, pp. 136–146, Apr. 1992.

[53] M. R. Drinkwater, R. Kwok, E. Rignot, H. Israelsson, R. G. Onstott, and D. P. Winebrenner, "Potential applications of polarimetry to the classification of sea ice," in *Microwave Remote Sensing of Sea Ice* (Geophysical Monograph). Washington, DC, USA: Amer. Geophys. Union, 1992.

[54] J.-S. Lee and E. Pottier, *Polarimetric Radar Imaging, From Basics to Applications*, B. J. Thompson, Ed. Boca Raton, FL, USA: CRC Press, 2009.

[55] H. Li, W. Perrie, Y. Zhou, and Y. He, "Oil spill detection on the ocean surface using hybrid polarimetric SAR imagery," *Sci. China*, vol. 59, no. 2, pp. 249–257, Feb. 2016.

[56] H. Li, W. Perrie, Y. He, J. Wu, and X. Luo, "Analysis of the polarimetric SAR scattering properties of oil-covered waters," *IEEE J. Sel. Topics Appl. Earth Observat. Remote Sens.*, vol. 8, no. 8, pp. 3751–3759, Aug. 2015.

[57] S. Cloude, D. Goodenough, and H. Chen, "Compact decomposition theory," *IEEE Trans. Geosci. Remote Sens.*, vol. 9, no. 1, pp. 28–32, Jan. 2012.

[58] R. K. Raney, J. T. S. Cahill, G. W. Patterson, and D. B. J. Bussey, "The $m-chi$ decomposition of hybrid dual-polarimetric radar data with application to lunar craters," *J. Geophys. Res.*, vol. 117, no. E12, May 2012.

[59] B. Slade, *Radarsat-2 Product Description*. Rickmond, BC, Canada: MacDonald, Dettwiler Assoc., 2011.

[60] T. Fritz and M. Eineder, "TerraSAR-X ground segment basic product specification document," German Aerosp. Center Abbreviated DLR, DLR, Germany, Tech. Rep., Oct. 2010. [Online]. Available: http://www.dtic.mil/dtic/tr/fulltext/u2/a515513.pdf

[61] D. Latini, F. D. Frate, and C. E. Jones, "Multi-frequency and polarimetric quantitative analysis of the Gulf of Mexico oil spill event comparing different SAR systems," *Remote Sens. Environ.*, vol. 183, pp. 26–42, Sep. 2016.

[62] T. Misra *et al.*, "Synthetic aperture radar payload on-board RISAT-1: Configuration, technology and performance," *Current Sci.*, vol. 104, no. 4, pp. 446–461, Feb. 2013.

[63] S. Skrunes, C. E. Jones, C. Brekke, B. Holt, and M. M. Espeseth, "On the effects of imaging geometry on multipolarization SAR features for oil spill observation," in *Proc. Living Planet Symp.*, 2016, p. 72.

[64] R. Shirvany, M. Chabert, and J. Y. Tourneret, "Estimation of the degree of polarization for hybrid/compact and linear dual-pol SAR intensity images: Principles and applications," *IEEE Trans. Geosci. Remote Sens.*, vol. 51, no. 1, pp. 539–551, Jan. 2013.

[65] A. H. S. Solberg, "Remote sensing of ocean oil-spill pollution," *Proc. IEEE*, vol. 100, no. 10, pp. 2931–2945, Oct. 2012.

[66] J. Coleman, *Oil Sea III*. Washington, DC, USA: Nat. Acad. Press, 2003.

[67] W. Alpers and H. A. Espedal, "Oils and surfactants," in *Synthetic Aperture Radar Marine User's Manual*, C. R. Jackson and J. R. Apel, Eds. Washington, DC, USA: NOAA NESDIS Office of Research and Applications, 2004, pp. 263–275

[68] G. Sun, K. J. Ranson, and V. I. Kharuk, "Radiometric slope correction for forest biomass estimation from SAR data in Western Sayani Mountains, Siberia," *Remote Sens. Env.*, vol. 79, nos. 2–3, pp. 279–287, 2002.

Martine M. Espeseth received the M.Sc. degree from the UiT The Arctic University of Norway, Tromsø, Norway, in 2015, where she is currently pursuing the Ph.D. degree with the Centre for Integrated Remote Sensing and Forecasting for Arctic Operations.

In 2016, she was a Visiting Ph.D. Student with the Jet Propulsion Laboratory, California Institute of Technology, Pasadena, CA, USA. Her research interests include remote sensing of polarimetric synthetic aperture radar and with a focus on compact polarimetry within both marine oil pollution and sea ice applications.

Stine Skrunes (S'12–M'15) received the M.Sc. and Ph.D. degrees from the UiT The Arctic University of Norway, Tromsø, Norway, in 2011 and 2014, respectively.

She holds a post-doctoral position with the Department of Physics and Technology, Centre for Integrated Remote Sensing and Forecasting for Arctic Operations, UiT The Arctic University of Norway. Her research interests include remote sensing of ocean areas, specifically by polarimetric synthetic aperture radar and with a focus on marine oil pollution.

Cathleen E. Jones (M'94) received the B.S. degree in physics from Texas A&M University, College Station, TX, USA, and the Ph.D. degree in physics from the California Institute of Technology, Pasadena, CA, USA.

She is currently a Radar Scientist with the NASA's Jet Propulsion Laboratory, California Institute of Technology, where she is involved in using radar remote sensing for studying natural disasters and monitoring critical infrastructure, primarily using high-resolution L-band PolSAR and InSAR based on UAVSAR data. Her research interests include the development of methods for determining oil slick characteristics and identifying levee deformation, seepage, and general subsidence rates using synthetic aperture radar, and detecting sinkhole precursor in InSAR-challenged areas.

Camilla Brekke (M'12) received the Cand.Sci. and Ph.D. degrees from the University of Oslo, Oslo, Norway, in 2001 and 2008, respectively.

In 2001, she was a System Developer with Ericsson, Asker, Norway. From 2001 to 2002, she was a Young Graduate Trainee with the European Space Agency, Noordwijk, The Netherlands. From 2002 to 2009, she was a Scientist with the Norwegian Defense Research Establishment, Kjeller, Norway. In 2009, she joined the Department of Physics and Technology, UiT The Arctic University of Norway, Tromsø, Norway, as an Associate Professor. From 2012 to 2013, she was a Visiting Scientist with the Jet Propulsion Laboratory, California Institute of Technology, Pasadena, CA, USA. She is currently with the Earth Observation Laboratory and the Centre for Integrated Remote Sensing and Forecasting for Arctic Operations, UiT The Arctic University of Norway. Her research interests include signal and image processing of synthetic aperture radar data for arctic and marine applications.

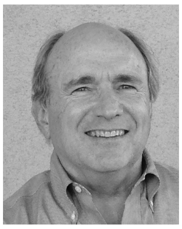

Benjamin Holt (M'88) received the B.S. degree from Stanford University, Stanford, CA, USA, in 1972, and the M.S. degree in physical oceanography from the University of Southern California, Los Angeles, CA, USA, in 1988.

In 1978, he joined the California Institute of Technology, Pasadena, CA, USA, where he is currently a Research Scientist with the Jet Propulsion Laboratory, Ocean Circulation Group, Earth Science Section. His research interests include using multisensor remote sensing data to examine the geophysical state of polar sea ice and snow, coastal oceanography and circulation, and the detection of marine pollutants, and new instrument development and techniques for microwave measurement of sea ice thickness.

Anthony P. Doulgeris (S'06–M'12) received the B.Sc. degree in physics from The Australian National University, Canberra, ACT, Australia, in 1988, and the M.Sc. and Ph.D. degrees in physics from the UiT The Arctic University of Norway, Tromsø, Norway, in 2006 and 2011, respectively.

He joined the Department of Physics and Technology, UiT The Arctic University of Norway, in 2007. He is currently an Associate Professor in applied Earth observation. His research interests include investigating remote sensing, pattern recognition, and multidimensional statistical modeling, in particular with polarimetric synthetic aperture radar images.

8

Paper II:

Interpreting backscattering from oil spills in view of system noise in polarimetric SAR imagery

M. M. Espeseth, C. Brekke, C. E. Jones, B. Holt, and A. Freeman

Under review in:
IEEE Transactions on Geoscience and Remote Sensing, 2019

Interpreting backscattering from oil spills in view of system noise in polarimetric SAR imagery

Martine M. Espeseth, Camilla Brekke, *Member, IEEE,* Cathleen E. Jones, *Member, IEEE,* Benjamin Holt, *Member, IEEE,* and Anthony Freeman, *Fellow, IEEE*

***Abstract*—The effects of both system additive and multiplicative noise on X-, C-, and L-band Synthetic Aperture Radar (SAR) data covering oil slicks are examined. Prior studies have attempted to characterize such oil slicks, primarily through analysis of polarimetric SAR data. Here we factor in system noise that is added to the backscattered signal, introducing artifacts that can easily be confused with random and volume scattering. This confusion occurs when additive and/or multiplicative system noise dominates the measured backscattered signal. Polarimetric features used in this study are shown to be affected by both additive and multiplicative system noise, some more than others. This study highlights the importance of considering specifically multiplicative noise in the estimation of the signal-to-noise ratio (SNR). Using TerraSAR-X and Radarsat-2 we demonstrate that the majority of the oil slicks signal is highly dominated by noise artifacts. The SNR from TerraSAR-X and Radarsat-2 is below 0dB for the majority of the oil slick pixels when considering both the additive and multiplicative noise, rendering these data unsuitable for any analysis of the scattering properties and characterization. In particular, we find there is no need to invoke exotic scattering mechanisms to explain characteristics of the data. The SNR based on additive noise should at least be above 10dB. The SNR involving both additive and multiplicative noise should at least be above 0dB. We also recommend a noise subtraction for any polarimetric analysis when characterizing the oil. However, the noise subtraction reduces the oil-sea contrast for some features and should be avoided for any oil slick detection purposes.**

***Index Terms*—Synthetic Aperture Radar, UAVSAR, Radarsat-2, TerraSAR-X, SNR, additive noise, multiplicative noise, oil spill**

I. INTRODUCTION

Polarimetric Synthetic Aperture Radar (SAR) data has been utilized in multiple remote sensing investigations of marine oil spills (see, e.g., [1]–[3]). Most studies have focused on oil slick detection, in an effort to identify polarimetric features that demonstrate high detection capabilities for different kinds of oil under various wind and ocean conditions (see, e.g., [1], [4]–[6]). After a slick has been detected, investigators then seek to extract more information about the oil slick. Such characterization of oil slicks includes extraction of physical properties such as the dielectric constant, the volumetric fraction of the oil in an oil-water mixture, and distinguishing between various types of oil. Studies by [2], [3], [7] have addressed the potential of polarization diversity in a SAR system to yield this kind of information about the characteristics of the oil, which could be very important in a potential oil spill recovery, as knowledge about, e.g., the oil type, or the internal variations within the oil slick might facilitate more efficient clean-up operations. Oil slick characterization is only possible if signal backscattered from the oil slick is separable within the measured signal. Unfortunately, oil slicks seen in polarimetric SAR data are particularly susceptible to misinterpretation due to noise contamination of their low backscatter values, and the importance of properly evaluating the noise is emphasized.

The measured signal in all SAR systems contains noise in addition to the signal of interest, which is the normalized radar-cross-section (RCS), (σ^0), of the target. In general, there are three imaging effects to consider when attempting to recover the RCS. These are listed in [8] and are as follows; (i) scaling of the RCS due to propagation, antenna pattern, and processing effects; (ii) spatial correlation induced by the processing; and (iii) bias in the estimated RCS due to system noise. Several potential sources that contribute to the additive noise power (the bias in the estimated RCS); are the thermal noise and quantization noise from the analog-to-digital conversion (ADC) [9].

Freeman [9] demonstrated the effect of additive noise on polarization signatures for a typical Bragg scatterer, and discussed the effect of this type of noise on the radar measurements. Several studies have conducted a ”noise analysis”, containing information about the signal-to-noise ratio (SNR) of the various polarization channels of different investigated mediums like an oil slick, clean sea, biogenic slick, etc. (see, e.g., [2], [10], [11]). In these studies, the authors usually verify whether the measured signal is above the noise floor, and further evaluate the need to discard some of the polarization channels (often the cross-polarization channel is discarded for oil slick analysis). The noise floor is often set to the noise-equivalent-sigma-zero (NESZ) that is given in the product file of the data. However, even though the signal is above the noise floor, the measured signal still contains noise. Minchew et al. [10] identified that the measured signal should be 6dB above the noise floor, while [12] identified this limit to be between 7-8dB. Both studies concluded this level above the noise floor based on the measured intensity values as a function of the incidence angle. For oil slick characterization and extraction of physical properties using polarimetric SAR data, these results imply that the backscattered signal needs to be well above the noise power, i.e., noise floor.

M. M. Espeseth and C. Brekke are with the Department of Physics and Technology, UiT The Arctic University of Norway, 9037 Tromsø, Norway.

C. E. Jones, B. Holt, and A. Freeman are with the Jet Propulsion Laboratory, California Institute of Technology, Pasadena, CA 91125 USA

Manuscript received Month XX, 201X; revised Month XX, 201X; accepted Month X, 201X. Date of publication Month XX, 201X; date of current version Month X, 201X. (Corresponding author: M. M. Espeseth (martine.espeseth@uit.no))

It is possible to detect oil slicks so long as the oil/sea backscatter contrast is high, which means the backscatter from the oil slick can be close to the noise floor of the radar, provided the ocean surface return is well above the noise floor. Unfortunately, instrumental noise might still influence the detection capability using SAR, which was demonstrated by Angelliaume et al. [13] using an oil slick detection algorithm. In the same study, the authors added noise to a scattering vector from a high SNR airborne instrument with full-polarimetric capability and calculated the probability of detection using a set of polarimetric features. They discovered that the performance of the oil slick detection for some polarimetric features was severely deteriorated by the instrumental additive noise.

When studying oil slicks with SAR, multiplicative noise has traditionally not been considered (see, e.g., [5], [10], [13]–[16]). The multiplicative noise raises the noise floor, hence reducing the overall SNR in the data. The main objective of this study is to understand the sensitivity to both additive and multiplicative noise power for a set of well known and commonly used polarimetric features for observing marine oil slicks. More specifically, the analysis covers (1) how the feature values behave as a function of both the simulated noise and true noise (additive and multiplicative) within the radar measurements; (2) identifying the minimum SNR below which the data are too contaminated by the noise to provide reliable information about the surface properties from oil-covered surfaces; and (3) exploring the feature behavior when the additive noise power is subtracted from the second order sample covariance and coherency matrix. The analysis is based on quad-polarimetric data from the L-band sensor Uninhabited Aerial Vehicle Synthetic Aperture Radar (UAVSAR), the C-band sensor Radarsat-2 (RS-2), and dual-polarimetric (two copolarization channels) data from the X-band sensor TerraSAR-X (TS-X) obtained off Norway during a series of oil-on-water field campaigns.

II. NOISE ARTIFACTS IN SAR

As highlighted in Section I, various imaging effects have to be taken into consideration when recovering the RCS. The upcoming discussion includes the various artifacts and noise introduced in SAR, with a special focus on marine oil spills. This section also discusses the measures that are applied in this study for considering some of the noise/artifacts impacting the measured backscattered signal.

A. *Aliasing*

Well-known artifacts that can cause confusion in interpreting a SAR image are ambiguities due to aliasing in both the azimuth and range direction [9]. Aliasing in the range direction is caused by simultaneously receiving different pulses [9]. Azimuth ambiguities are caused by finite sampling of the radar data as a result of azimuth sidelobes that extent beyond the width of the main lobe [17]. The degree of aliasing and the separation distance at which they occur is controlled by the pulse repetition frequency (PRF) [17]. As a result of azimuth aliasing the signal from any target is repeated (maybe several times) with a fraction of the main signal equal to the azimuth ambiguity ratio. For bright targets such as ships these ambiguities are sometimes observed as ghosts in the SAR image. In this study we have selected oil spill areas that are not contaminated by azimuth ambiguities from ships. Nevertheless, these darker areas will be corrupted by ambiguous signals from nearby clean sea areas, that are brighter than the oil spill. The contrast between oil and sea can be high, and therefore a fraction of the SAR signal from the surrounding clean sea will be present in oil-covered pixels.

Table I shows the ambiguity levels for the three sensors investigated. The total ambiguity ratio in TS-X is $<$-16dB [18] for the stripmap dual-polarimetric mode (used in this study). This ratio was in [18] calculated based on the average ratio between the signal power and the aliased power that is caused by azimuth and range ambiguities for one pixel. For RS-2 the azimuth and range ambiguities are usually both -35 dB [19], except for the higher incidence angles, for which the range ambiguity drops to -25 dB. Range ambiguities are usually not significant noise sources for airborne systems such as UAVSAR, and typical azimuth ambiguity levels are estimated at -24 dB [Scott Hensley, personal communication, May 2019]. In this study the ambiguity levels are factored into the multiplicative noise ratio when estimating the SNR.

B. *Cross-talk*

For polarization diverse data, cross-talk and channel imbalance between the various polarization channels are unavoidable because of leakage between the polarization channels. An extra processing step (see, e.g., [20], [21]) involving for example assumptions about the scattering medium, is sometimes performed to reduce cross-talk by balancing the amplitude and the phase between channels. The most significant, and most readily observed, effect of unbalanced polarization channels, due to cross-talk, will be higher apparent levels of HV backscatter. In cases of severe cross-talk the target signal for each polarization channel may be contaminated and alter the interpretation and estimation of physical parameters using a given model (e.g., tilted Bragg model [22]).

In Table I, the estimated cross-talk value for RS-2 is -32dB ([23], [24]), but various values between -30dB and -40dB have been reported (see, e.g., [23], [25]). The estimated cross-talk prior to any cross-talk calibration of the UAVSAR is generally on the order of -30dB [26]. The antenna cross-talk can only be corrected if the quad-polarimetric scattering matrix is available (see, e.g., [27], [28]). Cross-talk removal has been performed on the quad-polarimetric Radarsat-2 products prior to receiving the data [23]. The HH-VV dual-polarimetric mode of TerraSAR-X is used for this study, where the two cross-polarization channels are not acquired. Hence, cross-talk between the two copolarization channels are insignificant. No cross-talk removal is performed on the UAVSAR data.

C. *Effects from sidelobes*

While measuring the response from the surface, sidelobes might spatially smear the signal around a target. The peak-to-sidelobe ratio (PSLR) and integrated sidelobe ratio (ISLR)

TABLE I

AMBIGUITY LEVELS, CROSS-TALK, PSLR, ISLR, AND NESZ (ADDITIVE NOISE) OF THE UAVSAR, RS-2, AND TS-X. THE VALUES OF THE TS-X ARE FROM DUAL-POLARIZATION STRIPMAP.

	UAVSAR	**RS-2**	**TS-X**
Ambiguity level [dB]	$\approx$-24 (az.)[a]	-35/-35 (az./rg.) (FQ1-26) [19] -35/-25 (az./rg.) (FQ28-31)	$<$-16 [18]
Cross-talk [dB]	-30 [26]	$<$-32 [23], [24]	NA
PSLR [dB]	-21[b] [26]	$<$-18 [29]	-25 [18]
ISLR [dB]	-17.67[c] [26], [30]	$<$-14.9 [29]	-18 [18]
NESZ [dB]	-30 to -50 [26]	-31 to -39 [31]	-19 [18]

[a] Ambiguity level (azimuth (az.)) of UAVSAR was provided by Scott Hensley (JPL), personal communication 2019.

[b] The UAVSAR PSLR value was provided by Brian Hawkins (JPL) (personal communication 2019) using a weighting factor $\eta = 0.5$ [26]

[c] The UAVSAR ISLR was calculated using equation (22) in [30] with a weighting factor $\eta = 0.5$ [26].

measure the SAR performance in resolving a weak target (for example oil) in the presence of a strong target (for example ships/rigs). The PSLR is defined as the ratio between the height of the largest sidelobe and the height of the main lobe (expressed in dB) [17]. The ISLR is the ratio of the integrated energy in the sidelobes to the amount of energy in the main lobe (also expressed in dB) [17]. A high value (i.e., low ratio) in both the PSLR and ISLR indicate that the signal is smeared out along and across track, and could potentially generate a bright cross at a given point target (for example ships). Hence, low values (i.e., high ratio) of PSLR and ISLR are desirable, and the PSLR level is recommended to be approximately -20dB [17]. In Table I, TS-X and UAVSAR have acceptable values of the PSLR, namely -25dB and -21dB, respectively. The PSLR for RS-2 is $<$-18dB [29], which satisfies the tolerance level ($<$-17dB) for oil spill detection identified in [32], but not the criteria set by [17]. There are some ships surrounding the oil slicks in some of the SAR scenes used in this study. Hence, the measured signal within the oil slick might be impacted by the sidelobes due to the response from the neighboring ships. In this study, this is mitigated by masking out the ships and its corresponding bright cross along several pixels in the range and azimuth direction prior to selecting the regions of interest (ROIs). Therefore, the oil slick regions studied here will not be located near the ships nor the bright cross. But the clean sea pixels surrounding the oil slick will still have a significant effect on the measured signal from the oil slick if the ISLR is high. This is because signals from nearby clean sea pixels could spillover (due to the sidelobes) into darker, oil-covered areas by a factor that adds up to be equivalent to the ISLR. The SNR for oil-covered pixels will then be reduced due to contributions from neighboring clean sea signals, which are not oil. The ISLR is therefore factored into the multiplicative noise ratio in estimation of the SNR for this study.

D. *Block adaptive quantization*

Another noise source is introduced by block adaptive quantization (BAQ) compression. The BAQ compression is performed on all three sensors evaluated in this study (UAVSAR [33], RS-2 [31], TS-X [18], [34]). The SAR signals are digitized using an ADC followed by the BAQ to reduce on-board data storage requirements and downlink rate [31]. The BAQ is a lossy data compression technique that introduces additive quantization noise in the data and depends on the backscattered signals in the scene. The key term here is ”block”: BAQ algorithms take a block of raw data and normalize to the average value of the quantized radar signals. The data are then re-quantized around that mean signal value. Thus an 8:3 BAQ algorithm behaves like a perfect 3-bit ADC, optimized so that ”local” mean signal level for that block of samples falls right in the ”sweet spot” of the ADC performance curve. The quad-polarization mode of RS-2 uses a 3-bit BAQ, which introduces a BAQ noise degradation that is -14dB lower than the mean signal level [31]. The quad-polarization modes of UAVSAR use an 8-bit BAQ [35]. BAQ quantization noise will reduce the SNR (see, e.g., [34], [36]), as a result of the adaptive scaling and re-quantization of the SAR signal [34]. The quantization noise contribution is relative to the mean signal level for the block of signals used [32]; for signal blocks where clean sea dominates the calculation of mean signal, the BAQ noise should be calculated relative to that level. The BAQ noise is already included in the additive noise power provided in TS-X [18]. The quantization noise is therefore considered for the UAVSAR and RS-2 when estimating the SNR.

E. *Thermal system noise*

The signal measured at the antenna must be larger than the thermal noise radiated in the radar system to enable an evaluation of the backscattering properties of the targets. The thermal noise is additive, and is usually considered the dominating factor in the NESZ and when calculating the overall scene SNR, where higher thermal noise results in reduced SNR. The thermal noise is assumed Gaussian white noise and is added to the observed signal. NESZ is defined in terms of the radar backscatter coefficient of an area that will appear at the same strength in the image as the thermal noise. For this study, the additive noise using the NESZ is considered for all sensors investigated when estimating the SNR, when simulating noise to the UAVSAR, and when subtracting the noise from the data with the objective of reducing the impact of the additive noise present in the polarimetric measurements. Typical NESZ (thermal noise) values for each sensor investigated in this study are shown in Table I.

III. ADDITIVE AND MULTIPLICATIVE NOISE IN POLARIMETRIC SAR

For nominally calibrated polarimetric SAR data, the measured scattering matrix, $\boldsymbol{M}$, is related to the target scattering matrix, $\boldsymbol{S}$, via [37]:

$$\boldsymbol{M} = \boldsymbol{S} + \boldsymbol{N} \tag{1}$$

where $\boldsymbol{S} = [S_{HH}, S_{VH}, S_{HV}, S_{VV}]^T$ are the target scattering coefficients without noise (presumably), and $\boldsymbol{N} = [n_{HH}, n_{VH}, n_{HV}, n_{VV}]^T$ represents the complex additive noise. The H represents horizontal and V is vertical polarization on either transmit or receive. The $\boldsymbol{N}$ is assumed to be complex Gaussian white noise with zero mean. The noise in the HH, VH, HV, and VV polarization channel measurements are uncorrelated with each other and to the target scattering coefficients [9].

Equation (1) excludes the multiplicative noise factors, and to account for this, we suggest the following model for the measured RCS for clean sea and oil slicks;

$$\sigma_{pq}^{0,m} = \sigma_{pq}^{0} + \sigma_{pq}^{n} + \sigma_{pq}^{AVG} MNR \tag{2}$$

where σ_{pq}^{0} is the RCS of the target, p is the polarization on transmit, q is the polarization on receive, and σ_{pq}^{n} is the NESZ (additive noise power), i.e., $|n_{pq}|^2$. The σ_{pq}^{AVG} is the average signal for each polarization channel that impacts the measured signal $\sigma_{pq}^{0,m}$. For ocean applications with small coverage and no land, the σ_{pq}^{AVG} can be approximated to the mean signal level of homogeneous clean sea scatterers. The MNR is the multiplicative-noise-ratio (MNR) that factors in the ISLR, BAQ, and ambiguity-to-signal ratio (AMB). The $\sigma_{pq}^{0,m} = \langle |M_{pq}|^2 \rangle$, where $\langle\rangle$ denotes spatial averaging, and in this study a sliding 9×9 averaging window is used to reduce speckle, but it will not eliminate it. To be able to perform any useful characterization the σ_{pq}^{0} from the oil slick must be larger than both the additive and multiplicative noise factors. This is determined using the SNR, and the upcoming section shows how the SNR is estimated using both the additive and the multiplicative noise components.

A. Estimation of the SNR

The SNR is an integral function of several sensor properties, including the gain on transmit and receive, carrier frequency, temperature, bandwidth, altitude and so forth. The SNR^{A} (signal-to-additive noise ratio) is estimated from the data and sensor properties and is based on the ratio between the RCS and the relative amount of the additive noise (NESZ), i.e.:

$$SNR_{pq}^{A} = \frac{\sigma_{pq}^{0}}{\sigma_{pq}^{n}} = \frac{\sigma_{pq}^{0,m} - \sigma_{pq}^{n}}{\sigma_{pq}^{n}}. \tag{3}$$

The SNR is equal to 1 (or SNR = 0dB) when the additive noise and the backscattered power are equal. The NESZ varies as a function of slant range (due to the antenna elevation pattern) and is the noise added to the observed signal. The NESZ is often given in the product file (nominal values) of the various sensors and the NESZ is normally at its lowest near mid-swath, resulting in a convex curve along the range profile.

The SNR in (3) excludes the multiplicative noise component (see (2)). Using the suggested model in (2), the SNR with both the additive and multiplicative noise, here named SNR^{A,M}, can be expressed as

$$SNR_{pq}^{A,M} = \frac{\sigma_{pq}^{0,m} - (\sigma_{pq}^{n} + \sigma_{pq}^{AVG} MNR)}{\sigma_{pq}^{n} + \sigma_{pq}^{AVG} MNR}. \tag{4}$$

Here, σ_{pq}^{AVG} is the average intensity in the scene, and MNR is defined as (in linear unit) [30];

$$MNR = ISLR + 1/QNR + AMB_t \tag{5}$$

where AMB$_t$ is the total ambiguity-to-signal ratio (range and azimuth). Since oil slicks are surrounded by clean sea, the signals from clean sea areas are repeated (due to aliasing) in the oil-covered areas by a factor equal to AMB$_t \sigma_{pq}^{AVG}$ (aliased power). We assume here that azimuth ambiguities dominate the aliased signals. QNR is the quantization noise given as

$$QNR = 10 \log_{10}(2^{2N_b}) \tag{6}$$

where N_b is the number of bits. The QNR for RS-2 using the 3-bit BAQ is given as -14dB [31], whereas the QNR for the UAVSAR is estimated from the above equation. As mentioned in Section II, the QNR is already integrated in NESZ for TS-X, and is therefore not factored into the MNR. The nominal ISLR values of each sensor are shown in Table I, and these are the ones used. Note that the ISLR values for RS-2 are also given in the product file. Due to lack of information about how the ISLR is calculated, there are some uncertainties associated with these values. For example, whether the ratio given is for both range and azimuth or only one dimension. We treat the ISLR as the two-dimensional case (range and azimuth).

IV. SCATTERING PROPERTIES AND POLARIMETRIC SAR FEATURES

This section discusses the relationship between the polarimetric SAR features and their interpretation with respect to the scattering properties.

Bragg scattering theory is often used to explain scattering from the ocean, where a relationship is established between the ocean surface roughness and its properties and the incoming electromagnetic wave [22], [38]. Various two-scale Bragg models have been explored that include both the small- and large-scale ocean surface roughness ([22], [39], [40]). The tilted Bragg model has been frequently used for modelling the backscatter from clean sea and oil (see, e.g., [3], [10]), and the X-Bragg model has also been used for oil spill and sea surface studies (see, e.g., [1], [41]–[44]). The scattering process from a slick that dampens the capillary and small gravity ocean waves has often been called non-Bragg. The authors in [45] listed some possible scattering types that the literature considers non-Bragg. These are volumetric scattering, multiple scattering, double-bounce scattering, and a non-polarized component caused by the breaking waves and the surface film. The non-polarized component was acknowledged as the most realistic explanation of the non-Bragg scattering [45]. Studies have demonstrated, using high SNR SAR data, that Bragg scattering also occurs within oil slicks (see, e.g., [10], [14]).

Many different polarimetric features can be derived from polarimetric SAR data. In this study, we limit the choice of polarimetric features to those most frequently found in the literature, see Table II. The expected value of pure additive system noise, i.e., Gaussian white noise, is derived for each feature and is presented in Appendix A Table IV.

TABLE II

Overview of polarimetric features investigated. See e.g., [46] for the calculations of the pseudo probabilities (p_i) and eigenvectors (e_i) from the coherency matrix. See Appendix B for the Stokes vector (S_0, S_1, S_2, and S_3). ϕ_{HH} and ϕ_{VV} are the phases of the complex scattering vectors M_{HH} and M_{VV}.

$PD = \sigma_{VV}^{0,m} - \sigma_{HH}^{0,m}$	$H = -\sum_{i=1}^{3} p_i \log_3 p_i$
$r_{CO} = \Re(\langle M_{HH} M_{VV}^{\star} \rangle)$	$H_{CO} = -\sum_{i=1}^{2} p_i \log_2 p_i$
$\gamma_{HH/VV} = \sigma_{HH}^{0,m} / \sigma_{VV}^{0,m}$	$\alpha = \sum_{i=1}^{3} p_i \cos^{-1}(\lvert \boldsymbol{e_i}(1) \rvert)$
$\rho_{CO} = \frac{\lvert \langle M_{HH} M_{VV}^{\star} \rangle \rvert}{\sqrt{\langle \lvert M_{HH} \rvert^2 \rangle \langle \lvert M_{VV} \rvert^2 \rangle}}$	$DoP = \frac{\sqrt{S_1^2 + S_2^2 + S_3^2}}{S_0}$
$\sigma_{\phi_{CO}} = std(\phi_{HH} - \phi_{VV})$	$\chi = \frac{1}{2} \sin^{-1}\left(-\frac{S_3}{DoP S_0}\right)$

The polarization difference (PD) has a low sensitivity to the incidence angle and look direction when observing an oil slick, as well as having a high oil-sea contrast [12]. Previous studies have observed low PD values for low SNR areas like oil slick surfaces (see, e.g., [47]), and higher PD for clean sea surfaces. According to [48], the backscattered intensities over the ocean are divided into two components; one polarized component associated with the two-scale Bragg model, and one non-polarized component. The non-polarized component is caused by wave breaking from steep and rough patches on the surface. The non-polarized component is removed in PD, and we are left with a difference between the Bragg scattering components of HH and VV [48].

The copolarization ratio ($\gamma_{HH/VV}$) has been investigated in multiple studies (see, e.g., [2], [10], [47]), and according to the tilted Bragg scattering model, this feature is independent of the damping of small capillary waves by the oil. $\gamma_{HH/VV}$ is, in the tilted Bragg model, a function of the dielectric properties, the incidence angle, and the tilt angles [22]. The $\gamma_{HH/VV}$ is often used as input when estimating the dielectric constant to extract the volumetric fraction of oil in the oil-sea mixture. In order extract the volumetric oil fraction, the system noise needs to be low in the two copolarization channels. The studies in [3], [49], [50] used low noise floor radars on airplanes to extract the oil fraction. Using spaceborne satellites with higher noise floor this might be a challenge. For a high oil-sea contrast in this feature, the oil slick must be thick enough relative to the wavelength within the medium or have a high oil content in the oil-sea mixture. According to theoretical models, $\gamma_{HH/VV}$ is close to 1 at lower incidence angles, and decreases with increasing incidence angles [51]. Data-based estimates of $\gamma_{HH/VV}$ yield lower values for clean sea areas compared to an oil-covered surface [10]. Unfortunately, the presence of additive noise might result in higher $\gamma_{HH/VV}$ values for oil-covered areas due to low SNR. As the noise power increases and becomes much larger than the HH and VV intensities, $\gamma_{HH/VV}$ will tend towards 1 (assuming the noise in each polarization is at a similar level).

The real part of the copolarization cross product (r_{CO}), the magnitude of the copolarization correlation coefficient (ρ_{CO}), and the copolarized phase difference (ϕ_{CO}) are features that depend on $\langle M_{HH} M_{VV}^{\star} \rangle$. The $\langle M_{HH} M_{VV}^{\star} \rangle$ term is only independent of the noise if the noise power is decorrelated with the target scattering coefficients and the noise power from the other polarization channels (see, e.g., [9]), i.e.;

$$\begin{aligned} \langle M_{HH} M_{VV}^{\star} \rangle &= \langle (S_{HH} + N_{HH})(S_{VV}^{\star} + N_{VV}^{\star}) \rangle \\ &= \langle S_{HH} S_{VV}^{\star} \rangle + \langle S_{HH} N_{VV}^{\star} \rangle \\ &+ \langle N_{HH} S_{VV}^{\star} \rangle + \langle N_{HH} N_{VV}^{\star} \rangle \\ &= \langle S_{HH} S_{VV}^{\star} \rangle . \end{aligned} \tag{7}$$

Lower values of r_{CO} and ρ_{CO} have been observed for oil slicks compared to clean sea surfaces [2], consistent with what one would expect to see for pure random noise (see Table IV in Appendix A). Kasilingam et al. [52] reported that ρ_{CO} is insensitive to changes in the short-scale roughness, and could therefore be sensitive to variation in the dielectric properties between clean sea and oil slicks. Low ρ_{CO} values may imply depolarization effects. The expected value of ρ_{CO} for pure noise is 0. Depolarization in the backscattered signal may be due to the presence of complex surfaces, multiple-scattering surface layers, but may also be attributed to the presence of system noise [53]. The latter explanation is the one explored in this study.

The HH-VV phase difference (ϕ_{CO}) is not frequently used to examine oil spills with SAR, but its standard deviation is, i.e., $\sigma_{\phi_{CO}}$. The $\sigma_{\phi_{CO}}$ feature is another measure of the degree of correlation between S_{HH} and S_{VV}. The expected value of ϕ_{CO} should be independent of the additive noise factor because the complex noise components measured in the various polarization channels decorrelate with each other and with the scattering coefficients (see (7)). However, $\sigma_{\phi_{CO}}$ will depend on the noise power. This is significant because the expected value of a given feature may be independent of the noise, but its variance might strongly depend on it. $\sigma_{\phi_{CO}}$ has been found to increase with the presence of oil (see, e.g., [54]–[57]), and this behavior was according to [54], [55] explained by the different scattering process (Bragg vs. non-Bragg) between clean sea and oil. Some studies have showed that the broadening of ϕ_{CO} could be due to system noise (see, e.g., [10], [16], [43]). Minchew et al. [10] discovered no difference between the $\sigma_{\phi_{CO}}$ for oil and clean sea except in the presence of instrument noise for one UAVSAR scene. Alpers et al. [45] presented different theories on the broadening of the copolarization phase difference due to the presence of oil, for example; (1) the broadening might occur due to the fact that the Bragg waves are tilted by long waves; (2) instrument noise; (3) the inhomogeneity of the scattering medium due to irregular oil slick patches of various thickness. In [43], [58], suggested that the broadening of $\sigma_{\phi_{CO}}$ and the HH/VV channels were influenced by the system noise at high incidence angles ($\theta \approx 34$) using TS-X images. In this study, we investigate whether this explanation is, in fact, the one most consistent with the observations.

Two types of entropy measures are evaluated, including a dual-polarized one that can be estimated from the TS-

X scenes. The first is the copolarization entropy (H_{CO}) calculated from the sample 2×2 coherency matrix based on the HH and VV channels, and the second is the entropy (H) calculated from the sample 3×3 coherency matrix (including the HV channel). The entropy, $H \in \{0, 1\}$, describes the randomness of the scattering, where $H = 1$ indicates a random mixture of scattering mechanisms and $H = 0$ represents a single scattering response [46]. Gaussian white noise gives an entropy close to 1, and could therefore be confused with multiple and random scattering. The type of scattering that dominates is defined by the mean alpha angle (α) $\in \{0, 90°\}$: low α values represent surface scattering, intermediate α volume scattering, and high values double-bounce scattering [46], [59]. For pure random noise, α is 60° [59], so if the additive noise term dominates, the mean α angle will be located in the intermediate α value range. Several oil spill studies have used the H/α method on SAR data from spaceborne satellites and found high H and α values for oil-covered surfaces compared to clean sea surfaces (see, e.g., [6], [56], [60]–[62]). Explanations of this phenomena are often "multiple scattering mechanisms" or departure from the "Bragg scattering" within the oil slicks. In this work, we challenge these explanations by showing that instrument noise can easily account for observed signatures from SNR oil slick surfaces in the H/α space.

Two features that are frequently used in the compact-polarimetric studies (see, e.g., [5], [63]–[67]), namely the degree of polarization (DoP) and the ellipticity angle (χ) are investigated. Both are calculated from the Stokes vector from a hybrid-polarity SAR system. Reciprocity ($S_{HV} = S_{VH}$) is often assumed when calculating the Stokes vector. The influence of system noise might be different in the Stokes vector with and without the reciprocity assumption. To investigate this, we generate two sets of Stokes vectors (reciprocity and non-reciprocity) resulting in two sets of DoP and χ features. A $DoP = 1$ corresponds to fully polarized (fully deterministic) scattered wave, which is equivalent to $H = 0$ [68]. Low DoP values has been reported in oil-covered areas [5], [65], [66]. This has been explained by the presence of non-Bragg scattering characterized by "high depolarization" of the backscattered signal from the oil slick surface. The DoP also exhibits poor detection performance using high SNR airborne data [13]. Here we investigate whether system noise is the more likely explanation of these effects, as indicated in [13].

Studies have observed a sign-reversal of the χ (see, e.g., [66]) for mineral oil slicks. The sign-reversal of the mineral oil slicks was explained in [69] to be caused by different scattering mechanisms between the oil-covered and clean sea surfaces. However, this sign-reversal was only observed in the spaceborne satellite, RS-2, and not in the UAVSAR data. This study investigates whether the system noise is the cause of this "sign-reversal", and not differences in the scattering process between oil and clean sea surfaces. This was also suspected, but not verified in [45].

V. DATA

Polarimetric information was acquired from a set of eight RS-2, three TS-X, and three UAVSAR scenes with various types of oil, metocean conditions, range of incidence angles, NESZ values, and signal return from oil slicks and clean sea. The data are radiometrically calibrated and a 9×9 filter mask is applied to all the scenes when calculating the polarimetric features. When radiometrically calibrating the TS-X data we do not subtract the estimated noise powers in the HH and VV channels as described in the calibration stage in the TS-X product description [18]. This is because we want to be consistent in comparing the measured scattering vector from all sensors. Table III lists sensor properties, time of acquisition, wind information, incident angle, NESZ, and the estimated MNR used in this study.

All these scenes were acquired during a series of oil-on-water exercises in the North Sea from the years 2011, 2012, 2013, 2015, and 2016, respectively. The wind speeds range from 1.3 to 8 m/s (see Table III). The reader is referred to [2], [14], [47] for additional information about these exercises. The data from the UAVSAR and RS-2 used in this study were acquired in the quad-polarimetric (QP) SAR mode, i.e., transmitting and receiving on both the horizontal and vertical polarization channels. The TS-X scenes were acquired with the HH-VV dual-polarimetric SAR mode. The first three TS-X scenes overlap with three of the RS-2 scenes with less than one hour time difference (see [47]). All the scenes capture different concentrations of mineral oil in the oil-water mixtures. The scenes (TS-X and RS-2) from 2011 also contain crude oil.

TABLE III

SENSORS USED, TIME OF ACQUISITION, WIND INFORMATION AROUND ACQUISITION TIME, MEAN INCIDENCE (INC.) ANGLE, NOMINAL MEAN NESZ, AND ESTIMATED MNR. THE QUAD-POLARIMETRIC MODE WAS USED WHEN THE UAVSAR (L-BAND) AND THE RS-2 (C-BAND) SCENES WERE ACQUIRED. ALL THE TS-X (X-BAND) SCENES WERE ACQUIRED IN THE SSC (SINGLE-LOOK COMPLEX) DUAL-POLARIMETRIC (DP) (HH-VV) STRIPMAP MODE. THE WIND INFORMATION IS FROM [47], [70]. TWO MNR VALUES ARE GIVEN FOR RS-2 SINCE THE RANGE AMBIGUITY LEVEL CHANGES DEPENDING ON THE BEAM USED.

Sensor	Date (Time UTC)	Wind m/s	Inc. angle (°)	NESZ (dB)	MNR (dB)
UAVSAR	09-06-2015 (09:56)	5	55-66	-44	-16.76
UAVSAR	11-06-2015 (08:46)	8	41-44	-51	
UAVSAR	11-06-2015 (09:18)	8	54-57	-45.5	
RS-2	08-06-2011 (06:00)	1.6-3.3	47	-33	-11.21
RS-2	08-06-2011 (17:28)	1.6-3.3	36	-34	-11.38
RS-2	15-06-2012 (06:20)	4	31	-35	-11.38
RS-2	15-06-2012 (17:49)	3	49	-31	-11.21
RS-2	11-06-2013 (17:20)	5	29	-36	-11.38
RS-2	11-06-2015 (17:27)	6	36	-34	-11.38
RS-2	15-06-2016 (06:07)	7	42	-32	-11.38
RS-2	15-06-2016 (17:36)	8	41	-33	-11.38
TS-X	08-06-2011 (06:23)	1.6-3.3	28	-23[a]	-13.88
TS-X	08-06-2011 (17:12)	1.6-3.3	21	-23[a]	
TS-X	15-06-2012 (17:29)	3.5	41	-23[a]	

[a] Two NESZ in VV and HH channels and the mean of the two are taken.

ROIs are extracted from each SAR scene. For each oil slick ROI, there is a corresponding clean sea ROI at approximately the same incidence angle. This is done to avoid any incidence angle effects when comparing the oil and clean sea ROIs.

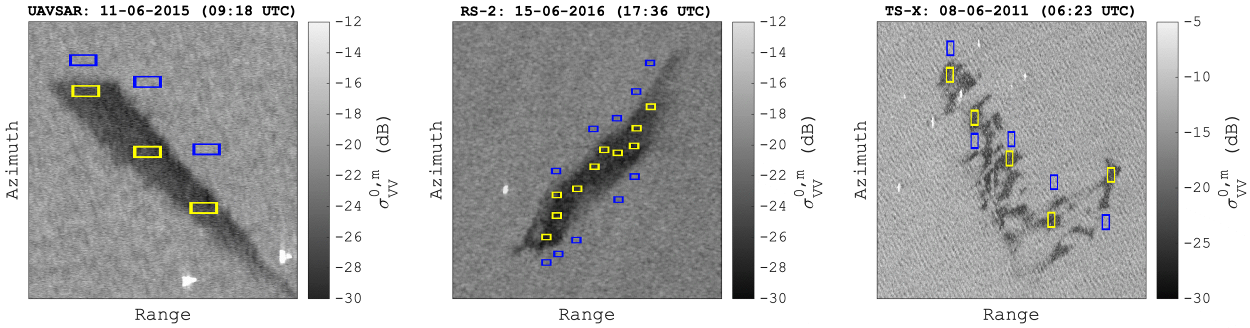

Fig. 1. VV-intensity (in dB) images of UAVSAR, Radarsat-2 (RS-2), and TerraSAR-X (TS-X) covering oil slicks from one of the oil-on-water exercises in the North Sea. The blue ROIs represent clean sea, while the yellow ROIs represents oil-contaminated areas. The scenes are cropped and scaled for display purposes.

There are between 4-10 non-overlapping ROIs within each UAVSAR, RS-2, and TS-X scene. The number of ROIs per scene is constrained by the slick size and our 9×9 pixel averaging window. Further, the surrounding ships are masked out along with a large portion of the pixels spanning the range and azimuth direction from these ships. This is done to eliminate undesirable sidelobe effects from these bright targets in the scene (see Section II). Second, the same number of pixels (728 corresponding to the size of the smallest ROI) are selected at random within the various sized ROIs. A representative scene and the corresponding ROIs from each of the three sensors is shown in Fig. 1.

The mean measured RCS of a set of pixels randomly selected within these ROIs are displayed in Fig. 2 as a function of SNR^A (signal-to-additive noise ratio) (left panels) and mean incidence angle (right panels). The right panels of Fig. 2 shows lines spanning the 5th and 95th percentiles, the mean intensity (marker), and the nominal NESZ. From the top-left panel in Fig. 2, the separation of the VV backscatter values by frequency (X-, C-, and L-band) is readily seen. For a given surface roughness, X-Band (TS-X) tends to give brighter returns than C-Band (RS-2), which is in turn brighter than the longer wavelength L-Band (UAVSAR). Some VV backscatter data points from both RS-2 and TS-X have mean intensity values close to the noise floor. Whereas some HH backscatter data points from RS-2 have mean intensity values below the noise floor. All the UAVSAR data points from both the HH- and VV-intensity measurements are well above the noise floor. Most of the HV-intensity values from RS-2 have SNR^A values below 3dB and most of the signals from oil and clean sea are below the noise floor (see bottom panels of Fig. 2).

The range of the incidence angles for RS-2 and TS-X spans $20° - 40°$. For UAVSAR, the range of incidence angles is slightly higher at $40° - 65°$. There is a trend of increasing decreasing intensity values as the incidence angle increases in each of the media (oil and clean sea), for RS-2 and TS-X (see the right-most panels of Fig. 2).

The impact of wind is challenging to observe for this study, since the incident angle is not constant across the scenes. In theory, the backscatter increases with wind speed due to the increase in small-scale ocean surface roughness, and the backscatter decreases with increasing incidence angle. For example, at high incidence angle and low wind speeds more contributions from system noise is expected. For this study the objective is to observe trends between polarimetric feature values and contribution from various noise sources in the Bragg scattering region (wind speed in 3-12 m/s and incidence angles in $20° - 60°$ [71]).

Cross-talk between co- and cross-polarization measurements might be significant for some of the UAVSAR measurements. This is because the additive noise floor (NESZ) in UAVSAR data is low ($<$ -40dB), and mean VV backscatter values range from -17dB to -32dB, whereas the mean HV backscatter values range from -35dB to -42dB, approximately (see Fig. 2). This yields a difference of $>$10dB, and the cross-polarization channel could have contributions from the copolarization channels. For this study, the features based on the cross-polarization are H, α, DoP, and χ, which might be particularly exposed to the cross-talk contamination.

VI. IMPACTS OF MULTIPLICATIVE NOISE IN SNR

In this study, both the additive and multiplicative noise is used in estimation of the SNR. Common practice is to only calculate the SNR based on the additive noise power, i.e., NESZ. A reason for this is that the NESZ often is available in the product file of various sensors, whereas the multiplicative factors are often left out. Unfortunately, the SNR will be overestimated because of this, and taking proper account of the multiplicative noise components will reduce the SNR values (see, e.g., [34]). Therefore, this section demonstrates the effects of including the multiplicative noise components, namely the ISLR (for all sensors), quantization noise (for RS-2 and UAVSAR), and the ambiguity ratio (for all sensors). The SNR^A (signal-to-additive noise ratio) is estimated using (3). The SNR^{A,M} (signal-to-additive and multiplicative noise ratio) is estimated using (4), where the ISLR values (linear units) of each sensor (see Table I) is used and the mean of clean sea pixels within all ROIs in each scene is set to σ^{AVG}. Fig. 3 shows the relationship between SNR^A and SNR^{A,M} using the VV and HH channels, where SNR^{A,M} is lower than SNR^A. With the SNR$^A_{VV}$, all the data points are located above 0dB, which is no longer the case with the SNR$^{A,M}_{VV}$, where most of

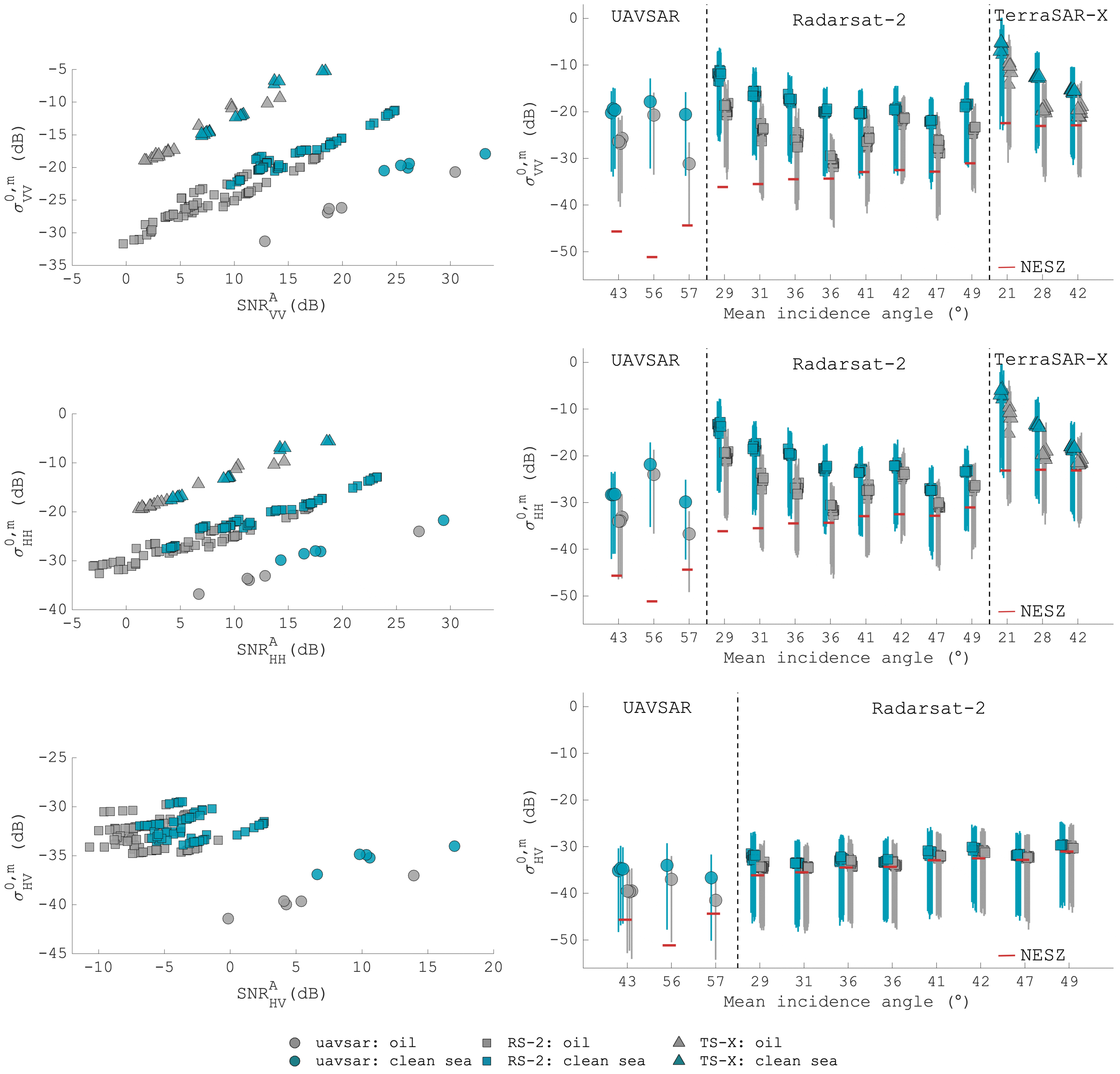

Fig. 2. Left panels; mean intensity values versus the signal-to-noise (SNR) ratio in dB based on the additive noise power (labeled SNR^{A}) for the three polarization channels (VV, HH, and HV, respectively). Right panels; The 5th, mean intensity, and 95th percentiles for each slick and clean sea region versus the mean incidence angle for each scene. The gray lines are slightly shifted to left in order to improve the discrimination in the plot. The bottom panels show the HV channel, where there are no ROIs from the TS-X scenes since these were acquired in the HH-VV dual-polarization SAR mode.

the oil data points from RS-2 now have SNR^{A,M} below 0dB, indicating little signal from the oil slick itself. The oil and clean sea markers for TS-X are located close to the red line indicating that SNR^{A} and SNR^{A,M} are very similar. All the markers from the UAVSAR have SNR^{A,M} values above 10dB, except for one oil marker that has SNR^{A,M} around 7dB.

The multiplicative noise contribution tends to dominate for high SNR^{A} values. For example, the SNR$_{VV}^{A,M}$ and SNR$_{HH}^{A,M}$ is on average 11.2dB and 5.3dB lower than SNR$_{VV}^{A}$ and SNR$_{HH}^{A}$ for the oil slick areas in the UAVSAR. For the oil slicks areas in RS-2, the SNR$_{VV}^{A,M}$ and SNR$_{HH}^{A,M}$ is on average 8.7dB and 6.7dB lower than SNR$_{VV}^{A}$ and SNR$_{HH}^{A}$. Finally, for the oil slicks areas in TS-X, the SNR$_{VV}^{A,M}$ and SNR$_{HH}^{A,M}$ is on average 2.8dB and 2.5dB lower than SNR$_{VV}^{A}$ and SNR$_{HH}^{A}$.

VII. RESULTS AND DISCUSSION

This section is divided into three subsections reflecting the objectives presented in Section I. Subsection (1) presents and discusses the feature sensitivity to the additive and multiplicative noise power. Subsection (2) demonstrates how the noise

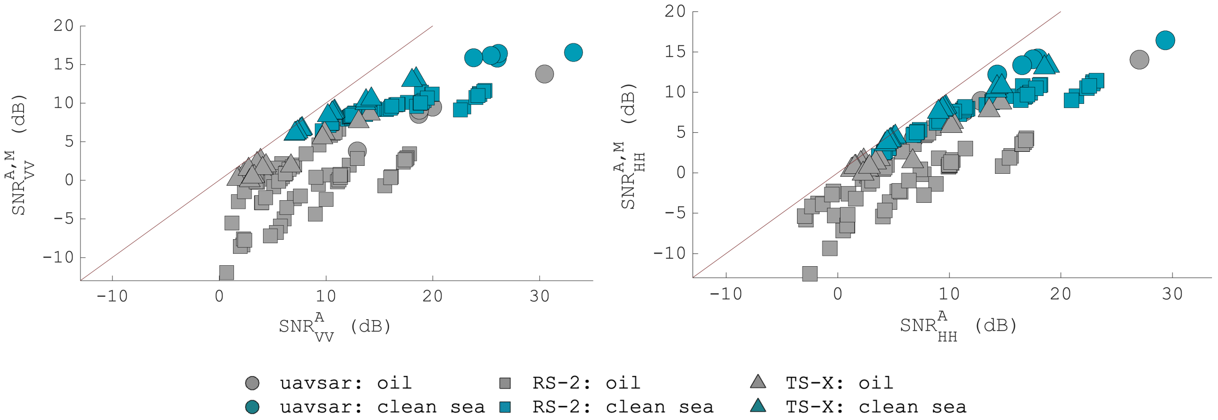

Fig. 3. Relationship between the mean SNR^{A} (signal-to-additive noise ratio) versus the mean SNR^{A,M} (signal-to-additive and multiplicative noise ratio) for the UAVSAR, RS-2, and TS-X ROIs. The red line is where SNR^{A} and SNR^{A,M} are equal.

affects the H/α decomposition, and how the SNR threshold is identified. Finally, subsection (3) illustrates how each of the different features behaves when the additive noise power is subtracted.

(1) Feature sensitivity to additive and multiplicative noise

We aim to provide an understanding of the sensitivity to both the additive and multiplicative noise for the set of features investigated, and to further highlight which features are strongly affected by the noise for the two investigated media (oil and clean sea). Figs. 4-7 show the mean of a given feature for a set of ROIs plotted against the SNR$^{A}_{HH}$ (left panels) and SNR$^{A,M}_{HH}$ (right panels) in dB. The continuous lines show the results of our simulations of adding noise to the high-SNR UAVSAR data (see Appendix C). The simulated noise power plots are not shown for PD and r_{CO}, which is due to the fact that the simulated noise powers cancels in the calculation of PD and decorrelates in r_{CO}. For RS-2 and TS-X the SNR$^{A}_{HH}$ is calculated from the RCS and the NESZ given in the product file, and for the UAVSAR the 5th order polynomial with updated coefficients are used (similar to [26]). The SNR$^{A,M}_{HH}$ is calculated from (4) with MNR given in Table III. Because both SNR$^{A}_{HH}$ and SNR$^{A,M}_{HH}$ are functions of $\sigma^{0,m}_{HH}$, the values plotted are the mean for the same set of pixels randomly selected within each ROI.

Polarization difference (PD)

In the left panels of Fig. 4, lower PD values of the oil-covered areas compared to the clean sea regions can be seen. This observation corroborates previous findings [47]. The reduction in PD due to the presence of oil is most likely caused by the dampening of the ocean surface roughness [48]. The PD is expected to be close to zero for pure random noise, assuming the noise in the HH and VV channels are similar. A slight trend of increasing PD values with SNR$^{A}_{HH}$ and SNR$^{A,M}_{HH}$ for all the three sensors is observed, especially for the oil markers. However, there is a wide spread in the PD values across the SNR$^{A}_{HH}$ which might be interpreted as sensitivity to the oil properties and metocean conditions, that vary across the scenes used in this analysis. However, less spreading is observed for the SNR$^{A,M}_{HH}$, which are more consistent with a simple, downward linear trend of decreasing PD with decreasing SNR.

In conclusion, the downward trend in PD due to the presence of oil is entirely consistent with a Bragg scatter model for which the VV backscatter is greater than the HH (the high SNR case), with increasing levels of noise added for which the HH and VV expected values are the same, and therefore $PD \rightarrow 0$ (the low SNR case).

Real part of the copolarization cross product (r_{CO})

The oil has lower r_{CO} (real part of the copolarization cross product) values than the clean sea (right panels of Fig. 4). Again, this matches previous findings [2], [47], [72]. The authors of [72] explained this observation as the presence of a non-Bragg scattering process within the oil slick. However, our SNR$^{A,M}_{HH}$ results show a simple downward linear trend in r_{CO} as SNR decreases. The reduction of the r_{CO} values in the presence of oil is therefore most likely related to the low backscattering return from the oil slick, resulting in high influence of the decorrelation effects from system noise. The expected value of r_{CO} for pure random noise is 0. r_{CO} values are high at lower incidence angle, where less noise is expected, for all three sensors. At high incidence angle (small markers in the right panels of Fig. 4) the r_{CO} is

For r_{CO}, the results for different radar frequencies are differentiated at higher SNR; these results indicate that for this particular parameter, X-band is more sensitive to oil characteristics than C-band, which is more sensitive than L-band. No other parameter shows this clear separation between all three bands.

Copolarization ratio ($\gamma_{HH/VV}$)

Applying a tilted Bragg model, the $\gamma_{HH/VV}$ values from the oil slick areas are expected to be slightly larger than for

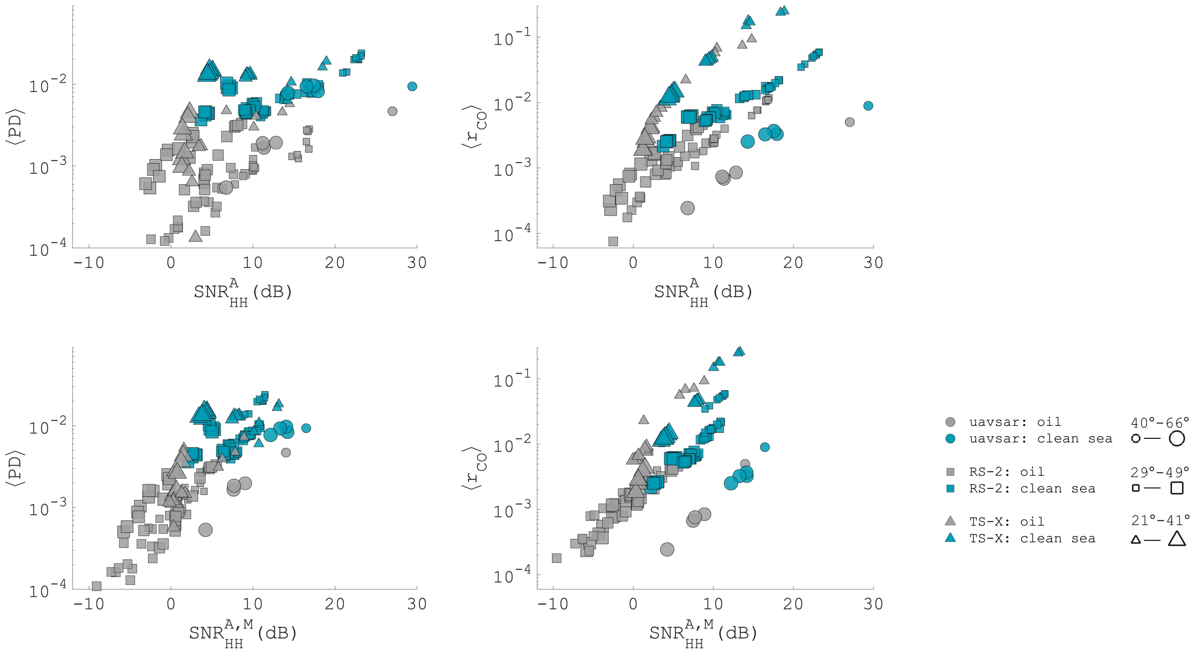

Fig. 4. Top: mean of PD and r_{CO} versus SNR$_{HH}^{A}$(dB). Bottom: mean of PD and r_{CO} versus SNR$_{HH}^{A,M}$(dB). A log-scale is applied on all y-axis to better illustrate the trend. The expected PD and r_{CO} of pure noise is 0 in linear units.

the clean sea areas, depending on the concentration of oil on the surface [10]. This fits our high SNR observations in the left panels of Fig. 5. For pure random noise, $\gamma_{HH/VV}$ is close to 1 (see Table IV), as illustrated with the "N" symbol in Fig. 5. For the clean sea results, larger sized markers indicating a higher incidence angle, are located below the smaller markers for each sensor, confirming that $\gamma_{HH/VV}$ decreases as a function of increasing incidence angle (see, e.g., [10], [12]). Similar to the PD results, we again see a wide spread in the oil slick $\gamma_{HH/VV}$ values across the SNR$_{HH}^{A}$ which can be interpreted as sensitivity to the oil properties and metocean conditions. Again the large spread in values for clean ocean even at high SNR, a strong dependence on metocean conditions is likely consistent with [12]. But less spreading is observed for the SNR$_{HH}^{A,M}$ results and, in general, $\gamma_{HH/VV}$ increases with decreasing SNR$_{HH}^{A}$ and SNR$_{HH}^{A,M}$. This trend matches well with our simulations of adding increasing levels of noise to the UAVSAR (continuous lines), and corroborates the observations of Minchew et al. [10] at high incidence angles. Here the increasing dominance of noise over backscatter explains the $\gamma_{HH/VV}$ observations, with this feature eventually approaching the value 1 with increasing noise power.

Magnitude of the copolarization correlation coefficient (ρ_{CO})

According to the literature, the ρ_{CO} feature tends to generate higher values for clean sea compared to oil-covered surfaces (see Section IV). The center panels of Fig. 5 supports this, as most of the clean sea markers are above the oil markers. If the measured signal is heavily contaminated by noise, the expected ρ_{CO} value is 0, as indicated by the "N" symbol in Fig. 5. Adding noise to the UAVSAR data results in decreasing ρ_{CO} values as both the SNR$_{HH}^{A}$ and SNR$_{HH}^{A,M}$ decreases. The spaceborne markers (squares and triangles) align well with the UAVSAR simulations, once all the noise sources are properly accounted for (right-hand panel). This was also pointed out in [13], where the instrumental noise induced a decorrelation effect between the HH and VV. Note that ρ_{CO} is not exactly 1 for the high-SNR clean sea UAVSAR data; for which $SNR_{HH}^{A} = 30$dB and $SNR_{HH}^{A,M} = 18$dB, which can be explained by the presence of multiplicative noise (which lowers the effective SNR) once that is taken into account (right-hand panel). The reduction in ρ_{CO} for the oil in all cases is most likely due to system noise and not to exotic scattering properties within the oil.

Standard deviation of the copolarization phase difference ($\sigma_{\phi_{CO}}$)

As shown in right panels of Fig. 5, $\sigma_{\phi_{CO}}$ has lower values for clean sea than for oil slicks. This observation has also been reported in previous studies (see, e.g., [54]–[57]). The $\sigma_{\phi_{CO}}$ is uniformly distributed, and the expected value of $\sigma_{\phi_{CO}}$ for pure Gaussian noise is 1.81 (see Table IV Appendix A). The $\sigma_{\phi_{CO}}$ values tend to increase with decreasing SNR$_{HH}^{A}$ and SNR$_{HH}^{A,M}$ values (see center panels of Fig. 5), consistent with our simulations adding noise to the UAVSAR results.

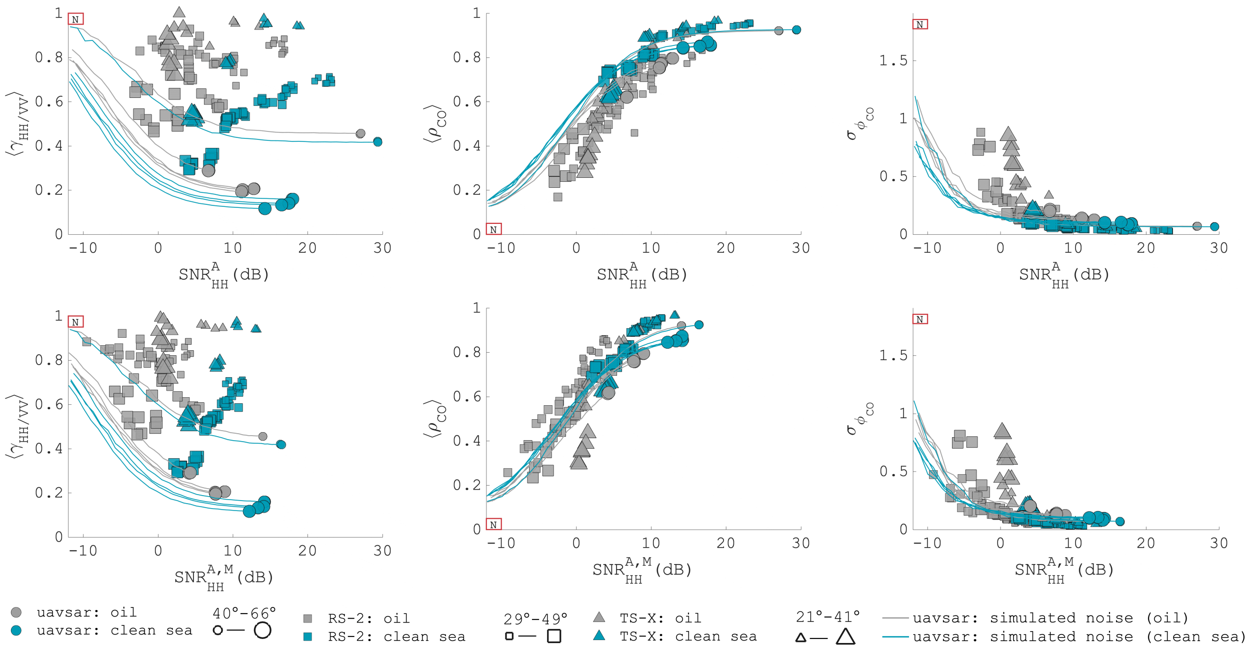

Fig. 5. Top: mean of $\gamma_{HH/VV}$, mean of ρ_{CO}, and standard deviation of ϕ_{CO} versus SNR$^{A}_{HH}$(dB). Bottom: mean of $\gamma_{HH/VV}$, mean of ρ_{CO}, and standard deviation of ϕ_{CO} versus SNR$^{A,M}_{HH}$(dB). The circular markers are the mean values of the ROIs from the UAVSAR data, while grey and blue continuous lines represent the degree of simulated noise power added to the UAVSAR. The legend of incidence angle ranges is on the bottom. The box with "N" is the expected feature value of Gaussian white noise (see Table IV in Appendix A).

As pointed out in [45] and confirmed by Fig. 5, this extreme broadening of the HH-VV phase difference distribution is most likely due to instrumental noise rather than a different type of scattering within the oil slicks.

Entropy (H_{CO} and H)

Higher entropy values (both H and H_{CO}) are observed for the oil than the clean sea, which matches previous findings (see, e.g., [6], [56], [60]–[62]). However, this difference is mainly due to higher noise contribution in the measured oil slick signal compared to the signal from the clean sea. The left and center panels of Fig. 6 support this, where both H and H_{CO} increase with decreasing SNR$^{A}_{HH}$ and SNR$^{A,M}_{HH}$, following the trend lines for the simulated noise added to UAVSAR data. The correspondence is more marked in the SNR$^{A,M}_{HH}$ results. The high entropy is clearly related to the high noise power in the data, and not differences in scattering processes between oil and clean sea.

Mean alpha angle (α)

Higher α values are observed for the oil than for the clean sea. This aligns with previous findings, but the more likely explanation for higher α values is higher noise power, rather than different scattering properties between the clean sea and the oil. Complex Gaussian white noise will have a mean α value of 60°. The observations of α shown in the right panels of Fig. 6 increase towards 60° as the SNR$^{A}_{HH}$ and SNR$^{A,M}_{HH}$ decreases. Again, the SNR$^{A,M}_{HH}$ results fit better with the simulated noise at lower SNR values, compared to SNR$^{A}_{HH}$. The discussion on the H and α continues in subsection (2), where the noise effects on the H/α space are investigated.

Degree of polarization (DoP)

In the left panels of Fig. 7, the color-filled squares and circles for each class (oil and clean sea) represent the non-reciprocity case, and the DoP values for which reciprocity is assumed are indicated by non-filled boxes and circles. The continuous lines represent the noise added to the UAVSAR data when reciprocity is not assumed, while the dashed lines are for the scenario in which reciprocity is assumed. There is a clear difference between the clean sea and the oil markers, where lower DoP values of the oil are observed for both the reciprocity and the non-reciprocity case. The expected value of DoP for Gaussian white noise is 0 for non-reciprocity and 0.5 with the reciprocity assumption. In general, the DoP increases with increasing SNR$^{A}_{HH}$ and SNR$^{A,M}_{HH}$ (see left panels of Fig. 7). As pointed out in [68], the DoP feature is similar to $1-H$, where low DoP indicates high depolarization. The DoP has been used to measure the departure from Bragg, and as shown here, the observed departure from Bragg ($DoP \approx 1$) occurs at low SNR. At low SNR$^{A}_{HH}$ and SNR$^{A,M}_{HH}$ the DoP

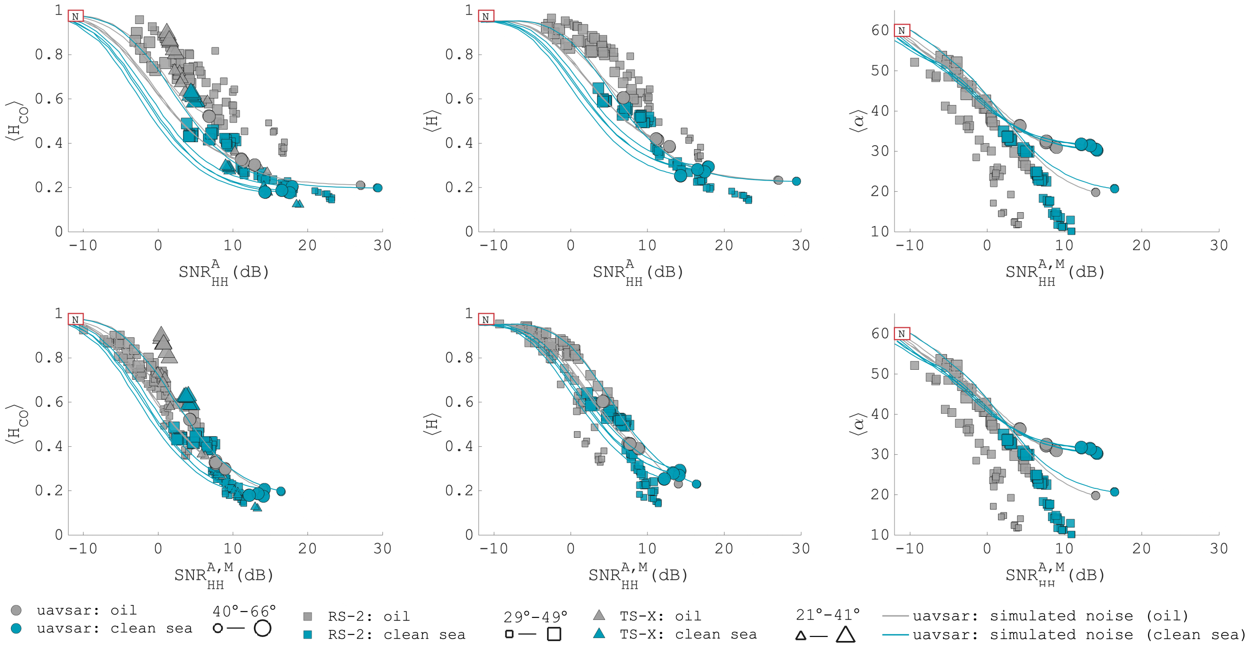

Fig. 6. Top: mean of H_{CO}, H, and α versus SNR^{A}_{HH}(dB). Bottom: mean of H_{CO}, H, and α versus $\mathrm{SNR}^{A,M}_{HH}$(dB). The circular markers are the mean values of the ROIs from the UAVSAR data, while grey and blue continuous lines represent the degree of simulated noise power added to the UAVSAR data. The legend of incidence angle ranges is given on the bottom. The box with ”N” is the expected feature value of Gaussian white noise (see Table IV in Appendix A).

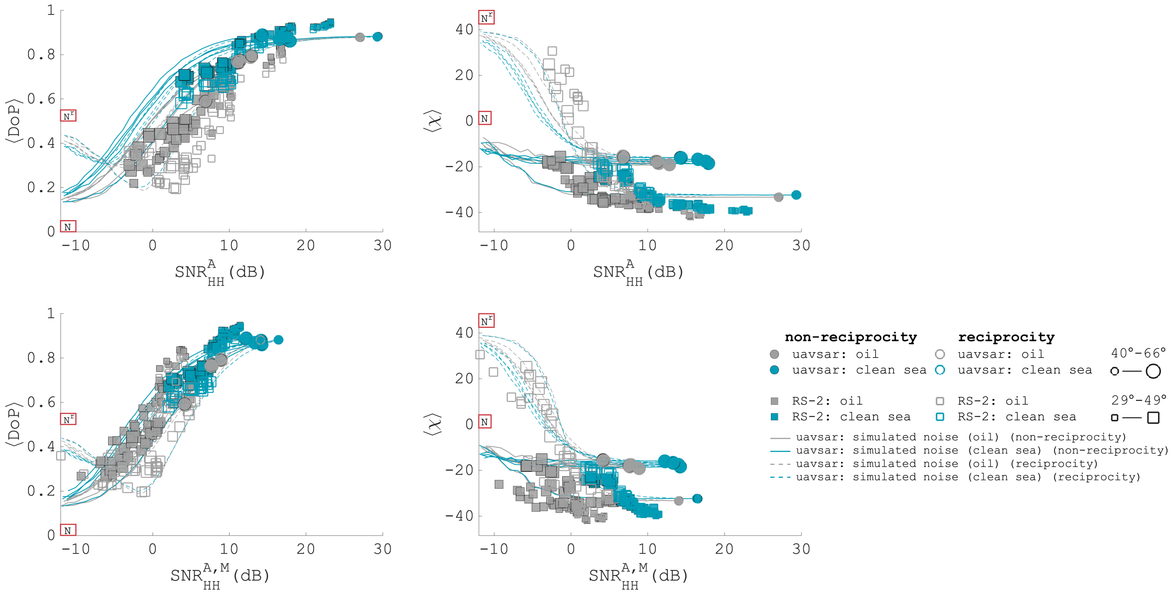

Fig. 7. Top: mean of DoP and χ versus SNR^{A}_{HH}(dB). Bottom: mean of DoP and χ versus $\mathrm{SNR}^{A,M}_{HH}$(dB). The circular markers are the mean values of the ROIs from the UAVSAR data, while grey and blue continuous (dashed) lines represent the degree of simulated noise power added to the UAVSAR data for the non-reciprocity (reciprocity) case. The boxes with ”N^{r}” and ”N” are the expected feature value of Gaussian white noise for reciprocity and non-reciprocity cases (see Table IV in Appendix A).

starts to increase for the reciprocity-assumed case, which is a result of the extra noise component in S_3 of the DoP expression (see Appendix B). Again, the $\text{SNR}_{HH}^{A,M}$ fits better with the simulated noise compared to SNR_{HH}^{A}. The strong correlation of the DoP values with the SNR_{HH}^{A} in Fig. 7 matches the observation in [13].

Ellipticity angle (χ)

Like the DoP, the χ is calculated from two Stokes vectors (reciprocity and non-reciprocity assumed case). Few differences between the oil and the clean sea markers can be seen for the non-reciprocity case in the right panels of Fig. 7. As the noise increases the mean of the χ approaches the value 0. In general, χ is always positive for the non-reciprocity case, but a decreasing trend of the χ as the SNR_{HH}^{A} and $\text{SNR}_{HH}^{A,M}$ increases is identified. However, for the reciprocity case, the χ of both the real and simulated noise have a more rapid decrease with increasing SNR_{HH}^{A} and $\text{SNR}_{HH}^{A,M}$. Again, the $\text{SNR}_{HH}^{A,M}$ fits the simulated noise better. This is easily explained by the extra noise component in S_3, for which a clear sign-reversal is identified when the noise power increases. The only factor contributing to the sign-reversal is the S_3 parameter since this is the only component in χ that can either be negative or positive (see Appendix B). χ is also affected by the reciprocity assumption, especially at low SNR. Therefore, the presence of a sign-reversal in χ for oil spill data in polarimetric SAR is accounted for by noise.

(2) Noise in the H/α decomposition

The motivation behind this section is to investigate the behavior of the H/α space as a function of both the SNR^{A} and $\text{SNR}^{A,M}$ using only real data from RS-2 and UAVSAR. The H and α are both calculated from the 3×3 sample coherency matrix using a 9×9 averaging filter mask.

The ocean backscatter is dominated by resonance scattering also known as Bragg scattering, within the SAR incidence angles $20^\circ - 60^\circ$ (see, e.g., [71]), and for low to moderate wind $3 - 12$ m/s. The H/α space has been used frequently to interpret the scattering properties (see, e.g., [6], [10], [56], [60]–[62]). Minchew et al. [10] observed Bragg scattering within the oil slick region using UAVSAR data. The authors concluded that the departure from the Bragg region within the oil slick was mainly due to the instrumental noise, which is verified here based on Fig. 8. The Bragg scattering region (see [59]) is defined within the black boxes in Fig. 8 and the markers are colored based on their SNR_{HH}^{A} (top panels) in dB. Similar results applies for SNR_{HH}^{A}, which is not shown, but the SNR values are higher with VV compared with HH. Each marker represents one pixel from the set of 728 pixels that are randomly selected within each ROI.

The majority of the oil markers fall outside the Bragg region due to the high level of noise. This confirms the observations in [10] and the discussion in [45]. There is a remarkable correlation between increasing α and H values as the SNR^{A} decreases, and a decrease in SNR^{A} results in a clear departure from the Bragg region. The clean sea markers are, as expected, mostly located within the Bragg region. But even here, when the additive noise power increases some markers fall outside this region.

The center and bottom panels in Fig. 8 show blue and red histograms, that are calculated based on SNR_{HH}^{A} and $\text{SNR}_{HH}^{A,M}$ values originated from the Bragg scattering region (blue) and outside this region (red). These panels contain information about the SNR threshold that is recommended before the data is too contaminated by the additive and multiplicative noise for any meaningful polarimetric scattering analysis.

The peak overlap within the blue and red histograms is around SNR_{HH}^{A} =10dB. Considering the bottom panels of Fig. 8, this peak overlap within the red and blue histograms varies between 0-8dB for the $\text{SNR}_{HH}^{A,M}$, where no clear threshold is observed. The oil markers inside the Bragg region in the top panel of Fig. 8 indicate a higher signal return compared to the oil indicated by markers outside this region. Unfortunately, the contribution from the multiplicative noise sources is high inside the Bragg region despite the high SNR_{HH}^{A} for the oil (larger than 10dB). In the bottom-left panel of Fig. 8, the mean and standard deviation of the $\text{SNR}_{HH}^{A,M}$ inside the box (Bragg region) are 3.2 ± 1.8dB. Since the H/α is extremely sensitive to the presence of noise, we conclude that the H/α is not recommended for extracting information about the scattering properties within oil slicks, at least with existing sensors that do not have much higher SNR for oil returns.

(3) The impact of subtracting the additive noise

This section shows the effect of subtracting the additive noise from the covariance/coherency matrix prior to calculating the features, and whether this procedure can produce reliable feature value of low-backscattered targets like the oil slick as studied here. Only scenes from RS-2 are used. In this part of the study, we only consider the additive noise component (not the multiplicative noise factor) since it is unclear how the multiplicative noise impacts the off-diagonal elements in the coherency matrix, and subtracting the additive noise is a common procedure in the literature [10], [73]–[76]. The noise cannot be removed from the complex target scattering matrix, but previous studies have subtracted the noise power from the diagonal elements in the second order sample covariance matrix (see, e.g., [73]–[76]). The features investigated in this work can all be estimated from either the sample covariance or the coherency matrix, allowing us to evaluate the effect of the noise subtraction. The nominal NESZ provided in the RS-2 product file of each scene is used when subtracting the noise power from the sample covariance/coherency matrix. This is because the estimated NESZ values using the method suggested in [75] and [76] shows close to the same values as the nominal NESZ (see Appendix D).

Fig. 9 shows the feature sensitivity to the noise subtraction using only the RS-2 ROIs from both the oil-covered (squares) and the clean sea (diamonds) surfaces. Noise subtraction can only be performed for the set of features that are function of one or more intensity components. The r_{CO} and PD are left out in Fig. 9, since noise subtraction will not have any effect in these two features. Recall, r_{CO} is the real part of the correlation between the complex HH and VV measurements. The complex noise components decorrelate with each other and to the signal (see (7)), and is therefore not a function of the noise power (σ^n). The PD is the difference between the VV and HH intensities, and only one noise power in HH and VV channels are provided and assumed equal. Hence, the two noise components in PD cancel.

All the features shown in Fig. 9 are affected by the noise subtraction. In general, the difference between the mean feature value between the original and the noise subtracted feature increases with the noise, i.e., SNR_{HH} decreases.

Recall from the previous section, that the $\gamma_{HH/VV}$ tends towards the value 1 as the noise power increases. Having a decrease in $\gamma_{HH/VV}$ after noise subtraction indicates that noise power contributed significantly to a higher $\gamma_{HH/VV}$ value, especially for the oil markers. The noise subtraction for the oil markers has a larger effect than for the clean sea markers, which is due to higher SNR for the clean sea than for the oil slick. Hence, the $\gamma_{HH/VV}$ values are more similar between the oil and clean sea after the noise subtraction.

For Gaussian white noise, the ρ_{CO} is 0. Hence, subtracting the noise should increase the ρ_{CO} values, which is clearly demonstrated in the top-center panel of Fig. 9. As pointed out in Section IV, previous studies found low ρ_{CO} for oil-covered areas, and this was explained by the different scattering properties between clean sea and oil-covered surfaces. Here, subtracting the noise resulted in similar ρ_{CO} values between the two classes, indicating that the variation in ρ_{CO} between the oil and the clean sea is most likely due to the additive noise.

Further, a decrease in both H_{CO} and H as a result of the noise subtraction is also demonstrated in the top-right and center-left panels of Fig. 9. This is expected as random noise contributes to high entropy values. However, there is still a trend with increasing entropy (both H_{CO} and H) as the SNR_{HH} decreases after noise subtraction. Since intermediate entropy values are expected also for oil-covered regions, subtracting the noise results in a more reasonable entropy value for the oil markers.

The α increases with the noise power for both the original and the noise subtracted markers. For Gaussian white noise, the α is expected to be in the area around 60° (see Table IV Appendix A). Based on the differences between the dashed and continuous lines, the α values after noise subtraction have decreased, especially for low SNR. The majority of the markers seems to be below $\alpha = 42.5°$, which is the upper threshold of the Bragg scattering region. We conclude that the noise subtraction has an effect on the α.

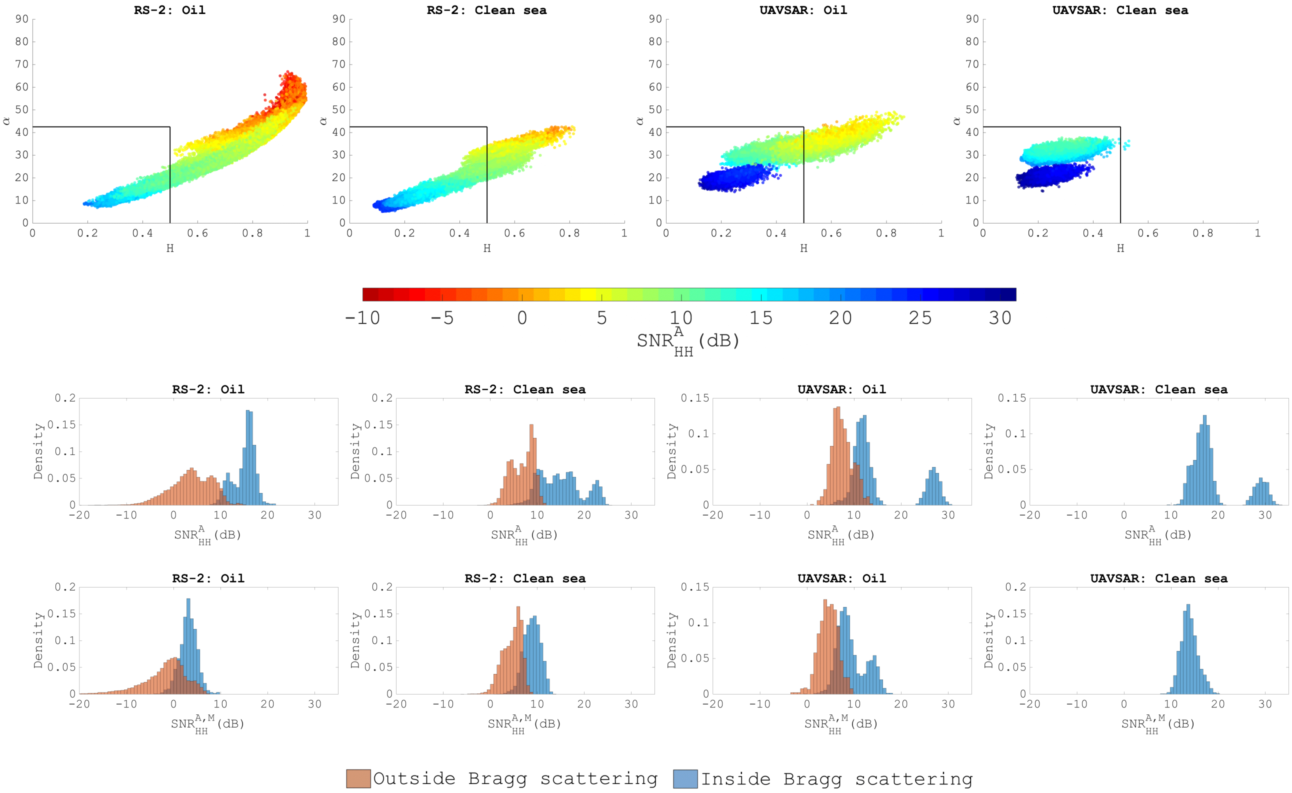

Fig. 8. H/α plots of RS-2 and the UAVSAR data containing clean sea and oil slicks. The difference in, e.g., incidence angle and metocean conditions might cause the difference between the colored markers within each panel. Top: the markers are colored based on the SNR^{A}_{HH} level. Center: histograms of the SNR^{A}_{HH} values inside and outside the Bragg scattering region. Bottom: histograms of the $\mathrm{SNR}^{A,M}_{HH}$ values inside and outside the Bragg scattering region.

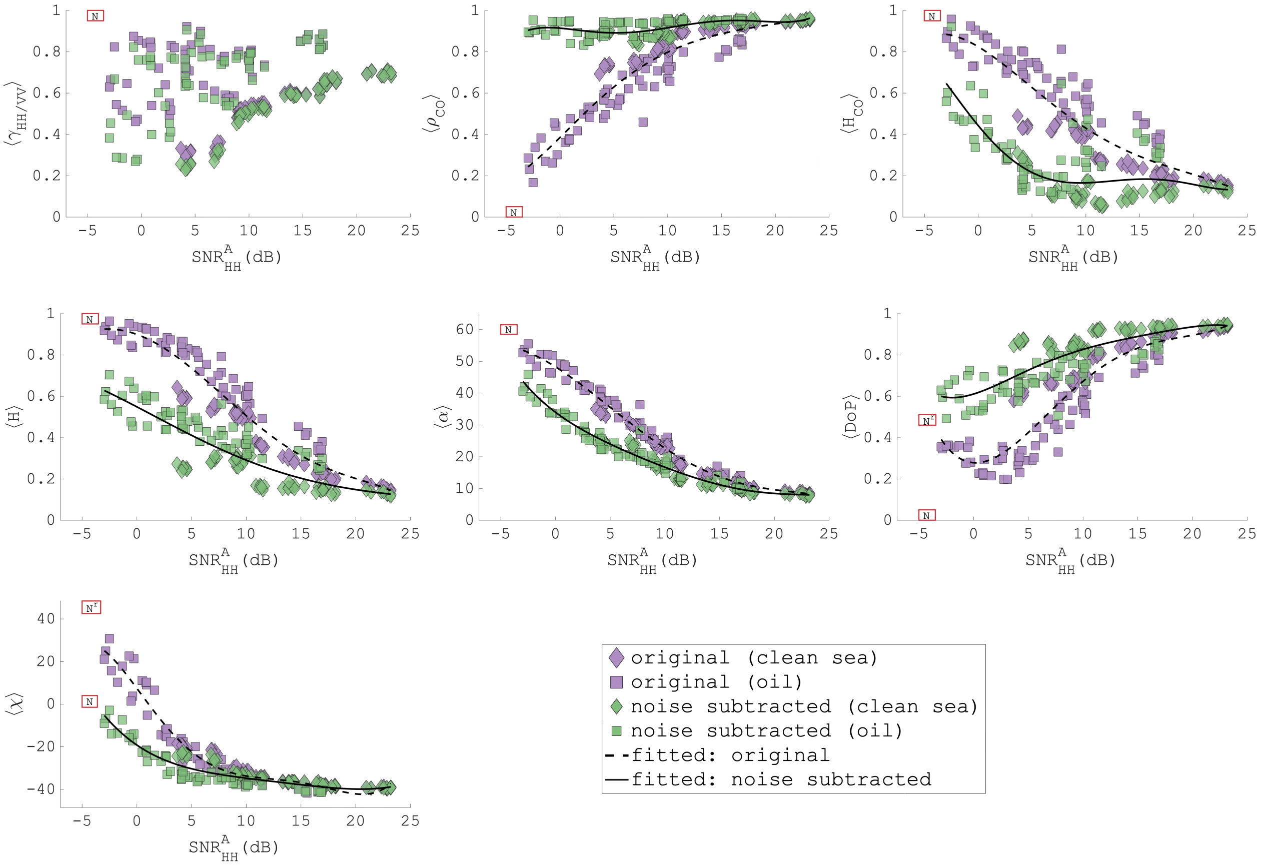

Fig. 9. The effect of noise subtraction on the mean feature value (of both clean sea (diamond) and oil (square) ROIs) versus the SNR_{HH} (dB) using RS-2 data. The box with the ”N” symbol is the expected feature value of pure random noise. The DoP and χ are from the reciprocity-assumed Stokes vector, but both ”N^r” and ”N” is shown.

Subtracting the noise resulted in similar DoP values between clean sea and oil, and higher values after the noise subtraction are identified (center-right panel of Fig. 9). This is expected as the noise will generate lower DoP values. In this panel, only the reciprocity-assumed DoP is used. The DoP is a child parameter from the Stokes vector, where the Stokes vector is calculated using the method presented in [63], which is based on the elements from the 3×3 covariance matrix, from which the noise is subtracted. After the noise subtraction the oil markers are almost aligned with the clean sea markers. Hence, the DoP shows a poorer contrast between the oil and the clean sea after the noise subtraction, and any oil/sea contrast seen in this feature can be explained by noise. As demonstrated in the previous section, the χ changed sign when the noise increased. A sign reversal is no longer visible after the noise subtraction, and most of the χ values are negative after this procedure. Thus, this feature becomes useless for oil spill detection due to similar values between the clean sea and oil markers.

VIII. CONCLUSIONS

The system noise in SAR data will have an influence on the interpretation of the scattering properties, particularly for low backscatter targets like oil slicks. Mischaracterizations can arise if all of the various noise sources (see Sections II and III) are not considered. Oil spill detection is still possible for noisy data, simply due to the marked contrast in the backscatter levels. This study explored the limitation of satellite SARs to perform reliable oil spill characterization using scattering properties from polarimetric features. Additionally, it might also be possible to identify regions of thicker oil within a slick, since thicker oil may have lower backscatter return. This is due to higher damping of the small capillary and gravity waves, and noise thus contributes a larger fraction of the measured signal than for thinner oil films.

This study shows the impact of including both additive and multiplicative noise factors in the estimation of the SNR. From spaceborne sensors such as RS-2 and TS-X, the majority of the measured signal is comprised of noise originating from various sources, dominating the backscattered signal from the oil itself. This is demonstrated by SNR^{A,M} having values close to or even less than 0dB. However, this is not the case for the UAVSAR, which has much higher SNR.

All the features investigated are influenced by both additive and multiplicative noise, some more than others. However, the PD, $\gamma_{HH/VV}$ and r_{CO} had highest spread in their feature values as a function of the SNR^{A}, which was reduced significantly for SNR^{A,M}. The remaining features (ρ_{CO}, H, H_{CO}, α, DoP, χ) simulated by adding noise to UAVSAR data show a similar trend with the corresponding feature extracted from TS-X and RS-2 data. This trend is observed at different incidence angles and low to moderate wind speed range (3-8 m/s). Additive noise has often been misinterpreted as random scattering within the oil layer that results in high H, H_{CO}, α, and low ρ_{CO} and DoP. This type of scattering has been given the name "non-Bragg". In this study, we find that there is no need to invoke such exotic scattering mechanisms – properly accounting for noise in the data means that Bragg scatter plus noise can adequately explain the observed results for both oil slicks and clean sea.

In the literature, high H and α values have been hypothesized and reported for mineral oil slicks. However, as demonstrated in this study, the high H and α values are most likely related to the high levels of system noise. With high SNR SAR data, e.g., from UAVSAR, the H/α values representing oil slick fall within the Bragg scattering region. We recommend that the SNR^{A} should be $\geq$10dB prior to any scattering theory analysis using polarimetry. No clear threshold was identified for SNR^{A,M}, and future analysis should therefore be performed to study this effect. Obviously, the majority of the measured signal from an oil slick should be from the oil slick itself and not other noise sources, indicating that the SNR^{A,M} should at least be above 0dB.

After noise subtraction, the features representing the oil slick had values similar to the ones from the clean sea areas, indicating that the performance of the oil slick detection might be compromised after noise subtraction. We conclude that subtracting the noise power should be performed prior to any polarimetric analysis for characterization purposes, and such measures should be used with a great deal of caution in oil slick detection.

Future studies could include a sensitivity analysis of noise contamination in various scattering models (e.g., tilted Bragg model [22]), and characterization of multiplicative noise effects on polarization features. Here we have treated MNR as another additive noise contribution, but there may still be subtle, residual correlations between MNR terms that we have not accounted for. Additionally, investigating how the noise influences the characterization of various oil types might also be valuable. Finally, we note that higher SNR instruments are needed to study oil characterizations with SAR.

ACKNOWLEDGMENT

The authors thank Yngvar Larsen at NORCE for his valuable comments and discussion in Section II, and A. Malin Johansson at UiT for valuable discussions and for helping to improve the manuscript. This research is financed in part by CIRFA (RCN Grant no. 237906). This research was carried out in part at the Jet Propulsion Laboratory, California Institute of Technology, under contract with the National Aeronautics and Space Administration (Task Order NNN13D788T). The Radarsat-2 and data Products ©MDA LTD. 2011-2013,2015,2016. TerraSAR-X ©DLR, and provided by InfoTerra. UAVSAR data can be downloaded from uavsar.jpl.nasa.gov or from the Alaska Satellite Facility (www.asf.alaska.edu).

APPENDIX A
THE EXPECTED FEATURE VALUE OF NOISE

Table IV contains the theoretical expected feature value of pure Gaussian random noise. These expected feature values could be a result of random/volume scattering from an ideal target (not the case for oil slicks), or specular reflection that has close to zero return towards the sensor and the measured signal is then dominated by system noise.

A. *Noise - ellipticity feature*

The ellipticity is defined as;

$$\chi = \frac{1}{2}\sin^{-1}\left(\frac{-S_3}{DoPS_0}\right) = \frac{1}{2}\sin^{-1}\left(\frac{-S_3}{\sqrt{S_1^2+S_2^2+S_3^2}}\right). \tag{8}$$

For non-reciprocity Stokes vector, where $S_1 = \frac{1}{2}(\sigma^n_{HH} - \sigma^n_{HV} + \sigma^n_{VH} - \sigma^n_{VV})$, $S_2 = 0$, and $S_3 = 0$ the χ^n is:

$$\begin{aligned}\chi^n &= \frac{1}{2}\sin^{-1}\left(\frac{-0}{\sqrt{(\frac{1}{2}(\sigma^n_{HH} - \sigma^n_{HV} + \sigma^n_{VH} - \sigma^n_{VV}))^2}}\right)\\ &= \frac{1}{2}\sin^{-1}(0) = 0.\end{aligned} \tag{9}$$

For reciprocity Stokes vector, where $S_1 = \frac{1}{2}(\sigma^n_{HH} - \sigma^n_{VV})$, $S_2 = 0$, and $S_3 = -\sigma^n_{HV}$ the χ^n is:

$$\begin{aligned}\chi^n &= \frac{1}{2}\sin^{-1}\left(\frac{-(-\sigma^n_{HV})}{\sqrt{(-\sigma^n_{HV})^2 + (\frac{1}{2}(\sigma^n_{HH} - \sigma^n_{VV}))^2}}\right)\\ &\overset{\sigma^n_{HH}\approx\sigma^n_{VV}}{=} \frac{1}{2}\sin^{-1}\left(\frac{1}{1}\right) = \frac{1}{2}(90^\circ) = 45^\circ.\end{aligned} \tag{10}$$

In the last part of (10), we assume equal noise power in the two copolarization channels $\sigma^n_{HH} \approx \sigma^n_{VV}$ (often assumed, see e.g., [74]).

APPENDIX B
NOISE IN THE STOKES VECTOR

The Stokes vector from a hybrid-polarity (HP) SAR system when transmitting on right-hand (R) circular and receiving on the linear horizontal (H) and vertical (V) polarization channels is given as [63]

$$\begin{aligned}S_0 &= \langle|M_{RH}|^2 + |M_{RV}|^2\rangle\\ S_1 &= \langle|M_{RH}|^2 - |M_{RV}|^2\rangle\\ S_2 &= 2\Re\langle M_{RH}M^\star_{RV}\rangle\\ S_3 &= -2\Im\langle M_{RH}M^\star_{RV}\rangle\end{aligned} \tag{11}$$

TABLE IV

EXPECTED POLARIMETRIC FEATURE VALUE OF ADDITIVE COMPLEX GAUSSIAN WHITE NOISE. COMPLETE EXPRESSION OF THE STOKES VECTOR, BOTH FOR THE RECIPROCITY AND NON-RECIPROCITY CASES CAN BE FOUND IN APPENDIX B.

Feature expression	**Assumption(s)**
$PD^n = \sigma^n_{VV} - \sigma^n_{HH} \approx 0$	$\sigma^n_{HH} \approx \sigma^n_{VV}$
$r^n_{CO} = \Re\left(\langle n_{HH} n^\star_{VV}\rangle\right) \approx 0$	$\langle n_{HH} n^\star_{VV}\rangle \approx 0$
$\gamma^n_{HH/VV} = \frac{\sigma^n_{HH}}{\sigma^n_{VV}} \approx 1$	$\sigma^n_{HH} \approx \sigma^n_{VV}$
$\rho^n_{CO} = \frac{\Re(\langle n_{HH} n^\star_{VV}\rangle)}{\sqrt{\sigma^n_{HH}\sigma^n_{VV}}} \approx \frac{0}{\sqrt{\sigma^n_{HH}\sigma^n_{VV}}} \approx 0$	$\langle n_{HH} n^\star_{VV}\rangle \approx 0$
$\sigma_{\phi^n_{CO}} = std(\phi^n_{CO}) = \sqrt{Var(\phi^n_{CO})} = \sqrt{\frac{1}{12}(2\pi)^2} = \sqrt{\frac{1}{3}}\pi \approx 1.81$	$\phi^n_{CO} \sim U[-\pi, \pi]$
$H^n = -\sum_{i=1}^{3} p^n_i \log_3 p^n_i = -\frac{1}{3}\sum_{i=1}^{3}\log_3(1/3) = -\frac{1}{3}\sum_{i=1}^{3}(-1) \approx 1$ $p^n_i = \frac{\lambda_i}{\lambda_1+\lambda_2+\lambda_3} = \frac{1}{3}$ (eigenvalues (λ) of $\boldsymbol{T_{3\times3}} = \sigma^n \boldsymbol{I_{3\times3}}$)	$\sigma^n_{HH} \approx \sigma^n_{VV} \approx \sigma^n_{HV}$ $\langle n_{jk} n^\star_{lm}\rangle = 0$, for $j \neq l$ or $k \neq m$
$H^n_{CO} = -\sum_{i=1}^{2} p^n_i \log_2 p^n_i = -\frac{1}{2}\sum_{i=1}^{2}\log_2(1/2) = -\frac{1}{2}\sum_{i=1}^{2}(-1) \approx 1$ $p^n_i = \frac{\lambda_i}{\lambda_1+\lambda_2} = \frac{1}{2}$ (eigenvalues (λ) of $\boldsymbol{T_{2\times2}} = \sigma^n \boldsymbol{I_{2\times2}}$)	$\sigma^n_{HH} \approx \sigma^n_{VV}$ $\langle n_{jk} n^\star_{lm}\rangle = 0$, for $j \neq l$ or $k \neq m$
$\alpha^n = \sum_{i=1}^{3} p_i \cos^{-1}\left(\lvert\boldsymbol{e_i}(1)\rvert\right) = \frac{1}{3}\sum_{i=1}^{3}\cos^{-1}\left(\lvert\boldsymbol{e_i}(1)\rvert\right)$ $\approx \frac{1}{3}(\cos^{-1}(1) + \cos^{-1}(0) + \cos^{-1}(0)) \approx \frac{1}{3}(90^\circ + 90^\circ) \approx 60^\circ$ $p^n_i = \frac{\lambda_i}{\lambda_1+\lambda_2+\lambda_3} = \frac{1}{3}$ (eigenvalues (λ) of $\boldsymbol{T_{3\times3}} = \sigma^n \boldsymbol{I_{3\times3}}$) $\boldsymbol{T_{3\times3}E} = \sigma^n \boldsymbol{I_{3\times3}E} = \boldsymbol{\Lambda E} \implies \boldsymbol{E} = [\boldsymbol{e}_1, \boldsymbol{e}_2, \boldsymbol{e}_3] = \begin{bmatrix}1 & 0 & 0\\0 & 1 & 0\\0 & 0 & 1\end{bmatrix}$	$\sigma^n_{HH} \approx \sigma^n_{VV} \approx \sigma^n_{HV}$ $\langle n_{jk} n^\star_{lm}\rangle = 0$, for $j \neq l$ or $k \neq m$
$DoP^n = \frac{\sqrt{S_1^2+S_2^2+S_3^2}}{S_0} \approx \begin{cases}\frac{0}{2\sigma^n} = 0 & \text{non-reciprocity}\\ \frac{\sigma^n}{2\sigma^n} = 0.5 & \text{reciprocity}\end{cases}$	$\sigma^n_{HH} \approx \sigma^n_{VV} \approx \sigma^n_{HV} \approx \sigma^n_{VH}$ $\langle n_{jk} n^\star_{lm}\rangle = 0$ for $j \neq l$ or $k \neq m$
$\chi^n = \frac{1}{2}\sin^{-1}\left(\frac{-S_3}{DoP S_0}\right) = \frac{1}{2}\sin^{-1}\left(\frac{-S_3}{\sqrt{S_1^2+S_2^2+S_3^2}}\right)$ $\approx \begin{cases}\frac{1}{2}\sin^{-1}\left(\frac{0}{\sqrt{(\frac{1}{2}(\sigma^n_{HH}-\sigma^n_{HV}+\sigma^n_{VH}-\sigma^n_{VV}))^2}}\right) = 0 & \text{non-reciprocity}\\ \frac{1}{2}\sin^{-1}\left(\frac{-(-\sigma^n_{HV})}{\sqrt{(-\sigma^n_{HV})^2+(\frac{1}{2}(\sigma^n_{HH}-\sigma^n_{VV}))^2}}\right) = \frac{1}{2}\sin^{-1}(1) = 45^\circ & \text{reciprocity}\end{cases}$	see Appendix A-A. $\langle n_{jk} n^\star_{lm}\rangle = 0$ for $j \neq l$ or $k \neq m$

where the M_{RH} and M_{RV} are the measured HP complex scattering coefficients and can be expressed as [77]

$$\begin{aligned} M_{RH} &= \frac{1}{\sqrt{2}}(M_{HH} - jM_{VH}) \\ M_{RV} &= \frac{1}{\sqrt{2}}(M_{HV} - jM_{VV}) \end{aligned} \tag{12}$$

using the linear complex scattering coefficients. The Stokes vector can be expressed using the linear complex scattering coefficients in the following way (without assuming reciprocity);

$$\begin{aligned} S_0 &= \frac{1}{2}\langle(|M_{HH}|^2 + |M_{VV}|^2 + |M_{HV}|^2 + |M_{VH}|^2) \\ &\quad - 2\Im(M_{HH}S^\star_{VH}) - 2\Im(M_{HV}M^\star_{VV})\rangle \\ S_1 &= \frac{1}{2}\langle(|M_{HH}|^2 - |M_{VV}|^2 - |M_{HV}|^2 + |M_{VH}|^2) \\ &\quad - 2\Im(M_{HH}M^\star_{VH}) + 2\Im(M_{HV}M^\star_{VV})\rangle \\ S_2 &= \langle\Re(M_{HH}M^\star_{HV}) + \Re(M_{VH}M^\star_{VV}) - \Im(M_{HH}M^\star_{VV}) \\ &\quad + \Im(M_{VH}M^\star_{HV})\rangle \\ S_3 &= \langle\Im(M_{HH}M^\star_{HV}) + \Im(M_{VH}M^\star_{VV}) + \Re(M_{HH}M^\star_{VV}) \\ &\quad - \Re(M_{VH}M^\star_{HV})\rangle. \end{aligned} \tag{13}$$

The Stokes vector with the noise power, i.e., writing out the $M_{pq} = S_{pq} + \sigma^n_{pq}$, where p and q is polarization on transmits and receive is

$$\begin{aligned} S_0 &= \frac{1}{2}\langle(|S_{HH}|^2 + |S_{VV}|^2 + |S_{HV}|^2 + |S_{VH}|^2 + \sigma^n_{HH} \\ &\quad + \sigma^n_{HV} + \sigma^n_{VH} + \sigma^n_{VV}) - 2\Im(S_{HH}S^\star_{VH}) - 2\Im(S_{HV}S^\star_{VV})\rangle \\ S_1 &= \frac{1}{2}\langle(|S_{HH}|^2 - |S_{VV}|^2 - |S_{HV}|^2 + |S_{VH}|^2 + \sigma^n_{HH} \\ &\quad - \sigma^n_{HV} + \sigma^n_{VH} - \sigma^n_{VV}) - 2\Im(S_{HH}S^\star_{VH}) + 2\Im(S_{HV}S^\star_{VV})\rangle \\ S_2 &= \langle\Re(S_{HH}S^\star_{HV}) + \Re(S_{VH}S^\star_{VV}) - \Im(S_{HH}S^\star_{VV}) \\ &\quad + \Im(S_{VH}S^\star_{HV})\rangle \\ S_3 &= \langle\Im(S_{HH}S^\star_{HV}) + \Im(S_{VH}S^\star_{VV}) + \Re(S_{HH}S^\star_{VV}) \\ &\quad - \Re(S_{VH}S^\star_{HV})\rangle. \end{aligned} \tag{14}$$

In [63], the author expressed the Stokes vector using elements from the 3 × 3 covariance matrix assuming reciprocity ($S_{HV} = S_{VH}$). The Stokes vector with the noise elements and assuming reciprocity becomes

$$\begin{aligned} S_0 &= \frac{1}{2}\langle(|S_{HH}|^2 + |S_{VV}|^2 + 2|S_{HV}|^2 + \sigma^n_{HH} + 2\sigma^n_{HV} \\ &\quad + \sigma^n_{VV}) - 2\Im(S_{HH}S^\star_{HV}) - 2\Im(S_{HV}S^\star_{VV})\rangle \\ S_1 &= \frac{1}{2}\langle(|S_{HH}|^2 - |S_{VV}|^2) - 2\Im(S_{HH}S^\star_{HV}) + \sigma^n_{HH} \\ &\quad - \sigma^n_{HV} + \sigma^n_{HV} - \sigma^n_{VV} + 2\Im(S_{HV}S^\star_{VV})\rangle \\ S_2 &= \langle\Re(S_{HH}S^\star_{HV}) + \Re(S_{HV}S^\star_{VV}) - \Im(S_{HH}S^\star_{VV})\rangle \\ S_3 &= \langle\Im(S_{HH}S^\star_{HV}) + \Im(S_{HV}S^\star_{VV}) + \Re(S_{HH}S^\star_{VV}) \\ &\quad - |S_{HV}|^2 - \sigma^n_{HV}\rangle. \end{aligned} \tag{15}$$

As seen in the equation above, an extra noise component in S_3 is present, which was not present when reciprocity was not assumed.

APPENDIX C
ADDING NOISE TO THE UAVSAR

We want to compare measured additive noise with simulated noise in the SAR measurements. This is performed by generating independently, for each polarization channel, complex random Gaussian white noise ($\boldsymbol{N}$ term in equation (3)) with zero mean and variance equal to the noise power added. Addition of simulated noise to the measured signal is performed on the complex scattering coefficient prior to any filtering and feature calculation, i.e.,

$$\hat{S}_{pq} = M_{pq} + \frac{1}{\sqrt{2}}(X + jY), X \sim N(0, \sigma_n), Y \sim N(0, \sigma_n) \tag{16}$$

where σ_n is equal to the NESZ + Δ_n. The $\frac{1}{\sqrt{2}}$ accounts for the two components in the complex signal. Δ_n increases with +1dB for every iteration until the SNR is equal to -10dB. For example, if NESZ is -45dB, the first iteration has a noise variance (in dB) equal to -44dB. Note that this procedure is only applied to the UAVSAR, due to its high initial SNR for both the oil slick and the clean sea regions.

APPENDIX D
THE VALIDITY OF THE NOMINAL NOISE FLOOR

To verify the NESZ provided in the product files, we estimate the NESZ from both RS-2 and UAVSAR data using two methods [75], [76], based on the theory in [73], [74]. Once the estimates of the NESZ are obtained, a comparison with the nominal NESZ values from the product file is carried out. The reason for estimating the NESZ is to verify the accuracy of the nominal NESZ, since the NESZ is used to estimate the SNR.

The authors of [75] suggested an approach to estimate the NESZ using a method based on the minimum eigenvalue of the 4×4 sample coherency matrix, named the eigenvalue-based (EB) estimator of NESZ, i.e., NESZ$_{EB}$. The fourth (minimum) eigenvalue represents the noise power, i.e., the NESZ. The second method tested was suggested in [76], and uses the maximum likelihood (ML) to estimate the NESZ, i.e., NESZ$_{ML}$. To estimate the NESZ based on the ML estimator, a given number of samples are needed (see [76] for more details). The number of samples is given within a window that steps across the two cross-polarization coefficients (HV and VH). The same is the case for the EB estimator, since the sample coherency matrix is calculated using a smoothing filter with a given window size, i.e., number of samples. To evaluate the robustness in terms of the window size, the EM and the ML estimator of the NESZ is carried out with several window sizes using an averaging filter mask.

The estimation of the NESZ is performed over a clean sea area across the full range within each RS-2 and UAVSAR scene. Figs. 10 and 11 show the two estimators using only one RS-2 scene acquired 8 June 2011 and one UAVSAR scene acquired 11 June 2015. The estimated NESZ based on the EB-estimator (the left panel of Fig. 10) seems to converge towards a given value as the window size increases. The EB estimator is very sensitive to the window size, as expected based on the study in [76], where the authors show that the EB estimator is biased. Therefore, [76] suggested an unbiased and more efficient estimator of the noise power, namely the ML estimator. The estimator's sample size independence is observed in the right panel of Figs. 10 and 11.

The estimated NESZ of both the EB (with large window size) and the ML estimator is about ±1dB from the nominal NESZ values for all the RS-2 scenes used in this study. Therefore, we consider the nominal NESZ values from RS-2 trustworthy to use in the analysis. Unfortunately, since no quad-polarimetric data are available in the TS-X products, the ML and EB methods cannot be applied. The estimated NESZ of the UAVSAR is higher than the nominal values by more than 10dB for some incidence angles. This is consistent with the influence of ISLR as a multiplicative noise term (see Table I), reducing the effective SNR for UAVSAR data by up to 15dB as seen in Fig. 3. The cross-talk contamination/leakage from the copolarization into the cross-polarization channels may also contribute to this high deviation between the nominal and the estimated NESZ.

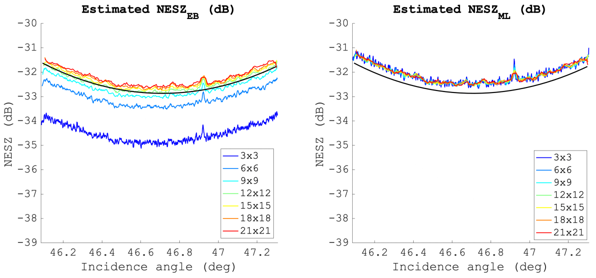

Fig. 10. Estimation of the noise powers NESZ$_{EB}$ and NESZ$_{ML}$ of one RS-2 scene (8 June 2011 at 05:59 UTC) using various window sizes when smoothing with an averaging filter mask. The black continuous line shows the nominal NESZ values for the given RS-2 product.

REFERENCES

[1] A.-B. Salberg, Ø. Rudjord, and A. H. S. Solberg, "Oil Spill Detection in Hybrid-Polarimetric SAR Images," *IEEE Trans. Geosci. Remote Sens.*, vol. 52, no. 10, pp. 6521 – 6533, Oct. 2014.

[2] S. Skrunes, C. Brekke, and T. Eltoft, "Characterization of marine surface slicks by Radarsat-2 multipolarization features," *IEEE Trans. Geosci. Remote Sens.*, vol. 52, no. 9, pp. 5302–5319, Sep. 2014.

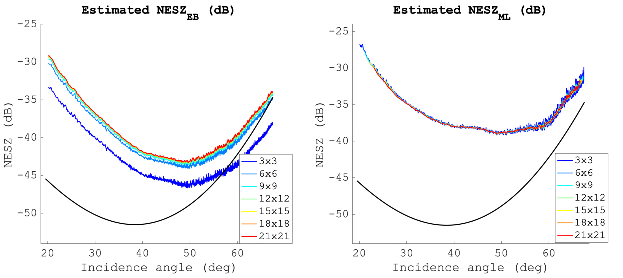

Fig. 11. Estimation of the noise powers NESZ$_{EB}$ and NESZ$_{ML}$ of one UAVSAR scene (11 June 2015 at 08:46 UTC) using various window sizes when smoothing with an averaging filter mask. The black continuous line shows the nominal NESZ values for the given UAVSAR product.

[3] B. Minchew, "Determining the mixing of oil and sea water using polarimetric Synthetic Aperture Radar," *Geophys. Res. Lett.*, vol. 39, no. 16, Aug. 2012.

[4] B. Fiscella, A. Giancaspro, F. Nirchio, P. Pavese, and P. Trivero, "Oil spill detection using marine SAR images," *Int. J. Remote Sens.*, vol. 21, no. 18, pp. 3561–3566, 2000.

[5] R. Shirvany, M. Chabert, and J.-Y. Tourneret, "Ship and Oil-Spill Detection using the Degree of Polarization in Linear and Hybrid/Compact Dual-Pol SAR," *IEEE J. Sel. Topics Appl. Earth Observ. Remote Sens.*, vol. 5, no. 3, pp. 885 – 892, Jun. 2012.

[6] M. Migliaccio, A. Gambardella, and M. Tranfaglia, "SAR polarimetry to observe oil spills," *IEEE Trans. Geosci. Remote Sens.*, vol. 45, no. 2, pp. 506 – 511, Feb. 2007.

[7] S. Angelliaume, O. Boisot, and C.-A. Guérin, "Dual-Polarized L-band SAR Imagery for Temporal Monitoring of Marine Oil Slick Concentration," *Remote Sens.*, vol. 10, no. 1012, pp. 1–17, Jun. 2018.

[8] C. Oliver and S. Quegan, *Understanding Synthetic Aperture Radar Images*. SciTech Publishing Inc., 2004.

[9] A. Freeman, "The effects of noise on polarimetric SAR data," *IEEE Geoscience and Remote Sensing Symposium, 1993. IGARSS '93. Better Understanding of Earth Environment., International*, vol. 2, pp. 799–802, 1993.

[10] B. Minchew, C. E. Jones, and B. Holt, "Polarimetric Analysis of Backscatter From the Deepwater Horizon Oil Spill Using L-Band Synthetic Aperture Radar," *IEEE Trans. Geosci. Remote Sens.*, vol. 50, no. 10, pp. 3812–3830, Oct. 2012.

[11] D. Latini, F. D. Frate, and C. E. Jones, "Multi-frequency and polarimetric quantitative analysis of the Gulf of Mexico oil spill event comparing different SAR systems," *Remote Sens. Environ.*, vol. 183, pp. 26 – 42, 2016.

[12] S. Skrunes, C. Brekke, C. E. Jones, M. M. Espeseth, and B. Holt, "Effect of wind direction and incidence angle on polarimetric SAR observations of slicked and unslicked sea surfaces," *Remote Sens. Environ.*, vol. 213, pp. 73 – 91, Aug. 2018.

[13] S. Angelliaume, P. C. Dubois-Fernandez, C. E. Jones, B. Holt, B. Minchew, E. Amri, and V. Miegebielle, "SAR imagery for detecting sea surface slicks: Performance assessment of polarization-dependent parameters," *IEEE Trans. Geosci. Remote Sens.*, vol. 56, no. 8, pp. 4237 – 4257, Aug. 2018.

[14] S. Skrunes, C. Brekke, C. E. Jones, and B. Holt, "A Multisensor Comparison of Experimental Oil Spills in Polarimetric SAR for High Wind Conditions," *IEEE J. Sel. Topics Appl. Earth Observ. Remote Sens.*, vol. 9, no. 11, pp. 4948–4961, Nov. 2016.

[15] M. M. Espeseth, S. Skrunes, C. E. Jones, C. Brekke, B. Holt, and A. P. Doulgeris, "Analysis of Evolving Oil Spills in Full-Polarimetric and Hybrid-Polarity SAR," *IEEE Trans. Geosci. Remote Sens.*, vol. 55, no. 7, pp. 4190–4210, July 2017.

[16] A. Buono, C. R. De Macedo, F. Nunziata, D. Velotto, and M. Migliaccio, "Analysis on the effects of sar imaging parameters and environmental conditions on the standard deviation of the co-polarized phase difference measured over sea surface," *Remote Sens.*, vol. 11, no. 1, 2018.

[17] I. G. Cumming and F. H. Wong, *Digital Processing of Synthetic Aperture Radar data*. Artech House, 2005.

[18] T. Fritz and M. Eineder, "TerraSAR-X Ground Segment Basic Product Specification Document (doc: TX-GS-DD-3302)," *DLR*, Oct. 2013.

[19] A. Luscombe, "Radarsat-2 image quality and mode maintenance and enhancement," *EOS SAR Cal/Val Working Group Meeting, Pasadena*, 2009.

[20] T. L. Ainsworth, L. Ferro-Famil, and J.-S. Lee, "Orientation angle preserving a posteriori polarimetric SAR calibration," *IEEE Trans. Geosci. Remote Sens.*, vol. 44, no. 4, pp. 994–1003, Apr. 2006.

[21] S. Quegan, "A unified algorithm for phase and cross-talk calibration of polarimetric data-theory and observations," *IEEE Trans. Geosci. Remote Sens.*, vol. 32, no. 1, pp. 89–99, Jan. 1994.

[22] G. R. Valenzuela, "Theories for the interaction of electromagnetic and oceanic waves - a review," *Boundary-Layer Meteorology*, vol. 12, no. 1-4, pp. 61–85, Jan. 1978.

[23] R. Touzi, R. K. Hawkins, and S. Cote, "High-precision assessment and calibration of polarimetric RADARSAT-2 SAR using transponder measurements," *IEEE Trans. Geosci. Remote Sens.*, vol. 51, no. 1, pp. 487–503, Jan. 2013.

[24] A. P. Luscombe, K. Chotoo, and B. D. Huxtable, "Polarimetric calibration for RADARSAT-2," *IGARSS 2000. IEEE 2000 Int. Geosci. Remote Sens. Symp. (IGARSS) Taking the Pulse of the Planet: The Role of Remote Sensing in Managing the Environment. Proceedings (Cat. No.00CH37120)*, vol. 5, pp. 2197–2199, 2000.

[25] D. Williams, Y. Wang, M. Chabot, P. L. Dantec, R. Caves, Y. Wu, K. James, A. Thompson, and C. Vigneron. (2015) Radarsat-2 Image Quality and Calibration Update 2015. [Online]. Available: http://SARcv.ceos.org/site_media/media/documents/03_RADARSAT-2_Image_Quality_and_Calibration_Update_CEOS_2015.pdf

[26] A. G. Fore, B. D. Chapman, B. P. Hawkins, S. Hensley, C. E. Jones, T. R. Michel, and R. J. Muellerschoen, "UAVSAR Polarimetric Calibration," *IEEE Trans. Geosci. Remote Sens.*, vol. 53, no. 6, pp. 3481–3491, Jun. 2015.

[27] R. Touzi, P. W. Vachon, and J. Wolfe, "Requirement on antenna cross-polarization isolation for the operational use of c-band sar constellations in maritime surveillance," *IEEE Geosci. Remote Sens. Lett.*, vol. 7, no. 4, pp. 861–865, Oct 2010.

[28] A. Freeman, J. J. van Zyl, J. D. Klein, H. A. Zebker, and Y. Shen, "Calibration of stokes and scattering matrix format polarimetric sar data," *IEEE Trans. Geosci. Remote Sens.*, vol. 30, no. 3, pp. 531–539, May 1992.

[29] D. Williams, Y. Wang, G. Fitzgerald, R. Caves, M. Chabot, N. Gibb, Y. Wu, A. Thompson, P. Allan, and C. Vigneron. (2017) Radarsat-2 Image Quality and Calibration Update 2017. [Online]. Available: http://SARcv.ceos.org/site_media/media/documents/RADARSAT-2_Image_Quality_and_Calibration_Update_CEOS_2017.pdf

[30] S. Hensley, S. Oveisgharan, S. Saatchi, M. Simard, R. Ahmed, and Z. Haddad, "An error model for biomass estimates derived from polarimetric radar backscatter," *IEEE Trans. Geosci. Remote Sens.*, vol. 52, no. 7, pp. 4065–4082, Jul. 2014.

[31] "Radarsat-2 product description," *MacDonald, Dettwiler and Associates Ltd., Rickmond, BC, USA, RN-SP-52-1238*, vol. Issue 1/13, 2016.

[32] M. Vespe and H. Greidanus, "SAR image quality assessment and indicators for vessel and oil spill detection," *IEEE Trans. Geosci. Remote Sens.*, vol. 50, no. 11, pp. 4726–4734, Nov 2012.

[33] S. Hensley. (2015) 3rd Advanced Course on Radar Polarimetry, ESA-ESRIN. [Online]. Available: http://seom.esa.int/polarimetrycourse2015/files/UAVSAR_SHensley.pdf

[34] J. Mittermayer, M. Younis, R. Metzig, S. Wollstadt, J. M. Martinez, and A. Meta, "TerraSAR-X system performance characterization and verification," *IEEE Trans. Geosci. Remote Sens.*, vol. 48, no. 2, pp. 660–676, Feb. 2010.

[35] S. Hensley, "New Missions, UAVSAR," *in Proc. POLinSAR, Frascati, Italy*, 2015.

[36] X. Li, H. Qi, B. Hua, H. Lei, and W. Yu, "A study of spaceborne SAR raw data compression error based on a statistical model of quantization interval transfer probability", journal="Science China Information Sciences," vol. 53, no. 11, pp. 2352–2362, Nov 2010.

[37] S. R. Cloude, *Polarisation Applications in Remote Sensing*, First, Ed. Oxford University Press, 2010.

[38] J. Wright, "Backscattering from capillary waves with application to sea clutter," *IEEE Trans. Antennas Propag.*, vol. 14, no. 6, pp. 749–754, Nov. 1966.

[39] I. Hajnsek, E. Pottier, and S. R. Cloude, "Inversion of surface parameters from polarimetric SAR," *IEEE Trans. Geosci. Remote Sens.*, vol. 41, no. 4, pp. 727–744, Apr. 2003.

[40] A. Iodice, A. Natale, and D. Riccio, "Retrieval of soil surface parameters via a polarimetric two-scale model," *IEEE Trans. Geosci. Remote Sens.*, vol. 49, no. 7, pp. 2531–2547, Jul. 2011.

[41] A. Buono, F. Nunziata, and M. Migliaccio, “New generation polarimetric SARs for sea oil slick observation: Full-polarimetric vs compact-polarimetric architectures,” in *2016 Proc. IEEE Int. Geosci. Remote Sens. Symp. (IGARSS)*, July 2016, pp. 2223–2226.

[42] J. Yin, J. Yang, Z. Zhou, and J. Song, “The Extended Bragg Scattering Model-Based Method for Ship and Oil-Spill Observation Using Compact Polarimetric SAR,” *IEEE J. Sel. Topics Appl. Earth Observ. Remote Sens.*, vol. 8, no. 8, pp. 3760–3772, Aug 2015.

[43] A. Buono, F. Nunziata, C. R. de Macedo, D. Velotto, and M. Migliaccio, “A Sensitivity Analysis of the Standard Deviation of the Copolarized Phase Difference for Sea Oil Slick Observation,” *IEEE Trans. Geosci. Remote Sens.*, vol. 57, no. 4, pp. 2022–2030, April 2019.

[44] A. Buono, F. Nunziata, and M. Migliaccio, “Analysis of Full and Compact Polarimetric SAR Features Over the Sea Surface,” *IEEE Geosci. Remote Sens. Lett.*, vol. 13, no. 10, pp. 1527–1531, Oct 2016.

[45] W. Alpers, B. Holt, and K. Zeng, “Oil spill detection by imaging radars: Challenges and pitfalls,” *Remote Sens. Environ.*, vol. 201, pp. 133–147, Nov. 2017.

[46] J.-S. Lee and E. Pottier, *Polarimetric Radar Imaging*, B. J. Thompson, Ed. CRC Press Taylor and Francis Group, 2009, no. 42-45.

[47] S. Skrunes, C. Brekke, T. Eltoft, and V. Kudryavtsev, “Comparing Near-Coincident C- and X-Band SAR Acquisitions of Marine Oil Spills,” *IEEE Trans. Geosci. Remote Sens.*, vol. 53, no. 4, pp. 1958–1975, Apr. 2015.

[48] V. Kudryavtsev, B. Chapron, A. Myasoedova, F. Collard, and J. Johannessen, “On dual co-polarized SAR measurements of the ocean surface,” *IEEE Geosci. Remote Sens. Lett.*, vol. 10, no. 4, pp. 761–765, Jul. 2013.

[49] O. Boisot, S. Angelliaume, and C. Guérin, “Marine Oil Slicks Quantification From L-band Dual-Polarization SAR Imagery,” *IEEE Trans. Geosci. Remote Sens.*, vol. 57, no. 4, pp. 2187–2197, April 2019.

[50] H. Li, W. Perrie, and J. Wu, “Retrieval of Oil–Water Mixture Ratio at Ocean Surface Using Compact Polarimetry Synthetic Aperture Radar,” *Remote Sens.*, vol. 11, no. 7, 2019.

[51] H. Lin, Q. Xu, and Q. Zheng, “An overview on SAR measurements of sea surface wind,” *Progress in Natural Science*, vol. 18, no. 8, pp. 913 – 919, Aug. 2008.

[52] D. Kasilingam, D. Schuler, J.-S. Lee, and S. Malhotra, “Modulation of polarimetric coherence by ocean features,” *IEEE Int. Geosci. Remote Sens. Symp.*, vol. 1, pp. 432–434, Jun. 2002.

[53] M. R. Drinkwater, R. Kwok, E. Rignot, H. Israelsson, R. G. Onstott, and D. P. Winebrenner, “Chapter 24. Potential Applications of Polarimetry to the Classification of Sea Ice,” *Microwave Remote Sensing of Sea Ice, Geophysical Monograph 68, American Geophysical Union*, Jan. 1992.

[54] D. Velotto, M. Migliaccio, F. Nunziata, and S. Lehner, “Dual-Polarized TerraSAR-X Data for Oil-Spill Observation,” *IEEE Trans. Geosci. Remote Sens.*, vol. 49, no. 12, pp. 4751–4762, Dec. 2011.

[55] M. Migliaccio, F. Nunziata, and A. Gambardella, “On the co-polarized phase difference for oil spill observation,” *Int. J. Remote Sens.*, vol. 30, no. 6, pp. 1587–1602, Apr. 2009.

[56] S. Singha, R. Ressel, D. Velotto, and S. Lehner, “A combination of traditional and polarimetric features for oil spill detection using TerraSAR-X,” *IEEE J. Sel. Topics Appl. Earth Observ. Remote Sens.*, vol. 9, no. 11, pp. 4979–4990, Nov. 2016.

[57] M. Migliaccio, F. Nunziata, A. Montuori, X. Li, and W. G. Pichel, “A multifrequency polarimetric SAR processing chain to observe oil fields in the Gulf of Mexico,” *IEEE Trans. Geosci. Remote Sens.*, vol. 49, no. 12, pp. 4729–4737, Dec. 2011.

[58] F. Nunziata, C. R. de Macedo, A. Buono, D. Velotto, and M. Migliaccio, “On the analysis of a time series of X–band TerraSAR–X SAR imagery over oil seepages,” *Int. J. Remote Sens.*, vol. 40, no. 9, pp. 3623–3646, 2019.

[59] S. R. Cloude and E. Pottier, “An entropy based classification scheme for land applications of polarimetric SAR,” *IEEE Trans. Geosci. Remote Sens.*, vol. 35, no. 1, pp. 68–78, Jan. 1997.

[60] W. Tian, Y. Shao, J. Yuan, S. Wang, and Y. Liu, “An experiment for oil spill recognition using Radarsat-2 image,” *IEEE Int. Geosci. Remote Sens. Symp.*, pp. 2761–2764, Jul. 2010.

[61] B. Zhang, W. Perrie, X. Li, and W. G. Pichel, “Mapping sea surface oil slicks using Radarsat-2 quad-polarization SAR image,” *Geophys. Res. Lett.*, vol. 38, Jul. 2011.

[62] M. Migliaccio, A. Gambardella, F. Nunziata, M. Shimada, and O. Isoguchi, “The PALSAR Polarimetric Mode for Sea Oil Slick Observation,” *IEEE Trans. Geosci. Remote Sens.*, vol. 47, no. 12, pp. 4032–4041, Dec. 2009.

[63] R. K. Raney, “Hybrid-Polarity SAR Architecture,” *IEEE Trans. Geosci. Remote Sens.*, vol. 45, no. 11, pp. 3397–3404, Nov. 2007.

[64] K. Raney, J. T. S. Cahill, G. W. Patterson, and D. B. J. Bussey, “The m-chi Decomposition of Hybrid Dual-Polarimetric Radar Data with Application to Lunar Craters,” *J. Geophys. Res.*, vol. 117, no. E12, May 2012.

[65] A. Buono, F. Nunziata, M. Migliaccio, and X. Li, “Polarimetric analysis of compact-polarimetry SAR architectures for sea oil slick observation,” *IEEE Trans. Geosci. Remote Sens.*, vol. 54, no. 10, pp. 5862–5874, Oct. 2016.

[66] Y. Zhang, Y. Li, X. S. Liang, and J. Tsou, “Comparison of oil spill classifications using fully and compact polarimetric SAR images,” *Applied Sciences*, vol. 7, no. 2, p. 193, Feb. 2017.

[67] F. Nunziata, A. Gambardella, and M. Migliaccio, “On the degree of polarization for SAR sea oil slick observation,” *ISPRS Journal of Photogrammetry and Remote Sensing*, vol. 78, pp. 41 – 49, 2013. [Online]. Available: http://www.sciencedirect.com/science/article/pii/S0924271613000221

[68] S. Cloude, D. Goodenough, and H. Chen, “Compact Decomposition Theory,” *IEEE Trans. Geosci. Remote Sens.*, vol. 9, no. 1, pp. 28–32, Jan. 2012.

[69] H. Li, W. Perrie, Y. He, J. Wu, and X. Luo, “Analysis of the Polarimetric SAR Scattering Properties of Oil-Covered Waters,” *IEEE J. Sel. Topics Appl. Earth Observ. Remote Sens.*, vol. 8, no. 8, pp. 3751–3759, Aug. 2015.

[70] S. Skrunes, C. Brekke, and M. M. Espeseth, “Assessment of the RISAT-1 FRS-2 mode for oil spill observation,” in *2017 IEEE Int. Geosci. Remote Sens. Symp. (IGARSS)*, July 2017, pp. 1024–1027.

[71] B. Holt, “SAR imaging of the ocean surface,” *Synthetic Aperture Radar Marine User's Manual*, no. 25-80, C. Jackson and J. Apel, Eds. U.S. Department of Commerce, National Oceanic and Atmospheric Administration, C. Jackson and J. Apel, 2004.

[72] F. Nunziata, A. Gambardella, and M. Migliaccio, “On the Mueller scattering matrix for SAR sea oil slick observation,” *IEEE Geosci. Remote Sens. Lett.*, vol. 5, no. 4, pp. 691–695, Oct. 2008.

[73] A. Freeman, J. Villasenor, and J. D. Klein, “Multi-frequency and polarimetric radar backscatter signatures for discrimination between agricultural crops at the Flevoland experimental test site.” *AIRSAR Workshop*, no. 92-28018, 1991.

[74] A. Freeman, “An Algorithm for estimating the noise levels in polarimetric SAR image data,” *Int. J. Remote Sens.*, vol. 15, no. 9, pp. 1791–1798, 1993.

[75] S. Hajnsek, K. P. Papathanassiou, and S. R. Cloude, “Removal of additive noise in polarimetric eigenvalue processing,” *IGARSS 2001. Scanning the Present and Resolving the Future. Proceedings. IEEE Int. Geosci. Remote Sens. Symp.*, vol. 6, pp. 2778–2780, 2001.

[76] M. Villano, “SNR and noise variance estimation in polarimetric SAR data,” *IEEE Geosci. Remote Sens. Lett.*, vol. 11, no. 1, pp. 278–282, 2014.

[77] P. Dubois-Fernandez, J.-C. Souyris, S. Angelliaume, and F. Garestier, “The Compact Polarimetry Alternative for Spaceborne SAR at Low Frequency,” *IEEE Trans. Geosci. Remote Sens.*, vol. 46, no. 10, Oct. 2008.

9

Paper III:

Oil Spill Response-Oriented Information Products Derived from a Rapid Repeat Time-Series of SAR Images

M. M. Espeseth, C. E. Jones, B. Holt, C. Brekke, and S. Skrunes

Submitted to
IEEE Journal of Selected Topics in Applied Earth Observations and Remote Sensing, 2019

Oil Spill Response-Oriented Information Products Derived from a Rapid Repeat Time-Series of SAR Images

Martine M. Espeseth, Cathleen E. Jones, *Member, IEEE,* Benjamin Holt, *Member, IEEE,* Camilla Brekke, *Member, IEEE,* and Stine Skrunes, *Member, IEEE*

***Abstract*—New quantitative and semi-automatable methods for analyzing oil slick evolution using a time series of L-band Synthetic Aperture Radar (SAR) images with short repeat time are developed and explored. In this study, two methods that are complementary in terms of identifying temporal changes within an oil slick are presented. The two methods reflect two ways of evaluating the oil slicks. The first method identifies regions within the slick that show persistently high damping ratio (the contrast between clean sea and oil intensity), using higher damping values as a proxy for increasing oil thickness. This method also weights the age of the scenes as the algorithm incorporates new images. The second method outputs the short-term drift pattern and the changes in the damping ratios and copolarization ratios between two scenes, proxies for thickness and emulsification. Both methods can aid in identifying regions of high priority for oil recovery. Due to the simplicity of the methods, they can be adapted to time series data from different types of sensors, e.g., optical and SAR imagery. The methods are demonstrated on three L-band Uninhabited Aerial Vehicle Synthetic Aperture Radar (UAVSAR) time series acquired in November 2016 over a persistent seep in the Mississippi Canyon block 20 (MC-20) of the Gulf of Mexico. The results of the two methods clearly show the movement and the weathering of the oil as a function of both time and location.**

***Index Terms*—oil spill, SAR, UAVSAR, polarimetry, damping ratio, copolarization ratio, oil spill response**

I. INTRODUCTION

Synthetic Aperture Radar (SAR) instruments are a key operational monitoring tool for detection of marine oil spills. Most commonly, a single SAR image is used to identify location, extent, and, if possible, the source of the spill. This information is often available in oil spill detection reports from operational services. Tools for quantifying the oil's characteristics and identifying their variations within a slick are still limited within operational systems. Within the research community, studies using a single SAR scene have demonstrated the potential to characterize physical properties within oil slicks, specifically the thickness and the volumetric fraction of oil [1]–[9]. Studies have observed that thicker oil, including weathered emulsified oil, causes more damping of the capillary and short gravity waves and thus appears darker in SAR than thinner oil layers (e.g., sheen)([3], [10]–[12]). With this information available, it is possible to detect actionable oil in an operational response setting.

A single SAR scene is valuable when obtaining a snapshot view of an oil spill. Tracking the evolution of a slick requires several images of the same slick, i.e., one must integrate scenes from several SAR sensors or repeat imaging with one sensor. The use of multiple SAR/optical images covering an oil spill/seep has proven to be very useful for extracting information about the drift pattern and the oil extent, two important factors that can aid in assessing the potential environmental impacts from such hazards. For example, both optical and SAR time series with a long revisit time (days/weeks) have been investigated [13]–[15].

An airborne SAR sensor can provide rapid repeat images to monitor how the slick drifts and weathers on the sea surface. In this study we consider how a series of SAR images acquired with short revisit time (minutes to hours) can be used to identify areas within oil slicks of relatively thicker or more persistent oil and their short-term drift patterns. This study introduces complementary information products that could be valuable in the recovery process, where timely knowledge of the spill is important. We demonstrate that combining the temporal aspect, using multiple SAR images with short repeat times, with characterization of an oil spill can provide new information to improve decision making during clean-up.

Studies with short repeat time series using SAR images have demonstrated the potential of using the damping ratio to extract information about the transport, evolution, and change in SAR properties on a short time scale (see [11], [16]). The methodologies presented in this study are aimed at creating map products that combine all of this information to quantify and visually depict the temporal evolution of the slick in an easily understandable representation.

From an oil spill response perspective, the first step in making a map usable by responders is to identify the oil slick using either manual or automatic segmentation algorithms. The purpose of this study is to take the next steps, namely a) developing methods for automatically identifying regions with persistent presence of thick oil, indicated by high damping over a period of time; and b) extracting information about the oil slick drift pattern to show where the thicker oil is moving. Such information can be used as input to improve the

M. M. Espeseth, C. Brekke, and S. Skrunes are with the Department of Physics and Technology, UiT The Arctic University of Norway, 9037 Tromsø, Norway (e-mail: martine.espeseth@uit.no; camilla.brekke@uit.no; stine.skrunes@uit.no).

C. E. Jones and B. Holt are with the Jet Propulsion Laboratory, California Institute of Technology, Pasadena, CA 91125 USA (e-mail: cathleen.e.jones@jpl.nasa.gov; benjamin.m.holt@jpl.nasa.gov).

Manuscript received Month XX, 201X; revised Month XX, 201X; accepted Month X, 201X. Date of publication Month XX, 201X; date of current version Month X, 201X. (Corresponding author: M. M. Espeseth.)

oil spill response and clean-up process by reducing reliance on visual analysis, which can lead to limited, biased or subjective conclusions. The analysis is conducted on three time series, each consisting of between 6 and 9 UAVSAR scenes, covering a persistent oil seep in the Gulf of Mexico. This area is used as the test case for demonstrating the potential of the suggested methods because the slick formed from the seep often exhibits variations in oil properties within the slick (see e.g., [11], [17]).

II. SELECTED SAR FEATURES

A number of features extracted from quad-polarimetric SAR products have been investigated for their ability to both detect and characterize oil (see e.g., [5], [6], [9], [18]). For daily monitoring, the single (one polarization channel)- or the conventional dual-polarization (one linear co- and cross-polarization channel) SAR mode is preferred over the quad-polarimetric mode (four polarization channels) due to their typically-larger image swath. However, using the single- or the dual-polarization SAR comes at a cost of less polarimetric information, which might result in limitations when, for example, attempting to characterize the oil slicks. In a response situation, where the oil spill location is already known, multi-polarization and high spatial resolution are more important than large spatial coverage.

The two main physical factors impacting the interaction between the incoming radar signal and the surface oil are the dielectric properties and the roughness of the scattering surface. In open water, the small-scale roughness induced by the wind is higher in the surrounding clean sea compared to the oil-covered area due to the oil dampening of the capillary and short gravity waves. The dielectric permittivity of seawater is much higher than that of oil. For a thin oil layer the oil dielectric properties do not affect the backscatter amplitude in a measurable way, but if the oil slick is thick (centimeter) or there is high concentration of oil in the oil/sea mixture, the dielectric properties observed by the radar may be altered by the presence of oil. SAR instruments measure only the response from the upper surface, not in the water column, due to little penetration of microwaves into seawater. Hence, the oil droplets located in the water column will not be detected by SAR.

We have selected two features that can be related to roughness and the dielectric property. The first feature is the contrast between the VV (vertical transmit and vertical receive) intensity in clean sea versus oil, named the damping ratio (DR_{VV}) (see [2]) and the second is the copolarization ratio contrast (CPR_c). The reasons for selecting these particular features are discussed in Sections II-A and II-B below.

The selected features are defined as

$$DR_{VV}(\theta) = \sigma_{VV}^{0,sea}(\theta)/\sigma_{VV}^{0}(\theta) \tag{1}$$

$$CPR_c(\theta) = \left(\frac{\sigma_{HH}^0(\theta)}{\sigma_{VV}^0(\theta)}\right)^{sea} / \left(\frac{\sigma_{HH}^0(\theta)}{\sigma_{VV}^0(\theta)}\right). \tag{2}$$

Here, σ_{VV}^0 is the VV-intensity normalized radar cross-section (σ^0), θ is the incidence angle, and $\sigma_{VV}^{0,sea}$ is the radar cross-section from the clean sea surrounding the oil slick. The copolarization ratio (CPR) is the ratio of the HH- (horizontal transmit and horizontal receive) and VV-intensity and is also normalized to clean sea in a similar manner to the damping ratio, and given the abbreviation CPR_c. The reason for normalizing the CPR is that the marine surface oil investigated in this study spans a significant range of incidence angles, thereby introducing an incidence angle dependency for this feature across the oil slick. Taking the ratio partially cancels this dependence. The VV return is in general higher than the HH return for ocean features, thereby producing CPR values between 0 and 1. The DR_{VV} can be extracted from a single-polarimetric SAR system, where only the VV channel is needed. The CPR_c needs a dual-polarimetric system with HH and VV capabilities (such as those carried by TerraSAR-X and the Radarsat Constellation Mission).

A. VV-Damping ratio

The damping ratio has been observed to show a high contrast between oil and clean sea. According to the Bragg scattering theory, the damping ratio is a measure of the difference in spectral energy density of the ocean surface waves between oil-free and oil-covered surfaces [10]. The damping ratio has been shown to be sensitive to relative thickness variations within mineral oil slicks, where thicker oil causes more damping of the capillary and short gravity waves ([3], [10]–[12]). Gade et al. [2] determined that the damping ratio increased with increasing Bragg wavenumber, and observed that L-band SAR measured a lower damping ratio compared to C- and X-band SAR at the same incidence angle. Under specific environmental conditions (wind speed approximately 5-6 m/s), an early study [19] also observed that a significant reduction in backscatter was correlated with the thickest parts of the oil. A recent study [20] based on a laboratory experiment using oil emulsion and crude oil with different thicknesses demonstrated that the damping ratio increased with oil thickness (using X- to Ka-band radars), but reached a maximum damping ratio value at a given oil thickness threshold at 1-2mm for oil emulsion. Higher damping was also reported for crude oil compared to emulsified oil in [20]. Airborne measurements and cruise surveys near the MC-20 slick (the same oil slick studied here) reported oil thickness in the range 0.04μm to 1mm (sheen to crude oil) [11], [13], [21]. Based on the experiment presented in [20], the damping ratio studied here will, most likely, increase with oil thickness. The damping ratio has been used in several oil spill studies to identify internal zones [3], [11], [22], to extract the volumetric mixing ratio of oil in water [6], and to identify areas containing thicker oil within a slick [12]. The VV channel is used when calculating the damping ratio in preference to the HH and HV channels because VV provides higher contrast between oil and clean sea and is less affected by the system noise [1], [23], [24].

B. Copolarization ratio

According to the tilted Bragg scattering model [25], the ratio of the two intensities HH and VV cancels the small-scale surface roughness. This model has been shown to accurately reproduce L-band SAR scattering from oil slicks using two different high signal-to-noise airborne instruments [5], [9].

The ratio is a function of the relative dielectric properties of the multi-layered medium (air, oil, and seawater), incidence angle, and the geometry of the ocean surface waves [25]. To obtain a high oil-to-sea contrast with this feature, the relative dielectric properties must be altered by the oil. This means that the oil layer thickness must be comparable to the penetration depth[1] of the radar (order of mm for L-band), so that the backscattered signal comes from the oil layer itself. Hence, the CPR might aid in the detection of the thickest oil within a slick [5]. In [5], the authors demonstrated, both theoretically and experimentally using UAVSAR data, that the CPR values were greater across oil-infested areas compared to oil-free areas for incidence angles spanning 30° to 60°. In this study, the CPR_c is used instead of CPR. The CPR_c is still a function of the same properties as the CPR, but produces values close to 1 for clean sea areas, and less than 1 for oil-infested areas.

III. Study area and data set

This study is based on three time series acquired with the L-band UAVSAR airborne sensor. The advantages of using the UAVSAR sensor are the fine resolution (approximately 2.5×1 m range and azimuth single look resolution), the high SNR [27], and the possibility of short repeat time between scenes. The three time series were collected in November 2016, covering an area of the MC-20 block in the Gulf of Mexico where there has been a persistent oil seep since 2004 [13], [14], [28] (see Fig. 1). This spill is well known and has been investigated in several previous studies, see e.g., [11], [13]–[15], [21], [28], [29].

One study [13] observed that the average slick area is approximately 14 km^2 per image (evident from both SAR and optical imagery) and with an estimated oil discharge rate of 48 to 1700 barrels/day. Another study, [15], observed on average 2.7 ± 2.4 km^2 per day using 42 TerraSAR-X scenes. The oil originates from the seafloor, which lies at a depth of 150 m in this location (MC-20 block) [14] and rises to the surface after undergoing different phases such as the plume phase and the post-terminal phase (see e.g., [30], [31], and references therein). The oil leaking from the seafloor might also start to diffuse or disperse when traveling towards the surface. After reaching the surface, the oil will continue to weather and move as a result of the ocean and wind conditions. Further, this persistent oil slick in the MC-20 block travels along the isobaths (generally southwest to northeast) [29], the drift and extent largely being controlled by the Mississippi River Plume dynamics, and the oil pathway aligned with the riverfront [14].

Table I contains information about the acquisition period and the number of acquisitions within each time series. The first time series (TS-1) was acquired November 15, 2016, the second time series (TS-2) was acquired two days later in the morning (local time) on November 17, and the third time series (TS-3) was acquired in the afternoon (local time) on November 17. The scenes were acquired approximately 20 minutes apart. Fig. 1 shows the study area and the slick extent in the three time series displayed in different tones of grey. The three time series were acquired under various wind and ocean conditions as shown in the panel of Fig. 1.

TABLE I
Overview of the acquisition period and number of acquisitions in each time series.

Time series ID	Date	Time period (UTC)	Number of scenes	Time between acquisition (min)
TS-1	15 Nov.	12:12-14:25	8	18-20
TS-2	17 Nov.	15:10-17:48	9	19-21
TS-3	17 Nov.	21:58-23:47	6	19-25

Wind information is obtained from three buoys located around the study site (Fig. 1). The NOAA BURL1 station is located approximately 45 km from the seep in the MC-20 block with an anemometer height of 38 meters. The other two buoys (buoy 42020, and buoy 42040) have an anemometer height of 4 meters, and are located approximately 78 km and 110 km from the site. The wind speed has been converted to equivalent neutral wind with an anemometer height of 10 meters (U10) [32], which resulted in a change of approximately ±1 m/s. The panels in Fig. 1 shows the wind vectors concurrent with each time series. The wind directions were relatively consistent within each time series, and the measured wind speeds from the two days, $3.8 - 6.6$ m/s, are within the theoretical range ($2 - 3$ m/s to $10 - 14$ m/s) where oil spill detection is possible [33], [34]. The wind directions are all orientated towards the south for the time period of TS-1, with a small westward component. On November 17 the wind directions were towards the north to northwest across the time period of TS-2 and TS-3.

A. Oil slick masks

The oil slick masks were obtained from the UAVSAR data by applying a Gaussian Mixture model to the DR_{VV} (see [35] for a thorough description of this unsupervised segmentation method). The output segments from this method are labeled as oil-free or oil-infested segments, resulting in a binary image, which was filtered using a connectivity filter to reduce the grainy patterns that result from radar speckle.

The slick masks for the scenes within one time series vary due to transport, spreading, and weathering processes. Therefore, all the individual masks are joined to form a new overall mask, that covers the entire oil slick extent across the given time series. The UAVSAR scenes are calibrated and multilooked to a pixel spacing of 5×7.2 m (slant range × azimuth). The DR_{VV}, CPR_c, and oil masks are georeferenced[2] creating a stack of UAVSAR scenes on the same latitude/longitude grid (see Figs. 2-4).

To simplify the discussion, the slicks are divided into regions, indicated by the red boxes. The look-direction is towards the left of the flight-direction, and three flight directions were used in the data collection of TS-1, which

---

[1] The penetration depth is defined as the depth at which the radar signal is attenuated to $1/e$ [26].

[2] Georeferenced using WGS84 and EPSG:4326.

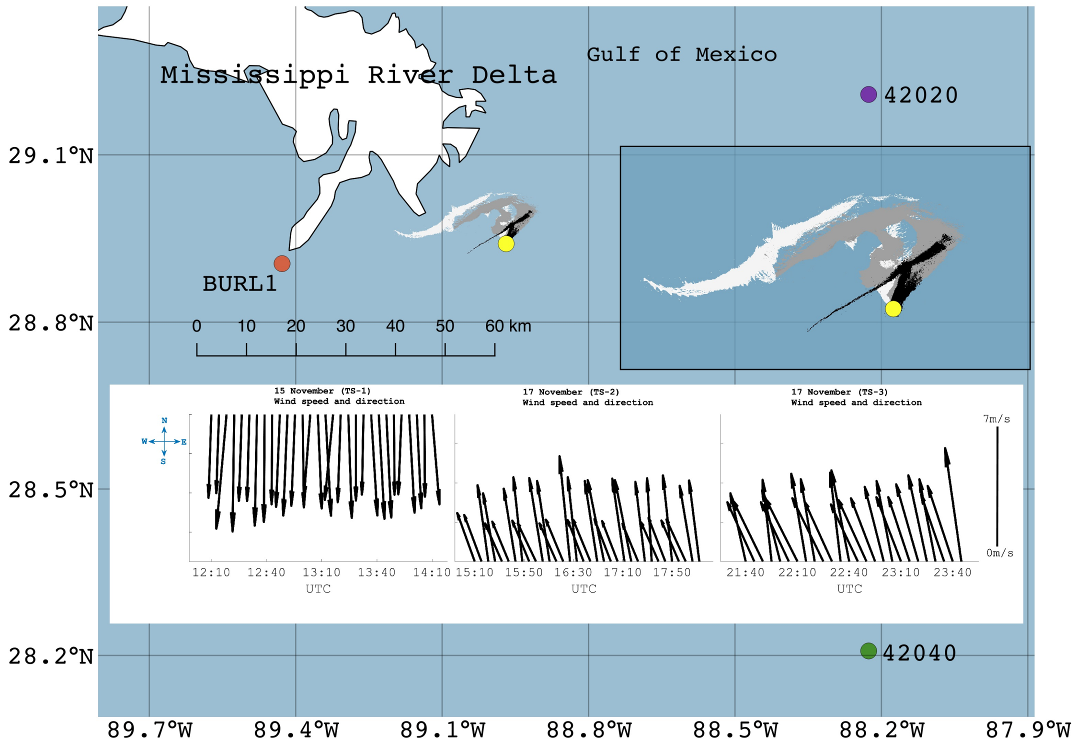

Fig. 1. Study area and the oil slick area covered by the UAVSAR. Wind information is collected from the NOAA BURL1 station (orange circle), NOAA buoy 42020 (purple circle), and NOAA buoy 42040 (green circle). The yellow circle shows the location of the persistent seep in the MC-20 block (see e.g., [11], [14]). The three different tones of grey show the coverage of the joint oil slick masks from the segmentation of the total set of scenes from TS-1, TS-2, and TS-3 (from dark to light respectively). The panel shows the evolution of the wind vectors from three buoys measured during the time period of the three sets of UAVSAR data. The wind velocities are converted to U10.

are indicated by labels FD_1, FD_2, and FD_3 in Fig. 2. This results in a slightly different incidence angle range across the slick; flight ID 001 had incidence angles spanning 44°-52°; flight ID 002 and 003 had incidence angles spanning 50°-55°; remaining flights (flight ID 004-008) had incidence angles spanning 46°-52° across the slick. Since all the flights were looking close to downwind, the effect on the look direction and the small incidence angle variations amongst the scenes (in TS-1) is small. Only one flight direction (FD_3) was used in the acquisition of the scenes in TS-2 and TS-3, and the incidence angles span approximately 40°±15° across the oil slicks. The flights in TS-2 and TS-3 were looking upwind. TS-2 and TS-3 were acquired under approximately the same imaging geometry, resulting in less deviation between the features investigated due to incidence angle variations and different look-direction. Also, the two features are normalized to the clean sea, which reduces the incidence angle variations across the oil slick and between the scenes (see Section II).

B. Short time area evolution of the persistent seep

The estimated area from the segmentation masks varies from 2 - 35 km^2, where the smallest areas are observed on November 15 (TS-1), and the larger areas are observed on November 17 (See Fig. 5). This matches [13], where on average of 14 km^2 per image was found across the three time series. The estimated areas within each time series (spanning approximately 2 - 4 hours) are similar. Hence, the total area does not change drastically over these short time series, which might allow identification of stable areas with approximately the same SAR backscatter intensity over time.

IV. METHOD

We are interested in identifying temporal changes in the investigated features that can be used to observe short-term oil slick drift. These changes are connected to the spreading and weathering processes of the oil slick, and are reflected in the backscattered signal. The damping ratio and copolarization ratio extracted from SAR have been frequently used in single scene analysis, and we want to demonstrate some examples of how these features can be used in a time series. Therefore, the changes in investigated feature values are explored as a function of time at various locations within the slick. By quantifying the change in the parameters we can obtain information about the *stability* of the SAR features in the oil slick as a function of time. Here, the stability is used as a measure of how little a feature value changes within a given area over a certain time interval. Different products derived from statistical analysis are used to evaluate whether a time series with short repeat time can provide complementary information to a single acquisition.

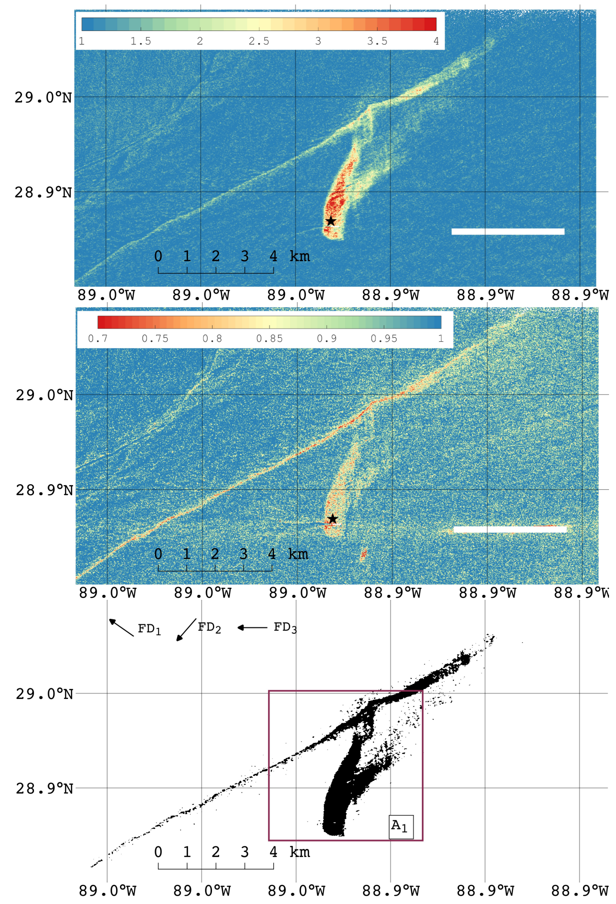

Fig. 2. The VV damping ratio (DR_{VV}) (top-left panel), the copolarization ratio contrast (CPR_c) (top-right panel), and the corresponding mask of the clean sea (background) and oil-infested areas (black) (bottom panel) from the TS-1 scene acquired at 13:09 UTC. The imaging direction of UAVSAR is to the left of the flight direction (FD). The sidelobes from the point target to the lower right is masked out. The black star is the approximate location of the seep (see e.g., [11], [14]).

One important step in a response action is to investigate the spill site for situational awareness. The mineral oil thickness might vary within the oil slick and create zones with varying characteristics that affect the SAR backscatter signal. Various containment and recovery equipment exist, e.g., mechanical, chemical, biological and/or physical methods, whose efficiency depends upon the oil thickness. Knowledge of the thicker oil's location and drift pattern could be used to identify locations where the response should be focused. In this study, we explore methods that capture how these zones change as a function of time and quantify the stability of these zones.

A. Method 1 – detection of stable regions within the oil slick

Method 1 identifies those locations where the VV damping ratio is consistently high throughout the time series. This is achieved by counting the number of scenes in which the DR_{VV} for a given pixel is above a certain threshold (T_h). Operationally, the most recent acquisition is the most important scene in a time series since it provides the latest status of an oil spill. To account for this, the stability level (SL) is calculated by applying higher weights to the more recent scenes. We use an exponentially weighted moving average filter, and the input to the SL is a binary image calculated as

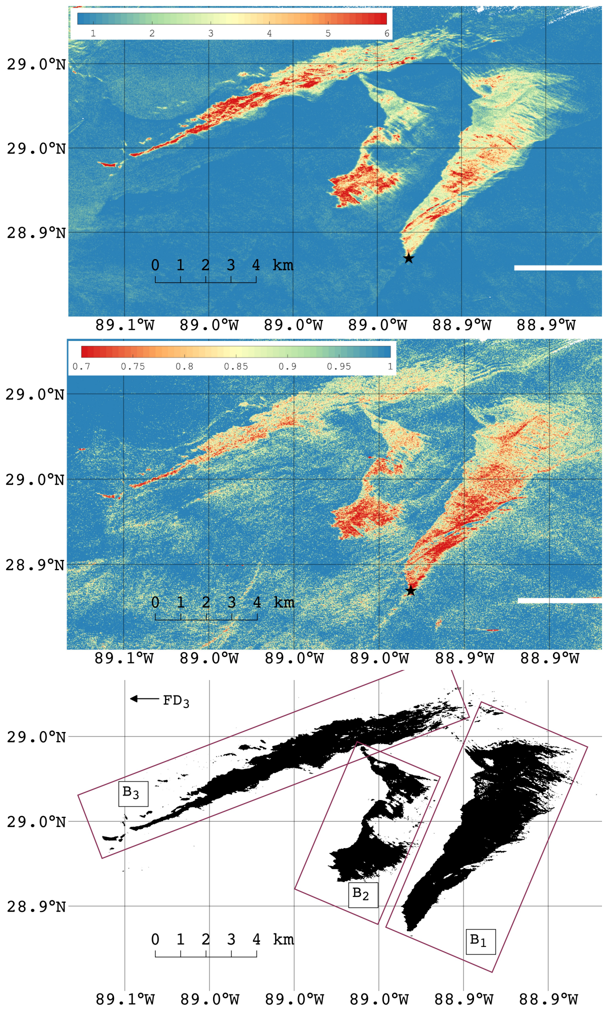

Fig. 3. The VV damping ratio (DR_{VV}) (top-left panel), the copolarization ratio contrast (CPR_c) (top-right panel), and the corresponding mask of the clean sea (background) and oil-infested areas (black) (bottom panel) from the TS-2 scene acquired at 16:11 UTC. The imaging direction of UAVSAR is to the left of the flight direction (FD). The sidelobes from the point target to the lower right is masked out. The black star is the approximate location of the seep (see e.g., [11], [14]).

$$B_i(x,y) = \begin{cases} 1 & \text{if } F_i(x,y) > T_h \\ 0 & \text{if } F_i(x,y) < T_h \end{cases} \tag{3}$$

where $i = [1, N]$, F$_i$ is the feature (for example the DR_{VV}) evaluated for scene i, $i = 1$ is the earliest image, $i = N$ is the most recent, and (x, y) is the spatial position in the scene. Further, the SL is calculated as;

$$SL_i(x,y) = \begin{cases} B_i(x,y) & i = 1 \\ \alpha B_i(x,y) + (1-\alpha) SL_{i-1}(x,y) & i > 1 \end{cases} \tag{4}$$

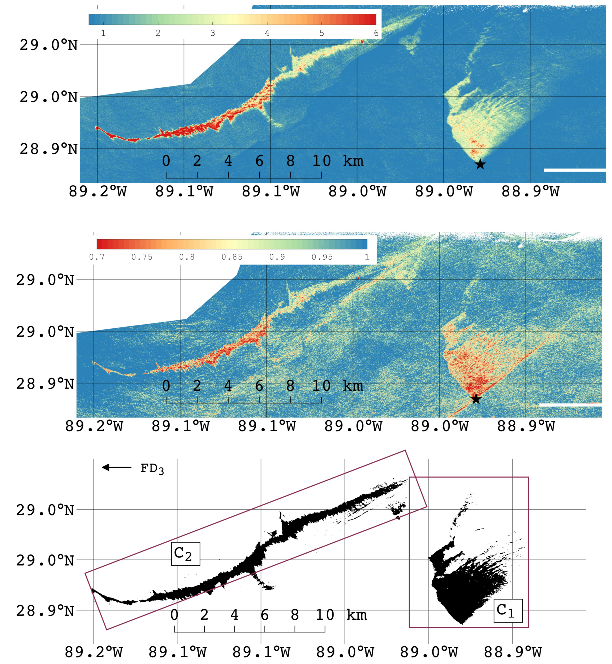

Fig. 4. The VV damping ratio (DR_{VV}) (top-left panel), the copolarization ratio contrast (CPR_c) (top-right panel), and the corresponding mask of the clean sea (background) and oil-infested areas (black) (bottom panel) from the TS-3 scene acquired at 23:27 UTC. The imaging direction of UAVSAR is to the left of the flight direction (FD). The sidelobes from the point target to the lower right is masked out. The black star is the approximate location of the seep (see e.g., [11], [14]).

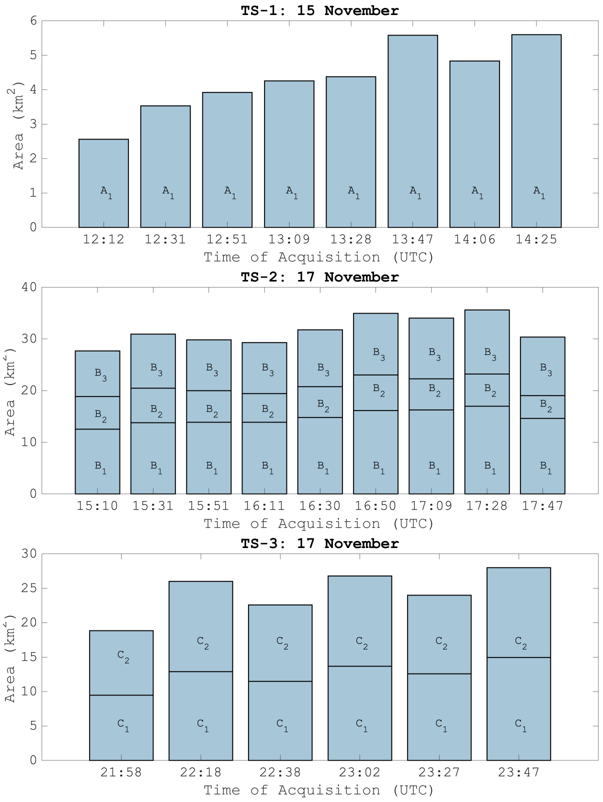

Fig. 5. The estimated area covered by oil from the segmentation masks. Each bar is divided in the regions defined in Figs. 2-4. Top left: TS-1. Top right: TS-2. Bottom: TS-3.

where $i = [1, N]$. SL_i is the level of stability measured at scene i. The coefficient α is the level of weighting, which is defined between 0 and 1. A high α discounts older observations faster, and for $\alpha = 1$ the $SL_i(x, y) = B_i(x, y)$, i.e., equal to the current binary image i. For $\alpha = 0$, $SL_i(x, y) = B_1(x, y)$, i.e., all new observations are discarded. Hence, in order to include and weight all scenes in a time series the α cannot be 0 nor 1.

The choice of α is somewhat arbitrary, but in this work α was set to 0.5. This gives the current observation equal weight to that of all previous observations combined. Maps of SL show the most recent measurement, i.e., SL_N. In order to obtain a realistic SL map, the total number of scenes must exceed 2 and $\alpha \in (0, 1)$, otherwise the SL is only a binary image. The values from the weighted running average filter are then scaled between 0% and 100% so that a value of 100% indicates completely stable oil pixels, i.e., the feature value for a given pixel location is always above T_h throughout the time series. The choice of T_h is tunable to cover the range of values within the scene, with high values of T_h used to identify the high damping ratio areas as a proxy for slick thickness. The benefits of using the weighted running average filter implemented in SL are that the weights are independent of the number of scenes available, and we can update the SL map whenever a new acquisition is obtained. To reduce radar speckle while preserving the spatial resolution, in this study the DR_{VV} is smoothed with a 5×5 moving average mask prior to the calculation of the SL.

B. Method 2 – radiometric change detection for identifying drift patterns

Method 2 investigates the change in the polarimetric information as a function of both time and space to create a map that can be used to understand short-term drift patterns. Change detection using SAR images have been widely explored for various applications such as monitoring vegetation, urban-, and agricultural areas. The surfaces of the clean sea and the oil slicks are highly non-stationary, and due to the dynamic changes within the slicks and the ocean, the backscattered signals vary from one acquisition to the next. Therefore, exploring changes on a pixel-to-pixel basis is inefficient. In this study, a window size of 5×5 pixels is used to obtain the local mean value from the input feature image (DR_{VV} or CPR_c). The difference in the mean (r_{DM}) feature value is calculated between the reference flight and the other flights in the following manner;

$$r_{DM} = \mu_{ID} - \mu_{\text{ref. flight}} \tag{5}$$

where ID is the flight ID, μ_{ID} is the local mean within a 5×5 window from scene ID, and $\mu_{\text{ref. flight}}$ is the local mean calculated from the reference flight. If the r_{DM} is close to 0, then no change has occurred between two scenes on average within the 5×5 neighborhood. Note that this method only considers two scenes, as opposed to method 1 that incorporates information from all the scenes in the time series.

V. RESULTS AND DISCUSSION

The two methods are applied to the three time series (TS-1, TS-2, and TS-3) to detect the stability of the features and drift patterns of the slicks. The sections below present the results and a discussion of how the methodology can be used.

A. Method 1 – detection of stable regions within the oil slick

The overall aim of the Stability Level (SL) method is to locate and quantify regions that have a consistently high damping ratio over a period of time. These areas are likely to be of special interest during a clean-up process. Given that it takes time to deploy boats to a spill, directing them to areas likely to have and to continue to retain thicker oil will reduced deployment time.

The range of DR_{VV} values is approximately 1 to 5 for the scenes in TS-1, between 1 and 8 for the scenes in TS-2, and between 1 and 10 for the TS-3 scenes. Here we calculate the SL (eq. 4) using all the scenes in each time series. The results of this procedure are shown in Fig. 6.

The different panels of Fig. 6 show the SL for thresholds T_h = 2, 3, and 4. Since a weighting factor of 0.5 is used (see eq. 4), a SL value above 50% will indicate that the latest acquisition and some scenes prior to the latest scene had a DR_{VV} above the threshold. Further, if the SL is below 50% the latest scene did not have a DR_{VV} above the threshold, but some prior scenes did. Regions of high SL values (above 98%) are colored dark red to clearly indicate the areas that are the most stable, and the center and right-most panels indicate regions where the DR_{VV} is relatively high (above 3) across the entire time series. Higher damping values likely indicate thicker or more emulsified oil.

For the TS-1 scenes (top panel of Fig. 6), the dark red areas become more constrained towards the southern part of the main slick (closer to the source of the seep) when the threshold of DR_{VV} increases. When a threshold of 4 is used, three main regions show 100% stability (dark red) in TS-2 scenes (the second row of Fig. 6), e.g., the slick in B_1 shows a stable region stretching from south to north. One small area on the southeast side of B_1 has a 100% stability. It would be logical to prioritize this particular area for potential clean-up. The oil slick in B_3 also shows an area of high SL over the 2 hour time period. The oil slick located in B_3 has been on the surface longer compared to the oil slick in B_1 and B_2. Potential reasons for having these high damping ratio values in B_3 are emulsification [36] and/or oil accumulation in the river-induced front from the plume river dynamics of the Mississippi River [14]. There is a high SL area in C_1. The elongated oil slick area in C_2 also has a stable region of high DR_{VV} values (above 4). This is of special importance since this slick region has been subject to weathering for a longer time period compared to the southeast part of the slick, closest to the source. The high DR_{VV} value might be a result of the formation of emulsions over time [36]. Additionally, the oil at the surface might initially be fairly thick/concentrated and then spreads out as sheen by winds and currents, and be pushed against the plume resulting in accumulation of oil along the fronts.

One drawback of this method is the need for tuning T_h, but for these three time series, a threshold of 3 seems reasonable since it managed to capture patches of high damping ratio values over a period of time. However, this threshold might differ from other oil types, sensors, and metocean conditions. This method does not account for the direction in which the thick oil is being transported by winds and currents, which is considered by method 2.

B. Method 2 – radiometric change detection for identifying drift patterns

Prior work combining short SAR time series of slick evolution with oil drift modeling showed that both wind and local currents can significantly affect short term drift patterns [37]–[39]. In coastal areas where the currents can change over short spatial scales, accurately modeling drift patterns is challenging. Method 2 calculates the difference in the local mean feature values (r_{DM}) between two scenes to identify drift patterns without the need for modeling or knowledge of local currents and wind. Method 2 is applied on TS-2 and TS-3 (Figs. 7-8). Similar results applies for TS-1 (not shown).

Information about persistent areas (the same media, oil or clean sea between the two scenes) and areas in transitions are shown in the top panels in Figs. 7 and 8, which is based on the oil slick masks from the segmentation method. The light red and blue colors correspond to areas that are persistent, while the dark red and blue colors show areas in transition between oil-coverage and clean sea or vice versa.

The second row of Figs. 7 and 8 shows the r_{DM} obtained using the DR_{VV} with the first flight in the given time series as the reference flight. The orange-red areas indicate where the DR_{VV} has increased in value from the first flight, while yellow colors indicate little change between the first flight to the flight ID investigated. Green-blue indicates areas where there has been a decrease in the DR_{VV}. The third row of Figs. 7 and 8 shows the r_{DM} using the CPR_c, where a similar interpretation applies. Notice that the colorbar is reversed for CPR_c compared to the colorbar used for DR_{VV} because oil causes a lower CPR_c value compared to clean sea, which is the opposite trend from that of the DR_{VV}. There are several possible r_{DM} images that could be displayed, but only three of them are shown in Figs. 7 and 8.

A clear oil drift pattern is observed within the three areas B_1, B_2, and B_3 (see Fig. 7). In general, the oil in B_1 and B_2 spreads out in the northwest direction, while the oil in B_3 moves in the southwest direction. The oil slick in B_1 is closest to the source of the oil (black star in Fig. 7). The red/orange band on the western part of B_1 in both the center and bottom panels of Fig. 7 indicates an increase (decrease) in the DR_{VV} (CPR_c). This red/orange band gets wider with time, indicating that the oil spreads out in the northwest direction, which is in

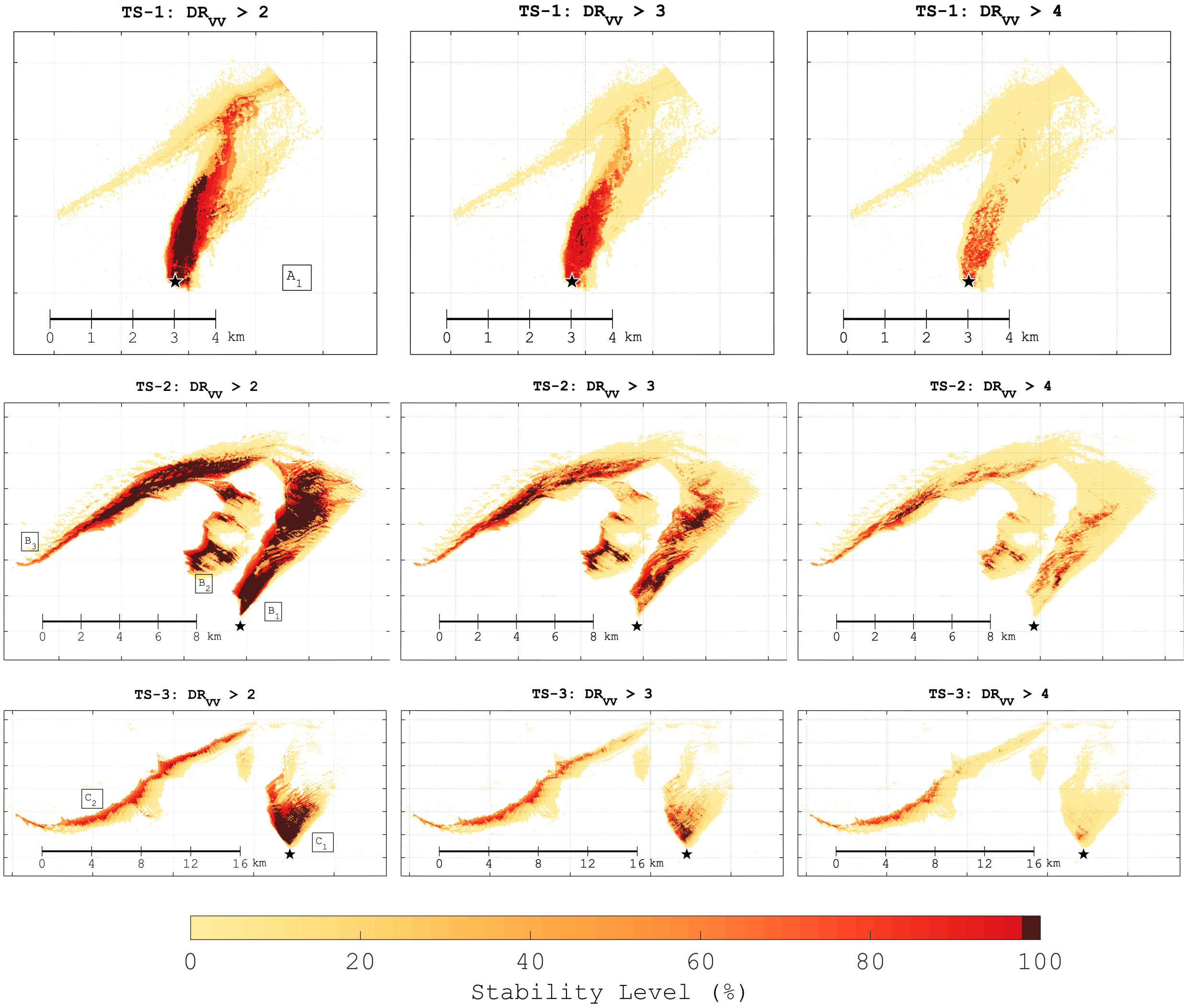

Fig. 6. Maps showing the stability level (SL) in % of the DR_{VV} for various values of T$_h$. The top row is the SL extracted from the TS-1 scenes, center row is the SL from the TS-2 scenes, and the bottom row is the SL from the TS-3 scenes. The black star is the approximate location of the seep (see e.g., [11], [14]).

accordance with the wind direction. However, on the east side of B$_1$, the DR_{VV} values decrease as a function of time, which might indicate that the oil is transported from the east (blue) to the west (red) regions. The same conclusion can be drawn from the CPR_c. As pointed out in [11], there is a convergence zone entering from the east side of B$_1$ at approximately 80 minutes after the first acquisition and moves northwards throughout the time series.

The slick spreads in the western part of B$_2$, similar to B$_1$ (see Fig. 7). Additionally, the r_{DM} using the DR_{VV} in the eastern part of the slick is decreasing, as indicated by the blue area. The same blue area is observed for the r_{DM} using the CPR_c. The oil slick in B$_3$ is located where the near-shore coastal current has a southwestern direction, as opposed to the slick in B$_1$ and B$_2$ where the ocean current is towards the northeast [16]. In B$_3$, the oil is transported with the coastal current towards the southwest, and not with the wind as the oil in B$_1$ and B$_2$. Again, for the oil slick in B$_3$, there are decreasing DR_{VV} values on the opposite side from where there is an increase, indicating oil movement. In general, the r_{DM} using the CPR_c (bottom panels of Fig. 7) shows a similar behavior as the r_{DM} for DR_{VV} (center panels of Fig. 7). The DR_{VV} and CPR_c are similar for B$_1$ and B$_2$, where the r_{DM} from CPR_c also captured the spreading of the oil.

The center (bottom) panels of Fig. 8 show the r_{DM} based on the DR_{VV} (CPR_c) for the TS-3 scenes. The effect of the wind can clearly be seen for the oil slick in C$_1$, where the DR_{VV} increases on the western part of C$_1$, and decreases on the eastern part of C$_1$. This is a result of the oil being transported from east to west by the wind. The same phenomena are observed for the CPR_c. For the oil slick in C$_2$, the effect of both the wind and the southwestern ocean current are present. First, the wind pushes the oil in the northwest direction, which can be seen by the red region being located

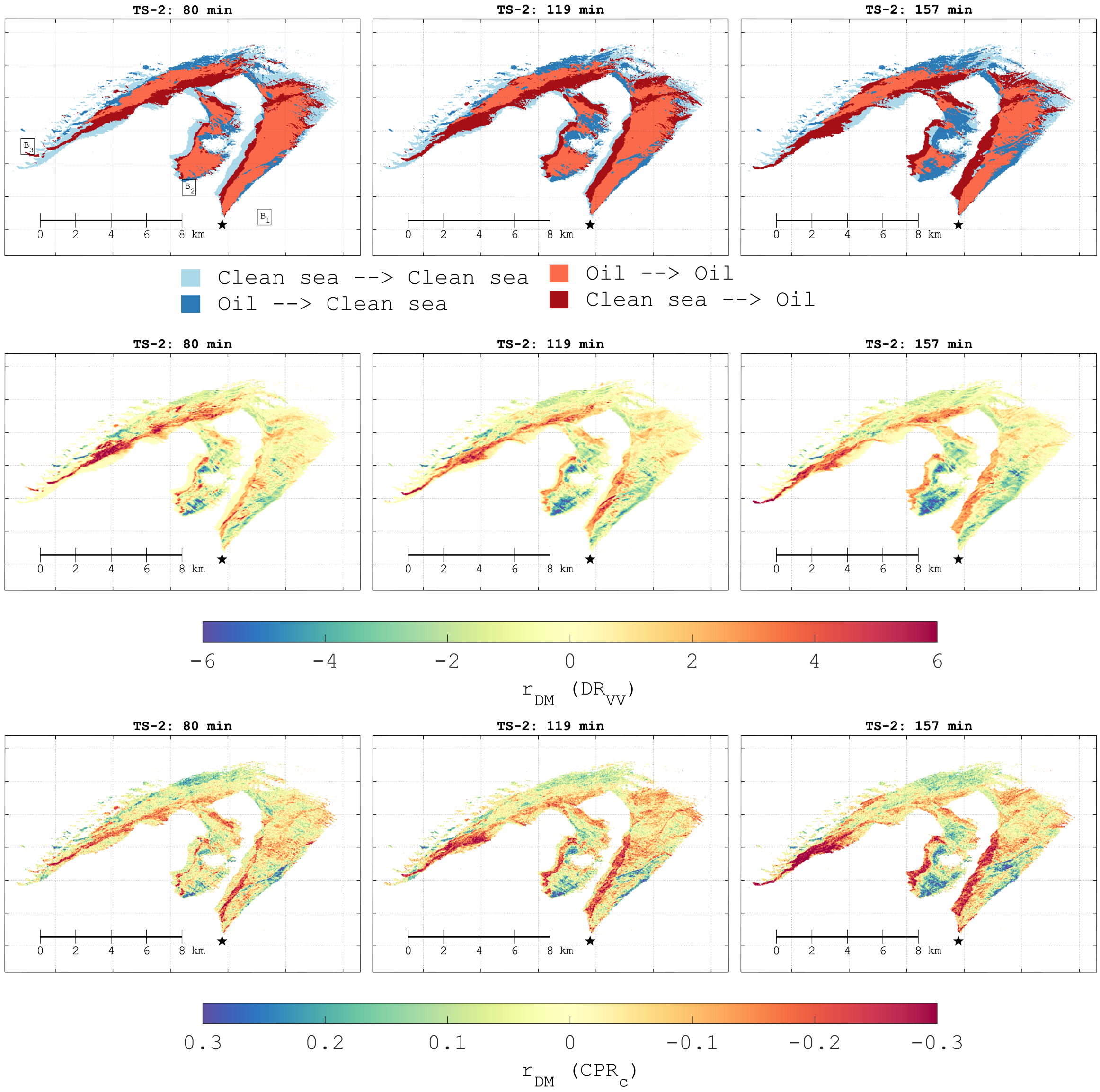

Fig. 7. Top panels: maps (based on the oil slick masks) showing the persistent areas colored light blue for clean sea and light red for oil. The areas in transition are colored dark blue or dark red for "clean sea→oil" or "oil→clean sea", respectively. The time (min) given in the header of each panel represents time since the first acquisition, i.e., the reference flight ID 000. Center panels: maps showing the local mean difference (r_{DM}) of the DR_{VV} between flight ID 000 and some of the other flights. The colors range from blue indicating a decrease in the DR_{VV} to red indicating an increase in the DR_{VV}. Bottom panels: maps showing the r_{DM} of the CPR_c between flight ID 000 and some of the other flights. The colors range from red indicating a decrease in the CPR_c, to blue indicating an increase in the CPR_c. The black star is the approximate location of the persistent seep in MC-20.

above the blue colored region in both the center and bottom panels of Fig. 8. This is also seen in the top panel of Fig. 8, where the red band (clean sea→oil) is above the dark blue area (oil→clean sea). In the south of the red band in C_2 there is a corresponding blue band that also gets wider with time, which reveals that the DR_{VV} decreases and CPR_c increases as the slick moves out of this area. Having similar observations of r_{DM} for both DR_{VV} and CPR_c might indicate an increase in the oil concentration, which could be a result of accumulation of oil due to the wind drag (most likely) and/or the riverfront, or to oil emulsification causing an increase in the damping ratio. The oil at the surface might also initially be fairly thick/concentrated and then spreads out as sheen by winds and currents, and be pushed against the plume resulting in accumulation of oil along the fronts.

VI. SUMMARY

Figs. 9 and 10 show close-up images of DR_{VV} (left panel), SL (when $DR_{VV} > 3$) (center panel), and r_{DM} (using DR_{VV}) (right panel) for the region closest to the source of the seep, i.e., southern part of B_1 (TS-2) and C_1 (TS-3). The left panel of Figs. 9 and 10 shows the last DR_{VV} image in the time series, in which variation of the oil characteristics with the slick is evident. The areas with high DR_{VV} values in the

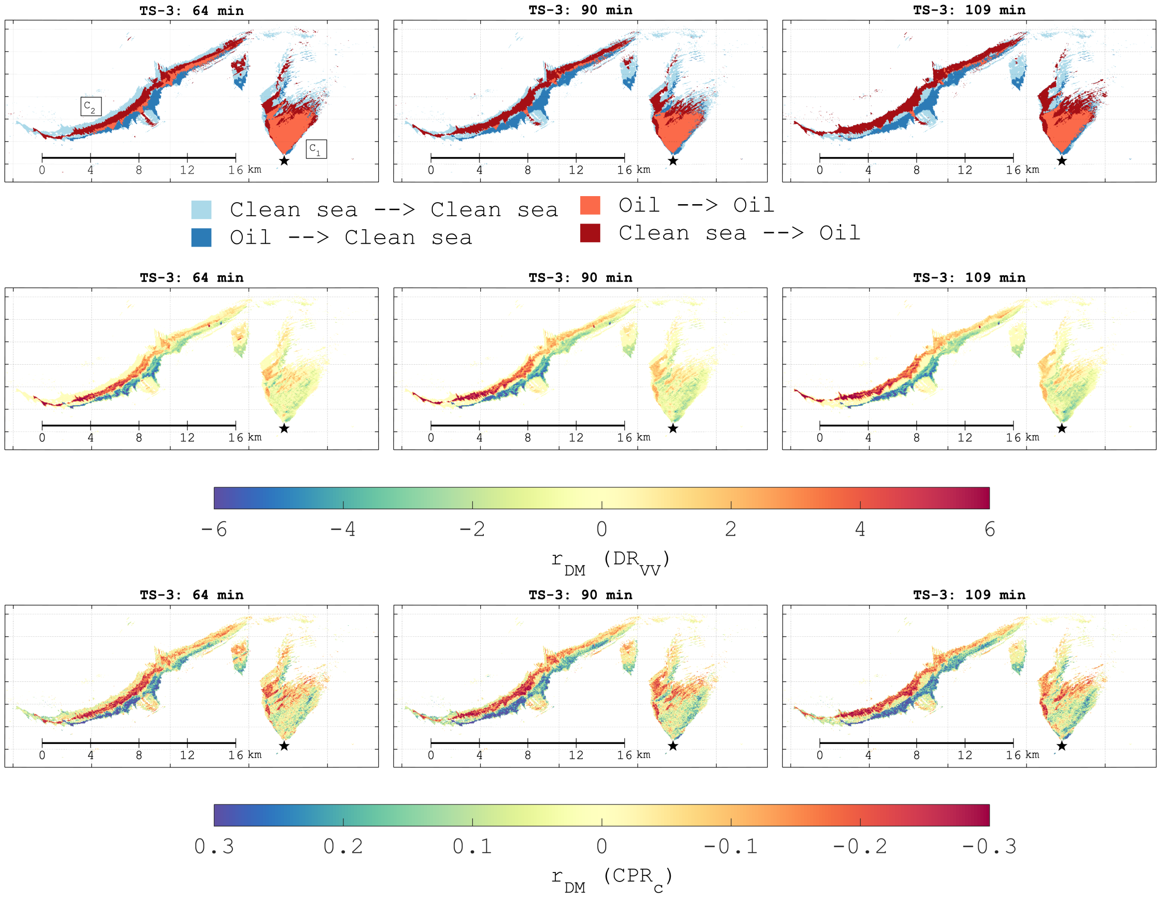

Fig. 8. Top panels: maps (based on the oil slick masks) showing the persistent areas colored light blue for clean sea and light red for oil. The areas in transition are colored dark blue or dark red for "clean sea→oil" or "oil→clean sea", respectively. The time (min) given in the header of each panel represents time since the first acquisition, i.e., the reference flight ID 000. Center panels: maps showing the local mean difference (r_{DM}) of the DR_{VV} between flight ID 000 and some of the other flights. The colors range from blue indicating a decrease in the DR_{VV} to red indicating an increase in the DR_{VV}. Bottom panels: maps showing the r_{DM} of the CPR_c between flight ID 000 and some of the other flights. The colors range from red indicating a decrease in the CPR_c, to blue indicating an increase in the CPR_c. The black star is the approximate location of the persistent seep in MC-20.

most recent image should be prioritized, but these areas do not hold information about the past, which the SL image provides. For comparison, the darkest red areas in SL (center panels) are where $DR_{VV} > 3$ in all the scenes of the time series. Therefore, SL shows both where the thicker oil was most recently (values >=50%) and where the oil has persistently been in a particular area (values approaching 100%). The SL map clearly locates the persistent high damping ratio areas within the slick. The dark red regions should therefore be prioritized as good starting points for the recovery operation.

The right panels in Figs. 9 and 10 shows where the oil is spreading/drifting based on the r_{DM} calculated with DR_{VV}. The oil slicks in both Fig. 9 and 10 are spreading towards the northwest. Having this information available could aid in navigating into the site and for further planning the timeline for recovery and use of field resources. The SL and r_{DM} maps provide complementary information to the single DR_{VV} image in a given time series.

VII. CONCLUSION

The overall goal of this study is to demonstrate two complementary semi-automated methods that can be used with time series data to produce maps showing the trends in slick transport and weathering without requiring visual inspection of each of the scenes, while also incorporating a memory of the evolution history. Two methods, SL and r_{DM}, are suggested, which are complementary in terms of identifying the zones of stability within a slick, the drift patterns of the slick, and the weathering and accumulation of oil to form higher damping surface layers. These are important aspects in the planning and execution of a clean-up process. The methods are summarized below.

Method 1: This method is used to identify patches within the slick that consistently exhibit a high damping ratio over a period of time, assumed to indicate thicker oil. The information obtained from the SL can be used in an oil spill recovery operation where high SL areas should be investigated first, and to direct crews to the site since

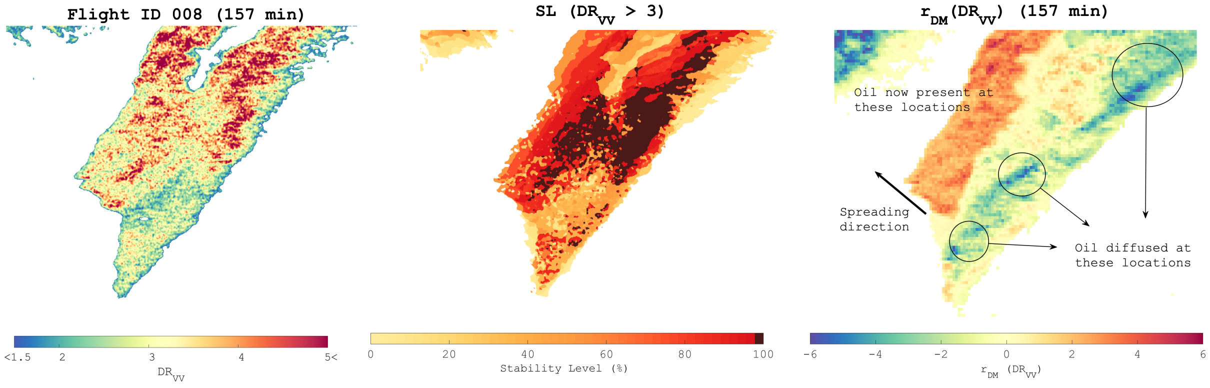

Fig. 9. Left: detailed DR_{VV} image of the lower part of B$_1$ from TS-2. Center: SL from the last scene in the time series (center image in second row of Fig. 6). Right: mean difference of the DR_{VV} between the first and last scenes in the time series (right image in second row of Fig. 7). The time (in min) since the first acquisition is shown in the header of left and right panels.

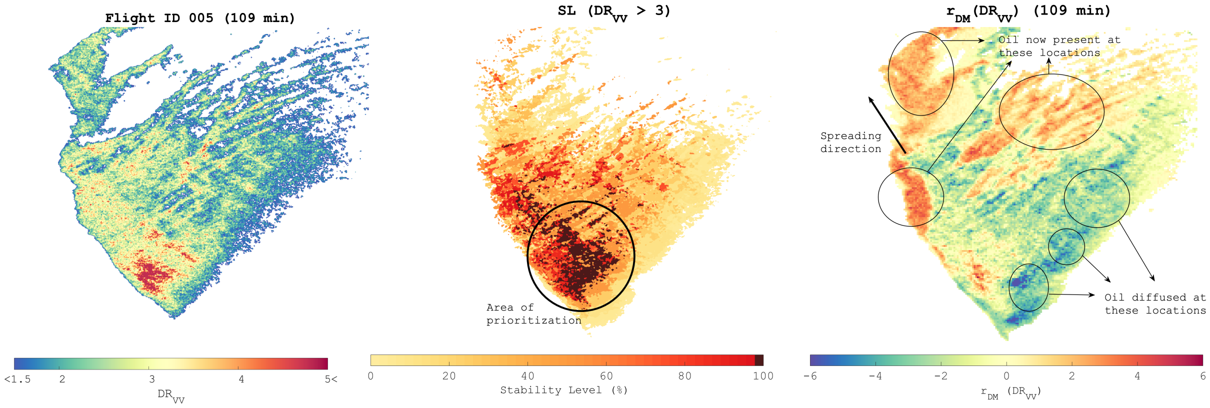

Fig. 10. Left: detailed DR_{VV} image of the lower part of C$_1$ from TS-3. Center: SL from the last scene in the time series (center image in second row of Fig. 6). Right: mean difference of the DR_{VV} between the first and last scenes in the time series (right image in second row of Fig. 7). The time (in min) since the first acquisition is shown in the header of left and right panels.

deployment from base could take a while, in particular in remote locations such as in the Arctic. It is only reasonable to use the SL-method over a short time period as the oil slick might drift sufficiently far that the slick masks are non-overlapping. Additionally, this method could also be well suited to obtain an overview of a persistent leak from platforms or pipelines. In the scenario studied here, the oil originates from a seep at the seafloor, and new oil is continuously emerging at the surface. Hence, the SL-method is suited for this type of scenario and the high SL values could be of special importance as they reveal patches of high damping ratio over a longer period of time. Further studies should be conducted on oil slicks that are spilled at the surface and not leaked from the seabed as in this case.

Method 2: The SL-method detects regions of consistently high DR_{VV} values, but it cannot detect where the oil is moving. The second method compliments this by obtaining an overview of the oil drift pattern using the mean change (r_{DM}) of both DR_{VV} and CPR_c and the difference in the oil masks between two scenes. Here, both information about the oil movement and the backscatter change within the oil slick can be obtained. The DR_{VV} and CPR_c demonstrated similar results in r_{DM}. The DR_{VV} can thus be recommended since only one polarization channel is needed to identify variations within the slick. Another goal of this method was to identify areas that the oil is moving to and from, i.e., small scale drift patterns.

The results are obtained under moderate wind conditions, and further research regarding other metocean conditions are necessary. Further testing is still required to confirm the relationship between relative oil thickness and damping ratio (DR_{VV}). One limitation of the two methods is that a clean sea region needs to be present in the SAR scene when calculating the DR_{VV}, but given the size of scenes from most remote sensing instruments, this is commonly not a limiting factor.

Scene to scene changes using airborne SAR is likely to be restricted to the actual backscattered properties of the target. The different sensor properties, such as different imaging geometries (look direction and incidence angle), frequency, polarization, resolution, swath width, etc., are likely to impact the scene to scene variations. A recent development is the introduction of SAR microsatellites[3] which may enable multiple observations on a daily basis. Combining such micro- and other spaceborne satellites, it might be possible to construct a time series of spaceborne SAR images with short time difference between scenes. The different sensor properties could obfuscate the observed changes on the surface between the scenes, which must be considered in a time series analysis. Due to the simplicity of the two methods, they could be adapted to other sensor types, such as optical satellites, but using other input features.

ACKNOWLEDGMENT

The authors would like to thank the Jet Propulsion Laboratory (JPL) National Aeronautics and Space Administration (NASA) team for the collection of the UAVSAR and in-situ data. Thanks also to Wenqing Tang at JPL for providing the algorithm for converting to equivalent neutral wind. This research is financed by CIRFA (RCN Grant no. 237906). This research was carried out in part at the Jet Propulsion Laboratory, California Institute of Technology, under contract with the National Aeronautics and Space Administration (Task Order NNN13D788T). UAVSAR data can be downloaded from the Alaska Satellite Facility (www.asf.alaska.edu).).

REFERENCES

[1] S. Skrunes, C. Brekke, T. Eltoft, and V. Kudryavtsev, "Comparing near-coincident C- and X-band SAR acquisitions of marine oil spill," *IEEE Trans. Geosci. Remote Sens.*, vol. 53, no. 4, pp. 1958 – 1975, Apr. 2015.

[2] M. Gade, W. Aplers, H. Hühnerfuss, V. R. Wismann, and P. A. Langes, "On the reduction of the radar backscatter by Oceanic Surface Films: Scatterometer Measurements and Their Theoretical Interpretation," *Remote Sens. Environ.*, vol. 66, no. 1, pp. 52–70, Oct. 1998.

[3] M. Gade, W. Alpers, H. Hühnerfuss, H. Masuko, and T. Kobayashi, "Imaging of biogenic and anthropogenic ocean surface films by the multifrequency/multipolarization SIR-C/X-SAR," *J. Geophys. Res. Oceans*, vol. 103, no. C9, pp. 18 851–18 866, Aug. 1998.

[4] S. Skrunes, C. Brekke, and T. Eltoft, "Characterization of Marine Surface Slicks by Radarsat-2 Multipolarization Features," *IEEE Trans. Geosci. Remote Sens.*, vol. 52, no. 9, pp. 5302–5319, Sept. 2014.

[5] B. Minchew, C. E. Jones, and B. Holt, "Polarimetric Analysis of Backscatter From the Deepwater Horizon Oil Spill Using L-Band Synthetic Aperture Radar," *IEEE Trans. Geosci. Remote Sens.*, vol. 50, no. 10, pp. 3812–3830, Oct. 2012.

[6] B. Minchew, "Determining the mixing of oil and sea water using polarimetric synthetic aperture radar," *Geophys. Res. Lett.*, vol. 39, no. 16, Aug. 2012.

[7] M. Migliaccio, F. Nunziata, and A. Buono, "SAR polarimetry for sea oil slick observation," *Int. J. Remote Sens.*, vol. 36, no. 12, pp. 3243–3273, Jun. 2015.

[8] A.-B. Salberg, O. Rudjord, and A. H. S. Solberg, "Oil Spill Detection in Hybrid-Polarimetric SAR Images," *IEEE Trans. Geosci. Remote Sens.*, vol. 52, no. 10, pp. 6521–6533, Oct. 2014.

[9] S. Angelliaume, P. C. Dubois-Fernandez, C. E. Jones, B. Holt, B. Minchew, E. Amri, and V. Miegebielle, "SAR imagery for Detecting Sea Surface Slicks: Performance Assessment of Polarization-Dependent Parameters," *IEEE Trans. Geosci. Remote Sens.*, vol. 56, no. 8, pp. 1–21, Aug. 2018.

[10] V. Wismann, M. Gade, W. Alpers, and H. Hühnerfuss, "Radar signatures of marine mineral oil spills measured by an airborne multi-frequency radar," *Int. J. Remote Sens.*, vol. 19, no. 18, pp. 3607–3623, Nov. 1998.

[11] C. E. Jones and B. Holt, "Experimental L-Band Airborne SAR for Oil Spill Response at Sea and in Coastal Waters," *Sensors*, vol. 18, no. 2, Feb. 2018.

[12] S. Skrunes, C. Brekke, and M. M. Espeseth, "Assessment of the RISAT-1 FRS-2 mode for oil spill observation," *IEEE Int. Geo. Remote Sens. Symp. (IGARSS)*, pp. 1024–1027, 2017.

[13] S. Sun, C. Hu, O. Garcia-Pineda, V. Kourafalou, M. L. Hénaff, and Y. Androulidakis, "Remote sensing assessment of oil spills near a damaged platform in the Gulf of Mexico," *Mar. Pollut. Bull.*, vol. 136, pp. 141–151, 2018.

[14] Y. Androulidakis, V. Kourafalou, T. Özgökmen, O. Garcia-Pineda, B. Lund, M. L. Hénaff, C. Hu, B. K. Haus, G. Novelli, C. Guigand, H. Kang, L. Hole, and J. Horstmann, "Influence of River-Induced Fronts on Hydrocarbon Transport: A Multiplatform Observational Study," *J. Geophys. Res. Oceans*, vol. 123, no. 5, pp. 3259–3285, 2018.

[15] F. Nunziata, C. R. de Macedo, A. Buono, D. Velotto, and M. Migliaccio, "On the analysis of a time series of X–band TerraSAR–X SAR imagery over oil seepages," *Int. J. Remote Sens.*, vol. 40, no. 9, pp. 3623–3646, 2019.

[16] C. E. Jones, M. M. Espeseth, B. Holt, and C. Brekke, "Measurement of Oil Slick Transport and Evolution in the Gulf of Mexico using L-band Synthetic Aperture Radar," *European Conference on Synthetic Aperture Radar (EUSAR)*, 2018.

[17] P. C. Genovez, C. E. Jones, S. J. S. Sant'Anna, and C. C. Freitas, "Oil slick characterization using a statistical region-based classifier applied to uavsar data," *J. Mar. Sci. Eng.*, vol. 7, no. 2, Feb. 2019.

[18] S. Skrunes, C. Brekke, and T. Eltoft, "Oil spill Characterization with multi-polarization C- and X-band SAR," *IEEE Int. Geo. Remote Sens. Symp. (IGARSS)*, 2012.

[19] B. Jones, "A comparison of visual observations of surface oil with Synthetic Aperture Radar imagery of the Sea Empress oil spill," *Int. J. Remote Sens.*, vol. 22, no. 9, pp. 1619–1638, Nov. 2001.

[20] I. Sergievskaya, S. Ermakov, T. Lazareva, and J. Guo, "Damping of surface waves due to crude oil/oil emulsion films on water," *Mar. Pollut. Bull.*, vol. 146, pp. 206 – 214, 2019.

[21] L. Herbst, E. DeCola, and K. Kennedy, "New pathways for developing and testing oil spill response equipment in real world conditions," *OCEANS 2016 MTS/IEEE Monterey*, pp. 1–6, 2016.

[22] C. E. Jones, M. M. Espeseth, B. Holt, C. Brekke, and S. Skrunes, "Characterization and discrimination of evolving mineral and plant oil slicks based on L-band Synthetic Aperture Radar (SAR)," *SPIE, SAR Image Analysis, Modeling, and Techniques XVI*, vol. 10003, 2016.

[23] W. Alpers and H. A. Espedal, "Chapter 11. Oils and Surfactants," *Synthetic Aperture Radar Marine User's Manual (NOAA/NESDIS), C.R. Jackson and J. R. Apel*, pp. 263–275, Sep. 2004.

[24] G. Franceschetti, A. Iodice, D. Riccio, G. Ruello, and R. Siviero, "SAR raw signal simulation of oil slicks in ocean environments," *IEEE Trans. Geosci. Remote Sens.*, vol. 40, no. 9, pp. 1935–1949, 2002.

[25] G. R. Valenzuela, "Theories for the interaction of electromagnetic and oceanic waves - A review," *Boundary-Layer Meteorology*, vol. 13, no. 1-4, pp. 61–85, Jan. 1978.

[26] S. R. Cloude, *Polarisation Applications in Remote Sensing*, F. edition, Ed. pp. 125-129: Oxford University Press Inc., New York, 2010.

[27] A. G. Fore, B. D. Chapman, B. P. Hawkins, S. Hensley, C. E. Jones, T. R. Michel, and R. J. Muellerschoen, "UAVSAR Polarimetric Calibration," *IEEE Trans. Geosci. Remote Sens.*, vol. 53, no. 6, pp. 3481–3491, Jun. 2015.

[28] S. D. Asl, J. Amos, P. Woods, O. Garcia-Pineda, and I. R. MacDonald, "Chronic, Anthropogenic Hydrocarbon Discharges in the Gulf of Mexico," *Deep Sea Research Part II: Topical Studies in Oceanography*, vol. 129, pp. 187 – 195, 2016, the Gulf of Mexico Ecosystem - before, during and after the Macondo Blowout.

[29] C. J. Warren, A. MacFadyen, and C. H. Jr., "Mapping Oil for the Destroyed Taylor Energy Site in the Gulf of Mexico," *International Oil Spill Conference Proceedings*, vol. 2014, no. 1, p. 299931, 2014.

[30] Ø. Johansen, H. Rye, and C. Cooper, "DeepSpill-Field Study of a Simulated Oil and Gas Blowout in Deep Water," *Spill Science & Technology Bulletin*, vol. 8, no. 5-6, pp. 433–443, 2003.

[31] J. Coleman, *Oil in the Sea III*. Washington DC, USA: National Academy Press, 2003.

[32] W. T. Liu and W. Tang, "Equivalent Neutral Wind," *JPL Publication 96-17*, 1996.

[33] W. Alpers and H. Hühnerfuss, "The damping of ocean waves by surface films: A new look at an old problem," *J. Geophys. Res. Oceans*, vol. 94, no. C5, pp. 6251–6265, May 1989.

[34] K. P. Singh, A. L. Gray, R. K. Hawkins, and R. A. O'Neil, "The Influence of Surface Oil on C-and Ku-Band Ocean Backscatter," *IEEE Trans. Geosci. Remote Sens.*, vol. GE-24, no. 5, pp. 738 – 744, Sep. 1986.

---

[3] see e.g., www.iceye.com for information regarding the first SAR microsatellite. Last visited 3rd of July 2018

[35] A. P. Doulgeris and T. Eltoft, “Scale mixture of Gaussian modelling of polarimetric SAR data,” *EURASIP Journal on Advances in Signal Processing*, no. 8, Jan. 2010.

[36] M. Fingas and B. Fieldhouse, “Studies on water-in-oil products from crude oils and petroleum products,” *Mar. Pollut. Bull.*, vol. 64, no. 2, pp. 272–283, Feb. 2012.

[37] H. A. Espedal, “Satellite SAR oil spill detection using wind history information,” *Int. J. Remote Sens.*, vol. 20, no. 1, pp. 49–65, 1999.

[38] C. E. Jones, K.-F. Dagestad, Ø. Breivik, B. Holt, J. Röhrs, K. H. Christensen, M. Espeseth, C. Brekke, and S. Skrunes, “Measurement and modeling of oil slick transport,” *J. Geophys. Res. Oceans*, vol. 121, no. 10, pp. 7759–7775, Nov. 2016.

[39] J. Röhrs, K.-F. Dagestad, H. Asbjørnsen, T. Nordam, J. Skancke, C. E. Jones, and C. Brekke, “The effect of vertical mixing on the horizontal drift of oil spills,” *Ocean Science*, vol. 14, no. 6, pp. 1581–1601, 2018.

/10

Paper IV:

Assessment of RISAT-1 and Radarsat-2 for Sea Ice Observations from a Hybrid-Polarity Perspective

M. M. Espeseth, C. Brekke, and M. Johansson

Published in:
Remote Sensing. vol. 9, no. 11, September 2017

remote sensing

Article

Assessment of RISAT-1 and Radarsat-2 for Sea Ice Observations from a Hybrid-Polarity Perspective

Martine M. Espeseth *, Camilla Brekke and A. Malin Johansson

Department of Physics and Technology, UiT The Arctic University of Norway, 9019 Tromsø, Norway; camilla.brekke@uit.no (C.B.); malin.johansson@uit.no (A.M.J.)

* Correspondence: martine.espeseth@uit.no; Tel.: +47-77645186

Received: 16 June 2017; Accepted: 21 October 2017; Published: 25 October 2017

Abstract: Utilizing several Synthetic Aperture Radar (SAR) missions will provide a data set with higher temporal resolution. It is of great importance to understand the difference between various available sensors and polarization modes and to consider how to homogenize the data sets for a following combined analysis. In this study, a uniform and consistent analysis across different SAR missions is carried out. Three pairs of overlapping hybrid- and full-polarimetric C-band SAR scenes from the Radar Imaging Satellite-1 (RISAT-1) and Radarsat-2 satellites are used. The overlapping Radarsat-2 and RISAT-1 scenes are taken close in time, with a relatively similar incidence angle covering sea ice in the Fram Strait and Northeast Greenland in September 2015. The main objective of this study is to identify the similarities and dissimilarities between a simulated and a real hybrid-polarity (HP) SAR system. The similarities and dissimilarities between the two sensors are evaluated using 13 HP features. The results indicate a similar separability between the sea ice types identified within the real HP system in RISAT-1 and the simulated HP system from Radarsat-2. The HP features that are sensitive to surface scattering and depolarization due to volume scattering showed great potential for separating various sea ice types. A subset of features (the second parameter in the Stokes vector, the ratio between the HP intensity coefficients, and the α_s angle) were affected by the non-circularity property of the transmitted wave in the simulated HP system across all the scene pairs. Overall, the best features, showing high separability between various sea ice types and which are invariant to the non-circularity property of the transmitted wave, are the intensity coefficients from the right-hand circular transmit and the linear horizontal receive channel and the right-hand circular on both the transmit and the receive channel, and the first parameter in the Stokes vector.

Keywords: synthetic aperture radar; multi-sensor; full-polarimetry; hybrid-polarity; sea ice

1. Introduction

Synthetic Aperture Radar (SAR) has been widely used for sea ice observation for many years [1,2]. Due to the large Arctic area to cover, sea ice monitoring has primarily relied on single- and dual-polarization SAR scenes. In the Arctic, the SAR instrument is of special importance due its ability to monitor the Earth's surface independent of sun and weather conditions. The capabilities of full-polarimetric (FP) SAR data has been used to improve the interpretability of sea ice classes and to extract information needed to make reliable and more accurate sea ice charts compared to single-polarization SAR data (see [3,4]). These ice charts may be used for example in the shipping, fishing, and oil industries. One drawback of the FP mode is the small spatial coverage compared to some single-polarization SAR modes. To enable both high spatial coverage and increased amount of polarimetric information, the compact polarimetry (CP) SAR mode was introduced [5]. The CP mode is in the coherent dual-polarization (DP) SAR group, where the choice of the polarization channels deviates from the conventional DP SAR. In [5], Raney suggested the hybrid-polarity (HP) mode;

transmitting a right-hand circular (R) polarized signal while receiving in two orthogonal coherent linear vertical (V) and horizontal (H) polarized channels. The HP mode has the advantages of simpler instruments and of improving the quality of the radar measurements in terms of minimizing sensitivity to crosstalk, simpler calibration of the radar signals, and decreased on-board resource requirements [5]. The HP mode is already integrated in recent/current satellite missions such as the Radar Imaging Satellite-1 (RISAT-1) and the Advanced Land Observing Satellite-2 (ALOS-2), and this configuration will also be present in the next Radarsat Constellation Mission [6].

Utilizing similarities between various polarization modes and sensors will enable a multi-sensor analysis resulting in enhanced information content in terms of coverage and sea ice observations. A larger area can be covered using two sensors compared to one. If the two sensors are operating in different polarization modes, for example FP and HP, an extended ice chart can be made using non-overlapping parts from each of the sensors' acquisitions if their relationship is known. In addition, a change detection procedure between two scenes with two different polarization modes can only be performed if the relationship between them is known. The aim of for this study is to identify this relationship between the Radarsat-2 (RS-2) FP and the RISAT-1 (RI-1) HP mode based on similarity and dissimilarity between the two polarization modes.

In this study we analyze the differences in polarimetric information content in three pairs of overlapping HP and FP SAR scenes from the RI-1 and RS-2 satellites, respectively. To enable a direct comparison between the RS-2 and RI-1 scenes, we simulate HP data from the RS-2 data. The scene pairs were acquired in relation to a sea ice field work campaign in the Fram Strait between August to September 2015. The campaign is a part of the Fram Strait Arctic Ocean Outflow Observatory and was hosted by the Norwegian Polar Institute, where, amongst other data, in-situ sea ice measurements were collected. In addition, the pairs have close to equal incidence angle spans, geographic overlap, and quasi-simultaneous time of acquisition.

Some previous studies for sea ice observation using SAR have simulated HP data from RS-2's FP mode (see e.g., [7–10]). The studies in [7–10] all investigated various polarimetric features extracted from a simulated HP system from RS-2. Moreover, Dabboor and Geldsetzer et al. [7,9] investigated the separability amongst various sea ice classes using a set of HP features, and both studies concluded with promising results on sea ice separability using compact polarimetry. The studies in [7–10] are all based on simulated HP data from RS-2, while in this study we compare both a real and a simulated HP system. However, one recent study (see [11]) used one of the RI-1 scenes in a neural network for sea ice classification. Singha et al. [11] investigated the relative performance of a set of HP features for distinguishing the sea ice classes that they labelled based on ice charts produced by the Danish meteorological institute. In addition, Singha et al. [11] classified the sea ice in one of the overlapping RS-2 and RI-1 pairs, and found approximately the same classification results for both sensors. Another way of using hybrid-polarity SAR data is through reconstruction of a pseudo quad-polarimetric covariance matrix [12]. Espeseth et al. [13] investigated various reconstruction methods for overlapping L- and C-band SAR covering Arctic sea ice, and discovered higher reconstruction accuracy for L-band compared to C-band. However, in this study we choose to evaluate the hybrid-polarity SAR data directly to avoid the scattering symmetry assumptions introduced in a reconstruction approach. Rao et al. [14] also investigated the differences between the two sensors (RI-1 and RS-2), but for sand, water, urban, and crop surfaces. Rao et al. [14] discovered that the RI-1 differed from RS-2 when comparing the backscattered intensity values for the various surfaces. Especially, a large difference (approximately 7–8 dB) was found for water and sand surfaces. They concluded that these differences were due to better calibration for RS-2 compared to RI-1, the non-circularity property of the transmitted wave, and high values of the noise-equivalent-sigma-zero (NESZ) of RI-1.

The main objective of this study is to identify the similarities and dissimilarities between a simulated and a real HP system. In addition, we investigate how the separability between sea ice classes are affected by the non-circularity of the transmitted wave. The objectives are addressed by using three overlapping RI-1 and RS-2 scene pairs with the focus to directly compare the two sensors and their corresponding modes (HP and FP). This is achieved by first homogenizing the dataset in terms of projecting the scenes onto a common grid with equal resolution, and further evaluating the data set in three ways; (1) through a noise analysis, where the backscattered intensities from the regions of interest in the SAR scenes are compared to the NESZ for each of the two sensors; (2) investigations of various multipolarization features extracted from selected sea ice regions; (3) comparison of the correlation between the two sensors to understand the relationship between a simulated and a real HP system.

This article is organized as follows. Section 2 presents the study area and the SAR scenes used, Section 3 briefly discusses polarimetric SAR theory, and Section 4 contains the results and discussions. Section 5 concludes this study.

2. Study Area and Data

2.1. Study Area

The two study areas are located in the Fram Strait; the first at approximate position 78°47.5′N and 6°31.5′W, and the second near the lle-de-France area (Northeast coast of Greenland) at position 78°8.9′N and 16°33.5′W. A large overview of the locations of the scenes and the positions of the research vessel (R/V) Lance can be seen in the top map in Figure 1.

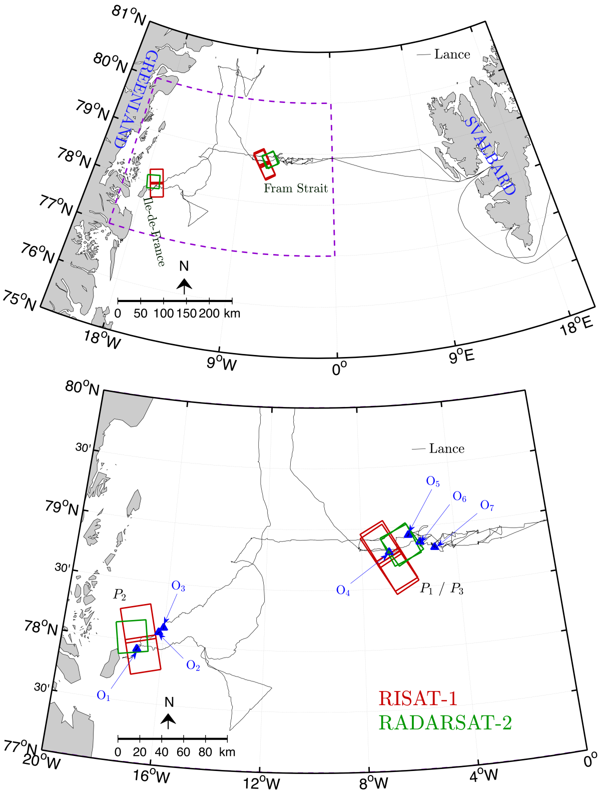

Figure 1. The top map shows the location of the scenes, R/V Lance's track positions (black lines), and the dashed purple square outlines the zoomed-in map on the bottom. The zoomed-in map shows marked areas on R/V Lance's track positions where relevant in-situ sea ice observations for this study were obtained.

The zoomed-in version (the bottom map) is the dashed purple square in the larger map. The zoomed-in version contains seven marked positions (indicated by an *O* symbol) and these positions correspond to the relevant in-situ sea ice observations from ice stations for the SAR scenes used in this study. Note that several other in-situ observations were made, but we only highlight the ones relevant for this study. In Section 2.5, information from these positions is discussed and linked to the regions that are investigated in the SAR scenes.

2.2. Sensor Properties and the SAR Scenes

Sensor properties of the SAR modes investigated for RI-1 and RS-2 are presented in Table 1. RI-1 has higher NESZ than RS-2, which could, in general, be a disadvantage for identifying sea ice types with low backscattering, e.g., grease ice. RI-1, however, has spatially finer resolution than RS-2, which might be an advantage in identifying more detailed sea ice structure like narrow ridges and rafting patterns [15].

Table 1. Properties of the overlapping RISAT-1 (RI-1) [16] and Radarsat-2 (RS-2) scenes [17]. Both sensors transmit waves with frequency in the C-band region.

Pair	Satellite	Date	Time (UTC)	Polarization Mode (Beam)	Incidence Angle (Deg)	NESZ (dB)	Resolution (rg [a] × az [b]) (m)	Scene Size (km)	Time Diff. (min)	Overlap (km ^{2})	Distance (km) to Lance
P_1	RI-1	6 Sept.	16:38	HP (FRS-1)	26.0 to 28.4	−17	2 × 3	30 × 25	13	313	26
	RS-2	6 Sept.	16:55	FP (FQ-13)	32.5 to 34.0	−33.5 to −35.7	5.2 × 7.6	25 × 25			17
P_2	RI-1	6 Sept.	18:13	HP (FRS-1)	45.8 to 47.5	−17	2 × 3	30 × 25	22	582	287
	RS-2	6 Sept.	18:35	FP (FQ-29)	46.8 to 48.0	−31.4 to −32.6	5.2 × 7.6	25 × 25			291
P_3	RI-1	7 Sept.	16:30	HP (FRS-1)	22.5 to 24.8	−17	2 × 3	30 × 25	4	232	52
	RS-2	7 Sept.	16:26	FP (FQ-5)	23.4 to 25.3	−34.5 to −37.2	5.2 × 7.6	25 × 25			32

[a] rg: slant range, [b] az: azimuth.

From Table 1, the images in scene pair #1 (P_1) are taken 13 min apart with low to intermediate incidence angles, while the scenes in pair #2 (P_2) have higher incidence angles and were taken 22 min apart. The scenes in the third pair (P_3) have low incidence angles and only 4 min between the acquisitions. The second last column of Table 1 gives the size of the overlapping area, while the last column contains the shortest distance between each of the scenes's bounding box and R/V Lance's position at acquisition time. In each pair, to obtain higher overlap to RS-2, there are two consecutive RI-1 scenes aligned in the azimuth direction (as seen in Figure 1). The two RI-1 scenes in each pair are merged to form one scene prior to the polarimetric analysis.

Figures 2–4 show the RS-2 and RI-1 scenes. The left-most image in Figures 2–4 is a red-green-blue (RGB) composite image (scaled for visual purposes), where the green band is the VV-intensity for RS-2, the red band is the RV-intensity from RI-1, and the blue band consist of only zero values. The overlapping area between the two sensors will then appear as yellow. The center image in Figures 2–4 is the RV-intensity from RI-1, while the right-most image is the VV-intensity from RS-2. The colorbar next to these intensity images are in decibel (dB). Note, the images in center and to the right show only the overlapping area (colored in yellow) in the RGB image.

2.3. SAR Pre-Processing

All the scenes are multi-looked and geo-coded such that each pixel covers approximately 8 × 8 m on the ground. The FRS-1 mode of RI-1 has finer resolution (almost doubled in range and azimuth direction compared to RS-2) and thus more pixels per ground cell compared to RS-2 (see Table 1). In order to get the same pixel spacing, more averaging is performed on the RI-1 products. The single look complex (SLC) products from both the RS-2 and RI-1 are converted to multi look complex (MLC) images and then projected on a spatial common grid with equal number of pixels on the ground. In addition, a co-registration (linear shift of the pixels in RS-2) is performed on the geo-coded products to adjust for the minor sea ice drift between the two scenes. Next, a 9 × 9 sliding window is applied on the geo-coded MLC RS-2 and RI-1 products. The latter procedure is mainly done in order to further reduce the speckle within the SAR scenes and to enhance interpretability [18]. The FRS-1 HP mode of

RI-1 represents a system where the right-hand circular is on transmit and linear horizontal and vertical polarizations are on receive.

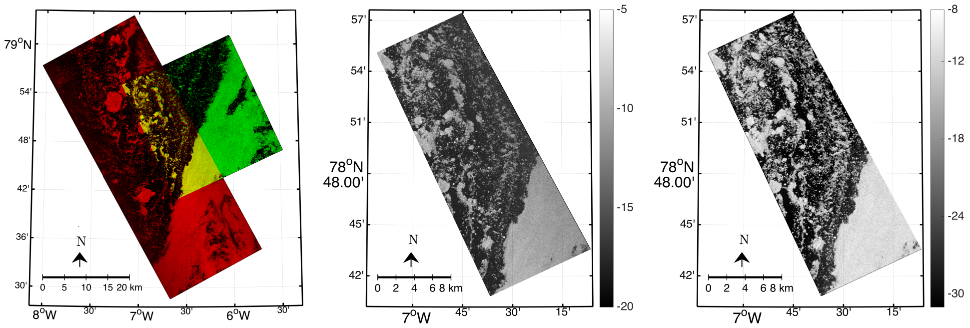

Figure 2. The left red-green-blue (RGB) composite image (scaled) of scene pair P_1, where the green band is the intensity of the linear vertical transmit and linear vertical receive channel (VV) from Radarsat-2 (RS-2) scene and red is the intensity of the right-hand circular transmit and vertical receive channel (RV) from RISAT-1 (RI-1) scene. Yellow indicates areas of overlap. The center (right) image is the RV (VV)-intensity of the overlapping area from RI-1 (RS-2). RS-2 Data and Products ©MDA LTD (2015)—All rights reserved. RI-1 ©2015-Antrix–All rights reserved.

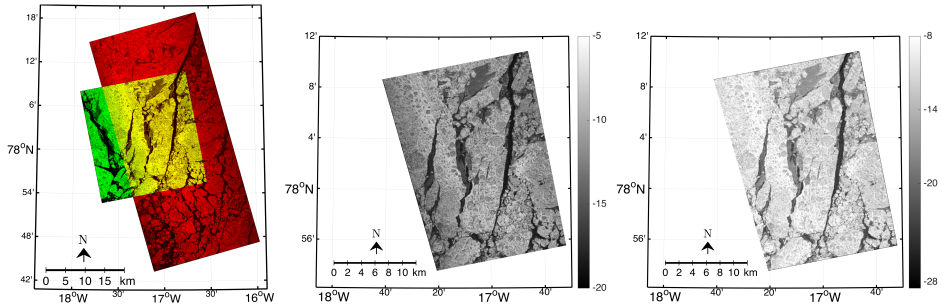

Figure 3. The left RGB image (scaled) of scene pair P_2, where the green band is the VV-intensity from RS-2 scene and red is the RV-intensity from RI-1 scene. Yellow indicates areas of overlap. The center (right) image is the RV (VV)-intensity of the overlapping area from RI-1 (RS-2). RS-2 Data and Products ©MDA LTD (2015)—All rights reserved. RI-1 ©2015-Antrix—All rights reserved.

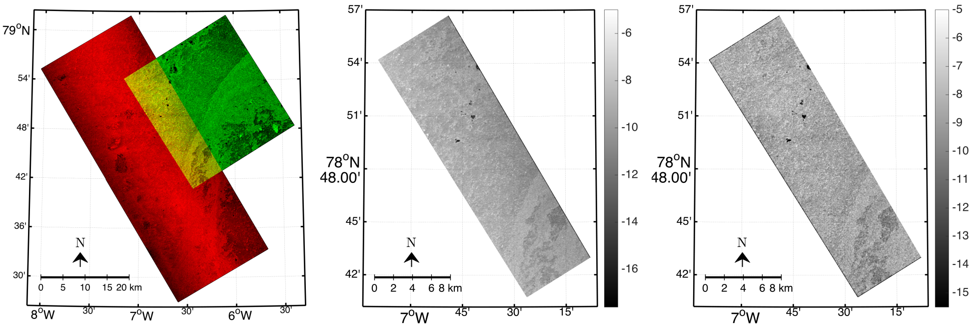

Figure 4. The left RGB image (scaled) of scene pair P_3, where the green band is the VV-intensity from RS-2 scene and red is the RV-intensity from RI-1 scene. Yellow indicates areas of overlap. The center (right) image is the RV (VV)-intensity of the overlapping area from RI-1 (RS-2). RS-2 Data and Products ©MDA LTD (2015)—All rights reserved. RI-1 ©2015-Antrix—All rights reserved.

2.4. Selection of ROIs and Profiles

We assume that no change has occurred in the sea ice properties between the scenes in each pair, justified by the small time difference. The investigated sea ice regions are manually selected using the intensities from both RI-1 and RS-2. The selection is based on finding regions of interest (ROIs) with varying intensity values. In addition, three profiles within each scene pair are selected for evaluation of the correlation between the two sensors. Figure 5 illustrates the ROIs investigated and the profiles, which are spatially equivalent for the RI-1 and RS-2 scenes. Figure 5 shows the ROIs overlaid the RI-1 scenes. Two sets of ROIs are selected for evaluation in P_1, four sets in P_2, and three sets in P_3; in total nine ROIs.

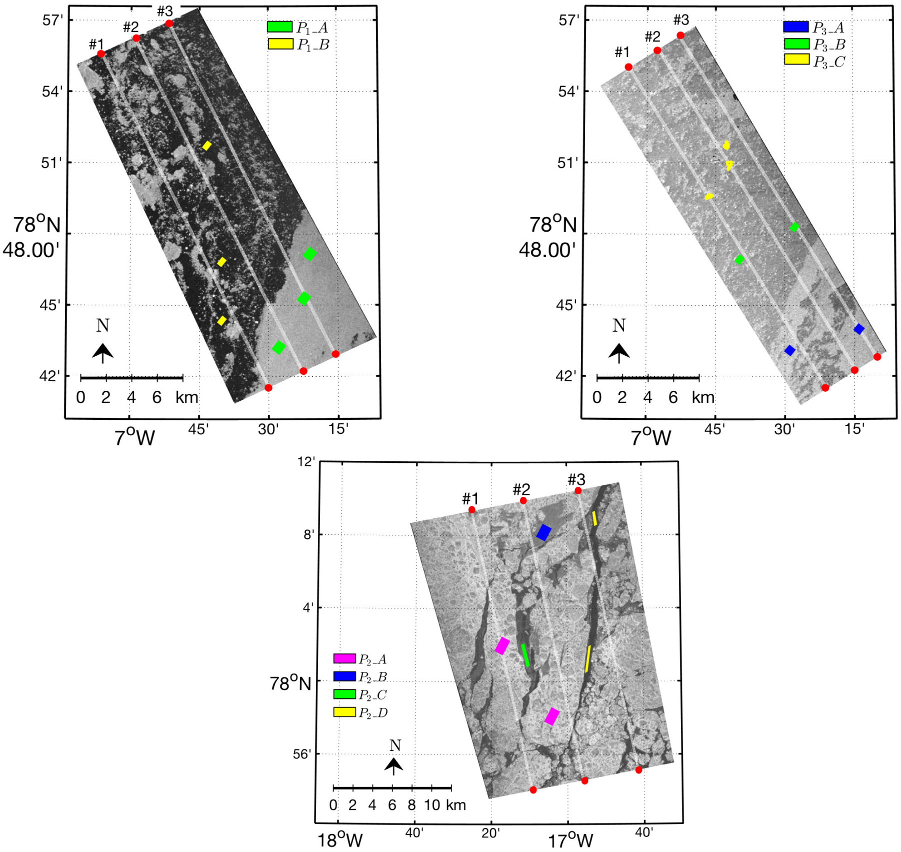

Figure 5. Illustrations of the regions of interest (ROIs) investigated. The ROIs are overlaid on top of RI-1 scenes for P_1 (**top left**), P_2 (**bottom**), and P_3 (**top right**). The profiles are indicated by light gray colored line between two red markers. The profiles are 50 pixels wide and passes through the azimuth direction.

2.5. In-Situ Information

The in-situ sea ice observations from dedicated ice stations near R/V Lance and some weather observations from the sea ice campaign are given in Table 2. This table is divided into two sections; one from the Ile-de-France area relevant for P_2; the second section from Fram Strait which is relevant for both P_1 and P_3. The scenes in P_2 are acquired close to the Ile-de-France area. Corresponding observations from R/V Lance were made 5 days prior to the P_2 acquisitions. Little change has occurred during these 5 days, which is confirmed by investigating two Sentinel-1 extra wide swath scenes, one from the day of the in-situ observations and one from the day of the two SAR acquisitions in P_2. The ice station observations from the Ile-de-France area are indicated by O_1, O_2, and O_3.

The observations showed varying sea ice types such as newly formed ice, nilas, leads, and thicker ice with snow cover. By investigating the SAR scenes and the observations, the selected ROIs are labelled as given in the right panel of Table 2.

Observations from R/V Lance in the area and close to the time of the acquisitions of P_1 and P_3 are given in the second section of Table 2 as O_4, O_5, O_6, and O_7. These observations showed scattered floes with thin ice (including frazil ice, grease ice, and nilas) up to 4 cm thick, and ice between 116–210 cm thick. In addition, the thin ice was often wet or covered with a very thin snow layer (<1 cm). Based on these observations and thickness measured the dark region named P_1_B is labelled as grease ice, while the brighter region P_1_A is labelled as first-year ice (FYI). The scenes in P_3 are acquired 24 h after P_1 at the same geographical position in the Fram Strait. The same observations from the P_1 area are also used when labelling the ROIs in P_3.

Some changes have occurred between P_1 and P_3 as can be seen in the intensity images in Figures 2 and 4. The temperature measured at the acquisition times (in vicinity of the two scenes in P_1, see last column in Table 1) of the scenes in P_1 was around 0 °C, while the temperature at acquisition times of the scenes in P_3 was around −2.5 °C. This gives a temperature drop of 2.5 °C. In addition, a small drop in relative humidity prior the acquisition of the scenes in P_3 was also measured between the two scenes. The effects from the temperature drop and reduction in relative humidity might have caused rime on the sea ice surface [19]. A new fresh snow layer between P_1 and P_3 was also seen during the on-board observations from ice stations near R/V Lance as indicated in the last row in Table 2 for O_7. These environmental factors might be the reasons for the different backscattering in the area covered by P_3 when compared to the same area the day before in P_1. Therefore, the ROIs P_3_A and P_3_B will most likely correspond to the same sea ice type defined for P_1_A and P_1_B, but with a new fresh snow layer. P_3_C is most likely melt ponds as these were also observed in the area. Note that the ice edge starting from the lower left corner across the intensity of the scenes in P_1 and P_3 is comparable.

Table 2. Overview of the in-situ observations (indicated by an *O* symbol) from sea ice stations near R/V Lance from the locations given in Figure 1. The right table shows the labelling of the ice types for the regions of interest (ROIs) investigated.

Area	ID	Date (Time) (UTC)	Observations	ROIs (Sea Ice Types)
Ile-de-France (P_2)	O_1	30.08 (22:19)	Newly formed ice and nilas (0.5–5 cm) with snow cover	P_2_A (FYI) P_2_B (Flooded FYI) P_2_C (Nilas/newly formed ice with snow cover) P_2_D (Leads)
	O_2	31.08 (11:48)	Newly formed ice and nilas (0.5–4 cm) with snow cover	
	O_3	31.08 (12:42)	Leads (2–3 cm), 110–235 cm thick ice and 5–8 cm snow cover	
Fram Strait (P_1 and P_3)	O_4	05.09 (11:20)	Scattered floes with 1–2 cm snow cover, melt ponds, and 137–210 cm thick ice	P_1_A (FYI) P_1_B (Grease/frazil ice)
	O_5	06.09 (07:25)	Newly formed frazil/ grease ice (3–4 cm)	P_3_A (FYI with fresh snow layer) P_3_B (Grease/frazil ice with fresh snow layer) P_3_C (Melt ponds)
	O_6	06.09 (12:56)	High melt pond coverage, 2 cm snow, and 104–187 cm thick ice	
	O_7	07.09 (07:42)	Snowfall, 3–4 cm fresh snow layer, and 116–130 cm thick ice	

3. Polarimetric Theory

The fundamental quantities measured by polarimetric SAR instruments are defined by the complex backscattering terms S_{ij}. Here, i and j are the polarizations of the transmit and receive channels in the radar system. The HP mode transmits only one circular polarization, either left (L) or right (R), and receives two orthogonal linear polarizations, namely horizontal and vertical [5]. The HP mode in RI-1 uses right circular transmit and linear horizontal and vertical receive. As pointed out by Touzi et al. [20], it is not possible to generate perfect circular polarization using current technology due to the phase errors in combining the horizontal and vertical with 90° phase difference when transmitting circular waves. Therefore, the transmitted waves in the HP mode of RI-1 will be more elliptical rather than circular, hence the non-circularity property of RI-1 [14]. The ellipticity angle (χ) of the transmitted wave can be obtained from the axial ratio (AR), which defines the ratio between the major and minor axis from the electric field vector. The AR has been used in, e.g., [14,20] when discussing the non-circularity in general for a HP system. It is well known that an AR of 0 dB indicates perfect circular, while values above 0 dB corresponds to elliptical, and values of infinity is linear polarization [20].

According to the RI-1 design description the AR was given as 1.1 dB for RI-1, which gives ellipticity angle of 37.8° (see [14] and references therein). However, Rao et al. [14] estimated the AR (from corner reflectors) and further calculated the ellipticity angle to be of 43°. Note that a perfect circular wave has an ellipticity angle of ±45°. However, this value was estimated by considering a small range of incidence angles. As highlighted in [20], the non-circularity of the transmitted wave increases with incidence angle [21]. In this study, the simulated complex HP scattering vector is synthesized by considering an AR of 0 dB, which is defined as:

$$\bar{k}_{(RH,RV)} = [S_{RH}, S_{RV}]^T, \tag{1}$$

where T denotes the transpose operator. In addition, we also investigate a scattering vector having an ellipticity angle of $-38°$ (AR = 1.1 dB). By exploring this, we will be able to investigate the effect of the non-circularity of the transmitted wave in relation to sea ice separability. Note, both the simulated complex HP scattering vectors are generated from the FP RS-2 data. To the author's knowledge, the majority of the published studies investigating the capabilities of the HP mode does not have real HP data, and therefore need to simulate the HP data from the FP data, according to this relation (for AR = 0 dB):

$$\bar{k}_{(RH,RV)} = \frac{1}{\sqrt{2}}[S_{HH} - iS_{HV}, -iS_{VV} + S_{HV}]^T, \tag{2}$$

where reciprocity is assumed ($S_{HV} = S_{VH}$). The simulation of the HP with $\chi = -38°$ becomes [22]:

$$\bar{k}_{(RH,RV)} = [\cos(\chi)S_{HH} + i\sin(\chi)S_{HV}, i\sin(\chi)S_{VV} + \cos(\chi)S_{HV}]^T. \tag{3}$$

Here, it is assumed that the orientation angle of the elliptical wave is 0.

To enable a direct comparison between the RS-2 and RI-1 scenes, we simulate HP data from RS-2 data according to Equations (2) and (3). The simulated Stokes vector from the FP RS-2 data is calculated according to the method suggested in [5]. The reader is referred to [5] for additional theory of the HP mode.

As previously mentioned in [23], RI-1 circular right better matches simulated circular left from RS-2 on transmit. Our investigations corroborate these findings; by inspecting the fourth element of the Stokes vector we see clear indications of a sign reversal being necessary to obtain a basis equal to that of simulated HP RS-2. To the author's knowledge, there is no prior explanation to this left/right sign reversal but possible explanations are (1) different sign conventions as indicated in [23], and (2) the definition of the direction of the propagated wave is reversed when comparing the circular transmitted wave for RI-1 and the simulated circular transmitted wave from RS-2. To compensate for this sign reversal, we multiply the fourth element of the Stokes vector with minus one for RI-1. This sign reversal is also taken into consideration when changing both the transmitted and received basis to RR and RL for RI-1.

There exists several multipolarization features that can be extracted from the SAR data. Table 3 shows the features that are investigated. This table is split into two, where Table 3a describes the features analytically and Table 3b groups the features according to the groups defined in [9]. In this study the Stokes vector (see [5]) and the corresponding child parameters given in Table 3a are used. In addition, we also selected the four backscatter intensities, which are also located in Table 3a. The features in Table 3 are calculated from the RI-1 scenes, and from the simulated HP data for the

RS-2 scenes using both ellipticity angles of $\chi = -45°$ (perfect right-hand circular) and $\chi = -38°$ (right-hand elliptical). Some of these features are used previously in a study based on simulated HP data from RS-2 [6] and real HP data from RI-1 [11]. The selection of the features in our study is based on having a mix of both ratio-based and non ratio-based features, and testing features that are also from the five groups defined in [9]. In this study we follow the grouping of features suggested in [9], where a set of HP features were categorized into four groups based on their correlation to one another and one independent group. The groups defined in Geldsetzer et al. [9] corresponded to different scattering mechanisms. Table 3b shows the HP features sorted according to the grouping defined in Geldsetzer et al. [9], and the last column shows the information about the dominant scattering type that each group is sensitive to. For the σ_{RR} and σ_{RL} the basis of the receiver is changed to right- and left- hand circular. When calculating the σ_{RR} and σ_{RL} for the simulated HP data from RS-2 with an ellipticity angle of $-38°$, the transmitted wave is $-38°$ (right-hand elliptical), while the received basis is $\pm 45°$ (perfect left- and right-hand circular).

The features in Group 1 respond to surface scattering, and the features that are in this group are q_0, q_3, σ_{RH}, σ_{RV}, and σ_{RL}. The σ_{RR} feature is categorized into Group 2 where depolarization due to volume scattering dominates. Further, $1-m$, $\rho_{(RH,RV)}$, and $\gamma_{(RR,RL)}$ respond to depolarization likely due to multiscattering from rough surfaces, which is Group 3, while $\gamma_{(RH,RV)}$ is in Group 4 where it responds to polarization differences in resonant Bragg scattering and also in the Fresnel coefficients (see [24,25] for more information). Finally, the independent group, where the features are likely to give additional information that may be complementary to the other features [9]. The α_s is categorized into the independent group, and this feature is a function of the q_1, q_2, and q_3 from the Stokes vector. The α_s is an approximation to the α (from the H/α-decomposition), and it describes the dominant scattering mechanism [22]. In addition, the α_s is closely related to the ellipticity angle [26]. These groups are used in the discussion part in Section 4 when exploring the features ability to separate various sea ice types as well the correlation between RI-1 and RS-2.

In order to evaluate the separability between the sea ice types, the two sample Kolmogorov-Smirnov (K-S) test is used [27]. The K-S test, from here and out named the K-S distance, is based on the maximum difference between two cumulative distributions. The K-S distance gives values between 0 and 1, where a K-S distance close to 0 indicates that the two cumulative distributions are equal, while a value close to 1 indicates unequal cumulative distributions. Good separability between two given samples is achieved if K-S is above 0.9 [9]. In this study, the K-S distance is calculated for each of the investigated features between the sea ice types within each scene. Hence, we can identify which features manage to separate pairs of different sea ice types for each sensor in all the scene pairs.

To enable investigation of the correlation between the two sensors, the Spearman's rank correlation coefficient (r_s) is used (see [28] for additional information on Spearman's correlation). The Spearman's correlation coefficient is calculated between two profiles (from RI-1 and RS-2) that passes through the azimuth direction, this is done to avoid any incidence angle effects. The Spearman's correlation assesses monotonic relationship (linear or not) and is also less sensitive to strong outliers than the commonly used Pearson correlation. The Spearman's correlation gives values between -1 and 1, where values of ± 1 imply full correlation, and no correlation for values corresponding to 0. In [29], the author classified the intervals of the correlation values obtained from Pearson correlation. Five classes were found, from "very weak" to "very strong". The same framework is utilized here when analysing the correlation values obtained from the Spearman's correlation coefficient.

Table 3. (a); an overview of the investigated hybrid-polarity (HP) features [5,9,26,30,31]. (b); the HP features sorted into groups. The features within a group have common scattering types that they are predominately sensitive to (see [9]).

(a)

HP Features	
Name	Formula
Stokes vector	$\boldsymbol{q} = \begin{bmatrix} q_0 \\ q_1 \\ q_2 \\ q_3 \end{bmatrix} = \begin{bmatrix} \langle \lvert S_{RH}\rvert^2 + \lvert S_{RV}\rvert^2 \rangle \\ \langle \lvert S_{RH}\rvert^2 - \lvert S_{RV}\rvert^2 \rangle \\ 2\Re\langle (S_{RH}S_{RV}^{\star})\rangle \\ -2\Im\langle (S_{RH}S_{RV}^{\star})\rangle \end{bmatrix}$
Degree of polarization	$\mathrm{m} = \frac{\sqrt{q_1^2+q_2^2+q_3^2}}{q_0}$
α angle	$\alpha_s = \frac{1}{2}\tan^{-1}\left(\frac{\sqrt{q_1^2+q_2^2}}{q_3}\right)$
Correlation coefficient	$\rho_{(RH,RV)} = \frac{\lvert\langle S_{RH}S_{RV}^{\star}\rangle\rvert}{\sqrt{\langle \lvert S_{RH}\rvert^2\rangle\langle \lvert S_{RV}\rvert^2\rangle}}$
Backscattered intensity coefficients	$\sigma_{RH}, \sigma_{RV}, \sigma_{RR}, \sigma_{RL}$
Ratio between RH and RV and circular ratio	$\gamma_{(RH,RV)} = \frac{\sigma_{RH}}{\sigma_{RV}}, \gamma_{(RR,RL)} = \frac{\sigma_{RR}}{\sigma_{RL}}$

(b)

Group Number	**HP Features**	**Dominant Scattering Type**
Group 1	σ_{RH} σ_{RV} σ_{RL} q_0 q_3	Surface scattering
Group 2	σ_{RR}	Depolarzation due to volume scattering
Group 3	$1-m$ $\gamma_{(RR,RL)}$ $\rho_{(RH,RV)}$	Depolarization due to multiscattering from rough surfaces
Group 4	$\gamma_{(RH,RV)}$	Polarization differences in resonant Bragg scattering and also in the Fresnel coefficients.
Independent group	q_1 q_2 α_s	Might be complementary to other parameters

4. Results and Discussion

This section presents the noise analysis where the backscattered intensities from the regions of interest in the SAR scenes are compared to the NESZ for each of the two sensors. Further, the separability between the various sea ice types are investigated through the K-S distance, and the correlation between selected profiles through the scene pairs are presented.

4.1. Noise Analysis

The returns from thin sea ice are low compared to other sea ice types (for example, ridges and multi-year ice), and the signal may be close to the noise floor, which introduce challenges when trying to separate different classes of thin sea ice [32]. The noise floor provided with the FRS-1 mode of RI-1 is given in [16] by a constant value of -17 dB. The noise floor of the fine quad-polarimetric SAR mode in RS-2 varies depending on the beam and incidence angle and is in the range -31.4 to -37.2 dB for the RS-2 scenes investigated in this study [17].

Figure 6 shows a signal-to-noise analysis of the ROIs representing various sea ice types we investigate. The 5th, 50th, and 95th percentiles of the HH, VV, and HV backscattering coefficients are calculated for each sea ice type in RS-2, and for the RH and RV backscattering coefficients for each sea ice type in RI-1. A star indicates the 50th percentile, and the horizontal continuous lines represent the 5th (bottom line) and 95th (top line) percentile for the backscattering coefficients. There are varying incidence angles in the three RS-2 scenes, which give various NESZ values for each of the sea ice types we investigate. Hence, the mean NESZ for each RS-2 scene is given in Figure 6. Across the copolarization backscattering coefficients of RS-2, only P_1_B has some values below the noise floor of RS-2. The sea ice types denoted by P_1_B, P_2_B, P_2_C, P_2_D, P_3_B, and P_3_C are either below or close to the noise floor in the HV backscattering coefficient in the RS-2 scenes.

Several of the sea ice types in the RI-1 scenes have pixels below or close to the noise floor, namely P_1_B, P_2_B, P_2_C, P_2_D, and P_3_C (see Table 2). Previous studies have indicated calibration issues related to the RI-1 sensor, and this might affect how the percentiles in Figure 6 are positioned above the NESZ. We will in Section 4.2 see better separability between some of the sea ice types for the RI-1 compared to RS-2. For example, the results in Section 4.2 show that features from RI-1 managed to separate P_2_B, P_2_C, and P_2_D, which are sea ice types that have backscattering values very close to the NESZ. Based on Figure 6, the signal-to-noise ratio is better for the RS-2 than for the RI-1.

4.2. Separability between the Sea Ice Types

The polarimetric feature values are calculated for each sea ice type for all the scene pairs, and an equal number of samples within two given ROIs representing two sea ice types are used as input to calculate the K-S distance. The results are presented in Figures 7–9. In these figures, the K-S distance values are given in a table, where values equal or above 0.9 are presented in bold, indicating good separability between two given sea ice types. The log-transformed version of the features are chosen when this increase the separability; these cases are indicated by "dB" after the feature name. The tables are separated into five sections, where each section corresponds to one of the five groups (see Table 3). These groups are used to link the separability between the various sea ice types obtained for a given feature to the scattering type dominating this group. For all figures, the values from the table are illustrated in a plot where the y-axis represents the K-S value (red dashed line for RI-1, green and blue line for simulated HP data from RS-2 with ellipticity angles of $\chi = -45°$ and $\chi = -38°$), and the x-axis is the polarimetric feature. Note, both ellipticity angles of $\chi = -45°$ and $\chi = -38°$ are present in the plots to show the effect of not having perfectly circular transmitted waves, while the table contains only the simulated HP with perfect circular on transmit. In the following, only the HP features from RI-1 and the simulated HP from RS-2 with perfect circular on transmits are discussed. The non-circularity property is discussed separately in Section 4.3 by considering the simulated HP systems with an ellipticity angle of $\chi = -38°$.

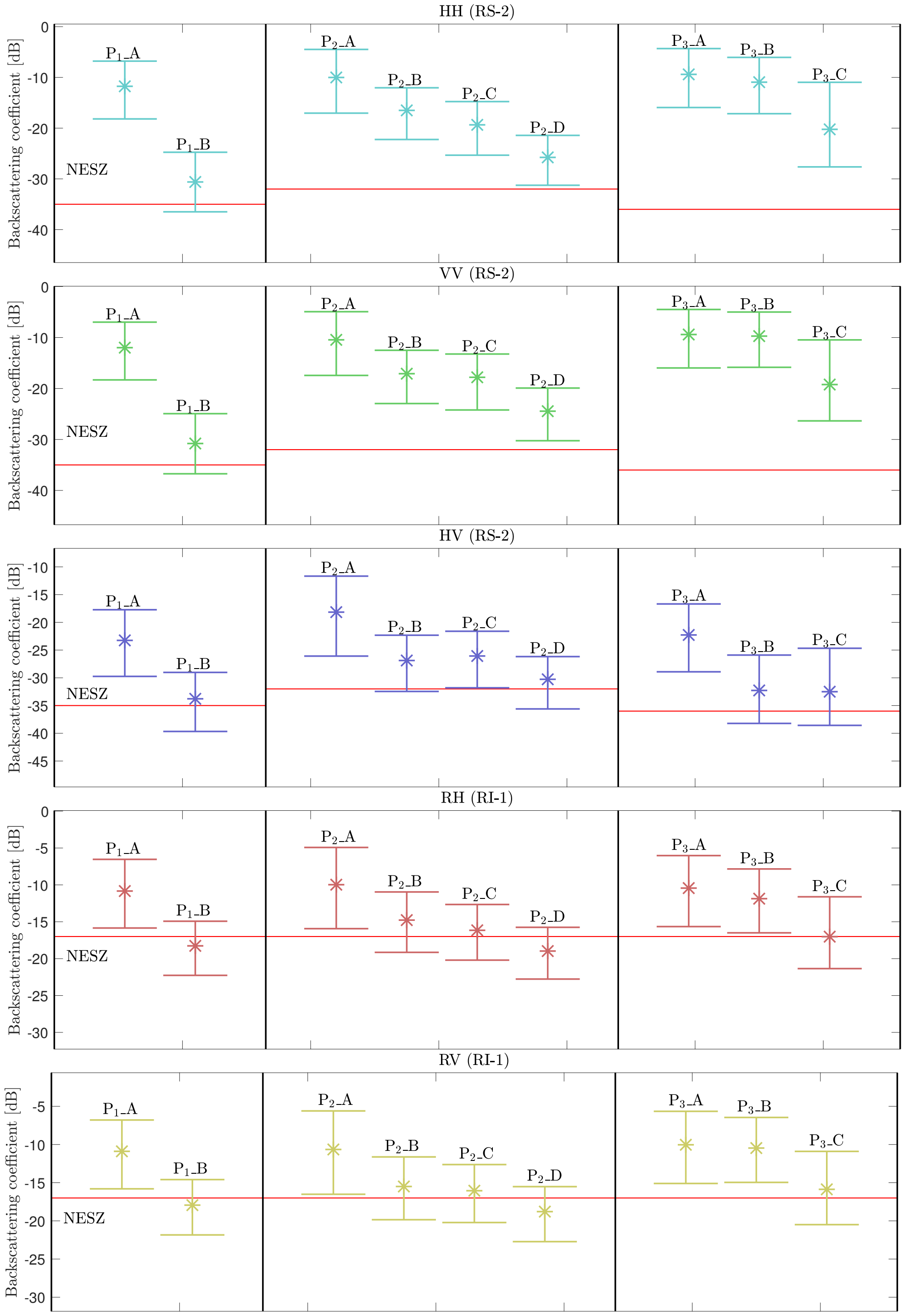

Figure 6. Signal-to-noise analysis of the backscattering intensity coefficients of the HH, VV, and HV for RS-2, and RH and RV for RI-1 for the investigated sea ice types. The 50th percentile is indicated by a star. The top and bottom horizontal continuous lines represent the 95th percentile and 5th percentile for the intensities, respectively. The red line represents NESZ. The y-axis represents the backscattering intensity coefficient, while the different sea ice types (i.e., ROIs) are aligned along the x-axis sorted by scene pair number.

4.2.1. Pair #1

The table in Figure 7 contains K-S values between the two sea ice types in P_1 (FYI and grease/frazil ice). Several of the features extracted from the RI-1 and the overlapping RS-2 scenes show high separability between P_1_A and P_1_B. $\gamma_{(RH,RV)}$, q_1, and α_s are the features with the lowest K-S values for the RI-1 scene, and $\gamma_{(RH,RV)}$, q_1, q_2, and α_s are the features with the lowest K-S values for RS-2. For the features in Groups 1 and 2, the separability of the sea ice types is almost identical for RI-1 and RS-2, whereas the features in Group 3 show higher separability between the two sea ice types using the RI-1 data. The feature in Group 4 show poorer separation (lower K-S distance) between the two sea ice types.

Group name	HP features	P_1_A vs. P_1_B	
		RI-1	RS-2
Group 1	σ_{RH}(dB)	**0.98**	**0.99**
	σ_{RV}(dB)	**0.99**	**0.99**
	σ_{RL}(dB)	**0.99**	**0.99**
	q_0(dB)	**0.98**	**0.99**
	q_3(dB)	**0.99**	**0.99**
Group 2	σ_{RR}(dB)	**0.98**	**0.98**
Group 3	$1-m$	**0.99**	**0.90**
	$\gamma_{(RR,RL)}$	**0.99**	**0.91**
	$\rho_{(RH,RV)}$	**0.99**	**0.90**
Group 4	$\gamma_{(RH,RV)}$	0.38	0.06
Independent group	q_1(dB)	0.58	0.84
	q_2(dB)	**0.99**	0.86
	α_s(dB)	0.80	0.82

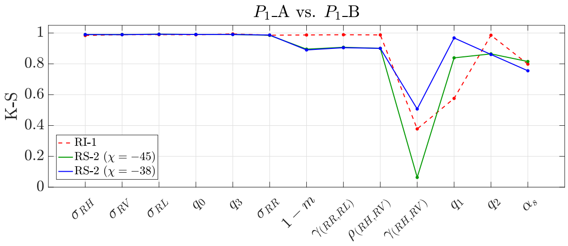

Figure 7. Left panel; a table containing the Kolmogorov-Smirnov (K-S) separability values between the two sea ice types in P_1. The first column shows the groups as described in Table 3. The values greater than 0.9 are in bold. Right panel; the corresponding values are shown in the plot for the two sea ice types, where the y-axis shows the K-S values calculated for the two sea ice types (i.e., ROIs) (red for the RI-1 features and green (blue) for the RS-2 features with an ellipticity angle of $\chi = -45°$ $(-38°)$), while the x-axis shows the corresponding features. Note that only the K-S values for RI-1 features and the RS-2 features using an ellipticity angle of $\chi = -45°$ is shown in the table.

4.2.2. Pair #2

Figure 8 contains K-S values between the four distinct sea ice types in P_2. Here, all the sea ice types are possible to separate according to the threshold set for the K-S (K-S > 0.9). The features yielding K-S values above or close to 0.9 between the four sea ice types using the RI-1 scene are σ_{RH}, σ_{RL}, q_0, and q_3. For the RS-2 scenes, features producing K-S > 0.9 are σ_{RH}, σ_{RL}, and q_3. The features in Groups 1 and 2 give high K-S values for all the pairs of the different sea ice types except between P_2_*B* and P_2_*C*. Recall from Table 2, that P_2_*B* and P_2_*C* are defined as flooded FYI and nilas with snow cover. P_2_C and P_2_D are the sea ice types (nilas and leads) with the lowest backscattering level (see Figure 6), and the features giving maximum separability between the two belong to Groups 1 and 2 for both RI-1 and RS-2. The features in Group 3 show different separability trends for the two sensors, while for the remaining features the separability of the paired sea ice types between RS-2 and RI-1 are very similar. The same observation for Group 3 is true for P_1. This might be related to the varying noise level in the two sensors, since features in Group 3 are sensitive to the depolarization effects. This difference might thus be because of RI-1 having higher noise floor than to RS-2. It is clear from this figure that the features in Group 4 and the independent group (last row in the table) show poor separability between the sea ice types using both RS-2 and RI-1 with minor exceptions.

Group name	HP features	P_2_A vs. P_2_B		P_2_A vs. P_2_C		P_2_A vs. P_2_D		P_2_B vs. P_2_C		P_2_B vs. P_2_D		P_2_C vs. P_2_D	
		RI-1	RS-2	RI-1	RS-2	RI-1	RS-2	RI-1	RS-2	RI-1	RS-2	RI-1	RS-2
Group 1	σ_{RH}(dB)	**0.98**	**0.99**	**1.00**	**1.00**	**1.00**	**1.00**	**0.93**	0.85	**1.00**	**1.00**	**1.00**	**1.00**
	σ_{RV}(dB)	**0.98**	**0.99**	**1.00**	**1.00**	**1.00**	**1.00**	0.61	0.29	**1.00**	**1.00**	**1.00**	**1.00**
	σ_{RL}(dB)	**0.98**	**0.99**	**1.00**	**1.00**	**1.00**	**1.00**	**0.98**	0.89	**1.00**	**1.00**	**1.00**	**1.00**
	q_0(dB)	**0.98**	**0.99**	**1.00**	**1.00**	**1.00**	**1.00**	**0.91**	0.69	**1.00**	**1.00**	**1.00**	**1.00**
	q_3(dB)	**0.95**	**0.94**	**1.00**	**1.00**	**1.00**	**1.00**	**0.99**	**0.97**	**1.00**	**1.00**	0.87	**0.94**
Group 2	σ_{RR}(dB)	**0.97**	**0.99**	**0.99**	**0.99**	**1.00**	**1.00**	0.23	0.64	**1.00**	**1.00**	**0.99**	**0.99**
Group 3	$1-m$	0.44	0.81	0.83	0.10	**0.97**	0.56	**0.97**	0.88	**1.00**	**0.97**	0.74	0.55
	$\gamma_{(RR,RL)}$	0.30	0.80	0.89	0.38	**0.97**	0.67	**0.97**	**0.97**	**1.00**	**0.97**	0.59	0.49
	$\rho_{(RH,RV)}$	0.46	0.81	0.81	0.16	**0.97**	0.67	**0.97**	**0.90**	**1.00**	**0.97**	0.76	0.65
Group 4	$\gamma_{(RH,RV)}$	0.03	0.12	0.59	0.56	0.68	0.66	0.62	0.67	0.71	0.75	0.11	0.13
Independent group	q_1(dB)	0.63	0.64	0.80	0.59	**0.91**	0.86	0.47	0.14	0.75	0.50	0.36	0.60
	q_2(dB)	0.39	0.60	0.58	0.49	0.87	**0.91**	0.52	0.37	**0.97**	0.75	0.86	**0.93**
	α_s(dB)	0.37	0.27	0.70	0.67	0.61	0.63	0.63	0.87	0.57	0.82	0.15	0.13

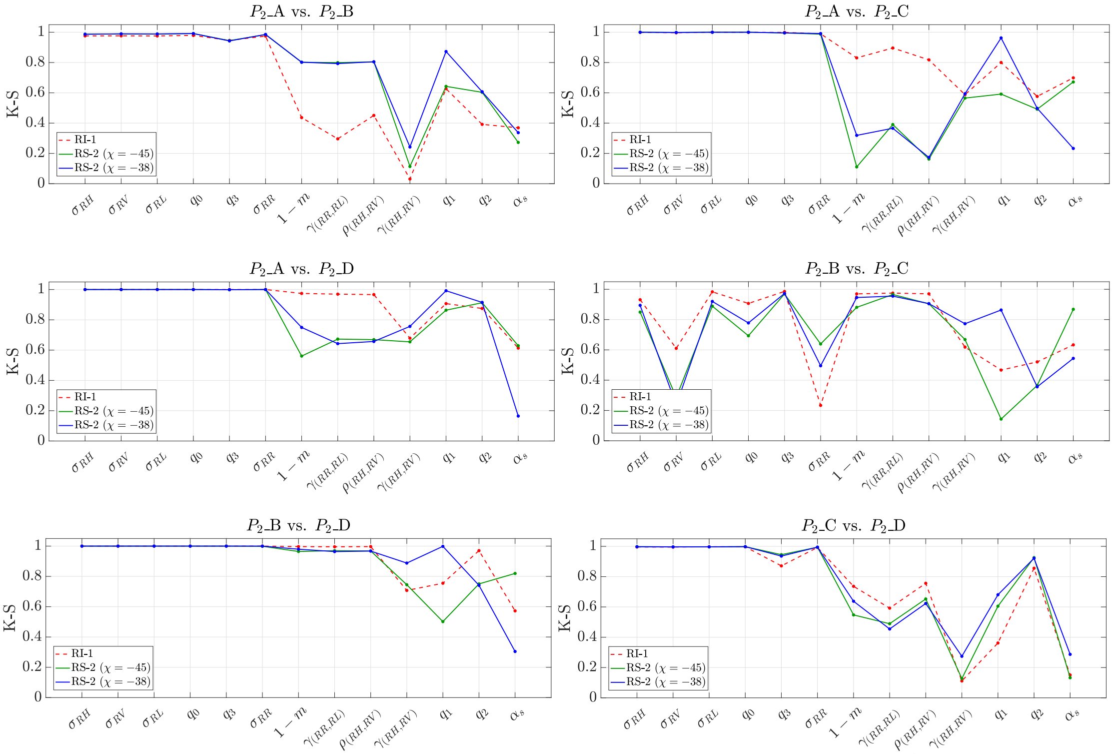

Figure 8. Top panel; a table containing the K-S values between all combinations of paired sea ice types in P_2. The first column shows groups as described in Table 3. The values greater than 0.9 are in bold. Bottom panels; the corresponding values are shown in the plots, where the y-axis shows the K-S values calculated for each of the paired sea ice types (i.e., ROIs) (red for the RI-1 features and green (blue) for the RS-2 features with an ellipticity angle of $\chi = -45°$ $(-38°)$), while the x-axis shows the corresponding features. Note that only the K-S values for RI-1 features and the RS-2 features using an ellipticity angle of $\chi = -45°$ is shown in the table.

4.2.3. Pair #3

The K-S values between the classes evaluated from P_3 are given in Figure 9. The separability values between P_3_A and P_3_C (the brightest and the darkest regions) are highest in Groups 1 and 2, where features responding to strong surface scattering and depolarization due to volume scattering are located. Note that the features in Groups 1 and 2 are all non ratio-based features. None of the RI-1 features give a K-S value above 0.9 when separating P_3_A and P_3_B, whereas all the features in Groups 2, 3, and 4 gives K-S values above 0.9 for the RS-2 scenes. These are the scenes with lowest incidence angle and sea ice with a new fresh snow layer. P_1_A and P_1_B were categorized as FYI and grease ice (see Table 2), while P_3_A and P_3_B were identified as the same ice types, but with a new fresh snow layer. It is interesting that the features in Group 1 (features dominated by surface scattering) show high separability values for the sea ice types in P_1, but the separation values decreases when a snow layer covers the similar sea ice types in P_3 (see Table 2). This corroborates the findings in [33], where the importance of volume and multiple scattering will increase with snow thickness. Therefore, the features in Group 1, where surface scattering dominates, show poor separability between P_3_A and P_3_B (FYI and grease ice with a fresh snow layer).

Group name	HP features	P_3_A vs. P_3_B		P_3_A vs. P_3_C		P_3_B vs. P_3_C	
		RI-1	RS-2	RI-1	RS-2	RI-1	RS-2
Group 1	σ_{RH}(dB)	0.66	0.74	**1.00**	**0.98**	**0.93**	**0.90**
	σ_{RV}(dB)	0.30	0.31	**0.99**	**0.98**	**0.98**	**0.96**
	σ_{RL}(dB)	0.36	0.37	**0.99**	**0.98**	**0.98**	**0.95**
	q_0(dB)	0.43	0.57	**1.00**	**0.98**	**0.97**	**0.94**
	q_3(dB)	0.16	0.10	**0.98**	**0.97**	**0.99**	**0.97**
Group 2	σ_{RR}(dB)	0.86	**0.97**	**0.99**	**0.95**	0.85	0.27
Group 3	$1 - m$	0.78	**0.97**	0.85	0.34	**0.98**	**0.96**
	$\gamma_{(RR,RL)}$	0.78	**0.96**	0.86	0.38	**0.98**	**0.96**
	$\rho_{(RH,RV)}$	0.72	**0.97**	0.87	0.36	**0.98**	**0.96**
Group 4	$\gamma_{(RH,RV)}$	0.85	0.81	0.53	0.44	0.43	0.40
Independent group	q_1(dB)	0.71	0.50	0.31	0.49	**0.92**	**0.90**
	q_2(dB)	0.22	0.39	**0.96**	0.60	**0.95**	0.34
	α_s(dB)	0.13	0.29	0.44	0.42	0.54	0.46

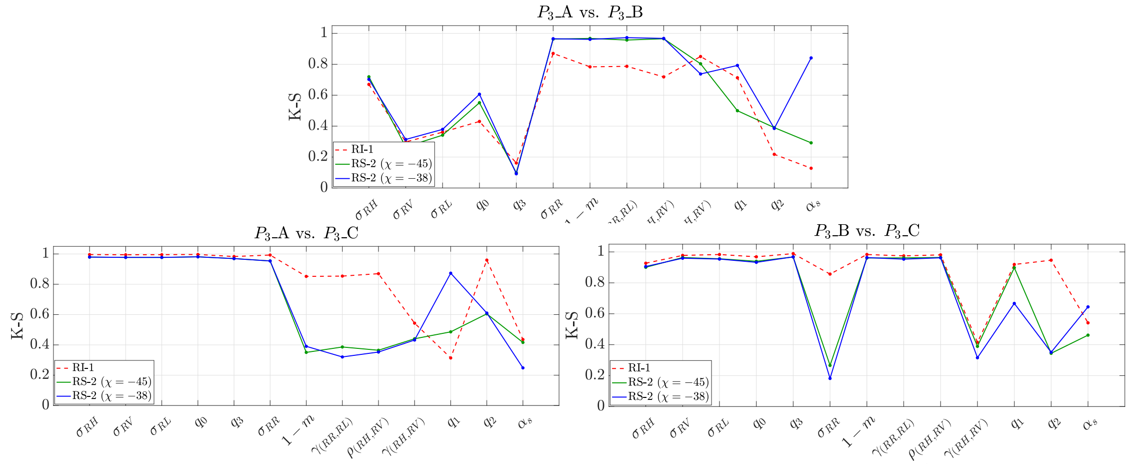

Figure 9. Top panel; a table containing the K-S values between all combinations of paired sea ice types in P_3. The first column shows groups as described in Table 3. The values greater than 0.9 are in bold. Bottom panels; the corresponding values are shown in the plots, where the y-axis shows the K-S values calculated for each of the paired sea ice types (i.e., ROIs) (red for the RI-1 features and green (blue) for the RS-2 features with an ellipticity angle of $\chi = -45°$ ($-38°$)), while the x-axis shows the corresponding features. Note that only the K-S values for RI-1 features and the RS-2 features using an ellipticity angle of $\chi = -45°$ is shown in the table.

4.2.4. Summary

From Figures 7–9, the separability values obtained from RS-2 and RI-1 features are similar across most of the pairwise combinations of the available sea ice types. However, the RI-1 features have slightly higher K-S values compared to the RS-2 features for the majority of the paired sea ice types. The majority of the panels in Figures 7–9 (7 out of 10) show differences for Group 3 between RI-1 and RS-2. One possible explanation for this behaviour might be the different NESZ for the two sensors. When increasing the additive noise of the simulated HP from the RS-2 products, the features in Group 3 were the ones most affected. This effect was confirmed by comparing the K-S values between the simulated HP data with and without an increase in the additive noise term. Note that the features in Group 4 are all ratio-based features.

In Figure 6, a higher NESZ is given for the investigated modes for the RI-1 products compared to the NESZ of RS-2. The RI-1 features still manage to separate the sea ice types that have backscattering coefficients close to the NESZ, which might indicate that the NESZ is lower than stated in the product description of RI-1 (as already highlighted by the calibration issue of RI-1 in [14]). In addition, the RI-1 products had finer resolution than the RS-2 product, and thus more averaging is performed for the RI-1 products to obtain the same ground resolution on the projected common grid. More averaging will reduce the speckle and increase class interpretability resulting in increased separability between the different sea ice types. There is also a trend in which group of features providing high separability as well as obtaining relative equal K-S values for the RI-1 and RS-2. Overall, the group of features that show equal separability between the sea ice types amongst all the scene pairs are Group 1 (the non ratio-based features), while amongst all the scene pairs the features in the independent group show the highest deviation between the K-S values obtained from RS-2 and RI-1. Evaluating all the K-S values together, the features that provide the overall highest separability are from Groups 1, 2, and 3, while the features that show poor separability are from Group 4 and the independent group.

4.3. The Non-Circularity Property

When simulating HP data from FP data using RS-2, we simulate perfect circular polarization on transmit. At the target, there might be an uncertainty associated with the actual transmitted wave, due to the non-circularity of a HP system in general, which was pointed out in [20] and tested in [14] for RI-1. These uncertainties are associated with, for example, propagation effects, transmitter, and antenna performance [34]. Therefore, a simulation on $\chi = -38^\circ$ (right-hand elliptical on transmit) from the RS-2 data was performed and compared to the RI-1 features and the simulated perfect circular HP from RS-2. The results are shown in Figures 7–9, where the blue line is the HP with $\chi = -38^\circ$, while the green line is $\chi = -45^\circ$. It is clear that the separability between the sea ice types are mostly similar for both $\chi = -38^\circ$ and $\chi = -45^\circ$. However, three features seem to be affected by the non-circularity property, these are q_1, $\gamma_{(RH,RV)}$, and α_s. Using q_1 and $\gamma_{(RH,RV)}$ the overall separability was higher for $\chi = -38^\circ$ between the majority of the paired sea ice types. However, using α_s the overall separability was higher for $\chi = -45^\circ$ between the majority of the paired sea ice types. All the features in Groups 1, 2, and 3 are stable when it comes to the ability to separate the various sea ice types for all the scene pairs, while unstable for Group 4 and the independent group, with the exception of q_2. This set of features (Group 4 and the independent group) is also found to show poor correlation between RS-2 and RI-1, which is discussed in Section 4.4.

4.4. Correlation between RS-2 and RI-1

The correlation between the two sensors are here evaluated through the Spearman's correlation coefficient (r_s) of three profiles in each scene pair shown in Figures 2–4. Three profiles are used to capture the variations along range direction in each scene pair. The three profiles are along azimuth direction, and the width of the profiles are the along range direction. The width of each profile is approximately 50 pixels. The mean along range direction is taken for each profile, leaving the resulting mean profile to be one pixel wide. Further, the correlation for a given feature extracted from RI-1 and RS-2 is calculated for each profile. The Spearman's correlation coefficients are shown in Table 4, where correlation values above 0.8 (strong to very strong correlation) are colored red. Note, log-transformed versions of the features are chosen when this increases the correlation; these cases are indicated by "dB" after the feature name.

For the three profiles in P_1 and P_2; a strong to very strong correlation is observed for the majority of the features in Groups 1 and 2 (non ratio-based features), while the majority of the ratio-based features and q_1 and q_2 fall in the very weak to moderate correlation categories (see discussion on the Spearman's correlation coefficient in Section 3). In addition, stronger r_s is found for the profiles in P_2 compared to the profiles in P_1. The r_s values for the profiles in P_3 are given in the last three columns in Table 3. Here, a strong to very strong correlation is observed for the features in Group 3. Note that the features in Group 1 gave a strong to very strong correlation in the three profiles in P_1 and P_2. This trend is not observed for the three profiles in P_3.

The profiles in P_3 are the ones which resulted in the lowest correlation amongst all the profiles. Compared to P_1 and P_2, the scenes in P_3 contain sea ice (grease ice and FYI) covered with a fresh snow layer. In addition the scenes in P_3 had the lowest incidence angle (22.5°–25.3°) compared to the other scene pairs. Further the variations in the r_s values across the three profiles within each scene pair are small.

Comparing the results from Figures 7 and 8 and the r_s in Table 4 it is possible to identify a trend between high separability between the investigated sea ice types and the strong Spearman's correlation for Groups 1 and 2. This is only true for scene pairs P_1 and P_2. The features that give mostly strong correlation in all scene pairs are σ_{RH}, q_0, and σ_{RR}. These are features from Groups 1 and 2. Note that σ_{RH}, q_0, and σ_{RR} had also high K-S distances between the majority of the sea ice types investigated. The remaining features show varying correlation coefficients across the scene pairs.

Table 4. The Spearman's correlation coefficient (r_s) (absolute value) between RI-1 and RS-2 for the three profiles in each pair (seen Figure 5). The r_s values that are above 0.8 (strong correlation) are colored red. The first column shows the groups as described in Table 3.

Group		**P$_1$**			**P$_2$**			**P$_3$**		
Name	**Profile #**	**1**	**2**	**3**	**1**	**2**	**3**	**1**	**2**	**3**
Group 1	σ_{RH} (dB)	0.80	0.88	0.82	0.90	0.93	0.96	0.70	0.85	0.89
	σ_{RV} (dB)	0.80	0.88	0.82	0.91	0.94	0.96	0.57	0.68	0.74
	σ_{RL} (dB)	0.80	0.88	0.83	0.90	0.94	0.96	0.59	0.70	0.78
	q_0 (dB)	0.83	0.88	0.83	0.90	0.92	0.94	0.65	0.80	0.86
	q_3 (dB)	0.84	0.87	0.83	0.75	0.90	0.92	0.64	0.61	0.61
Group 2	σ_{RR} (dB)	0.79	0.87	0.81	0.92	0.94	0.95	0.77	0.92	0.90
Group 3	$1 - m$	0.77	0.83	0.76	0.63	0.70	0.63	0.86	0.90	0.84
	$\gamma_{(RR,RL)}$	0.79	0.84	0.77	0.66	0.68	0.68	0.84	0.88	0.84
	$\rho_{(RH,RV)}$	0.78	0.84	0.76	0.64	0.71	0.65	0.86	0.89	0.84
Group 4	$\gamma_{(RH,RV)}$	0.06	0.14	0.16	0.16	0.27	0.51	0.59	0.79	0.81
Independent group	q_1 (dB)	0.65	0.76	0.66	0.48	0.64	0.84	0.56	0.72	0.70
	q_2 (dB)	0.75	0.84	0.78	0.37	0.34	0.73	0.17	0.44	0.45
	α_s (dB)	0.68	0.70	0.63	0.22	0.14	0.58	0.06	0.05	0.16

5. Conclusions

In this study we investigated the relationship between a real and a simulated HP system in three overlapping pairs of RI-1 and RS-2 scenes covering Arctic sea ice, with relatively small time difference between acquisitions and similar incidence angles. Thirteen HP features are evaluated both from real HP data (RI-1) and simulated HP data from RS-2.

Several polarimetric features from the two groups where surface scattering and depolarization due to volume scattering dominates showed great potential for separating various sea ice types based on the K-S values. We conclude that the HP mode of RI-1 and the simulated HP mode of RS-2 show comparable performance in separating the sea ice types. Amongst all the scene pairs, the features in the independent group had the highest deviation between the K-S values obtained from RS-2 and RI-1. Recall, the independent group contains features that likely give additional information that may be complementary to the groups sensitive to various scattering mechanisms.

The features that show poor separability are from the group that was sensitive to polarization differences in resonant Bragg scattering and also in the Fresnel coefficients, and from the independent group.

The NESZ provided with RI-1 is given as a constant value of −17 dB, and the backscattering values from some sea ice types were close to and sometimes below this value. We discovered a high separability between sea ice types that had backscattering values close to NESZ, which might indicate that the RI-1 quality in terms of NESZ is better than previously reported.

Three polarimetric features seem to be affected by not having a perfect circular wave on transmit, these are q_1, $\gamma_{(RH,RV)}$, and α_s. However, the separability between the different sea ice types using features from the groups where surface scattering and depolarization due to multiple/volume scattering dominates are similar for both ellipticity angles of $\chi = -38^\circ$ and $\chi = -45^\circ$. We therefore conclude that having a more elliptical wave on transmit will not affect the separability of the investigated sea ice types given that the correct features are selected.

For two of the three scene pairs (P_1 and P_2) we discovered a high Spearman's correlation between the profiles using the polarimetric features from RI-1 and RS-2 that are in groups where surface scattering and depolarization due to volume scattering dominates. For P_3 the features sensitive to depolarization due to volume and multiple scattering showed high correlation. These results might be explained by a snow layer contributing to more volume scattering in P_3 (see e.g., [33]), and our results indicate that the features that are sensitive to volume/multiple scattering give higher correlation between the two sensors. The Spearman's correlation for the features extracted from RS-2 and RI-1 profiles were relatively consistent across each scene pair. However, no individual feature showed strong to very strong correlation across all three scene pairs. Although the features σ_{RH}, q_0, and σ_{RR} showed strong to very strong correlation across all three scene pairs expect for 1–2 profiles which had moderate correlations between the sensors. Note, these features also gave high separability values between the majority of the paired ROIs, and were not so affected by the non-circularity property. Therefore, the features σ_{RH}, q_0, and σ_{RR} are recommended to use when the FRS-1 mode of RI-1 and RS-2 data are combined for change detection purposes or for increasing the coverage when monitoring the surface.

Future studies will include investigation of the the non-circularity property of the transmitted wave for a larger set of multipolarization features. We also wish to identify the reasons why some polarimetric features are affected by the non-circularity property and some are not.

Acknowledgments: RS-2 data were provided by NSC/KSAT under the Norwegian-Canadian Radarsat agreement 2015. The RI-1 data were provided by KSAT through CIRFA (RCN Grant no. 237906). This research is financed by CIRFA (RCN Grant no. 237906) and the NORRUSS program (RCN Grant no. 233896). Observations from 2015 were provided by the Fram Strait Arctic Ocean Observatory (http://www.npolar.no/framstrait). The authors extend their thanks to all who participated in the 2015 Fram Strait campaign.

Author Contributions: Martine M. Espeseth, Camilla Brekke, and A. Malin Johansson were all involved in the study design and writing of this paper. Martine M. Espeseth analyzed the data and made the figures and tables. Martine M. Espeseth and A. Malin Johansson ordered the satellite acquisitions. A. Malin Johansson collected the in-situ sea ice and accompanying measurements (in part with the Norwegian Polar Institute).

Conflicts of Interest: The authors declare no conflict of interest.

References

1. Maillard, P.; Clausi, D.A.; Deng, H. Operational Map-Guided Classification of SAR Sea Ice Imagery. *IEEE Trans. Geosci. Remote Sens.* **2005**, *43*, 2940–2951.
2. Walker, N.P.; Partington, K.C.; Woert, M.L.V.; Street, T.L.T. Arctic Sea Ice Type and Concentration Mapping Using Passive and Active Microwave Sensors. *IEEE Trans. Geosci. Remote Sens.* **2006**, *44*, 3574–3584.
3. Moen, M.A.N.; Doulgeris, A.P.; Anfinsen, S.N.; Renner, A.H.H.; Hughes, N.; Gerland, S.; Eltoft, T. Comparison of feature based segmentation of full polarimetric SAR satellite sea ice images with manually drawn ice charts. *Cryosphere* **2013**, *7*, 1693–1705.
4. Moen, M.A.N.; Anfinsen, S.N.; Doulgeris, A.P.; Renner, A.H.H.; Gerland, S. Assessing polarimetric SAR sea-ice classifications using consecutive day images. *Ann. Glaciol.* **2015**, *56*, 285–294.
5. Raney, R.K. Hybrid-Polarity SAR Architecture. *IEEE Trans. Geosci. Remote Sens.* **2007**, *45*, 3397–3404.
6. Dabboor, M.; Geldsetzer, T. Towards sea ice classification using simulated RADARSAT Constellation Mission compact polarimetric SAR imagery. *Remote Sens. Environ.* **2014**, *140*, 189–195.
7. Dabboor, M.; Geldsetzer, T. On the Classification of Sea Ice Types using Simulated Radarsat Constellation Mission (RCM) Compact Polarimetric SAR Parameters. In Proceedings of the ASPRS 2014 Annual Conference, Louisville, Kentucky, 23–28 March 2014.

8. Li, H.; Perrie, W. Sea Ice Characterization and Classification Using Hybrid Polarimetry SAR. *IEEE J. Sel. Top. Appl. Earth Obs. Remote Sens.* **2016**, *9*, 4998–5010.
9. Geldsetzer, T.; Arkett, M.; Zagon, T.; Charbonneau, F.; Yackel, J.J.; Scharien, T.K. All-Season Compact-Polarimetry C-band SAR Observations of Sea Ice. *Can. J. Remote Sens.* **2015**, *41*, 485–504.
10. Xi, Z.; Jie, Z.; Meijie, L.; Junmin, M. Assessment of C-band compact polarimetry SAR for sea ice classification. *Acta Oceanol. Sin.* **2016**, *35*, 79–88.
11. Singha, S.; Ressel, R. Arctic Sea Ice Characterization Using RISAT-1 Compact-Pol SAR Imagery and Feature Evaluation: A Case Study Over Northeast Greenland. *IEEE J. Sel. Top. Appl. Earth Obs. Remote Sens.* **2017**, *10*, 3504–3514.
12. Souyris, J.C.; Imbo, P.; Fjortoft, R.; Mingot, S.; Lee, J.S. Compact polarimetry based on symmetry properties of geophysical media: the $pi/4$ mode. *IEEE Trans. Geosci. Remote Sens.* **2005**, *43*, 634–646.
13. Espeseth, M.M.; Brekke, C.; Anfinsen, S.N. Hybrid-Polarity and Reconstruction Methods for Sea Ice With L- and C-Band SAR. *IEEE Geosci. Remote Sens. Lett.* **2016**, *13*, 467–471.
14. Rao, Y.S.; Meadows, P.; Kumar, V. Evaluation of RISAT-1 compact polarization data for calibration. In Proceedings of the 2016 IEEE International Geoscience and Remote Sensing Symposium (IGARSS), Beijing, China, 10–15 July 2016; pp. 3250–3253.
15. Eriksson, L.E.B.; Borenäs, K.; Dierking, W.; Berg, A.; Santoro, M.; Pemberton, P.; Lindh, H.; Karlson, B. Evaluation of new spaceborne SAR sensors for sea-ice monitoring in the Baltic Sea. *Can. J. Remote Sens.* **2010**, *36*, 56–73.
16. Misra, T.; Rana, S.S.; Desai, N.M.; Dave, D.B.; Rajeevjyoti; Arora, R.K.; Rao, C.V.N.; Bakori, B.V.; Neelakantan, R.; Vachchani, J.G. Synthetic Aperture Radar payload on-board RISAT-1: Configuration, technology and performance. *Curr. Sci.* **2013**, *104*, 446–461.
17. Slade, B. *Radarsat-2 Product Description*; MacDonald, Dettwiler and Associates Ltd.: Rickmond, BC, USA, 2011.
18. Oliver, C.; Quegan, S. *Understanding Synthetic Aperture Radar Images*; SciTech Publishing Inc.: Raleigh, NC, USA, 2004.
19. Drinkwater, M. Airborne and Satellite SAR Investigations of Sea-Ice Surface Characteristics. In *Oceanographic Applications of Remote Sensing*; CRC Press: Boca Raton, FL, USA, 1995; Chapter IV-A-3, pp. 339–357.
20. Touzi, R.; Charbonneau, F. Requirements on the calibration of Hybrid-Compact SAR. In Proceedings of the 2016 IEEE International Geoscience and Remote Sensing Symposium (IGARSS), Quebec City, QC, Canada, 13–18 July 2014; pp. 1109–1112.
21. Stutzman, W.L.; Thiele, G.A. *Antenna Theory and Design*; John Wiley and Sons Inc.: Hoboken, NJ, USA, 1981.
22. Lee, J.S.; Pottier, E. Polarimetric Radar Imaging: from basic to applications, In *Optical Science and Engineering*; CRC Press Taylor and Francis Group: Abingdon, UK, 2009.
23. Kumar, V.; Rao, Y.S. Comparative analysis of RISAT-1 and simulated RADARSAT-2 hybrid polarimetric SAR data for different land features. In Proceedings of the The International Archives of the Photogrammetry, Remote Sensing and Spatial Information Sciences, ISPRS Technical Commission VIII Symposium, Hyderabad, India, 7–12 December 2014; Volume XL-8.
24. Zhang, X.; Dierking, W.; Zhang, J.; Meng, J.; Lang, H. Retrieval of the thickness of undeformed sea ice from simulated C-band compact polarimetric SAR images. *Cryosphere* **2016**, *10*, 1529–1545.
25. Cloude, S.R. *Polarisation Applications in Remote Sensing*; Oxford University Press Inc.: New York, NY, USA, 2010; pp. 125–129.
26. Cloude, S.R.; Goodenough, D.; Chen, H. Compact Decomposition Theory. *IEEE Trans. Geosci. Remote Sens.* **2012**, *9*, 28–32.
27. Massry, F.J., Jr. The Kolmogorov-Smirnov Test for Goodness of Fit. *J. Am. Stat. Assoc.* **1951**, *46*, 68–78.
28. Corder, G.W.; Foreman, D.I. *Nonparametric Statistics for Non-Statisticians: A Step-by-Step Approach*; Wiley: Hoboken, NJ, USA, 2009.
29. Evans, J.D. *Straightforward Statistics for the Behavioral Sciences*; Brooks/Cole Publishing Company, The University of California: Baltimore, MD, USA, 1996.
30. Charbonneau, F.J.; Brisco, B.; Raney, R.K.; McNairn, H.; Liu, C.; Vachon, P.W.; Shang, J.; DeAbreu, R.; Champagne, C.; Merzouki, A.; Geldsetzer, T. Compact Polarimetry Overview and Applications Assessment. *Can. J. Remote Sens.* **2010**, *36*, 298–315.
31. Dabboor, M.; Howell, S.; Shokr, M.; Yackel, J. The Jeffries-Matusita distance for the case of complex Wishart distribution as a separability criterion for fully polarimetric SAR data. *Int. J. Remote Sens.* **2014**, *35*, 6859–6873.

32. Dierking, W. Mapping of Different Sea Ice Regimes Using Images From Sentinel-1 and ALOS Synthetic Aperture Radar. *IEEE Trans. Geosci. Remote Sens.* **2010**, *48*, 1045–1058.
33. Gill, J.P.S.; Geldsetzer, T.; Fuller, M.C. Sensitivity of C-band synthetic aperture radar polarimetric parameters to snow thickness over landfast smooth first-year sea ice. *Remote Sens. Environ.* **2015**, *166*, 34–49.
34. Sabry, R.; Vachon, P.W. A Unified Framework for General Compact and Quad Polarimetric SAR Data and Imagery Analysis. *IEEE Trans. Geosci. Remote Sens.* **2014**, *52*, 582–602.

11

Innovation

A key aspect of CIRFA is innovation that can aid the industry in utilizing remote sensing data to improve their monitoring and forecasting capabilities in the Arctic. Therefore, the innovation project conducted as part of this PhD work is presented in this thesis.

11.1 Objectives

The innovation project involves implementing an automatic algorithm that estimates the damping ratio of several SAR sensors and imaging modes. The future goal is to test and verify the relationship between the damping ratio (presented in Section 3.4.2) and the relative oil thickness for these products. This work was done in collaboration with KSAT located in Tromsø, in the time period February - June 2019. The main objectives were:

- To increase collaboration between the industry (KSAT) and CIRFA.
- To implement an algorithm that runs automatically on the SAR products.
- To test the algorithm on different sensors types/modes, oil types and oil slick areas provided by KSAT.
- To deliver the "damping ratio product" to NOFO during the oil-on-water exercise 2019, and to demonstrate its potential throughout and after the exercise.

11.2 Background Theory

Recall from Section 3.4.2 that the damping ratio (DR) is calculated as

$$DR_{x,y} = \frac{\sigma_y^{0,clean\ sea}}{\sigma_{x,y}^0}, \tag{11.1}$$

where $\sigma_y^{0,clean\ sea}$ represents a clean sea value at range position y, whereas $\sigma_{x,y}^0$ represents an intensity value at pixel location (x,y) (azimuth, range). $\sigma^{0,clean\ sea}$ is a clean sea profile of length equal to total number of pixels in range direction, and the same pixel value applies across azimuth direction for each range position.

To reduce the execution time of the algorithm, the estimation of the damping ratio can be done using the digital numbers (DN), and not on the radiometric calibrated sigma-nought values. This can be approximated by

$$DR_{x,y} = \frac{|DN_y^{clean\ sea}|^2 \sin(\theta_y) k_s}{k_s |DN_{x,y}|^2 \sin(\theta_y)} = \frac{|DN_y^{clean\ sea}|^2}{|DN_{x,y}|^2}, \tag{11.2}$$

where k_s is the calibration and processor scaling factor for SAR signals, and θ_y is the incident angle at range position y.

11.3 Product Overview

The algorithm was implemented at KSAT, primarily intended to run on scanSAR products from Radarsat-2, Sentinel-1, and COSMO-SKYMED. The drawback of the damping ratio is the need for a clean sea region, i.e., $\sigma^{0,clean\ sea}$. For the customers, the numerical values of the damping ratio are not relevant, and only the information about high or low damping is important (indicating relatively thick or thin oil). Hence, the damping ratio images strictly show the relative damping within oil slicks using different colors that reflects high or low damping ratio values. Currently, the color-scheme cannot be compared across different slicks within a scene, due to incident angle variations between the location of the slicks and the scaling that is performed on the damping ratio for each slick. It is well known that the VV polarization channel has the highest sea-oil contrast. Therefore, the VV-channel is used from all scanSAR DP (VV-VH) and FP SAR products.

During the project period at KSAT, the algorithm was tested on several oil types, such as produced water, mineral oil, and natural seep in various imaging modes and for different sensor types. One clear challenge of the damping ratio algorithm is low-wind areas, as these might influence the clean sea profile.

11.4 Implementation

The upcoming list describes the steps of the algorithm.

Trim land areas: The backscatter from land is high compared to the ocean, and could influence the clean sea profile. The land areas are therefore removed (set to NaN) using a SNAP graph[1].

Find clean sea profile: For homogeneous images, the clean sea profile decreases with increasing incidence angle. This profile is an array with length equal to the range of the image scene and is estimated by applying the median along the azimuth direction. The median is used since it is less affected by outliers (e.g., ships and low-wind areas).

Smooth clean sea profile: In the next step, a 3rd order polynomial function is fit to the median profile, to achieve a smoother profile. The fitted profile represents the $|DN^{clean\ sea}|^2$ in Equation 11.2.

Calculate the damping ratio: The fitted clean sea profile is divided by the DN image, according to Equation 11.2.

Extract oil slicks areas: Another input to the algorithm is the location of the oil slicks, which are provided by KSAT very shortly after the SAR image is acquired and downlinked. The oil slicks masks are segmented from SAR images by KSAT's operators daily. The oil slicks masks are used to create several damping ratio sub-images, where each sub-image covers one slick.

Outlier removal: The damping ratio values in each sub-image are scaled based on a lower and an upper percentile for each detected slick to remove outliers and for better visibility, and converted to uint-8. The damping ratio integer values are then linearly mapped to 11 colors representing low to high damping ratio. 11 colors were selected to visualise variations within the oil slick and were inspired by Figure 9 in [Fingas and Brown, 2014].

The fitted profile represents the $|DN^{clean\ sea}|^2$ in Equation 11.2. Figure 11.1 shows an example of the DN image (in VV) from Sentinel-1, and the bottom panel of Figure 11.1 shows the median profile along range direction and the fitted profile. There are several ships and platforms in the Sentinel-1 image, which can be seen as bright pixels. The effect of these bright spots cannot be observed in the median or fitted profiles of Figure 11.1.

The outputs of the algorithm are GeoTIFF-files and a PDF report. Figures 11.2-11.4 show

---

[1] European Space Agency (ESA) provides free open-source toolboxes, known as SNAP, for scientific exploitation (see `http://step.esa.int/main/`)

two examples of the damping ratio PDF-report that is generated automatically from the algorithm.

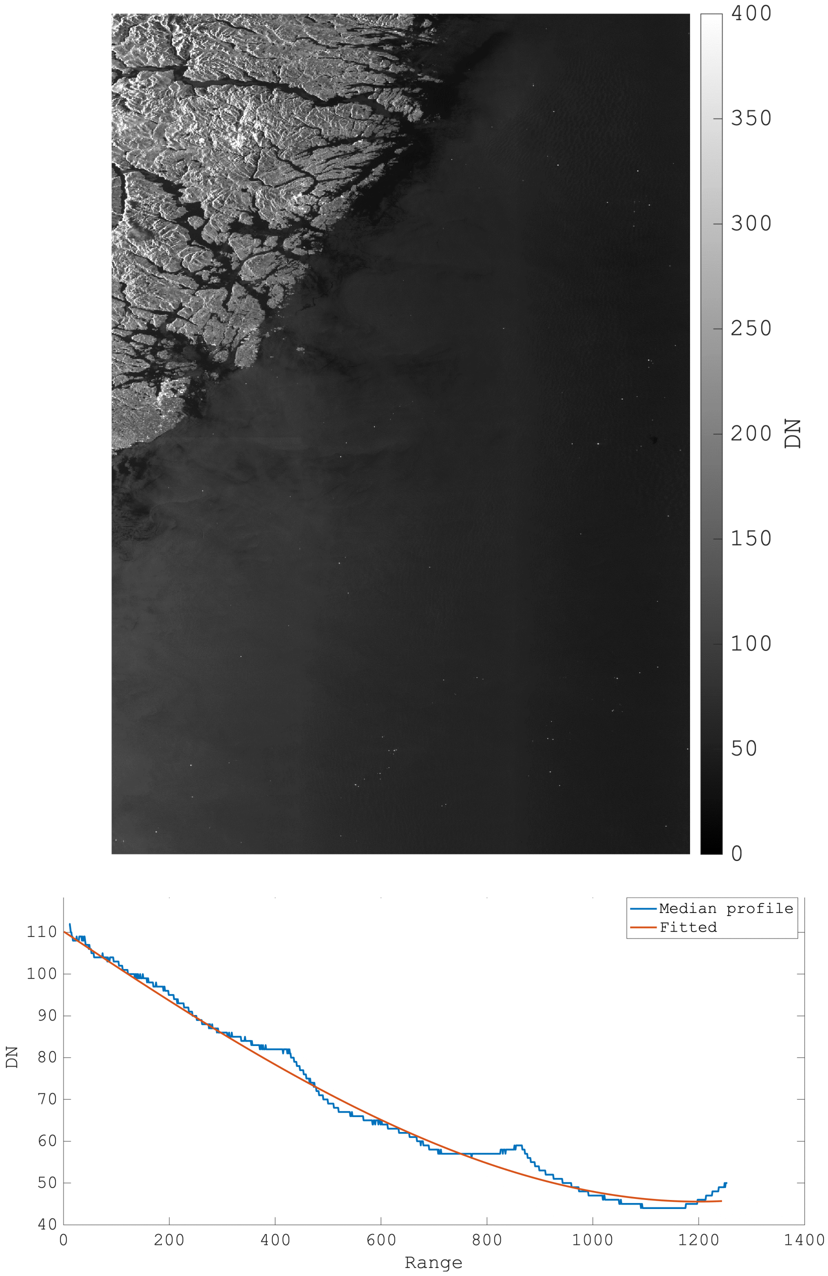

Figure 11.1: Top: Digital number image of the VV-channel from Sentinel-1 acquired 11 July 2018. Sentinel-1 from European Space Agency - ESA. Bottom: Median profile and the fitted profile along range direction of the DN image.

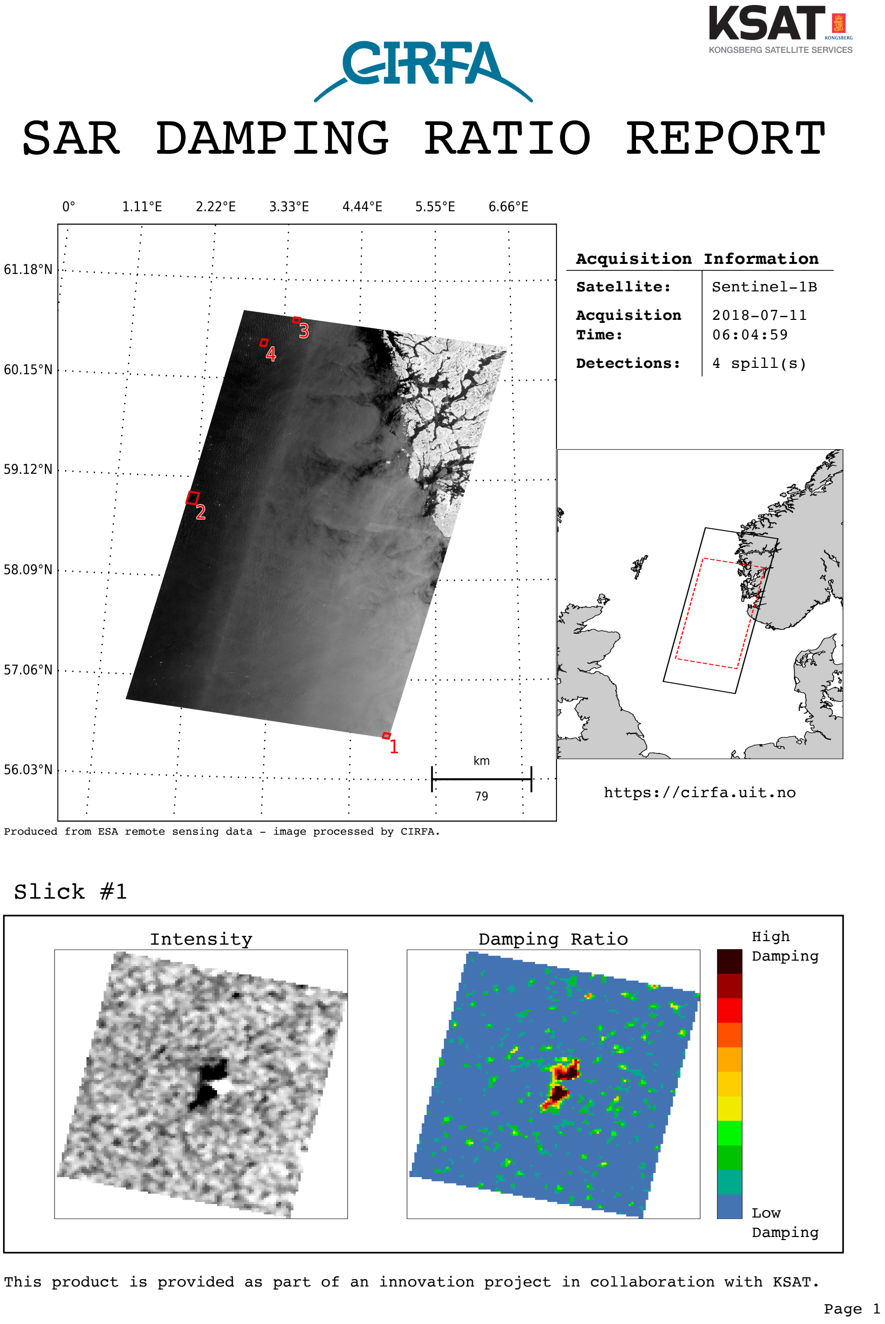

SAR DAMPING RATIO REPORT

Acquisition Information	
Satellite:	Sentinel-1B
Acquisition Time:	2018-07-11 06:04:59
Detections:	4 spill(s)

https://cirfa.uit.no

Produced from ESA remote sensing data - image processed by CIRFA.

Slick #1

This product is provided as part of an innovation project in collaboration with KSAT.

Page 1

Figure 11.2: Example of one SAR damping ratio report of an archived Sentinel-1 acquisition (page 1). See Figure 11.3 for the second page.

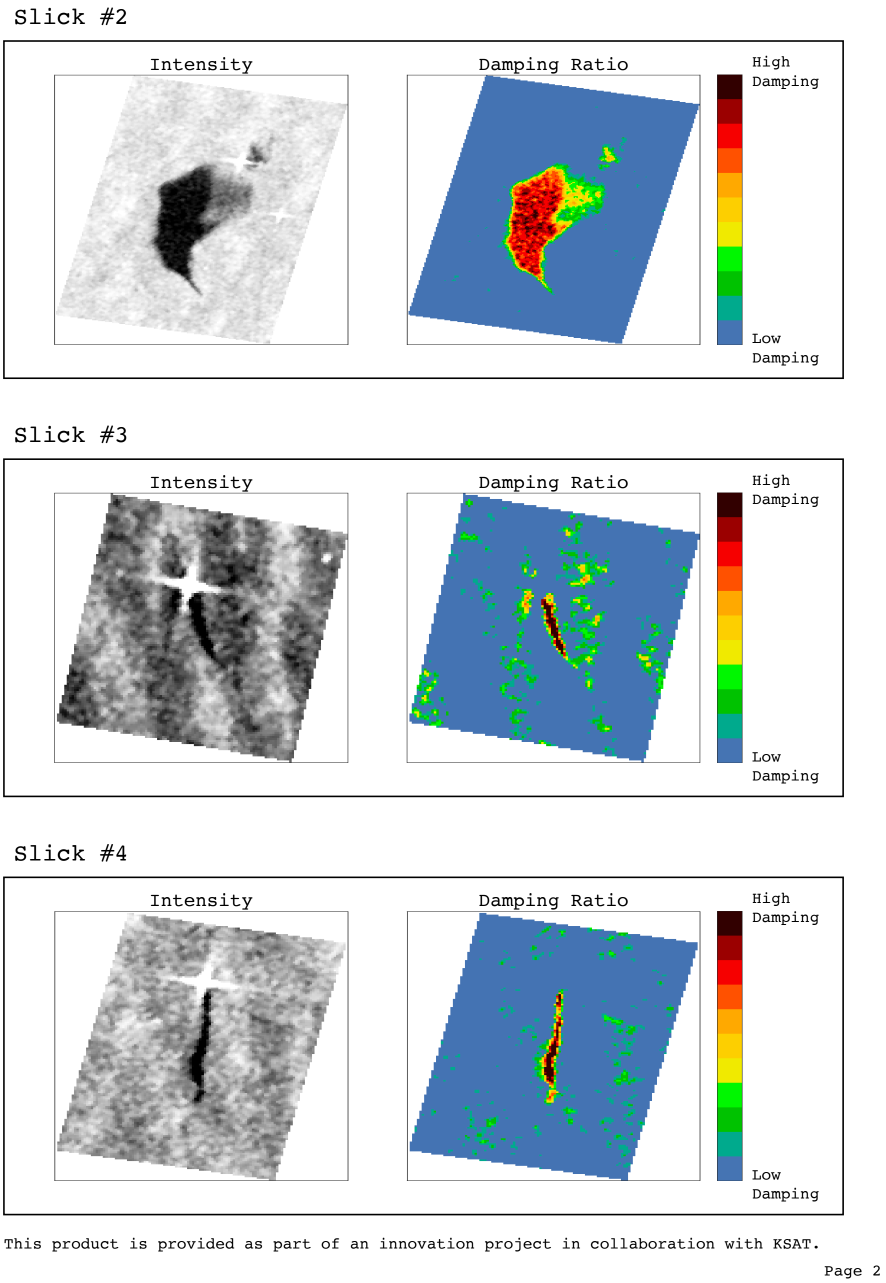

Slick #2

Slick #3

Slick #4

This product is provided as part of an innovation project in collaboration with KSAT.

Page 2

Figure 11.3: Example of one SAR damping ratio report of an archived Sentinel-1 acquisition (page 2).

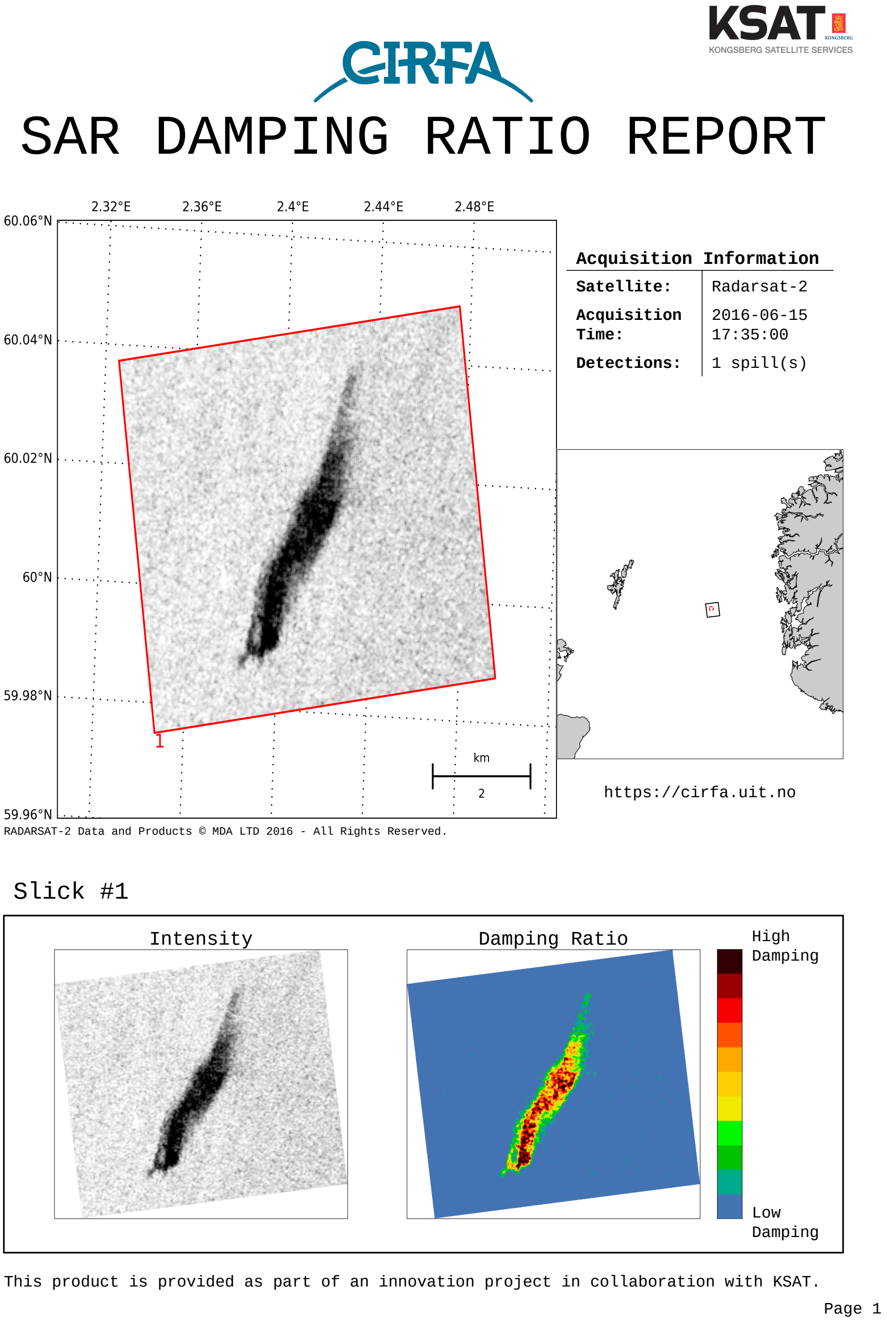

SAR DAMPING RATIO REPORT

RADARSAT-2 Data and Products © MDA LTD 2016 - All Rights Reserved.

Acquisition Information	
Satellite:	Radarsat-2
Acquisition Time:	2016-06-15 17:35:00
Detections:	1 spill(s)

https://cirfa.uit.no

Slick #1

This product is provided as part of an innovation project in collaboration with KSAT.

Page 1

Figure 11.4: Example of one SAR damping ratio report of an archived Radarsat-2 acquisition.

11.5 Demo during the Oil-On-Water 2019

One of the objectives of the innovation project was to test the work-flow of the algorithm during oil-on-water 2019. Figure 11.5 illustrates the workflow of the demonstration. First, KSAT's operators manually detected potential oil slicks from the SAR images. Following

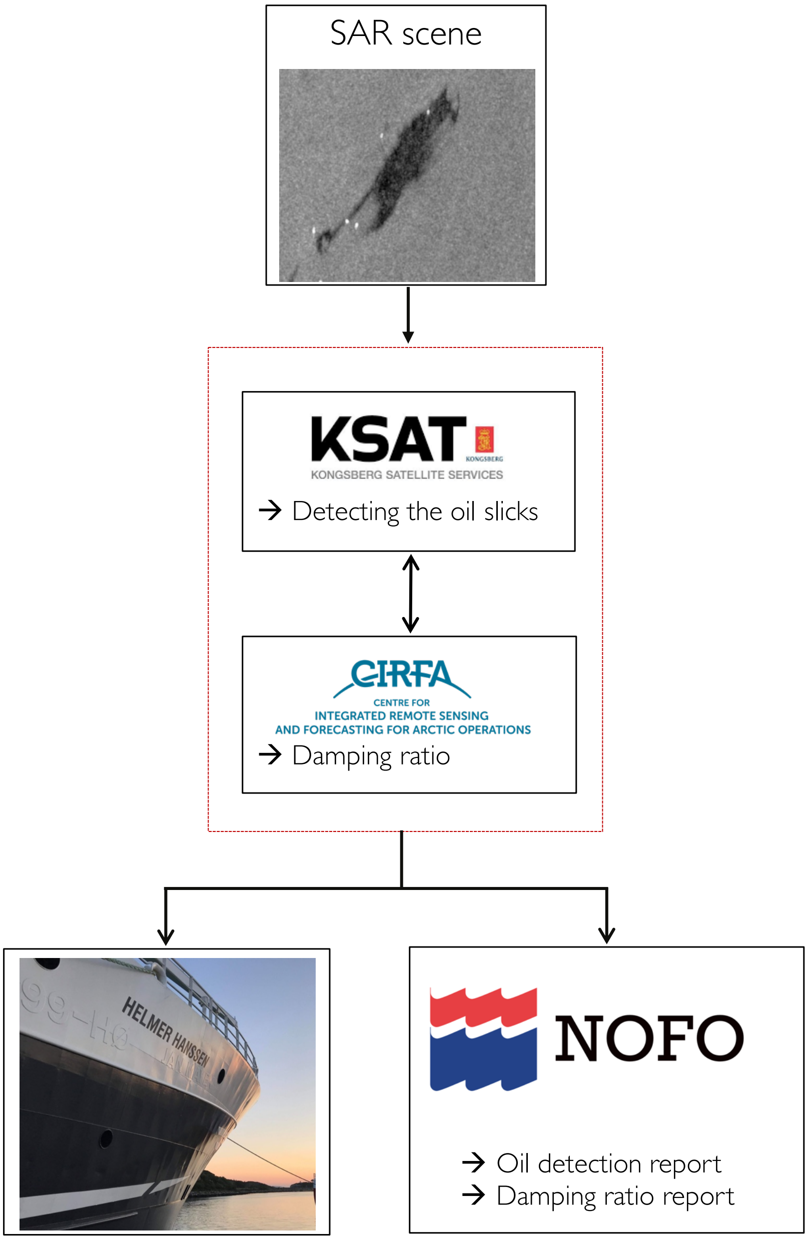

Figure 11.5: Work flow of the product delivery from KSAT to NOFO during the oil-on-water exercise 2019. The lower-left photo was taken by A. Malin Johansson (UiT).

this, the oil spill detection reports were delivered to the relevant customers. Once the operators were done, the damping ratio algorithm was triggered by files being uploaded to a server. After approximately 2 minutes the damping ratio algorithm had run to completion, and NOFO (responsible for the oil-on-water exercise) could download a Web Map Service (WMS)-layer into their system to inspect the relative damping ratio values within oil slicks in and around the exercise area. FF Helmer Hanssen (the research vessel in the exercise area) also received the product onboard. The damping ratio maps were then loaded into a system that was connected to the drones on-board the ship. The full system could then be used by the drone pilots to navigate the drone to the areas with relatively high damping ratio values within the oil slick. Unfortunately, during the oil-on-water exercise, the drone could not fly close to the SAR acquisition times due to strong winds and high waves. This system was therefore not used, but the damping ratio images were loaded into the system successfully. Additionally, there were some delays to the oil releases, which resulted in young slicks with little spreading in the early SAR acquisitions. Figure 11.6 shows two damping ratio images from Sentinel-1 and TerraSAR-X acquired shortly after the oil release. As observed in the top images of Figure 11.6 the slick is small compared to the spatial resolution of Sentinel-1. The rough sea can also be seen in the bottom images of Figure 11.6, where a clear wave pattern across the scene is visible. As a result of rough sea and a you slick, little internal variation can be seen. Despite the poor weather conditions, the entire workflow of the algorithm and the product delivery was successful.

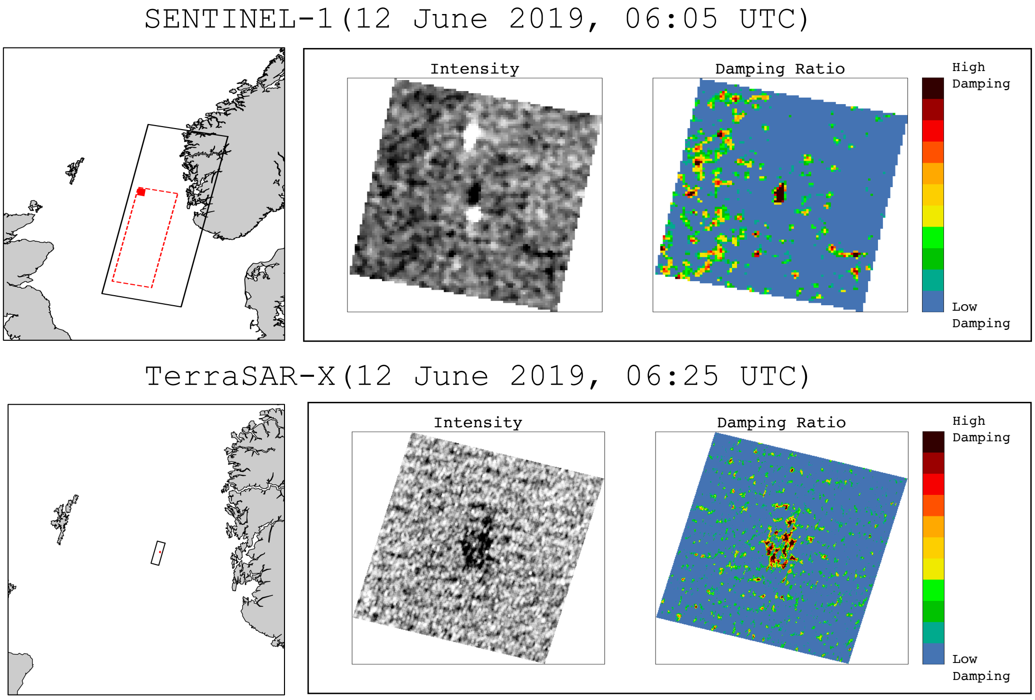

Figure 11.6: Damping ratio images from oil-on-water 2019 from Sentinel-1 and TerraSAR-X. Sentinel-1 from European Space Agency. TerraSAR-X © DLR
]

11.6 Future Scope

The innovation project is still in its infancy, and more work is necessary to identify the limitations and potential for the damping ratio algorithm. Different oil types must be considered, and preferably, the SAR image should overlap with in-situ measurements and/or optical data to test the relationship between the damping ratio and oil thickness. A more thorough investigation of how many classes to expect within an oil slick should be carried out. Maybe three classes could be sufficient; clean sea (zero damping), thin oil (low-medium damping) and thick actionable oil (high damping).

The minimum spatial resolution needed to capture internal variations through the damping ratio should also be identified. In Norwegian waters, the time difference between Sentinel-1 and Sentinel-2 (also Landsat-8) is long, and a complete overlap in time is impossible with Sentinel-1 and Sentinel-2, not even when using Radarsat-2 or TerraSAR-X. Therefore, optical data from airplanes is optimal. Further work is necessary both for this innovation project and in order to confirm the underlying theory of the damping ratio. It is therefore recommended that the project continue developing and testing of the damping ratio algorithm.

12

Conclusion

The papers presented in Chapter 7-10 cover topics related to the potential of the HP mode for oil spill and sea ice observations, the negative impact of system noise on the polarimetric data, and oil spill response-oriented information products derived from SAR data from an operational perspective. Section 12.1 briefly summarizes the four papers. Section 12.2 discusses and presents some future work and ideas.

12.1 Research Conclusions

FP SAR data for oil spill monitoring has been investigated for years, and several multi-polarization features have been suggested for detection and characterization purposes. The FP SAR comes at a cost of narrow swath width, making it challenging to utilize for operational purposes where coverage is essential. This is the main reason why the HP mode has been suggested as an alternative with more polarimetric information than the conventional DP modes and larger swath width (or finer resolution) than FP SAR. In order to understand the potential and limitations of the HP mode for any application, rigorous testing is necessary. Paper I confirms that the HP mode is almost as good as the FP mode when detecting various types of oil from clean sea under high wind conditions. The two-scale Bragg models are used for grouping the investigated FP and HP features into two categories, either dependent or independent of the small-scale ocean surface roughness. The features dependent on the small-scale ocean surface roughness had highest oil-sea contrast for the investigated oil types for both FP and HP SAR. Paper I recommends the HV- and VV-intensities as the optimal features for separating the various oil types from clean sea. This recommendation is based on a data set (from the UAVSAR) with very low noise floor. The HV- and VV-intensities are not possible to isolate using the HP mode, and the right-hand circular-circular (RR) and right-hand circular-linear (vertical) intensities are recommended for the HP mode. Paper I also demonstrated the importance of performing an incidence angle correction before segmenting the oil slicks.

FP SAR data has been used to improve the interpretability of various sea ice types compared to SP and the conventional DP modes. Unfortunately, the FP mode comes at a cost of narrow swath width, and since sea ice covers large areas, a wide coverage is preferred. The HP mode therefore has a great potential for sea ice monitoring with increased coverage without losing too much polarimetric information compared to FP SAR. Previous studies have concluded that HP data has a great potential for separating various sea ice types. Most studies have simulated HP data and compared it with FP data, and this was also done in Paper I. Paper IV was amongst the first studies to compare real versus simulated HP data for sea ice. Both real HP and simulated HP showed great potential for separating different sea ice types, such as first-year ice from grease ice and flooded first-year ice. Paper IV confirms that real HP mode is sufficient (for the investigated sea ice types in Paper IV) for sea ice characterization, as previous research has concluded based on the simulation of HP mode. Although Paper IV is based on only three overlapping Radarsat-2 and RISAT-1 SAR scenes, it is a good starting point for validating real HP data for sea ice monitoring.

FP SAR data provides a unique capability of measuring the complete scattering matrix and allow identification and extraction of the scattering processes for a given target. Polarimetry has been used to separate different types of oil and for estimation of physical properties (e.g., volumetric oil fraction) from the oil using physical models. Unfortunately, utilizing polarimetry for oil spill analysis might be risky, since system noise could contaminate the measured signal from these low-backscattering areas. For spaceborne SAR systems the noise floor is high compared to airborne SAR systems, and noise must be carefully considered. Paper II shows the impact of noise on different polarimetric features by identifying trends as a function of both multiplicative and additive system noise and validating against real and simulated noise. The majority of the features show a clear trend with system noise independent of the scene-to-scene variations such as the incidence angle and environmental conditions. Paper II is the first study that includes other noise sources than the known additive system noise, namely multiplicative system noise for oil slicks. The majority of all the satellite SAR signals from oil slicks falls close to or even below the noise floor, when both additive and multiplicative system noise sources are included. This study also recommends avoiding the use of the well known H/α decomposition for oil studies. A noise subtraction should be done before any polarimetric analysis when characterizing the oil. The noise subtraction reduces the oil-sea contrast for some features and should be avoided for oil slick detection purposes.

A single spaceborne SAR scene is valuable when identifying location, extent, and, possibly the source of the spill. Tracking the evolution of a slick requires several images of the same slick with short time difference between scenes. An oil spill drift model can also track the evolution, but these rely on accurate tuning, model design, and accurate wind and current information. An airborne SAR sensor could provide rapid repeat images to monitor how the slick drifts and weathers on the sea surface. Paper III introduces complementary information products that could be valuable in the recovery process, where timely knowledge of the spill is important. The methodologies presented in Paper III are aimed at creating maps that combine several SAR images to compose products that quantify and visually depict the temporal evolution of the slick in an easily understandable representation.

12.2 Future Outlook

Raney [2007] and Souyris et al. [2005] re-introduced the HP mode as a promising polarization mode that limits the trade-off between coverage and polarimetric information. Simulation of HP data has demonstrated its potential for separating, detecting, and classifying various surfaces. Testing of real HP data became possible with the availability of RISAT-1 data. Unfortunately, RISAT-1 is no longer active, but active satellites such as the RCM and ALOS-2 do offer the HP mode. More extensive testing and verification of the real HP mode should be pursued further when data from these sensors become available.

The damping ratio has been reported to increase with increasing oil thickness (see, e.g., [Gade et al., 1998, Wismann et al., 1998]), which is assumed in Paper III. Further investigations of this should be carried out to validate the relationship between the damping ratio and relative thickness under various environmental conditions and for different oil types. Relative thickness can be extracted from infrared images (see, e.g., [Fingas and Brown, 2014, Fingas and Brown, 2011]). In the visual part of the EM spectrum, the oil thickness can be classified based on its visual appearance on water, known as the Bonn Agreement Oil Appearance Code [BAO, 2017]. One way of investigating the potential of damping ratio is to compare coincident SAR images and optical data (infrared, ultraviolet, and visual). This requires extensive planning since the various instruments need to overlap in time and space. CIRFA participates in the oil-on-water exercises conducted by NOFO almost annually, which is a unique opportunity to collect such a data set. In June 2019, CIRFA together with NOFO and other collaborators collected data from both SAR and various optical instruments. The data set could aid in verifying the potential of the damping ratio and also other parameters alike.

Machine learning are interesting and popular tools when working with SAR data. Several machine learning algorithms, such as support vector machines, naive Bayes, k-means, and Gaussian mixture models, have been investigated for oil slicks and sea ice classifications over the years. More recently, deep learning-based machine learning approaches have also received increased attention for oil slick and ice studies using SAR. Three important areas within the field of oil spill remote sensing are: (1) detection, (2) separating mineral oil from look-alikes, and (3) extracting physical properties from the oil. There exist many studies on detecting and classifying oil slicks from the surrounding clean sea and look-alikes using machine learning algorithms (see, e.g., [Salberg and Larsen, 2018, Guo et al., 2017, Skrunes et al., 2015, Zhang et al., 2017, Girard-Ardhuin et al., 2005, Tong et al., 2019]). Most studies are based on few SAR images acquired with the same sensor. SAR monitoring of oil slicks at sea is complex, since it depends on several factors such as weather conditions, sensors properties, oil types, and weathering processes. More work is needed on collecting a data set with confirmed oil spills using several sensors, imaging modes, incidence angles, and a wide range of wind conditions in order to fully test whether oil slick detection and characterization could benefit from deep learning or machine learning algorithms. Published studies have already demonstrated some potential using deep learning algorithms in separating look-alikes from mineral oil spills (see, e.g., [Guo et al., 2017]), but can deep learning algorithms be useful to separate low-wind areas from mineral oil slicks using any imaging mode and sensor? With the large number of satellites available and the high frequency of oil spills, it might be possible to obtain a data set suitable for designing a reliable system that could be used operationally. One unexplored territory is using deep learning to estimated physical properties from the SAR data, such as the oil fraction in the oil-sea mixture or oil thickness. Studies (see, e.g., [Boisot et al., 2019, Li et al., 2019, Minchew, 2012]) have estimated the volumetric oil fraction from physical models. Could deep learning methods be more accurate and a more robust tool for such estimation? Additionally, deep learning methods could also be used to find a threshold in SAR images (maybe from the damping ratio) to identify thick (actionable oil) versus thin oil. Using deep learning for these tasks require a good training set with known properties, which is often challenging to collect for oil slicks.

The temporal resolution of spaceborne satellites is poor. A time series of SAR images can be obtained by combining several satellites, but it is challenging to find spaceborne SAR images that cover the same area every hour throughout one day. Oil spill drift modelling could be a useful tool to predict the drift direction and velocity of oil spills. Several interesting studies combining SAR images and oil drift models can be conducted. How can information from SAR improve the oil models? For example, how can SAR images can be used to improve and verify the oil predictions and the oil-covered area from the models? It has been shown that including drifters in the model improved the oil spill prediction. Drifters are not always available on site. Oil slick masks derived from SAR data could be used to initialize the model simulations, which has already been done in some studies (see, e.g., [Jones et al., 2016, Röhrs et al., 2018]). Further work could involve integrating several SAR images with short time difference to improve the initialization of the model. Additionally, since oil slicks have internal variations with regards to thickness, it could be very interesting to integrate this information into oil spill drift models. At last, it has been demonstrated that ocean surface wind can be extracted from SAR. The spreading and drift of oil spills depend strongly on the wind conditions. An interesting study could involve incorporating the SAR wind into the model to improve the predictions.

Over the years, several polarimetric features have been used to describe the scattering properties of oil slicks. As demonstrated in Paper II, various noise sources significantly impact the scattering properties measured using polarimetry. Some studies have claimed that mineral oil slicks have non-Bragg scattering, but other studies using data from low noise sensors have shown that Bragg scattering is predominant within oil slicks. Paper II quantitatively showed that the non-Bragg scattering is system noise in disguise. Surface scattering is considered the main scattering type for ocean features. Bragg scattering is often used to describe the scattering processes for the ocean and oil slicks, but other scattering processes, in the surface scattering category, could be non-resonant surface scattering within oil slicks and clean sea given the wide range of ocean wave components. Hence, Bragg scattering is not necessarily the complete description of the scattering mechanisms occurring at sea, and a study investigating non-resonant Bragg should be carried out to find an appropriate and more complete model of the ocean and oil backscatter.

Analysis of scattering properties for sea ice has also been done to separate different sea ice types. A similar study to Paper II should be performed to investigate how system noise influences the scattering properties of various sea ice types using polarimetry. Since system noise varies from sensor to sensor and also within imaging modes, it is crucial to understand the impact of different system noise sources to compare be able to across several sensors and imaging modes.

Multi-frequency SAR might contain more physical information about oil slicks and its properties such as thickness than multi-polarization SAR. L-band waves penetrate deeper into the surface compared to X-band waves. Hence, thick oil might be visible in all frequencies, whereas thin oil is better detected with X- and C-band radars [Gade et al., 1998]. Some studies have demonstrated this (see, e.g., [Gade et al., 1998]), but additional studies are encouraged to investigate whether oil slick characterization could benefit from using multi-frequency SAR sensors. In the oil-on-water exercise this summer, CIRFA together with DLR collected simultaneously multi-frequency (X-, S-, and L-band) and FP data from the airborne F-SAR instrument. Current analysis of this data might provide some recommendations on the potential of multi-frequency SAR.

There is often a gap between the industry and academia. CIRFA, which is an SFI with both research and industry partners involved, aims to fill the gap between the two worlds by collaborating and delivering ideas and products that can help the industry. Many industries have a drive towards innovation and want to transfer knowledge from academia to their use cases. The industry often contributes to data collection, which is an important foundation for advances within research. There is a strong connection between CIRFA and the industry partners, but more work is needed to communicate and feed results back to the industry in a form that is understood and appreciated by the industry partners.

A

Separability Measures

Measures of class separability through distance metrics is a useful tool when analyzing various targets in SAR data. There exists several separability metrics that can be used to measure and express the similarities or dissimilarities between two (or more) classes. Separability metrics can be based on the mean and/or variance or probability distributions. Several polarimetric features can be derived from SAR data. Identifying the appropriate separability measure for evaluating the feature's performance in separating/detecting various surfaces will always be a challenge. If the separability measure is unbounded, a comparison across different features becomes difficult. Therefore, bounded separability measures are used in this thesis. The bounded separability measures used in the presented papers are the Jeffries-Matusita (JM) distance (Paper I), the two-sample Kolmogorov–Smirnov (KS) statistical coefficient (Paper IV), and the Spearman's correlation coefficient (Paper IV). These are therefore presented in the upcoming subsections.

A.1 The Jeffries-Matusita Distance

JM distance is often used as a separability criterion for the optimal feature selection and also when evaluating classification results (see, e.g., [Dabboor and Geldsetzer, 2014b, Wang et al., 2018, Wei et al., 2019, Dabboor et al., 2014, Song et al., 2017, Tong et al., 2019]). The JM distance is bounded between $[0, 2]$ and is based on the mean and variance of two classes [Richards and Jia, 2006].

The JM distance between two classes i and j for normally distributed data is defined as [Richards and Jia, 2006]:

$$JM_{ij} = 2(1 - e^{-d_{ij}}) \tag{A.1}$$

where d_{ij} is the Bhattacharyya distance defined as:

$$d_{ij} = \frac{1}{8}(\boldsymbol{m}_j - \boldsymbol{m}_i)^T \left[\frac{\Sigma_i + \Sigma_j}{2}\right]^{-1} + \frac{1}{2}\ln\frac{\left[\frac{\Sigma_i+\Sigma_j}{2}\right]}{\sqrt{|\Sigma_i\Sigma_j|}}, \tag{A.2}$$

where $\boldsymbol{m}_j$ and $\boldsymbol{m}_i$ are the mean values of the two samples, and Σ_j and Σ_i are the covariances (or the standard deviations for one-dimensional case) of the two classes [Richards and Jia, 2006]. This distance measure can only be used for normally distributed data.

All features derived from SAR data are to some extent influenced by the incidence angle. The same incidence angle range should therefore be used when comparing two classes. Figure A.1 illustrates this, where two regions of interests (ROIs) (oil and clean sea) cover the same incidence angle range. Figure A.2 shows the corresponding histograms and the high JM distance (from equation A.1) between the two classes. The one-dimensional case is used in Paper I for oil versus sea separation.

The JM distance with the Bhattacharyya distance as input assumes Gaussian distribution of the input data, which may not always be the case for features derived from SAR data.

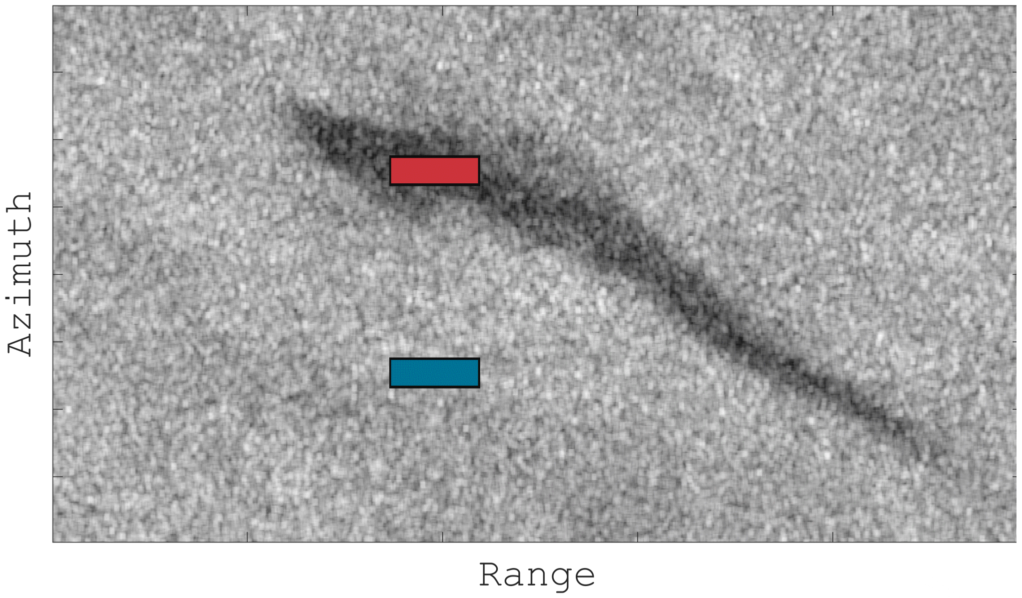

Figure A.1: The VV-intensity (in dB) and region of interests covering the oil slick (red box) and a clean sea area (blue box). Radarsat-2 data and Products © MDA LTD. 2015 - All Rights Reserved.

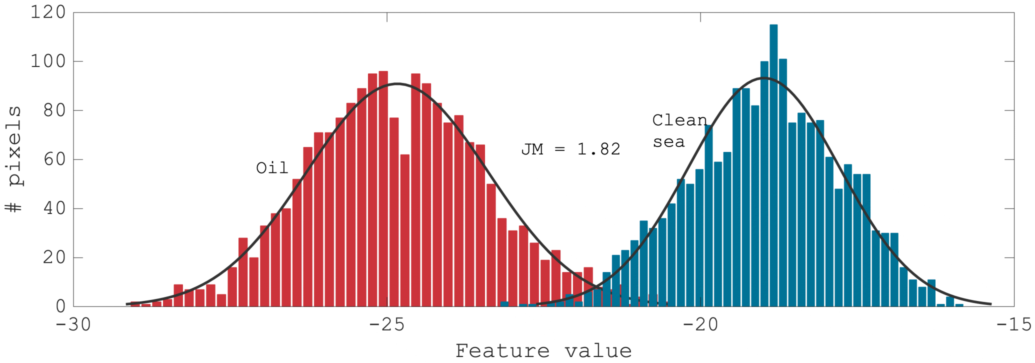

Figure A.2: Histograms of the VV-intensity (in dB) from pixels covering oil and clean sea (see Figure A.1). The Jeffries-Matusita distance between the two classes are also displayed in the plot.

A.2 Two-sample Kolmogorov–Smirnov Test

The two-sample KS test determines whether or not there is a statistically significant difference between two classes. The KS test is a non-parametric or distribution-free test [Massey, 1951], where the null hypothesis is that two classes are drawn from the same population distribution. The KS test outputs the KS statistic, which is used as a separability measure. The KS test is most sensitive around the median value and less sensitive at the extremes of the sample cumulative distribution functions (CDF) [Casey et al., 2016]. The KS test is therefore useful for identifying shifts in the probability distribution functions between two classes [Press et al., 2007].

The sample CDF is estimated from the probability density function, and since we are dealing with discrete random variables the sample cumulative distribution functions ($F_X(x)$) are estimated with a sum, i.e., [Stark and Woods, 2011]

$$F_X(x) = P(X \leq x) = \sum_{x_i \leq x} P(X = x_i) = \sum_{x_i \leq x} f(x_i), \tag{A.3}$$

where $P(X \leq x)$ represents the probability that the random variable X has a value less than or equal to x, and $f(x_i)$ is the probability density function (pdf). The two-sample KS test inputs two sample CDFs and test whenever their statistical distribution are the same (the null hypothesis is accepted), and is based on the maximum distance between the two sample CDFs ($F_{X_1}(x)$ and $F_{X_2}(x)$) [Press et al., 2007], i.e.,:

$$KS = \max\left(F_{X_1}(x) - F_{X_2}(x)\right) . \tag{A.4}$$

The KS statistic is only used in Paper IV, and the top panel of Figure A.3 shows the VV-intensity image from Radarsat-2 with two regions of interest of grease/frazil ice and first year ice (see Paper IV for more detailed descriptions of these sea ice types). The bottom panel of Figure A.3 shows their corresponding histograms, the CDFs, and the KS statistics between the two CDFs. The KS statistics, bounded between $[0, 1]$, are used to estimate the p-value. The p-value is the evidence against a null hypothesis. If the p-value is less than the significance level (for example 5%), then the null hypothesis is rejected. If the KS statistics is close to 1, then the two samples are considered different (their underlying distributions are different), whereas a value close to 0 indicates equal distribution and acceptance of the null hypothesis.

The two-sample KS takes the sample CDFs as input, whereas the JM distance uses the mean and variance of two classes as input. These measures are based on the similarity between two classes based on their statistical properties. However, to investigate the correlation and the degree of association between two classes, the Spearman and Pearson correlation coefficients are useful. The Spearman correlation coefficient (used in Paper IV) is discussed in the upcoming section.

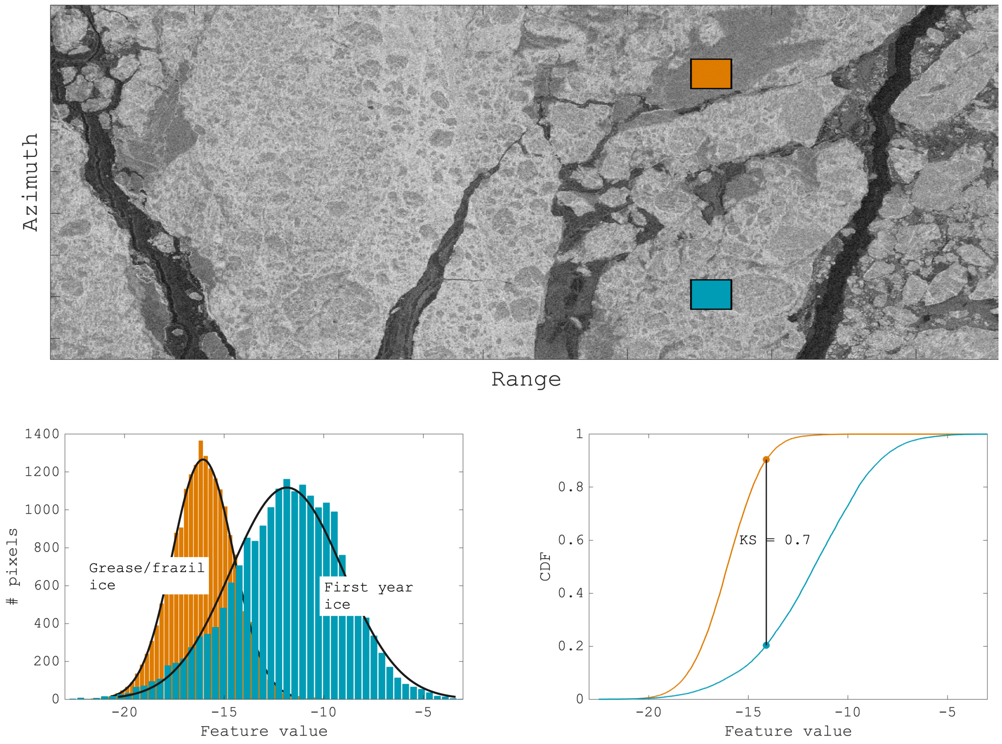

Figure A.3: Top: The VV-intensity (in dB) and region of interests covering grease/frazil ice (red box) and a first year ice (orange box). Radarsat-2 data and Products © MDA LTD. 2015 - All Rights Reserved. Bottom: Histograms (left panel) and CDF (right panel) of the VV-intensity (in dB) from pixels covering grease/frazil ice and first year ice. The two-sample KS statistic between the two classes is displayed in the right panel.

A.3 The Spearman Correlation Coefficient

The Spearman correlation coefficient considers the degree of association between two variables (X and Y) of the same size, and the parametric equivalent is the Pearson product-moment correlation [Corder and Foreman, 2009]. The Spearman correlation coefficient is defined as [Corder and Foreman, 2009]:

$$\rho_S = 1 - \frac{6\sum_i^N d_R^2}{n(n^2-1)} \tag{A.5}$$

where d_R is the difference between ranked pairs (rg(X)-rg(Y)) and n is number of data points [Corder and Foreman, 2009]. A vector is constructed by sorting the values in ascending order, and the rank corresponds to the value's position in the vector. If any values in the vector are tied then the rank is based on their average rank, named tied rank. For example, if $X = [1, 3, 4, 1, 3]$, then the ranked vector is $[1, 3, 5, 2, 4]$, and the tied rank vector is $rg(X) = [1.5, 3.5, 5, 1.5, 3.5]$.

If the Spearman correlation coefficient is close to 1 or -1 then the two variables have a nearly perfect positive or negative relationship, whereas a correlation close to 0 indicates a week or trivial relationship [Corder and Foreman, 2009]. The benefit of using Spearman's instead of Pearson's correlation coefficient is that the Spearman correlation coefficient is less sensitive to outliers. Figure A.4 shows an example of two scatter plots of the regions displayed in Figure A.3, where the Spearman correlation coefficients are calculated between two features (VV-intensity and the copolarization ratio (HH/VV)). The left panel shows a strong correlation, whereas the right panel shows none/trivial relationship between the two features [Corder and Foreman, 2009].

The Spearman correlation coefficient [Spearman, 1904] (also known as the Spearman rank correlation) is used in Paper IV to evaluate the correlation between features derived from Radarsat-2 and RISAT-1 overlaps.

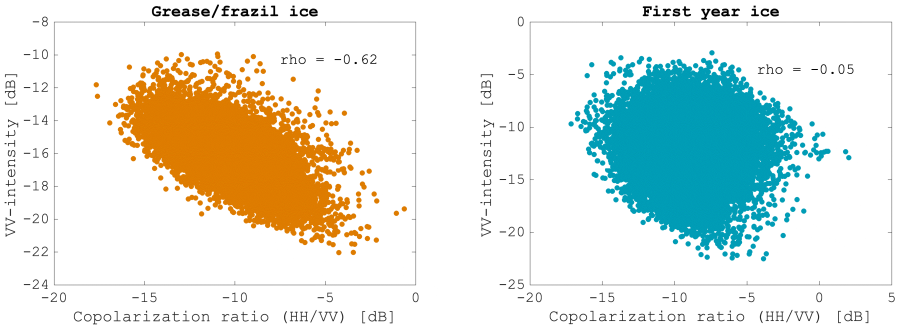

Figure A.4: Scatter plots of two sea ice regions (Grease/frazil ice and first year ice) shown in Figure A.3 with their corresponding Spearman correlation coefficients between two features (VV-intensity and the copolarization ratio).

Bibliography

[BAO, 2017] (2017). Bonn Agreement Oil Appearance Code. Bonn Agreement Aerial Operations Handbook, version 2017. (`www.bonnagreement.org/publications`, last accessed 1 September 2019).

[Ainsworth et al., 2006] Ainsworth, T. L., Ferro-Famil, L., and Lee, J.-S. (2006). Orientation angle preserving a posteriori polarimetric SAR calibration. *IEEE Trans. Geosci. Remote Sens.*, 44(4):994–1003.

[Alpers et al., 2017] Alpers, W., Holt, B., and Zeng, K. (2017). Oil spill detection by imaging radars: Challenges and pitfalls. *Remote Sens. Environ.*, 201:133–147.

[Alpers and Hühnerfuss, 1989] Alpers, W. and Hühnerfuss, H. (1989). The damping of ocean waves by surface films: A new look at an old problem. *J. Geophys. Res.*, 94(C5):6251–6265.

[Androulidakis et al., 2018] Androulidakis, Y., Kourafalou, V., Özgökmen, T., Garcia-Pineda, O., Lund, B., Hénaff, M. L., Hu, C., Haus, B. K., Novelli, G., Guigand, C., Kang, H., Hole, L., and Horstmann, J. (2018). Influence of River-Induced Fronts on Hydrocarbon Transport: A Multiplatform Observational Study. *J. Geophys. Res. Oceans*, 123(5):3259–3285.

[Angelliaume et al., 2018] Angelliaume, S., Dubois-Fernandez, P. C., Jones, C. E., Holt, B., Minchew, B., Amri, E., and Miegebielle, V. (2018). SAR imagery for detecting sea surface slicks: Performance assessment of polarization-dependent parameters. *IEEE Trans. Geosci. Remote Sens.*, 56(8):1–21.

[Asl et al., 2016] Asl, S. D., Amos, J., Woods, P., Garcia-Pineda, O., and MacDonald, I. R. (2016). Chronic, anthropogenic hydrocarbon discharges in the gulf of mexico. *Deep Sea Research Part II: Topical Studies in Oceanography*, 129:187 – 195. The Gulf of Mexico Ecosystem - before, during and after the Macondo Blowout.

[Atteia and Collins, 2013] Atteia, G. and Collins, M. J. (2013). On the use of Compact Polarimetry SAR for Ship Detection. *ISPRS Journal of Photogrammetry and Remote Sensing*, 80:1–9.

[Boisot et al., 2019] Boisot, O., Angelliaume, S., and Guérin, C. (2019). Marine Oil Slicks Quantification From L-band Dual-Polarization SAR Imagery. *IEEE Trans. Geosci. Remote Sens.*, 57(4):2187–2197.

[Brekke et al., 2014] Brekke, C., Holt, B., Jones, C. E., and Skrunes, S. (2014). Discrimination of oil spills from newly formed sea ice by synthetic aperture radar. *Remote Sens. Environ.*, 145:1–14.

[Brekke et al., 2017] Brekke, C., Skrunes, S., and Espeseth, M. M. (2017). Oil spill dispersion in full-polarimetric and hybrid-polarity SAR. In *IEEE Int. Geosci. Remote Sens. Symp. (IGARSS) Proceedings*, pages 1020–1023.

[Brekke and Solberg, 2005] Brekke, C. and Solberg, A. H. S. (2005). Oil Spill Detection by Satellite Remote Sensing. *Remote Sens. Environ.*, 95(1):1–13.

[Buono et al., 2019] Buono, A., Nunziata, F., de Macedo, C. R., Velotto, D., and Migliaccio, M. (2019). A Sensitivity Analysis of the Standard Deviation of the Copolarized Phase Difference for Sea Oil Slick Observation. *IEEE Trans. Geosci. Remote Sens.*, 57(4):2022–2030.

[Buono et al., 2016a] Buono, A., Nunziata, F., and Migliaccio, M. (2016a). Analysis of Full and Compact Polarimetric SAR Features Over the Sea Surface. *IEEE Geosci. Remote Sens. Lett.*, 13(10):1527–1531.

[Buono et al., 2016b] Buono, A., Nunziata, F., Migliaccio, M., and Li, X. (2016b). Polarimetric analysis of compact-polarimetry SAR architectures for sea oil slick observation. *IEEE Trans. Geosci. Remote Sens.*, 54(10):5862–5874.

[Canadian Space Agency, nd] Canadian Space Agency (n.d.). `http://www.asc-csa.gc.ca/eng/satellites/radarsat2/Default.asp` (last accessed 1 April 2019).

[Casey et al., 2016] Casey, J. A., Howell, S. E., Tivy, A., and Haas, C. (2016). Separability of sea ice types from wide swath C- and L-band synthetic aperture radar imagery acquired during the melt season. *Remote Sens. Environ.*, 174:314 – 328.

[Chuvieco and Huete, 2010] Chuvieco, E. and Huete, A. (2010). *Fundamentals of Satellite Remote Sensing*. CRC Press Taylor and Francis Group.

[Clemente-Colón and Yan, 2000] Clemente-Colón, P. and Yan, X.-H. (2000). Low-Backscatter Ocean Features in Synthetic Aperture Radar Imagery. *JOHNS HOPKINS APL TECHNICAL DIGEST*, 21(1):112–123.

[Cloude, 2010] Cloude, S. R. (2010). *Polarisation Applications in Remote Sensing. First edition*. Oxford University Press Inc., New York, pp. 125-129.

[Cloude et al., 2012] Cloude, S. R., Goodenough, D., and Chen, H. (2012). Compact Decomposition Theory. *IEEE Trans. Geosci. Remote Sens.*, 9(1):28–32.

[Coleman, 2003] Coleman, J. (2003). *Oil in the Sea III*. National Academy Press, Washington DC, USA.

[Collins et al., 2013] Collins, M. J., Denbina, M., and Atteia, G. (2013). On the Reconstruction of Quad-Pol SAR Data From Compact Polarimetry Data For Ocean Target Detection. *IEEE Trans. Geosci. Remote Sens.*, 51(1):591–600.

[Corder and Foreman, 2009] Corder, G. W. and Foreman, D. I. (2009). *Nonparametric Statistics for Non-Statisticians: A Step-by-Step Approach*. John Wiley & Sons.

[Cumming and Wong, 2005] Cumming, I. G. and Wong, F. H. (2005). *Digital Processing of Synthetic Aperture Radar data*. Artech House.

[Curlander and McDonough, 1991] Curlander, J. C. and McDonough, R. N. (1991). *Synthetic Aperture Radar, Systems & Signal Processing*. John Wiley & Sons, INC., Wiley Series in Remote Sensing.

[Dabboor and Geldsetzer, 2014a] Dabboor, M. and Geldsetzer, T. (2014a). On the Classification of Sea Ice Types using Simulated Radarsat Constellation Mission (RCM) Compact Polarimetric SAR Parameters. *ASPRS 2014 Annual Conference, Louisville, Kentucky*.

[Dabboor and Geldsetzer, 2014b] Dabboor, M. and Geldsetzer, T. (2014b). Towards sea ice classification using simulated RADARSAT Constellation Mission compact polarimetric SAR imagery. *Remote Sens. Environ.*, 140:189–195.

[Dabboor et al., 2014] Dabboor, M., Howell, S., Shokr, M., and Yackel, J. (2014). The Jeffries-Matusita distance for the case of complex Wishart distribution as a separability criterion for fully polarimetric SAR data. *Int. J. Remote Sens.*, 35(19):6859–6873.

[Denbina, 2014] Denbina, M. (2014). Iceberg Detection Using Polarimetric Synthetic Aperture Radar. *P.h.D. Dissertation, University of Calgary*.

[Dierking and Busche, 2006] Dierking, W. and Busche, T. (2006). Sea ice monitoring by L-band SAR: an assessment based on literature and comparisons of JERS-1 and ERS-1 imagery. *IEEE Trans. Geosci. Remote Sens.*, 44(4):957–970.

[Dierking et al., 2003] Dierking, W., Skriver, H., and Gudmandsen, P. (2003). SAR polarimetry for sea ice classification. *Proceedings of the Workshop on POLinSAR - Applications of SAR Polarimetry and Polarimetric Interferometry (ESA SP-529). 14-16 January 2003, Frascati, Italy*.

[Elachi and van Zyl, 2006] Elachi, C. and van Zyl, J. (2006). *Introduction to the Physics and Techniques of Remote Sensing*. John Wiley and Sons, Inc., Publication, second edition.

[Eriksson et al., 2010] Eriksson, L. E. B., Borenäs, K., Dierking, W., Berg, A., Santoro, M., Pemberton, P., Lindh, H., and Karlson, B. (2010). Evaluation of new spaceborne SAR sensors for sea-ice monitoring in the Baltic Sea. *Can. J. Remote Sens.*, 36(1):56–73.

[Espeseth et al., 2016] Espeseth, M. M., Brekke, C., and Anfinsen, S. N. (2016). Hybrid-polarity and reconstruction methods for sea ice with L- and C-band SAR. *IEEE Geosci. Remote Sens. Lett.*, 13(3):467–471.

[Espeseth et al., 2017] Espeseth, M. M., Skrunes, S., Jones, C. E., Brekke, C., Holt, B., and Doulgeris, A. P. (2017). Analysis of evolving oil spills in full-polarimetric and hybrid-polarity SAR. *IEEE Trans. Geosci. Remote Sens.*, 55(7):4190–4210.

[Ferraro et al., 2010] Ferraro, G., Baschek, B., de Montpellier, G., Njoten, O., Perkovic, M., and Vespe, M. (2010). On the SAR derived alert in the detection of oil spills according to the analysis of the EGEMP. *Mar. Pollut. Bull.*, 60(1):91 – 102.

[Fingas, 2011] Fingas, M. (2011). Introduction to oil chemistry and properties. *Oil Spill Science and Technology*.

[Fingas and Brown, 2014] Fingas, M. and Brown, C. (2014). Review of oil spill remote sensing. *Mar. Pollut. Bull.*, 83(1):9 – 23.

[Fingas and Brown, 2011] Fingas, M. and Brown, C. E. (2011). Chapter 6 - oil spill remote sensing: A review. In Fingas, M., editor, *Oil Spill Science and Technology*, pages 111 – 169. Gulf Professional Publishing, Boston.

[Fingas and Brown, 1997] Fingas, M. F. and Brown, C. E. (1997). Review of oil spill remote sensing. *Spill Science & Technology Bulletin*, 4(4):199 – 208. The Second International Symposium on Oil Spills.

[Fore et al., 2015] Fore, A. G., Chapman, B. D., Hawkins, B. P., Hensley, S., Jones, C. E., Michel, T. R., and Muellerschoen, R. J. (2015). UAVSAR Polarimetric Calibration. *IEEE Trans. Geosci. Remote Sens.*, 53(6):3481–3491.

[Freeman et al., 1992] Freeman, A., van Zyl, J. J., Klein, J. D., Zebker, H. A., and Shen, Y. (1992). Calibration of Stokes and scattering matrix format polarimetric SAR data. *IEEE Trans. Geosci. Remote Sens.*, 30(3):531–539.

[Fritz and Eineder, 2010] Fritz, T. and Eineder, M. (2010). TerraSAR-X ground segment basic product specification document.

[Gade et al., 1998] Gade, M., Alpers, W., Hühnerfuss, H., Masuko, H., and Kobayashi, T. (1998). Imaging of biogenic and anthropogenic ocean surface films by the multifrequency/multipolarization SIR-C/X-SAR. *J. Geophys. Res.*, 103(C9):18851–18866.

[Geldsetzer et al., 2015] Geldsetzer, T., Arkett, M., Zagon, T., Charbonneau, F., Yackel, J. J., and Scharien, T. K. (2015). All-season compact-polarimetry C-band SAR observations of sea ice. *Can. J. Remote Sens.*, 41(5):485–504.

[Gill et al., 2015] Gill, J. P. S., Geldsetzer, T., and Fuller, M. C. (2015). Sensitivity of C-band synthetic aperture radar polarimetric parameters to snow thickness over landfast smooth first-year sea ice. *Remote Sens. Environ.*, 166:34 – 49.

[Girard-Ardhuin et al., 2005] Girard-Ardhuin, F., Mercier, G., Collard, F., and Garello, R. (2005). Operational oil-slick characterization by SAR imagery and synergistic data. *IEEE J. Ocean. Eng.*, 30(3):487–495.

[Guo et al., 2017] Guo, H., Wu, D., and An, J. (2017). Discrimination of Oil Slicks and Lookalikes in Polarimetric SAR Images Using CNN. *Sensors*, 17(8).

[Hajnsek et al., 2009] Hajnsek, I., Jagdhuber, T., Schon, H., and Papathanassiou, K. P. (2009). Potential of Estimating Soil Moisture Under Vegetation Cover by Means of PolSAR. *IEEE Trans. Geosci. Remote Sens.*, 47(2):442–454.

[Hajnsek et al., 2003] Hajnsek, I., Pottier, E., and Cloude, S. R. (2003). Inversion of surface parameters from polarimetric SAR. *IEEE Trans. Geosci. Remote Sens.*, 41(4):727–744.

[Hensley et al., 2014] Hensley, S., Oveisgharan, S., Saatchi, S., Simard, M., Ahmed, R., and Haddad, Z. (2014). An error model for biomass estimates derived from polarimetric radar backscatter. *IEEE Trans. Geosci. Remote Sens.*, 52(7):4065–4082.

[Herbst et al., 2016] Herbst, L., DeCola, E., and Kennedy, K. (2016). New pathways for developing and testing oil spill response equipment in real world conditions. *OCEANS 2016 MTS/IEEE Monterey*, pages 1–6.

[Hollinger and Mennella, 1973] Hollinger, J. P. and Mennella, R. A. (1973). Oil spills: Measurements of their distributions and volumes by multifrequency microwave radiometry. *Science*, 181(4094):54–56.

[Holt, 2004] Holt, B. (2004). Chapter 2: SAR imaging of the ocean surface. *Synthetic Aperture Radar Marine User's Manual (NOAA/NESDIS), C.R. Jackson and J. R. Apel*, (25-80).

[Hühnerfuss, 2006] Hühnerfuss, H. (2006). Basic physicochemical principles of monomolecular sea slicks and crude oil spills. *Gade M., Hühnerfuss H., Korenowski*

G.M. (eds) Marine Surface Films. Springer, Berlin, Heidelberg, pages 21–35.

[Huynen, 1970] Huynen, J. R. (1970). Phenomenological theory of radar targets. *Ph.D. dissertation, Rotterdam: Drukkerij Bronder-Offset N.V.,*.

[Iodice et al., 2011] Iodice, A., Natale, A., and Riccio, D. (2011). Retrieval of soil surface parameters via a polarimetric two-scale model. *IEEE Trans. Geosci. Remote Sens.*, 49(7):2531–2547.

[ITOPF, 2002] ITOPF (2002). Fate of marine oil spills. *The International Tanker Owners Pollution Federation Limited, Technical report*.

[Jenkins and Jacobs, 1997] Jenkins, A. D. and Jacobs, S. J. (1997). Wave damping by a thin layer of viscous fluid. *Physics of Fluids*, 9(5):1256–1264.

[Jensen, 2000] Jensen, J. R. (2000). *Remote Sensing of the Environment, An Earth Resource Perspective*. Pearson, Prentice Hall.

[Johansson et al., 2017] Johansson, A. M., King, J. A., Doulgeris, A. P., Gerland, S., Singha, S., Spreen, G., and Busche, T. (2017). Combined observations of Arctic sea ice with near-coincident colocated X-band, C-band, and L-band SAR satellite remote sensing and helicopter-borne measurements. *J. Geophys. Res. Oceans*, 122(1):669–691.

[Jones et al., 2016] Jones, C. E., Dagestad, K.-F., Breivik, Ø., Holt, B., Röhrs, J., Christensen, K. H., Espeseth, M., Brekke, C., and Skrunes, S. (2016). Measurement and Modeling of Oil Slick Transport. *J. Geophys. Res.: Oceans*, 121(10):7759–7775.

[Jones et al., 2018] Jones, C. E., Espeseth, M. M., Holt, B., and Brekke, C. (2018). Measurement of oil slick transport and evolution in the gulf of mexico using L-band Synthetic Aperture Radar. *12th European Conference on Synthetic Aperture Radar (EUSAR)*.

[Jones and Holt, 2018] Jones, C. E. and Holt, B. (2018). Experimental L-band airborne SAR for oil spill response at sea and in coastal waters. *Sensors*, 18(2).

[Kennaugh, 1952] Kennaugh, E. M. (1952). Effects of type of polarization on echo characteristics. *The Ohio State University, Antennas Laboratory, Columbus, OH, Reports 381-1 to 394-24, 1949-1954 and Report 389-12 (M.Sc.thesis)*.

[Lee and Pottier, 2009] Lee, J.-S. and Pottier, E. (2009). *Polarimetric Radar Imaging: from basic to applications*. Optical Science and Engineering. CRC Press Taylor and Francis Group.

[Lee et al., 2000] Lee, J.-S., Schuler, D. L., and Ainsworth, T. L. (2000). Polarimetric SAR Data Compensation for Terrain Azimuth Slope Variation. *IEEE Trans. Geosci. Remote*

Sens., 38(5):2153–2163.

[Li and Perrie, 2016] Li, H. and Perrie, W. (2016). Sea Ice Characterization and Classification Using Hybrid Polarimetry SAR. *IEEE J. Sel. Topics Appl. Earth Observ. Remote Sens.*, 9(11):4998–5010.

[Li et al., 2019] Li, H., Perrie, W., and Wu, J. (2019). Retrieval of oil–water mixture ratio at ocean surface using compact polarimetry Synthetic Aperture Radar. *Remote Sens.*, 11(7).

[Li et al., 2016] Li, H., Perrie, W., Zhou, Y., and He, Y. (2016). Oil spill detection on the ocean surface using hybrid polarimetric SAR imagery. *Science China*, 59(2):249–257.

[Massey, 1951] Massey, J. F. J. (1951). The kolmogorov-smirnov test for goodness of fit. *Taylor & Francis, Ltd. on behalf of the Journal of the American Statistical Association*, 46(253):68–78.

[MDA, 2018] MDA (2018). Radarsat-2 product description. *MacDonald, Dettwiler and Associates Ltd., Rickmond, BC, USA, RN-SP-52-1238,Issue 1/14.*

[Migliaccio et al., 2009a] Migliaccio, M., Gambardella, A., Nunziata, F., Shimada, M., and Isoguchi, O. (2009a). The PALSAR polarimetric mode for sea oil slick observation. *IEEE Trans. Geosci. Remote Sens.*, 47(12):4032 – 4041.

[Migliaccio et al., 2009b] Migliaccio, M., Nunziata, F., and Gambardella, A. (2009b). On the co-polarized phase difference for oil spill observation. *Int. J. Remote Sens.*, 30(6):1589–1602.

[Migliaccio et al., 2005] Migliaccio, M., Tranfaglia, M., and Ermakov, S. A. (2005). A Physical Approach for the Observation of Oil Spills in SAR images. *IEEE J. Ocean. Eng.*, 30(3):496–507.

[Minchew, 2012] Minchew, B. (2012). Determining the mixing of oil and sea water using polarimetric synthetic aperture radar. *Geophys. Res. Lett.*, 39(16).

[Minchew et al., 2012] Minchew, B., Jones, C. E., and Holt, B. (2012). Polarimetric Analysis of Backscatter From the Deepwater Horizon Oil Spill Using L-Band Synthetic Aperture Radar. *IEEE Trans. Geosci. Remote Sens.*, 50(10):3812–3830.

[Misra et al., 2013] Misra, T., Rana, S. S., Desai, N. M., Dave, D. B., Rajeevjyoti, Arora, R. K., Rao, C. V. N., Bakori, B. V., Neelakantan, R., and Vachchani, J. G. (2013). Synthetic Aperture Radar payload on-board RISAT-1: configuration, technology and performance. *Current science*, 104(4).

[Moen et al., 2015] Moen, M.-A. N., Anfinsen, S. N., Doulgeris, A. P., Renner, A. H. H., and Gerland, S. (2015). Assessing polarimetric SAR sea-ice classifications using consecutive day images. *Annals of Glaciology*, 56(69):285–294.

[NOAA, nd] NOAA (n.d.). National Oceanic and Atmospheric Administration (NOAA): What is an oil seep? (`https://oceanservice.noaa.gov/facts/oilseep.html`, last accessed 4 September 2019).

[NOFO, nd] NOFO (n.d.). The Norwegian Clean Seas Association for Operating Companies (`https://www.nofo.no`, last accessed 18 June 2019).

[Nunziata et al., 2019] Nunziata, F., de Macedo, C. R., Buono, A., Velotto, D., and Migliaccio, M. (2019). On the analysis of a time series of X–band TerraSAR–X SAR imagery over oil seepages. *Int. J. Remote Sens.*, 40(9):3623–3646.

[Nunziata et al., 2013] Nunziata, F., Gambardella, A., and Migliaccio, M. (2013). On the degree of polarization for SAR sea oil slick observation. *ISPRS Journal of Photogrammetry and Remote Sensing*, 78:41 – 49.

[Nunziata et al., 2015] Nunziata, F., Migliaccio, M., and Li, X. (2015). Sea Oil Slick Observaion Using Hybrid-Polarity SAR Architecture. *IEEE J. Ocean. Eng.*, 40(2):426–440.

[Onstott and Shuchman, 2004] Onstott, R. G. and Shuchman, R. A. (2004). Chapter 3. SAR Measurements of Sea Ice. *Synthetic Aperture Radar Marine User's Manual (NOAA/NESDIS), C.R. Jackson and J. R. Apel*, `http://www.SARusersmanual.com/`, last accessed 24 May 2019.

[Panigraphi and Mishra, 2012] Panigraphi, R. and Mishra, A. (2012). Comparison of hybrid-pol with quad-pol scheme based on polarimetric information content. *International Journal of Remote Sensing*, 33(11):3531–3541.

[Pinel et al., 2014] Pinel, N., Bourlier, C., and Sergievskaya, I. (2014). Two-dimensional radar backscattering modeling of oil slicks at sea based on the model of local balance: Validation of two asymptotic techniques for thick films. *IEEE Trans. Geosci. Remote Sens.*, 52(5):2326–2338.

[Press et al., 2007] Press, W. H., Teukolsky, S. A., Vetterling, W. T., and Flannery, B. P. (2007). *Numerical recipes : the art of scientific computing*. Cambridge University Press, New York, NY, USA.

[Quegan, 1994] Quegan, S. (1994). A unified algorithm for phase and cross-talk calibration of polarimetric data-theory and observations. *IEEE Trans. Geosci. Remote Sens.*, 32(1):89–99.

[Raney et al., 2012] Raney, K., Cahill, J. T. S., Patterson, G. W., and Bussey, D. B. J. (2012). The m-chi Decomposition of Hybrid Dual-Polarimetric Radar Data with Application to Lunar Craters. *J. Geophys. Res. Planets*, 117(E12).

[Raney, 2007] Raney, R. K. (2007). Hybrid-Polarity SAR Architecture. *IEEE Trans. Geosci. Remote Sens.*, 45(11):3397–3404.

[Richards and Jia, 2006] Richards, J. A. and Jia, X. (2006). *Remote Sensing Digital Image Analysis. An Introduction. Fourth Edition*. Springer-Verlag Berlin Heidelberg.

[Röhrs et al., 2018] Röhrs, J., Dagestad, K.-F., Asbjørnsen, H., Nordam, T., Skancke, J., Jones, C. E., and Brekke, C. (2018). The effect of vertical mixing on the horizontal drift of oil spills. *Ocean Science*, 14(6):1581–1601.

[Sabry and Vachon, 2014] Sabry, R. and Vachon, P. W. (2014). A Unified Framework for general Compact and Quad Polarimetric SAR Data and Imagery Analysis. *IEEE Trans. Geosci. Remote Sens.*, 52(1):582–602.

[Salberg and Larsen, 2018] Salberg, A. and Larsen, S. O. (2018). Classification of ocean surface slicks in simulated hybrid-polarimetric SAR data. *IEEE Trans. Geosci. Remote Sens.*, 56(12):7062–7073.

[Salberg et al., 2014] Salberg, A.-B., Rudjord, O., and Solberg, A. H. S. (2014). Oil spill detection in hybrid-polarimetric SAR images. *IEEE Trans. Geosci. Remote Sens.*, 52(10):6521–6533.

[Schwartzberg, 1971] Schwartzberg, H. G. (1971). The movement of oil spills. *International Oil Spill Conference Proceedings*, 1971(1):489–494.

[Sergievskaya et al., 2019] Sergievskaya, I., Ermakov, S., Lazareva, T., and Guo, J. (2019). Damping of surface waves due to crude oil/oil emulsion films on water. *Mar. Pollut. Bull.*, 146:206 – 214.

[Shirvany et al., 2012] Shirvany, R., Chabert, M., and Tourneret, J.-Y. (2012). Ship and Oil-Spill Detection using the Degree of Polarization in Linear and Hybrid/Compact Dual-Pol SAR. *IEEE J. Sel. Topics Appl. Earth Observ. Remote Sens.*, 5(3).

[Shokr and Sinha, 1985] Shokr, M. and Sinha, N. (1985). *Methods of Satellite Oceanography*. University of California.

[Singh et al., 1986] Singh, K. P., Gray, A. L., Hawkins, R. K., and O'Neil, R. A. (1986). The Influence of Surface Oil on C-and Ku-Band Ocean Backscatter. *IEEE Trans. Geosci. Remote Sens.*, GE-24(5):738 – 744.

[Singha et al., 2013] Singha, S., Bellerby, T. J., and Trieschmann, O. (2013). Satellite oil spill detection using artificial neural networks. *IEEE J. Sel. Topics Appl. Earth Observ. Remote Sens.*, 6(6):2355–2363.

[Singha et al., 2018] Singha, S., Johansson, M., Hughes, N., Hvidegaard, S. M., and Skourup, H. (2018). Arctic sea ice characterization using spaceborne fully polarimetric L-, C-, and X-band SAR with validation by airborne measurements. *IEEE Trans. Geosci. Remote Sens.*, 56(7):3715–3734.

[Singha et al., 2016] Singha, S., Ressel, R., Velotto, D., and Lehner, S. (2016). A combination of traditional and polarimetric features for oil spill detection using TerraSAR-X. *IEEE J. Sel. Topics Appl. Earth Observ. Remote Sens.*, 9(11):4979–4990.

[Skrunes, 2014] Skrunes, S. (2014). Characterization of Low Backscatter Regions in the Marine Environment by Multipolarization C- and X-band Synthetic Aperture Radar Data. *PhD thesis, Faculty of Science and Technology, Department of Physics and Technology, UiT The Arctic University of Norway*.

[Skrunes et al., 2014] Skrunes, S., Brekke, C., and Eltoft, T. (2014). Characterization of Marine Surface Slicks by Radarsat-2 Multipolarization Features. *IEEE Trans. Geosci. Remote Sens.*, 52(9):5302–5319.

[Skrunes et al., 2015] Skrunes, S., Brekke, C., Eltoft, T., and Kudryavtsev, V. (2015). Comparing near-coincident C- and X-band SAR acquisitions of marine oil spill. *IEEE Trans. Geosci. Remote Sens.*, 53(4):1958 – 1975.

[Skrunes et al., 2017] Skrunes, S., Brekke, C., and Espeseth, M. M. (2017). Assessment of the RISAT-1 FRS-2 mode for oil spill observation. *IEEE Int. Geosci. Remote Sens. Symp. (IGARSS) Proceedings*, pages 1024–1027.

[Skrunes et al., 2018] Skrunes, S., Brekke, C., Jones, C. E., Espeseth, M. M., and Holt, B. (2018). Effect of wind direction and incidence angle on polarimetric SAR observations of slicked and unslicked sea surfaces. *Remote Sens. Environ.*, 213:73 – 91.

[Skrunes et al., 2016] Skrunes, S., Jones, C. E., Brekke, C., Holt, B., and Espeseth, M. M. (2016). On the Effect of Imaging Geometry on Multipolarization SAR Features for Oil Spill Observation. *Living Planet Symposium*.

[Solberg et al., 2004] Solberg, A. H. S., Brekke, C., Solberg, R., and Husoy, P. O. (2004). Algorithms for oil spill detection in Radarsat and ENVISAT SAR images. *IEEE Int. Geosci. Remote Sens. Symp. (IGARSS) Proceedings*, 7.

[Song et al., 2017] Song, D., Ding, Y., Li, X., Zhang, B., and Xu, M. (2017). Ocean Oil Spill Classification with RADARSAT-2 SAR Based on an Optimized Wavelet Neural Network.

Remote Sens., 9(8).

[Souyris et al., 2005] Souyris, J.-C., Imboa, P., Fjørtoft, R., Mingot, S., and Lee, J.-S. (2005). Compact Polarimetry Based on Symmetry Properties of Geophysical Media: The $\pi/4$ Mode. *IEEE Trans. Geosci. Remote Sens.*, 43(3):634–646.

[Spearman, 1904] Spearman, C. (1904). The proof and measurement of association between two things. *The American Journal of Psychology*, 100(3/4):441–471.

[Spreen and Kern, 2016] Spreen, G. and Kern, S. (2016). *Front Matter. Chapter 9: Methods of satellite remote sensing of sea ice*, pages 239–260. John Wiley & Sons, Ltd.

[Stark and Woods, 2011] Stark, H. and Woods, J. (2011). *Probability, Statistics, and Random Processes for Engineers (4th Edition)*. Pearson.

[Sun et al., 2018] Sun, S., Hu, C., Garcia-Pineda, O., Kourafalou, V., Hénaff, M. L., and Androulidakis, Y. (2018). Remote sensing assessment of oil spills near a damaged platform in the Gulf of Mexico. *Mar. Pollut. Bull.*, 136:141 – 151.

[Theodoridis and Koutroumbas, 2009] Theodoridis, S. and Koutroumbas, K. (2009). *Pattern Recognition Fourth Edition*. Elsevier.

[Tong et al., 2019] Tong, S., Liu, X., Chen, Q., Zhang, Z., and Xie, G. (2019). Multi-feature based ocean oil spill detection for polarimetric SAR data using random forest and the self-similarity parameter. *Remote Sens.*, 11(4).

[Touzi and Charbonneau, 2014] Touzi, R. and Charbonneau, F. (2014). Requirements on the calibration of Hybrid-Compact SAR. *IEEE Int. Geosci. Remote Sens. Symp. (IGARSS) Proceedings*, pages 1109–1112.

[Touzi et al., 2010] Touzi, R., Vachon, P. W., and Wolfe, J. (2010). Requirement on Antenna Cross-Polarization Isolation for the Operational Use of C-Band SAR Constellations in Maritime Surveillance. *IEEE Geosci. Remote Sens. Lett.*, 7(4):861–865.

[Tucker III et al., 2013] Tucker III, W. B., Perovich, D. K., Gow, A. J., Weeks, W. F., and Drinkwater, M. R. (2013). *Physical Properties of Sea Ice Relevant to Remote Sensing*, chapter 2, pages 9–28. American Geophysical Union (AGU).

[Vachon et al., 2004] Vachon, P. W., Monaldo, F. M., Holt, B., and Lehner, S. (2004). Chapter 5: Ocean surface waves and spectra. *Synthetic Aperture Radar Marine User's Manual (NOAA/NESDIS), C.R. Jackson and J. R. Apel*, pages 139–167.

[Valenzuela, 1978] Valenzuela, G. R. (1978). Theories for the interaction of electromagnetic and oceanic waves - a review. *Boundary-Layer Meteorology*, 13(1-4):61–85.

[van Zyl and Kim, 2010] van Zyl, J. and Kim, Y. (2010). *Synthetic Aperture Radar Polarimetry*. WILEY.

[van Zyl, 1990] van Zyl, J. J. (1990). Calibration of polarimetric radar images using only image parameters and trihedral corner reflector responses. *IEEE Trans. Geosci. Remote Sens.*, 28(3):337–348.

[Vespe and Greidanus, 2012] Vespe, M. and Greidanus, H. (2012). SAR image quality assessment and indicators for vessel and oil spill detection. *IEEE Trans. Geosci. Remote Sens.*, 50(11):4726–4734.

[Wang et al., 2018] Wang, Y., Qi, Q., and Liu, Y. (2018). Unsupervised Segmentation Evaluation Using Area-Weighted Variance and Jeffries-Matusita Distance for Remote Sensing Images. *Remote Sens.*, 10(8).

[Warren et al., 2014] Warren, C. J., MacFadyen, A., and Henry, C. (2014). Mapping Oil for the Destroyed Taylor Energy Site in the Gulf of Mexico. *International Oil Spill Conference Proceedings*, (1).

[Wei et al., 2019] Wei, S., Zhang, H., Wang, C., Wang, Y., and Xu, L. (2019). Multi-temporal SAR data large-scale crop mapping based on U-Net model. *Remote Sens.*, 11(1).

[Winebrenner et al., 1989] Winebrenner, D. P., Tsang, L., Wen, B., and West, R. (1989). Sea-ice Characterization Measurements needed for Testing of Microwave Remote Sensing Models. *IEEE J. Ocean. Eng.*, 14(2):149–158.

[Wismann et al., 1998] Wismann, V., Gade, M., Alpers, W., and Hühnerfuss, H. (1998). Radar signatures of marine mineral oil spills measured by an airborne multi-frequency radar. *Int. J. Remote Sens.*, 19(18):3607–3623.

[WMO-No.574, 2010] WMO-No.574 (2010). Sea-ice Information Services in The World. *Technical Report 574, World Meteorological Organization*.

[Wright, 1968] Wright, J. (1968). A new model for sea clutter. *IEEE Trans. Antennas Propag.*, 16(2):217–223.

[Xi et al., 2016] Xi, Z., Jie, Z., Meijie, L., and Junmin, M. (2016). Assessment of C-band compact polarimetry SAR for sea ice classification. *Acta Oceanol. Sin.*, 35(5):79–88.

[Yin et al., 2015] Yin, J., Yang, J., Zhou, Z., and Song, J. (2015). The Extended Bragg Scattering Model-Based Method for Ship and Oil-Spill Observation Using Compact Polarimetric SAR. *IEEE J. Sel. Topics Appl. Earth Observ. Remote Sens.*, 8(8):3760–3772.

[Zhang et al., 2011] Zhang, B., Perrie, W., Li, X., and Pichel, W. G. (2011). Mapping sea surface oil slicks using RADARSAT-2 quad-polarization SAR image. *Geophys. Res. Lett.*, 38(10).

[Zhang et al., 2016] Zhang, X., Zhang, J., Liu, M., and Meng, J. (2016). Assessment of C-band compact polarimetry SAR for sea ice classification. *Acta Oceanologica Sinica*, 35(5):79–88.

[Zhang et al., 2017] Zhang, Y., Li, Y., Liang, X. S., and Tsou, J. (2017). Comparison of oil spill classifications using fully and compact polarimetric SAR images. *Applied Sciences*, 7(2).